Synthesis of 1D Semiconductors

for Application in

Dye-Sensitized Solar Cells

Dissertation

zur Erlangung der Grades
„Doktor der Naturwissenschaften"
im Promotionsfach Chemie

am Fachbereich Chemie, Pharmazie und Geowissenschaften
der Johannes Gutenberg-Universität Mainz

JOHANNES GUTENBERG UNIVERSITÄT MAINZ

JG|U

Vorgelegt von

Patrick Leidich

geb. in Frankfurt am Main

Mainz, 2014

Dekan   ▉▉▉▉▉▉▉▉

Erster Berichterstatter: ▉▉▉▉▉▉▉▉▉▉

Zweiter Berichterstatter   ▉▉▉▉▉▉▉▉▉▉

Tag der mündlichen Prüfung   XX.XX.XXXX

II

Die hier vorliegende Arbeit wurde im Zeitraum von Dezember 2011 bis Oktober 2014 unter der Leitung von ████████████████████████ am Institut für Anorganische und Analytische Chemie der Johannes Gutenberg-Universität Mainz angefertigt.

Für meine Familie

Acknowledgements

List of Publications

[1] M. Siebold, **P. Leidich**, M. Bertini, G. Deflorio, J. Feldmann, E. M. Krupp, E. Halmschlager, Steve Woodward "Application of elemental bioimaging using laser ablation ICP-MS in forest pathology: distribution of elements in the bark of Picea sitchensis following wounding" *Analytical and Bioanalytical Chemistry*, **2012**, 402, 10, 3323-3331

[2] **Patrick Leidich**, Olga Linker, Martin Panthöfer, and Wolfgang Tremel, "Synthesis of single crystalline sub-micron rutile TiO2 rods using hydrothermal treatment in acidic media", *Crystal Engineering Communications*, **2014**, **16**, 8486-8491

[3] **Patrick Leidich**, Marc-Christian Müller, Aaron Gehl, Mihail Mondeshki, Martin Panthöfer, Wolfgang Tremel, "Mechanistic studies of hydrothermal growth of size-tunable tin(IV) oxide nanorods in aqueous HCl" *Zeitschrift für Anorganische und Allgemeine Chemie, submitted.*

[4] Michael Dietzsch, Renée Siegel, **Patrick Leidich**, Jürgen Senker, Wolfgang Tremel, "Stable Anhydrous Amorphous Calcium Carbonate Nanoparticles from Ionic Liquids" *submitted.*

[5] **Patrick Leidich**, Martin Panthöfer, Wolfgang Tremel, "Synthesis of Argutite GeO_2 sub-micron rods using a disintegration recrystallization process", *in preparation.*

[6] **Patrick Leidich**, Sanghyuk Wooh, Kookheon Char, Wolfgang Tremel, "Dye-sensitized Solar Cells from Anatase/Rutile Nanoparticle/Sub-Micron Rod Composite Electrodes: Influence of 1D Micro-Structures on the Device Performance", *in preparation.*

List of Content

List of Figures

List of Tables

Abstract

Initiated by their outstanding efficiency and concomitant low-cost, dye-sensitized solar cells (DSCs) represent a large field of research nowadays, as they also have a high potential for further industrial applications. DSCs show many interesting features, such that they are printable on transparent foil, which makes then light and flexible, and might enable them to be used in every-day items and therefore, they can also find application as portable power-supplies. All DSCs exhibit a photo-anode, consisting of a porous semiconductor and a dye, an electrolyte needed for regeneration of the dye, and two electrodes for charge collection. Several materials are suitable for the photo-anodes, important is not only the used compound, but also the morphology of the employed particles plays a crucial role for the efficiency of the DSC. On the one hand, the morphology has to exhibit a high surface area for dye adsorption, and, on the other hand, enable an efficient pathway to release the electrons from the device.

The present work focusses on the synthesis of such anisotropic semiconductors that enable the DSC to extract higher currents from the photo-anode. More precisely, this work is divided into two parts, the first aimed to investigate the growth of anisotropic micro- and nanostructured TiO_2 and SnO_2 as well as hybrid structures to combine the advantageous material's properties of TiO_2 and SnO_2. In the second part, these nanostructures were incorporated into photo-anodes and the impact of the anisotropic structures on the efficiency was tested. The growth of TiO_2 sub-micron rutile rods was established starting from a stable and easy to handle, solid state precursor via a disintegration-recrystallization process. The rods were analyzed using PXRD, TEM, DLS, and Raman spectroscopy. They were found to be single crystalline and size-tunable. The growth mechanism was identified to occur as a chemical transport reaction and was further investigated by taking snapshots and varying the reaction mixtures.The growth occurred when starting from nanomaterials that were instable against the reaction medium using HX (X = Cl, Br, I) as mineralizer. This technique was successfully transferred to SnO_2. Here, the single crystalline rods were found to grow in the range of 14 to 67 nm and were characterized by PXRD, TEM, and DLS. It was possible to trap the intermediate species of this chemical transport reaction, which was supposed to occur similar to this of TiO_2. The intermediate species was characterized by PXRD as well as Raman and ssNMR spectroscopy. Additionally, it was possible to establish a facile technique to grow anisotropic hybrid particles. Herein, the 1D structures of TiO_2 and SnO_2 served as template and were hydrothermally treated to yield hybrid structures with a 1D "core" and spherical TiO_2 nanoparticles of a size of about 5 nm on their surface as a "shell".

In the second part, the as-prepared particles were incorporated into photo-anodes and, subsequent to the functionalization with a dye, tested in DSCs. For TiO_2-based dye-sensitized solar cells, composite electrodes of rutile sub-micron rods and spherical anatase nanoparticles in various ratios were prepared to determine the most beneficial amount. It was possible to improve the efficiency by 34 % regarding the reference cell by incorporating 20 wt% rutile rods into the photo-anode. These solar cells were further characterized by electrochemical analysis indicating higher quantum efficiencies, charge

extraction, and electron diffusion coefficients for DSCs with rutile rods. For SnO_2-based dye-sensitized solar cells, it was proceeded analogously finding out that the highest efficiencies could be obtained with 100 wt% rods in the photo-anode. It could be shown that the nanorods synthesized following the chemical transport route did not perform well as DSCs although high quality electrode films and very high dye adsorptions could be achieved. The hybrid formation to $SnO_2@TiO_2$ particles, however, had a beneficial effect and was also characterized using electrochemical analysis showing an improved quantum efficiency and electron lifetime as compared to the reference.

Zusammenfassung

Seit ihrer ersten Beschreibung in 1991 sind Farbstoffsolarzellen zu einem wichtigen Forschungsthema gewachsen, was in ihren herausragenden Wirkungsgraden und den gleichzeitig geringen Herstellungskosten begründet liegt. Sie bieten viele interessante Eigenschaften und Herstellungsvarianten, so kann sie zum Beispiel auf transparente Folie gedruckt werden, sodass sie – leicht und biegbar – als transportierbare Stromquelle dienen können. Alle Farbstoffsolarzellen bestehen aus einer Photoanode, die ihrerseits aus einem porösen Halbleiter und einem Farbstoff besteht, einem Elektrolyt zur Regeneration des Farbstoffs, und zwei Elektroden, an denen der Strom abgegriffen wird. Generell sind verschiedene Halbleitermaterialien für die Anwendung als Photoanode gut geeignet, allerdings ist nicht nur die chemische Zusammensetzung an sich entscheidend, sondern auch die Morphologie der eingesetzten Partikel. Diese müssen auf der einen Seite eine hohe Farbstoffbeladung begünstigen, aber auf der anderen Seite auch effiziente Leiterstrukturen darstellen, sodass die generierten Ladungen möglichst verlustfrei an den Elektroden abgegriffen werden können.

Die vorliegende Arbeit beschäftigt sich mit der Optimierung effizienter Leiterstrukturen, um eine bessere Ladungsextraktion aus der Photoanode zu ermöglichen. Diese Arbeit ist in zwei Abschnitte unterteilt, zunächst wurde das Wachstum von anisotropen TiO_2 und SnO_2 Mikro- und Nanostrukturen, wie auch die Synthese von Hybridpartikeln, um die Eigenschaften beider Materialien zu kombinieren, untersucht. Im zweiten Teil wurden diese Partikel in Photoanoden inkorporiert und in Farbstoffsolarzellen getestet. Das Wachstum von einkristallinen TiO_2 Rutil Stäbchen mit einer mittleren Länge von 220 nm wurde ausgehend von einem festen und, bei Standardbedingungen, stabilen Ausgangsmaterial erreicht und erfolgte als Auflösung-Rekristallisationsprozess. Diese einkristallinen Stäbchen, deren Größe im Bereich von 80 nm und 1,3 µm einstellbar war, wurden mittels PXRD, TEM, DLS und Raman Spektroskopie untersucht. Die Voraussetzung an das Ausgangsmaterial, dass ein Wachstum erfolgt, war, dass es eine hohe Oberfläche aufwies und gegenüber der eingesetzten Säure instabil war. Dieses Wachstum, welches unter Verwendung von HX (X = Cl, Br, I) ablief, wurde als chemische Transportreaktion in Lösung identifiziert. Die Ergebnisse wurden von TiO_2 auf SnO_2 übertragen, sodass auch ein Wachstum von anisotropen Einkristallen, deren Länge kontrolliert werden

konnte, erfolgte. Hierbei gelang es, das Intermediat der chemischen Transportreaktion abzufangen und mittels PXRD, wie auch Raman und ssNMR Spektroskopie zu untersuchen. Des Weiteren war es möglich anisotrope Hybridpartikel in einem einfachen, hydrothermalen Verfahren herzustellen. Die Hybridpartikel bedienten sich der TiO_2 und SnO_2 Stäbchen als Kern, auf die sphärische TiO_2 Nanopartikel mit einer Größe von etwa 5 nm aufwuchsen.

Im zweiten Teil dieser Arbeit wurden aus den synthetisierten Partikeln Photoanoden hergestellt, und nach der Farbstoffbeladung, in Farbstoffsolarzellen vermessen. Bei TiO_2-basierten Farbstoff-solarzellen wurden Komposite aus Rutil Stäbchen und sphärischen Anatas Partikeln in verschiedenen Verhältnissen getestet. Hierbei war es, durch Inkorporation von 20 gew% Rutil Stäbchen, möglich den Wirkungsgrad um 34 % im Vergleich zur Referenz zu verbessern. Die Solarzellen mit den höchsten Wirkungsgraden wurden mittels elektrochemischer Analyse charakterisiert. Dies zeigte, dass durch den Einsatz anisotroper Strukturen die Quantenausbeute, Ladungsextraktion wie auch die Elektronendiffusionskoeffizienten verbessert wurden. Für SnO_2-basierte Farbstoffsolarzellen wurde analog vorgegangen, wobei hier Kompositelektroden keinen Vorteil boten; Elektroden, die 100 gew% Stäbchen beinhalteten, zeigten die höchsten Wirkungsgrade. Weiterhin ergaben die SnO_2 Stäbchen, die im sauren Milieu hergestellt wurden, nur geringe Wirkungsgrade, obwohl hohe Farbstoffbeladungen erzielt werden konnten. Allerdings war die Nutzung von $SnO_2@TiO_2$ Hybridpartikeln vorteilhaft, da diese in der elektrochemischen Analyse im Vergleich zur Referenz gesteigerte Quantenausbeuten und Elektronenlebenszeiten aufzeigten.

1

Introduction

1.1 General Interest

The world's population is constantly growing and requesting higher amounts of energy. Not only is the total amount of primary energy used rising due to the increasing population, but also the consumption of every individual is drastically increasing. The need for the energy of the population in China, a rising country, is about 16 000 kWh/person, while it lies at about 45 000 kWh/person in Germany. It is predicted that the consumption for China and other rising countries will drastically increase over the next years. In general, the overall consumption of primary energy arises annually by about 2.2 %, which leads to the fact that in 2008 more than double the amount of the energy was consumed as compared to 1971.[1] Worldwide, the production of energy relies on fossil resources for about 81 %, while another 6 % is represented by nuclear energy.[2] The remaining 13 % is produced by bio mass, hydroelectric power, and renewable energy sources, while the last represents only 0.8 %. The fossil energy sources have to be replaced soon, since most of them are predicted to last for no longer than 2050.[3] In addition, the increase of anthropogenic CO_2 has to be limited, given that it is the compound, which is mostly responsible for the greenhouse-effect.[4] Today, the alternatives to replace fossil energy sources by renewable energy sources are wind-, hydroelectric-, and solar-energy. The variety of materials that can convert solar light into electrical energy is huge, and was rising over the last decades. Materials, such as silicon, copper indium sulfides and selenides,[5–7] cadmium sulfides or tellurides,[8] were also developed and optimized for solar cell use. Still, the most commonly and commercially used material today is silicon. The drawback of silicon is that is has to be highly pure to be suitable for an application within a solar cell, which makes it an expensive material, although the raw material is rather cheap.[9]

1.2 Dye-Sensitized Solar Cells

A first step toward an affordable solar cell was done by Michael Grätzel and Brian O'Regan in 1991, as they published their results on a dye-sensitized solar cell (DSC), although the working principle and first patent has been around since the 1970s.[10,11] Ever since, the construction of DSCs has been a

_____

prominent topic of research and a constantly growing field. The first constructions of such devices were rather simple, while over time more and more components added up to produce high-efficiency cells. However, a basic DSC is easy to assemble and consists of only a few components:

(i)   Two transparent conductive glass sheets (TCOs), such as indium-doped tin oxide (ITO) or fluorine-doped tin oxide (FTO).

(ii)   A porous semiconducting layer, mostly composed of TiO_2, ZnO, Nb_2O_5, or SnO_2.

(iii)   A sensitizer to absorb visible light, commonly Ru-dyes are used, a standard dye is N719.

(iv)   A redox couple that acts as electrolyte, usually a solution containing the couple I^-/I_3^-.

The TCOs are used as substrate for both the photo-anode, which is the front-electrode, and the counter-electrode. A porous film of a semiconductor is sintered onto the TCO of the front electrode. This film usually consists of nanoparticles as small as or smaller than 10 nm, which results in a very large surface area that is crucial for the dye adsorption. Furthermore, this semiconducting layer is also needed for electron conduction. The dye acts as a sensitizer for visible light, while the electrolyte closes the electric circle with the counter-electrode and regenerates the dye. The counter-electrode is usually coated with a layer of Pt to catalyze the reduction of I_3^- to $3\ I^-$ to regenerate the electrolyte.[12]

The ideal working principle is as follows (Figure 1.1): (i) The dye or sensitizer S absorbs light and an electron is elevated into the excited state. (ii) The excited state has a higher energy than the conduction band of the semiconductor and, therefore, the electron is injected into the semiconductor. (iii) This injected electron travels through the porous semiconducting layer and is collected by the front-electrode. (iv) The oxidized sensitizer S^+, which is left behind after injection of an electron, is reduced by I^- in the electrolyte. (v) The formed I_3^- ions are regenerated to I^- at the counter-electrode.
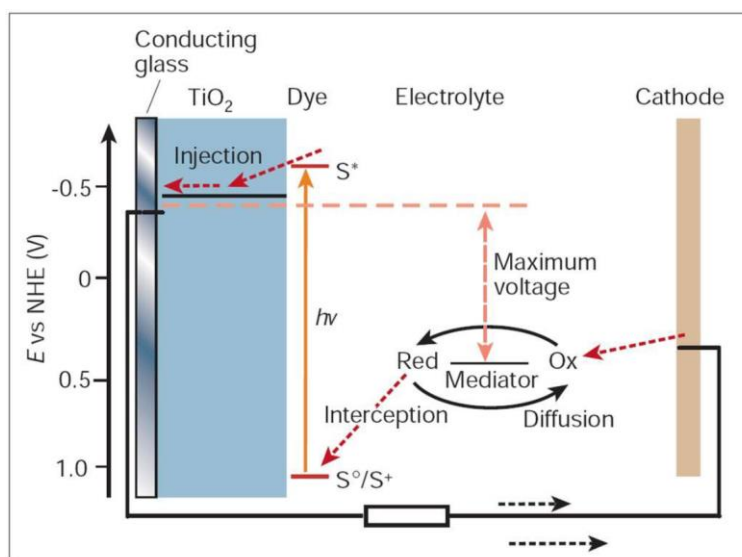
Figure 1.1 Working principle of a DSC in the corresponding energy scale against the normal hydrogen electrode. S^o and S^+ represent the sensitizer in its ground- and oxidized state. S* stands for the excited sensitizer.[13]

In theory, the maximum extractable voltage of such a device is given by the potential difference between the redox potential of the electrolyte and the semiconductor, from which the electron is injected into the TCO. The maximum obtained current is limited by the amount of adsorbed dye. In fact, many ways to lower the efficiency are possible and have to be suppressed in an efficient DSC. A high degree of defects in the semiconductor can decrease the obtained voltage by exposing a lower conduction band edge. However, a second path could be that the electrons are trapped in the defects. Additionally, the electrons in the semiconductor can recombine with the oxidized sensitizer, which is adsorbed on the surface and not yet reduced by the electrolyte. Also, a recombination of the electron in the semiconductor can easily recombine directly with available I_3^- to form I^-. Lastly, reduction of the electrolyte can also occur on the front-electrode if it is not masked by a blocking layer that is made by the same material as the porous semiconducting layer. During the pathway of the electron through the porous semiconducting layer, an electron has to pass through many particle-particle boundaries, considering the electrode has a certain thickness and the particles have a size of about 10 nm. Every boundary is a possible site where losses can occur due to recombination. The film thickness was best determined to be in the range between 8 - 12 µm, while here is the best compromise between a high light harvesting efficiency and the possible path length that an electron can walk.[14]

1.3 *J-V*-Characteristics of a Dye-Sensitized Solar Cell

To describe the performance of a solar cell, a few characteristics are of particular interest. Most interesting is the efficiency η, but also the obtained short circuit current I_{sc}, the short circuit current density J_{sc}, the open circuit voltage V_{oc}, the maximum Power P_m, and the fill factor FF.

The short circuit current is the total extracted current from the cell under short circuit conditions, which can be visualized by an electric circuit without any resistances, in which the current can flow without any losses. Thus, I_{sc} is dependent on the amount of adsorbed dye, which also correlates with the illuminated area. Therefore, the J_{sc} is introduced and defined as I_{sc} per area.

The open circuit voltage V_{oc} is the highest obtainable voltage, which can be visualized by an electric circuit with a very high resistance, in which no current flows. The power is the product of current and voltage, while only the power density P, the product of current density J and voltage V, is of interest concerning solar cells. The maximum power point P_m is reached when the product of current density and voltage maximizes. The corresponding current density and voltage are assigned to J_m and V_m. The fill factor is defined by

$$FF = \frac{V_m \cdot J_m}{V_{oc} \cdot J_{sc}}.$$

The efficiency η is described by the quotient

$$\eta = \frac{P_{out}}{P_{in}} = \frac{V_{oc} \cdot J_{sc} \cdot FF}{P_{in}}.$$

_____

Figure 1.2 shows a typical *J-V*-curve with all important characteristics marked: J_{sc} is represented by the intersection of the *J-V*-curve with the y-axis, while V_{oc} is represented by the intersection with the x-axis. In addition to the typical *J-V*-curve, the power density is plotted as a function of the voltage, which indicates the maximum power point P_m to be where the square underneath the *J-V*-curve maximizes.
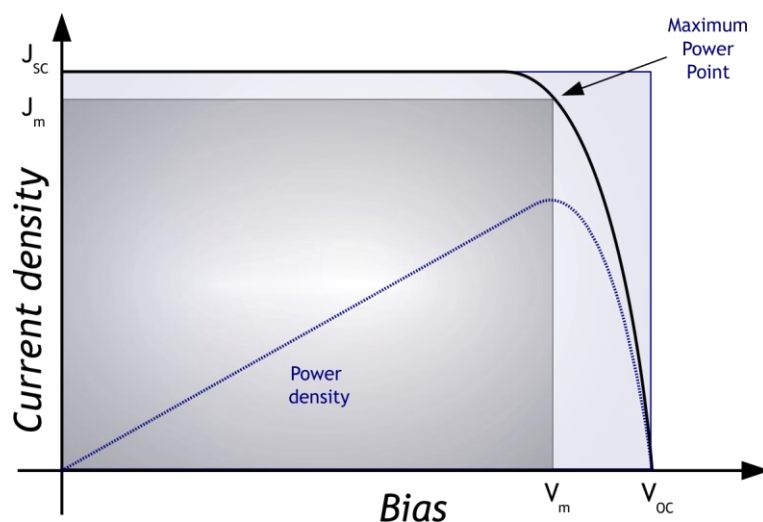
Figure 1.2 Schematic diagram of the solar cell characteristics visualizing a *J-V*-curve and *P-V*-curve. J_{sc} and V_{oc} represent the highest achieved current density and voltage. P_m is the point in the diagram where the maximum power can be extracted with the corresponding current density J_m and voltage V_m.[15]

1.4 Electrode Materials

Many materials are suitable to act as the porous semiconducting layer, while TiO_2,[16–18] ZnO,[19–21] Nb_2O_5,[22,23] and SnO_2[24,25] are the most prominent ones, due to their band edge positions and dye adsorption properties, as well as their electron conduction velocity, respectively. During the course of this work, only TiO_2 and SnO_2 will be the topic of research. These two compounds exhibit the best known chemistry as well as DSC characterization and, at the same time, show a very similar chemical behavior due to a few reasons: Ti and Sn both have four free electrons in their outer electron shell and exhibit similar radii as Ti^{4+} and Sn^{4+} and, therefore, also similar chemical behavior.[26] Nevertheless, a few differences in their oxides are still present. TiO_2 is known in three different crystal structures, rutile, anatase, and brookite. All three show different features concerning their stability and the properties of later DSCs. Rutile is the thermodynamically stable phase for crystallites larger than 10 - 18 nm, depending on their chemical surrounding. Anatase is meta-stable, but becomes thermodynamically stable in the regime smaller than 10 - 18 nm. It exhibits a larger band-gap, higher conduction band edge, and faster electron conduction as compared to rutile. Brookite has the highest conduction band edge of all three, but plays no role in the application of DSCs due to its instability and challenging preparation.[27] In contrast, SnO_2 only crystallizes in the form of the mineral cassiterite, which is a rutile-type crystal structure. The advantage of SnO_2 is that it offers an extraordinarily fast electron conduction of

_____

magnitudes higher than anatase-TiO$_2$. The disadvantages are the lower conduction band edge and the high degree of combinatorial losses.[28–30] The position of the band-gap edges of SnO$_2$, anatase TiO$_2$, and the excited state of the Ru-dye N719 can be seen in Figure 1.3.
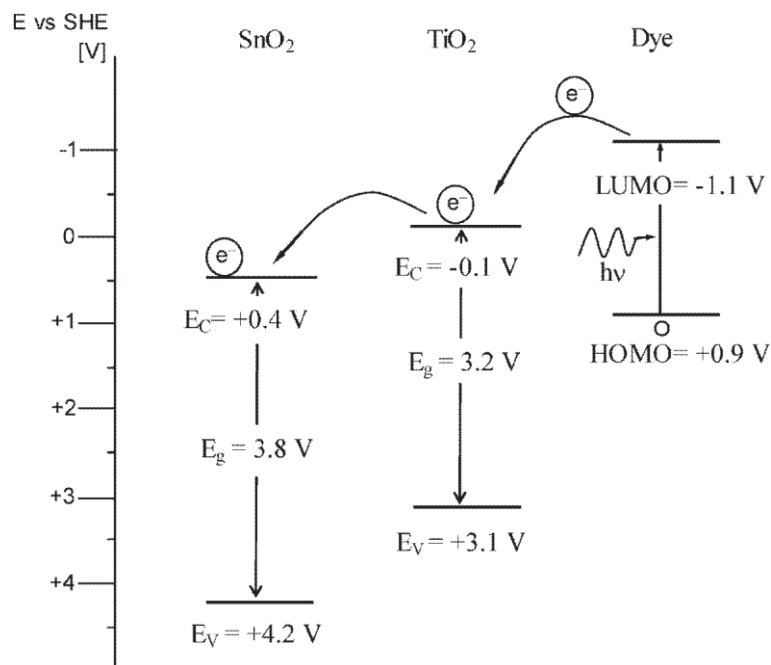
Figure 1.3 Band-gaps and band positions TiO$_2$ and SnO$_2$, as well as the potential of HOMO and LUMO of the Ru-dye N719. The possible electron path is indicated by the arrows from the dye to TiO$_2$ and, finally, SnO$_2$.[25]

The motivation for this work focused on the design of novel 1D semiconductors and their applicability to DSCs. These structures should enable a fast electron conduction and a reduced recombination rate. The main attention was drawn onto the two compounds of TiO$_2$ and SnO$_2$. In principle this thesis is divided into two parts. The first part, Chapters 2 - 4, describe the synthesis, development, and characterization of the used particles. The second part, Chapters 5 and 6, deals in detail with the application of the synthesized particles in DSCs.

Chapter 2 describes the synthesis and characterization of TiO$_2$ sub-micron rods. These rods turned out to be phase-pure and single-crystalline. Additionally, the length of the rods can be altered by adjusting of the acid concentration. Various acids were evaluated to enable this reaction, while it turned out that only HCl, HBr, and HI were able to facilitate the formation of TiO$_2$ sub-micron rods. The employed precursors revealed that a growth could only occur when a certain instability against the employed acid was present. A $[TiCl_6]^{2-}$ ion or a similar hydrated or hydroxylated specie was assumed to be responsible for the found growth mechanism via a disintegration-recrystallization process.

Chapter 3 transfers the procedure optimized for TiO$_2$ to SnO$_2$. Herein, a similar reaction pathway could be found. It was possible to establish a growth of single-crystalline SnO$_2$ nanorods when using HCl, HBr, or HI as a mineralizer acid. The nanorods were size-tunable and phase-pure. It was possible to trap the intermediate species in the disintegration-recrystallization process, which proceeded similarly

_____

to the one of TiO_2, by addition of a sterically demanding cation. This intermediate was analyzed by various methods such as ssNMR spectroscopy, Raman spectroscopy, as well as PXRD and was determined to be $[SnCl_5H_2O]^-$.

Chapter 4 describes the pathway to form 1D hybrid particles starting from a 1D single-component material. It was meant to be a second reaction step following the rod formation in Chapters 2 and 3. Various methods were tested to perform a hybrid formation, yielding hybrid particles that were completely covered with a "shell" of TiO_2 and did not form excessive TiO_2. Additionally, the employed methods should yield a large amount of product and a constant appearance of hybrid particles. It was shown that it was possible to form $SnO_2@TiO_2$ and $TiO_2@TiO_2$ hybrid particles in a facile reaction. The final particles exhibited a thin "shell" of spherical TiO_2 nanoparticles enclosing the 1D "core".

Chapter 5 is concerned with the formation of photo-anodes out of the synthesized particles based on TiO_2 as the main component. The use of composite electrodes of spherical anatase nanoparticles and rutile sub-micron rods was shown to be beneficial as compared to the single component DSCs. The most advantageous content of 1D structures was determined to be in-between 10 wt% and 20 wt% rutile sub-micron rods and was further characterized using electrochemical analysis. Additionally, the hybrid particles were tested upon their suitability for DSCs. In a brief Excursus, it was shown that the synthesized particles are promising for optimization of the electrode films toward thinner solid-state devices using perovskites, such as $CH_3NH_3PbI_3$, as sensitizers.

Chapter 6 discusses the application of SnO_2 nanoparticles in DSCs. As a first step, an optimization by employing composite electrodes was tested. For this purpose, composite films were made containing spherical and 1D nanoparticles, functionalized with the Ru-dye N719, and tested as DSCs. In a second step, particles that were not yet known in literature, *i.e.* acidic SnO_2 nanorods and $SnO_2@TiO_2$ hybrid particles, were employed in electrodes and their properties in DSCs were evaluated by *J-V*-measurements, as well as further electrochemical analysis. Herein, it was shown that the use of the second reaction step from bare acidic SnO_2 nanorods toward $SnO_2@TiO_2$ hybrid particles had a beneficial effect on the efficiency and showed a behavior that was in-between this of SnO_2 and TiO_2, in concerns of V_{oc}, J_{sc}, charge extraction, and quantum efficiency.

1.5 References

1   International Energy Agency, World Energy Outlook, **2010**.
2   International Energy Agency, Key World Energy Statistics, **2010**.
3   Bundesministerium für Wirtschaft und Technologie, Ausgabe August **2010**
4   E. Monnin, E. J. Steig, U. Siegenthaler, K. Kawamura, J. Schwander, B. Stauffer, T. F. Stocker, D. L. Morse, J.-M. Barnola, B. Bellier, D. Raynaud and H. Fischer, *Earth Planet. Sci. Let.*, 2004, **224**, 45–54.
5   L. Li, A. Pandey, D. J. Werder, B. P. Khanal, J. M. Pietryga and V. I. Klimov, *J. Am. Chem. Soc.*, 2011, **133**, 1176–1179.

6   N. Naghavi, S. Spiering, M. Powalla and D. Lincot, *Prog. Photovolt. Res. Appl.*, 2003, 437–443.

7   P. Liska, K. R. Thampi, M. Grätzel, D. Brémaud, D. Rudmann, H. M. Upadhyaya and A. N. Tiwari, *Appl. Phys. Lett.*, 2006, **88**, 203103.

8   D. Liu and P. V. Kamat, *J. Phys. Chem.*, 1993, 10769–10773.

9   S. R. Wenham and M. A. Green, *Prog. Photovolt. Res. Appl.*, 1996, 3–33.

10 B. C. O'Regan and M. Grätzel, *Nature*, 1991, 737–740.

11 H. Gerischer, M. E. Michel-Beyerle, F. Rebentrost and H. Tributsch, *Electrochim. Acta*, 1968, **13**, 1509–1515.

12 A. Hagfeldt, G. Boschloo, L. Sun, L. Kloo and H. Pettersson, *Chem. Rev.*, 2010, **110**, 6595–6663.

13 M. Grätzel, *Nature*, 2001, 338–344.

14 M. Ihara, M. Kanno and S. Inoue, *Phys. E*, 2010, **42**, 2867–2871.

15 A. Birkel, Johannes Gutenberg-Universität Mainz, 2012.

16 S. Nakade, Y. Saito, W. Kubo, T. Kitamura, Y. Wada and S. Yanagida, *J. Phys. Chem. B*, 2003, **107**, 8607–8611.

17 N. J. Cherepy, G. P. Smestad, M. Grätzel and J. Z. Zhang, *J Phys Chem B*, 1997, 9342–9351.

18 van de Lagemaat, J. and A. J. Frank, *J. Phys. Chem. B*, 2000, **104**, 4292–4294.

19 E. Galoppini, J. Rochford, H. Chen, G. Saraf, Y. Lu, A. Hagfeldt and G. Boschloo, *J Phys Chem B*, 2006, **110**, 16159–16161.

20 J.-J. Wu, G.-R. Chen, H.-H. Yang, C.-H. Ku and J.-Y. Lai, *Appl. Phys. Lett.*, 2007, **90**, 213109.

21 M. Saito and S. Fujihara, *Energy Environ. Sci.*, 2008, **1**, 280.

22 S. G. Chen, S. Chappel, Y. Diamant and A. Zaban, *Chem. Mater.*, 2001, **13**, 4629–4634.

23 K. Sayama, H. Sugihara and H. Arakawa, *Chem. Mater.*, 1998, **10**, 3825–3832.

24 C. Prasittichai and J. T. Hupp, *J. Phys. Chem. Lett.*, 2010, **1**, 1611–1615.

25 S. Gubbala, V. Chakrapani, V. Kumar and M. K. Sunkara, *Adv. Funct. Mater.*, 2008, **18**, 2411–2418.

26 Y. Zhao, J. Liu, L. Shi, S. Yuan, J. Fang, Z. Wang and M. Zhang, *Appl. Catal. B*, 2011, **103**, 436–443.

27 D. Reyes-Coronado, G. Rodríguez-Gattorno, M. E. Espinosa-Pesqueira, C. Cab, R. de Coss and G. Oskam, *Nanotechnology*, 2008, **19**, 145605.

28 A. Green, E. Palomares, S. Haque, J. Kroon and J. Durrant, *J Phys Chem B*, 2005, **109**, 12525–12533.

29 A. J. Frank, N. Kopidakis and Lagemaat, Jao van de, *Coord. Chem. Rev.*, 2004, **248**, 1165–1179.

30 A. Kay and M. Grätzel, *Chem. Mater.*, 2002, **14**, 2930–2935.

_____

2

Growth of Titanium Dioxide Sub-Micron Rods

This Chapter partly contains a reproduction adapted from Crystal Engineering Communications **2014**, 16, 8486 - 8491, reproduced by permission of the Royal Society of Chemistry Copyright 2014.[1]

2.1 Introduction

Titanium dioxide, TiO_2, is one of the most widely used metal oxides with a broad range of applications including bio-separation,[2] sensors,[3] energy storage,[4] solar cells,[5,6] catalysis and photo-catalysis.[7,8] It is abundant and cheap, chemically stable and non-toxic, while having a relatively high photo-catalytic activity. Therefore, TiO_2 has been intensively studied and used as a photo-catalyst in both fundamental research and practical applications,[9–14] such as coatings for self-cleaning surfaces,[15,16] as photo-catalyst for water splitting,[7,8,13,15] and as photo-anodes in dye-sensitized solar cells.[5,6,15,16]

TiO_2 is polymorph, exhibiting the crystal structures of rutile, anatase, and brookite, while rutile is the only stable phase in the phase diagram. Anatase and brookite are metastable. Banfield and co-workers investigated the phase stability of TiO_2 as a function of its particle size and demonstrated that rutile as a bulk material is more stable than anatase.[17–19] A crossover in stability to anatase occurs for particle sizes smaller than 14 nm due to the surface energy contribution.[17–20] Furthermore, initial size effects are crucial for the transformation behavior of a mixture of anatase (5.1 nm) and brookite particles (8.1 nm). In a first step, anatase transforms to brookite and rutile, and subsequently single-phase rutile is formed.[21] Wet chemical preparation methods for TiO_2 generally favor the formation of anatase.[21–24] Therefore, anatase nanoparticles can easily be made. Brookite is more difficult to synthesize, therefore, it has no important industrial applications so far.

Structural stability of crystals can be predicted and explained using the Pauling rules, however, the nucleation and growth of the different TiO_2 polymorphs are determined by the precursor chemistry, *i.e.* the reactants.[25–31] However, the kinetics of particle formation are related to the broad variety of experimental conditions used for the synthesis of the different TiO_2 phases, which make a comparison of formation mechanisms difficult.

The material's properties of TiO_2 nanoparticles are a function of crystal structure, nanoparticle size, and morphology, and therefore, strongly dependent on the method of synthesis.[22,23,32] Wet chemical

approaches use high boiling organic solvents with detergents, such as SDS and CTAB, to acquire control over size and morphology. Anatase nanoparticles have been made from aqueous solution, starting from titanium alkoxide precursors, where single-phase anatase nanoparticles with diameters ranging from 6 - 30 nm were formed under acidic and basic conditions.[33] In strong acids, the product usually contained a large fraction of brookite nanoparticles.[34,35] Larger anatase particles are difficult to prepare because of the phase transformation to rutile due to the surface to bulk energy ratio. Single-phase brookite particles (0.3 - 1 μm) have been prepared by hydrothermal treatment of amorphous titania in NaOH.[36] The mechanism is related to the formation of sodium titanate, which subsequently transforms to TiO_2.[37–44] Brookite nanoparticles in the size range of 5 - 10 nm were obtained by thermolysis of $TiCl_4$ in aqueous HCl,[31] where the phase composition of the reaction product was dependent on the Ti/Cl ratio. Phase mixtures with a brookite content of 80 % could be obtained for Ti/Cl ratios of 17 - 35. The brookite nanoparticles could be separated by selective precipitation of rutile. For higher Ti/Cl ratios, pure rutile particles were obtained. Phase-pure rutile nanoparticles have been prepared from $TiCl_4$, $TiCl_3$ in HCl, or from titanium isopropoxide in nitric acid.[28,29,45,46] Recently, synthetic methods for the three phases have been compared to determine the effect of crystal structure on the physical properties.[30,47] An understanding of the key parameters determining phase selection and crystal growth is crucial for a successful technological application of TiO_2.

Here, we present a fast and facile one-pot synthesis of rutile sub-micron rods using the microwave-assisted hydrothermal treatment method. These sub-micron particles are single crystalline, and, moreover, it was possible to tune the length of the sub-micron rods by adjusting the acid concentration. The approach using a microwave-assisted hydrothermal treatment was utilized to gain insight into the growth of the rutile rods and also to propose a mechanism and to identify the driving force behind their formation. Compared to conventional hydrothermal reactions in stainless steel autoclaves, microwave-assisted reactions offer several advantages, such as rapid heating, due to a direct response of the solvent to microwaves, and short cooling cycles, due to the lower heat capacity of the reaction vessel. Owing to the fast cooling time, it is possible to quench the reaction to take "snapshots" of the reaction. *Ex-situ* structural investigation of the reaction intermediates enables us to gain information concerning the rod formation (*i.e.* morphological, chemical, and crystallographic). Another advantage of the microwave-assisted reaction are short reaction times of 1 - 2 h[44,48] as compared to conventional hydrothermal reactions that require typically 24 h or more.[37–42,49–51] The resulting rutile sub-micron rods are suitable for various applications, such as photo-catalysis and electrodes for dye-sensitized solar cells.

2.2 Synthesis of Single Crystalline Rutile Sub-Micron Rods

Methods using a hydrothermal treatment to obtain nano- or sub-micron-structured titania (TiO_2) of the two most prominent titanium oxides, anatase and rutile, are numerous.[52,53] To investigate a growth

starting from nano-structured titania powder, an acidic route employing HCl as mineralizer and reactant was chosen. TiO_2-P25 was used as titania precursor, mixed with 6 M HCl, and treated by a fast heating microwave-assisted hydrothermal method. After a reaction time of 90 min and a working pressure of 30 bar, a white powder was obtained in this facile one-pot synthesis. The precursor TiO_2-P25 was composed of the crystalline TiO_2 phases anatase and rutile. We determined the mixture to contain 87.3(6) wt% anatase and 12.6(6) wt% rutile by powder X-ray diffraction, as can be seen in the appendix in Figure A1 and Table A1. The crystallite sizes were modeled to 41(1) nm and 70(2) nm for the two phases, respectively. This precursor is made by fuming the liquid Ti^{4+} precursor $TiCl_4$ using a continuous injection into a flame behind the torch. The precursor decomposes immediately, and the TiO_2 powder can be collected in the area directly behind the flame. By varying the gas flow through the torch and the flow rate of the liquid precursor, it enabled Evonik (formerly Degussa) to change the particle sizes (Aeroxide TiO_2 P25 or P90). Nevertheless, through this production method, only a short heating time is realized, since the resulting powder immediately leaves the heated region. Therefore, the resulting particles are poorly crystalline. It exhibits the crystalline phases anatase and rutile, though different ratios are obtained. Additionally, up to 13 wt% of the mixture could be shown to be amorphous.[54] Due to this preparation method and the low crystallinity, it served as superior precursor, since the powder was easy to handle, did not require humidity or oxygen free atmosphere, and retained a high reactivity.

The powder X-ray diffraction pattern was modeled by Rietveld refinement (see Figure 2.1). The diffraction data of the product revealed the major phase of 96.5(5) wt% to be rutile with calculated crystallite sizes of 221 (6) by 112 (1) nm. Minor impurities of anatase (3.5(5) wt %) could be detected via PXRD as well.

Figure 2.1 Rietveld refinement (black line) of the X-ray powder diffraction data (red dots) and residuum (red line) of rutile sub-micron rods after a microwave-assisted hydrothermal treatment for 90 min. The black ticks indicate the reference diffraction positions of rutile, while the red ticks show the reflex positions of anatase. The structure modeling according to the PXRD-data was performed by ████████████.

_____

As a complemetary technique to X-ray diffraction, Raman spectroscopy was performed. In Figure 2.2 the Raman spectra of the obtained rutile particles, as well as two references of anatase-type and rutile-type TiO_2, are displayed. The most intense band of anatase-type TiO_2 was found at 144 cm^{-1}. This band was further identified in the spectrum of the investigated rutile sub-micron rods, confirming the presence of traces of anatase in the product. The Raman band at 144 cm^{-1} was found to be usually about ten-fold stronger than every other Raman band found in all TiO_2 crystal structures. The fact that only a very weak Raman peak was found in the hydrothermally treated samples indicated the low amount of anatase present in these samples. The rather broad bands at 440 and 610 cm^{-1} were assigned to the E_g and A_{1g} phonons of the TiO_2 rutile structure. Melendres *et al.* investigated compacted samples of nanostructured titania regarding their band evolution upon thermal treatment dependent on the grain size of the precursor material. They found that the band width was not mainly a function of grain size, meaning the broadening was not caused by Raman scattering of surface phonons. Moreover, they described the band width as a result of internal defects of the investigated titania powders. The origin of the broad band found at 240 cm^{-1} has been frequently discussed, since it is not caused by one of the four Raman-active zone center ($k = 0$) phonons. Several explanations were proposed, including a disorder induced band.[55]
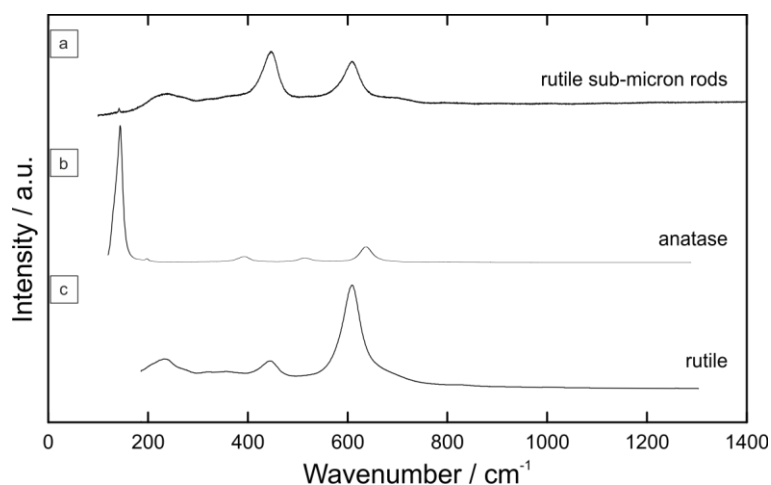
Figure 2.2 Raman data obtained from rutile sub-micron rods (top) and reference Raman data of anatase (center ID R0777055582) as well as rutile (bottom, ID R110109). Reference data originates from rruff-database. The measurements were performed by ███████.

TEM measurements revealed that the samples were rod shaped, as displayed in Figure 2.3. The titania sub-micron rods had a length between 100 and 400 nm. Figure 2.3a) shows an overview image of titania rods. The rods were composed of rutile and exhibited different lengths and widths. The sizes determined by PXRD gave the mean value of sizes averaged over the ensemble, which did fit to the mean sizes determined by TEM. It has to be considered that the size variation ranged from 100 to 400 nm. It happened regularly that twinned particles could be observed, while the existence of triple-, four-, and five-fold twinned particles could also be found, but only very rarely as compared to single-twinned particles. Figure 2.3b) displays a closer image of one rod, exhibiting well-formed facets. Figure 2.3c)

shows a close-up image of the tip of a rod, also displaying the lattice fringes of the crystal. The lattice distance was determined to be 3.25 Å, which fits to a growth in the c-direction. This image also demonstrated the high crystallinity up into the very tip of the rod.
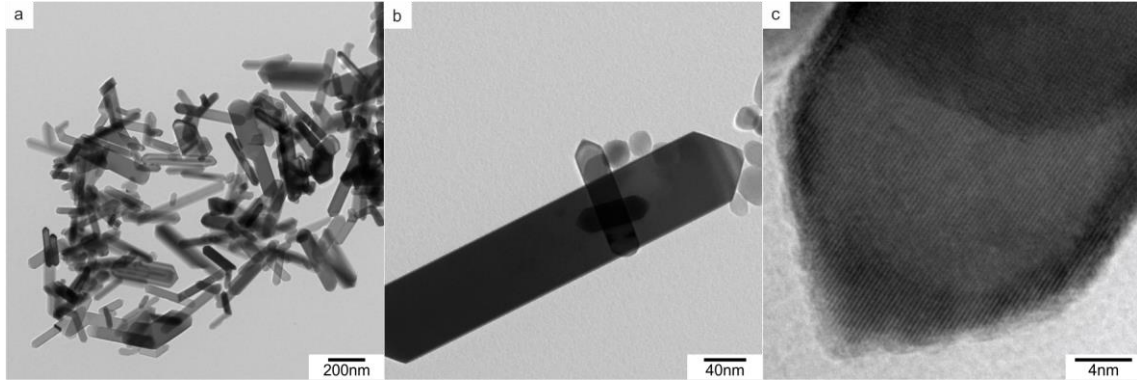
Figure 2.3 TEM image of rutile sub-micron rods obtained after a treatment time of 90 min: a) shows an overview image of several sub-micron rods, b) a well-faceted rod, and c) a close-up image of the tip of a sub-micron rod.

Electron diffraction of various sub-micron rods was performed. The selected area electron diffraction (SAED) patterns and corresponding TEM images are displayed in Figure 2.4. The first image (Figure 2.4a)) displays two particles, one of which was twinned, and the corresponding SAED pattern as inset. For Figure 2.4b) the most intense reflection in the electron diffraction pattern was chosen (inset), and the corresponding dark-field TEM image recorded. The domains that cause this reflex appear bright in the TEM image. The two aligned rods belong to this reflex. These two particles were oriented next to each other and, therefore, the reflection position coincided for both particles. Choosing one reflection of the set of reflections in the inset in Figure 2.4a) that did not fit to the most intense reflection led to Figure 2.4c). Here, the domain belonging to the second part of the twinned particle was shown bright, indicating that this set of reflections belongs to the second part of the crystal twin. Due to its different orientation, the reflection positions did not coincide with the other two crystalline domains. In addition to the well-formed facets, the SAED images and dark-field images confirm the particles to be single-crystalline. As further confirmation, nano-electron diffraction and a corresponding HR-TEM image can be seen in the Appendix (Figure A2). Here, a high angle annular dark field transmission electron microscopy (HAADF TEM) image of a single rod is displayed. Electron diffraction was measured at both tips and the shaft of the rod. All three diffraction patterns subsided and, therefore, confirm the single crystallinity.

_____
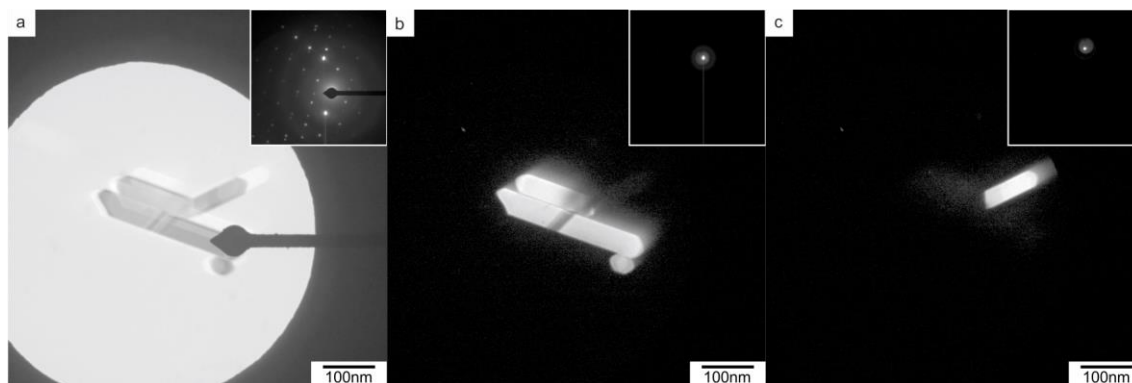
Figure 2.4 TEM images and corresponding electron diffraction patterns: a) bright-field TEM image of two sub-micron rods, one of them was twinned, with the corresponding selected area electron diffraction (SAED) pattern as inset, b) dark-field TEM image resulting after reflex picking, the chosen reflex was the most intense reflection, as shown in the inset, c) dark-field TEM image of the second part of the twinned particle made by picking another reflection, which did not belong to the set of the most intense reflection (shown in inset). The measurement was conducted by ███████████████.

Rutile sub-micron rods with a mean length of 221 nm, as calculated from PXRD data, were dispersed in DMSO and analyzed using dynamic light scattering (DLS). The possibility to measure DLS showed that the dispersion was stable for at least 30 min, which is unexpected for particles of this size. Figure 2.5 shows the results of the measurements. In a) the apparent diffusion coefficient is plotted as a function of the scattering vector q^2, where a linear fit with a positive slope can be seen. Thus, the diffusion coefficient was dependent on the scattering angle, which indicates the sample to be polydisperse as can be seen in a): This observation further confirms TEM results as previously described. The hydrodynamic radius was determined to be 200.5 nm $\pm$ 3.9 nm using the Stokes-Einstein equation while assuming a pseudo-spherical geometry. The sizes determined by DLS are about 1.8-fold larger than by XRD. This increase can be attributed to solvation and aggregation of particles in solution. Additionally, a rotational component of the diffusion coefficient could be determined indicating the particles to be anisotropic. In Figure 2.5b) the autocorrelation functions for the angles 30°, 90°, and 120° with the according bi-exponential fitting functions are displayed. It can be seen that all function correlate at similar correlation times, which indicates the sample to not be strongly aggregated. Aggregation would lead to a shift to higher correlation times for small angles due to the angular dependence of the particle form factor, which weights larger particles more strongly at small angles than at large angles.[56]
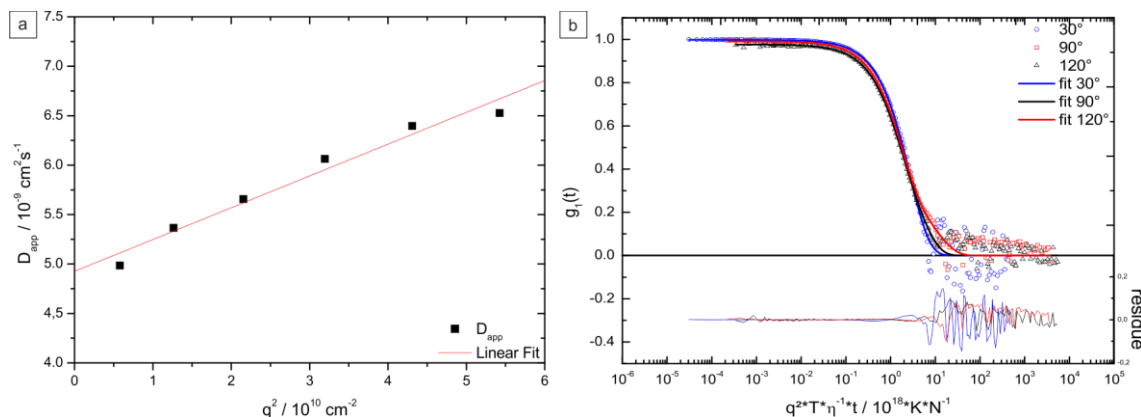
Figure 2.5 Dynamic light scattering results of sub-micron rutile rods dispersed in DMSO. a) Apparent diffusion coefficients as a function of the scattering vector q^2 in the range of $30° \leq \theta \leq 120°$, b) universally-scaled and normalized field autocorrelation functions measured at $30°$, $90°$, and $120°$, together with bi-exponential fitting functions and appending residues. The measurement and data treatment was performed by ▮▮▮▮▮▮▮.

These results were achieved by employing a hydrothermal treatment of TiO_2-P25 and 6 M HCl within a duration of 90 min at a working pressure of 30 bar. In this reaction, polydisperse rutile single crystals with well-formed facets and a length of 100 - 400 nm were generated.

By changing the concentration of HCl, it was possible to gain a certain control over the length of the resulting sub-micron rods. Using 3 M HCl led to a growth of shorter rods of a length of 80 - 120 nm, while using concentrated HCl (12 M) led to rods of a length of 500 nm - 1.3 µm (Figure 2.6). There were probably several reasons for that, *i.e.* the precursor material dissolved faster in higher concentrated HCl, and, therefore, larger amounts of Ti^{4+} were available, forming longer TiO_2 particles. Cl^- ions were already reported to facilitate the formation of rutile particles. In acidic medium, TiO_2 is known to exhibit positively charged surfaces.[46,57] The available anions perform a directing effect on the growth of TiO_2 particles by surface attraction. Here, SO_4^{2-} is known to have a directing effect to grow anatase particles, however Cl^- promotes a growth of rutile-type particles. Thus, HCl did not only dissolve the precursor, but Cl^- also served as mineralizing agent. High concentrations of HCl clearly increased the velocity of the reaction: using 12 M HCl, the precursor material was already depleted after less than 80 % of the time, as compared to the reaction using 6 M HCl. In contrast, using lower concentrations of HCl, the reaction velocity was decreased, and, therefore, reaction time had to be increased to have a quantitative reaction. The aspect ratio d_{length}/d_{width} changed as compared to the standard reaction conditions using 6 M HCl upon variation of the HCl concentration: increasing the concentration to 12 M, the ratio grew as well, while lowering the concentration to 3 M decreased the ratio. When HCl concentrations of 2 M or less were employed, no reaction occurred. The lower HCl concentration was not sufficient for the TiO_2-P25 precursor to dissolve under hydrothermal conditions, and, therefore no reaction took place.

_____
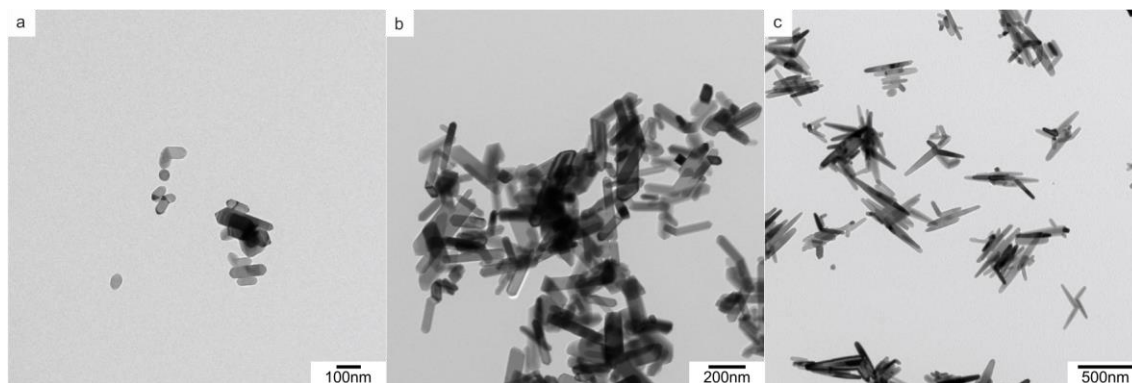
Figure 2.6 TEM images of sub-micron rods using different acid concentrations, which led to a variation in length of the resulting rods. The higher the used acid concentration was, the longer the resulting rods became. The used acid concentrations were a) 3 M, b) 6 M, and c) 12 M, respectively.

2.3 Growth Mechanism and Snapshots of Rutile Sub-Micron Rods

Although classical hydrothermal treatments are employed in many fields of synthetic chemistry, the understanding of hydrothermal reactions in general, as well as particularly the prediction of the product remains challenging. Properties of the solvent change drastically, and, hence, its ability for stabilization and possibility to undergo reactions change.[58] So far, there is neither a model to simulate the exact behaviors of solvents and reactants, nor a model for product prediction. Today autoclaves, automatically taking samples during the reaction, are available, giving the opportunity to analyze snapshots of the reaction in a classical hydrothermal treatment, and, therefore, gain more insight into the "black box" of hydrothermal treatment.

Herein, a different approach was chosen: a fast heating method was employed in a microwave-assisted hydrothermal treatment. Moreover, not only is the heating procedure very quick due to the self-heating effect of the solvent induced by microwaves, but also the cool-down rates are high, as a consequence of the low thermal capacity of the reaction vessel. Cooling down from 240 °C to room temperature is possible in less than 30 min, meaning this technique enables a quenching of the reaction. In this part, snapshots of the reaction using TiO_2-P25 and 6 M HCl were taken and the results are discussed. Unless stated differently, the ramping time up to a pressure of 30 bar was kept at 10 min (30 bar are equal to a temperature of about 230 - 240 °C).

In Figure 2.7 TEM images and XRD patterns of the most important snapshots are displayed, as they indicate different stages during the reaction: a) after the ramping time, b) after the initial 15 minutes during the common growth and c) after the completed reaction. In Figure 2.7a) the reaction was quenched immediately after the ramping time. It was evident that the reaction already started during the ramping time: the first rods were formed, but the precursor material was still the main fraction. Additionally, the rutile fraction increased from 13(6) wt% in the precursor to 36(1) wt%, according to the modeled PXRD data (Figure 2.7g), see also in the Appendix Table A1 and Figure A1). Also, the

mean crystallite size for the rutile crystals increased from 70(2) nm to 111(4) nm. After a reaction time of 15 min (Figure 2.7b) and f)), plenty well-formed rods were already obtained. The fraction of rutile increased simultaneously to 60(2) wt% with a size of 135(4) nm. After a reaction time of 90 min (Figure 2.7c) and e)), all precursor was depleted with respect to the TEM images, and the reaction was considered to be completed. The samples then had a rutile fraction of 96.5(5) wt% and a crystallite size of 221(6) nm. Thereby, all mentioned crystallites were anisotropic and also modeled accordingly; all sizes refer to the length of the sub-micron rods.

Replacing HCl by HBr was another way to decelerate the reaction velocity, which is displayed in Figure 2.7d). Now, agglomerates were found, while first rods were present as well. Comparing these agglomerates to the images in Figure 2.7a) and b) revealed that they were also present when HCl was used as acid. It was suggested that these agglomerates occur at the beginning of the reaction: the precursor dissolved to form an instable intermediate, which decomposed again to form rutile rods. It was considered to grow in a short-distance chemical-transport-reaction in solution. It was assumed that the agglomerates were the center of the chemical transport reaction, during quenching they formed blurry, supposable amorphous boundaries by decomposing the formed intermediate species. Due to a lack of possibility to purify the sample to only yield these agglomerates and the short distance to remaining other material, further investigation using electron diffraction was not possible.
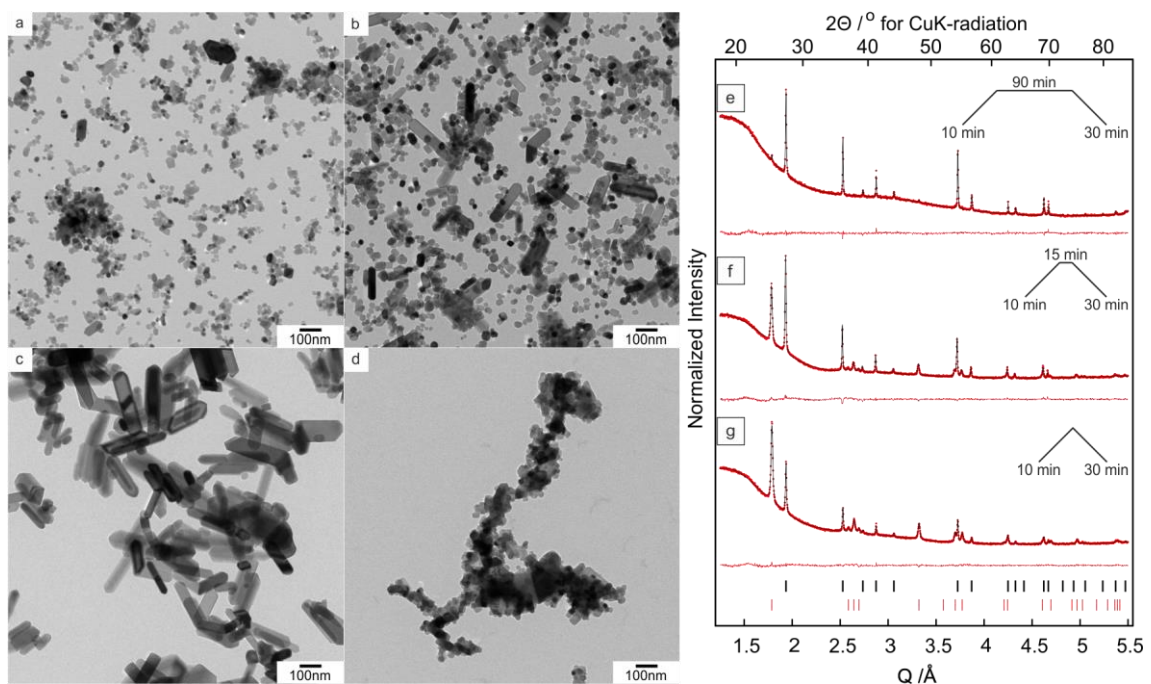
Figure 2.7 Reaction snapshots after ramping time only (a), 15 min heating time (b), and after 90 min heating time (c). Image d) displays an intermediate obtained by replacement of HCl by HBr, and, therefore, a reduced reaction velocity. XRD-patterns on the right (e - g) c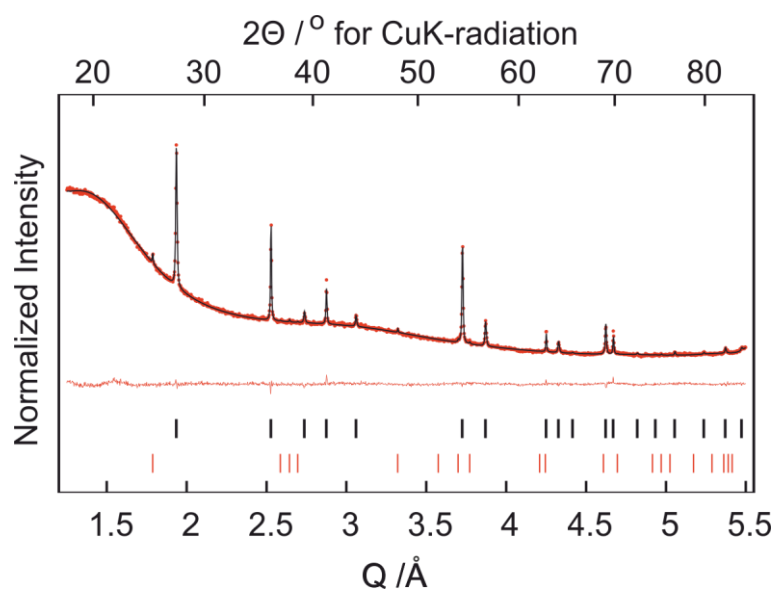orrespond to the TEM images of the reaction snapshots in c) - a), insets show heating profiles. Rietveld refinement (black line) of the X-ray powder diffraction data (red dots) and residuum (red line) of the samples. The black ticks indicate the reference diffraction positions of rutile, while the red ticks show the reflex positions of anatase. The modeling of the PXRD data was performed by ▮▮▮▮▮▮▮▮▮▮▮▮.

Figure A3 in the Appendix displays TEM snapshots with different ramping times and reaction pressures, no further heating time, and the reactions quenched directly after the ramping time. In Figure A3a, b the ramping times were changed to 7 min and 5 min, respectively, while the reaction pressure of 30 bar remained unchanged. It showed that the first product particles could even be collected after such a short reaction time. The first rods were already formed, which proved that the reaction proceeds rather fast in the first stages of the reaction. A lower pressure of 20 bar and, thus, a lower temperature, also facilitated the precursor to decompose into rods (Figure A3c)), but compared to the TEM images in Figure 2.7a), the number of formed rods was less. As a consequence of the TEM images displayed in Figure A3, it can be concluded that initial rod formation is a very quick process, occurring already in the first 5 minutes of the reaction when ramping up to a pressure of 30 bar. Decreasing the pressure to 20 bar led to a decreased rod formation in the first minutes of the reaction (Figure A3c)). The reaction pressure, and thereby the temperature, was found to be the parameter to change to control the reaction velocity. The start of the reaction occurred very quickly during the ramping time, and the resulting sub-micron rods were not monodisperse. It was assumed that nucleation took place over the whole reaction time, and, therefore, a size variation was found in the final product.

The heating time was also changed beyond the point of time when all precursor was already depleted, and the reaction was, therefore, considered to be completed. By elongation of the reaction time, a secondary growth of the rutile particles was observed. Figure 2.8 displays TEM overview images just after the reaction completed, after an elongated reaction time, and a close-up image of rods after an elongated reaction time. Just after the reaction time completed (Figure 2.8a)), it was regularly observed that particles align next to each other with respect to their c-axis. This observation was made, no matter whether the reaction mixture was stirred throughout the reaction or not. The alignment was found for every combination of single crystals and crystal twins, and rarely only two rods aligned next to each other; most of the time three to five particles aligned next to each other. Figure 2.8b) displays a TEM image after an elongated reaction time. Herein, several particles that merged together were observable. In the middle a "check mark"-like particle (see arrow in Figure 2.8) was present. This kind of particle probably occurred when a few crystal-twins aligned next to each other and merged together over time in the reaction medium. At the upper left part of the TEM image, a trapezium-like particle (see arrow in Figure 2.8) was found, which emerged when two single crystal rods of different lengths fused together. Over time in the reaction medium, the formed rods obviously did not dissolve again, as described for the first step of the formation of the rods. Nevertheless, the formed sub-micron rods underwent a further transformation in the reaction medium at temperatures up to 240 °C, due to a certain instability caused by surface defects. Figure 2.8c) displays a close-up image of two sub-micron rods, one of them being single-crystalline, the other one twinned. At the interface of the two particles, an intermediate of the merging process was found. The brighter area, as compared to the solid rods between the two rods, signalized that particles coalesced together, which could be observed at this point. As soon as the

merging process was completed, it was not possible to detect the prior interface anymore, and, therefore, to support the suggested mechanism. Also, HR-TEM measurements did not lead to a finding of the prior interface by searching for defects at the merging border.
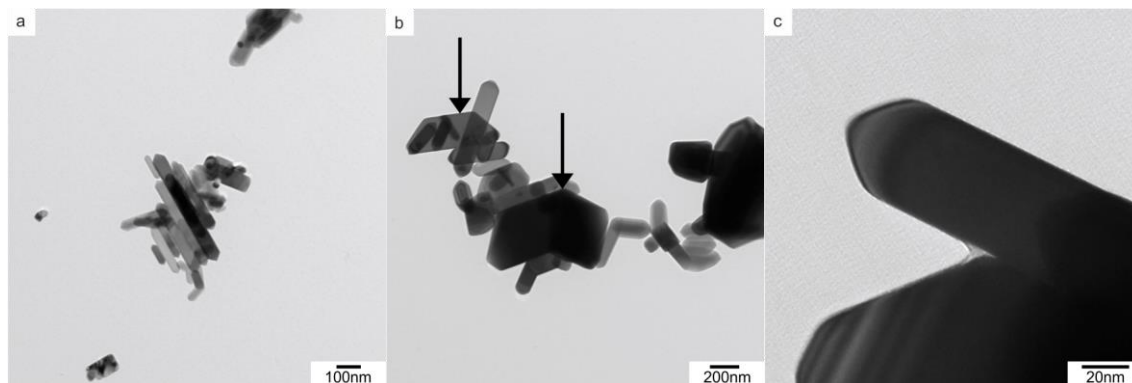
Figure 2.8 TEM images of sub-micron rods that aligned next to each other, frequently observed after 90 min reaction time (a). After an elongated reaction time, it was possible to find larger particles, while it seemed that aligned particles merged together, no matter if the aligned particles were single-crystals or twinned crystals (b). Close-up image possibly showing a quenched intermediate of the merging process (c).

The central question was whether the reaction occurred only starting from titania precursor, if the precursor had to have a certain crystalline phase or size, or if the reaction takes place starting from every titanium source.

Various solid-state titania precursors were tested to perform a transformation to rutile sub-micron rods. First, micron-sized phase-pure anatase and rutile precursors were employed, while the rutile precursor was made by heating TiO_2-P25 powder. Due to Ostwald ripening and thermally induced phase transformation, micron-sized rutile particles were obtained. These, as well as commercially available anatase precursor, did not lead to any growth forming rod-shaped particles via the discussed hydrothermal route. The TEM images of the precursors and results can be seen in Figure A4 in the Appendix.

Rutile nanoparticles were made by ball milling TiO_2-P25, wherein the energy input facilitated a phase transformation to rutile, while the particle sizes remained unchanged. Anatase nanoparticles were made by a basic thermal decomposition of a metal-organic titanium complex. Figure 2.9a) - c) shows the employed precursor materials (XRD patterns and TEM images as insets), d) - f) displays the products received after hydrothermal treatment. Here, it is clearly visible that using anatase and TiO_2-P25 led to a growth of sub-micron rods, while rutile nanoparticles remained unchanged, and as compared to the precursor, only a certain ripening occurred. The reason was that rutile is the thermodynamically stable crystal structure, and, therefore, the used HCl solution was not able to dissolve the precursor. This was observed before, when already formed rods did not re-dissolve, although the reaction time was increased far beyond the time needed for a complete depletion of precursor. Instead, it was observed that particles merged together in a secondary growth. In contrast, the anatase precursor was instable concerning a phase transformation and performed a transformation to rutile sub-micron rods. The TiO_2-P25 precursor

_____

was a mixture of anatase and rutile, whereat the particles were highly defectious and probably, therefore, instable toward the reaction medium. The anatase particles had a smaller diameter, and, thereby, a higher surface as compared to TiO_2-P25 (ca 128 m²/g vs. 50 m²/g, for details see Table 5.1). As the dissolution process takes place on the surface, it was assumed that the precursor dissolved faster and provided more Ti^{4+} ions to grow sub-micron rods. Thus, the rods using anatase nanoparticles became longer than the ones having TiO_2-P25 as precursor. Using molecular precursors also led to a rutile sub-micron rod formation, while the used titanium precursors were instable concerning water, acids, air or heat. Partial, a colorless precipitate, most likely titanium oxide/hydroxide, formed immediately, which easily dissolved with stirring prior to the hydrothermal heating process. The formed rods were also larger as compared to the product using TiO_2-P25 as precursor. The reaction mechanism using molecular precursors was not closely investigated. Nevertheless, it was already known that precursors such as $TiCl_4$ decompose in HCl solutions below 80 °C to form anatase nanoparticles. This fact could mean that by using this instable molecular precursor, a two-step reaction occurred during the hydrothermal treatment. Therefore, the length of the formed rods did not become significantly longer as compared to using solid-state precursors. The TEM images of the product when molecular precursors were used can be found in the Appendix in Figure A6.
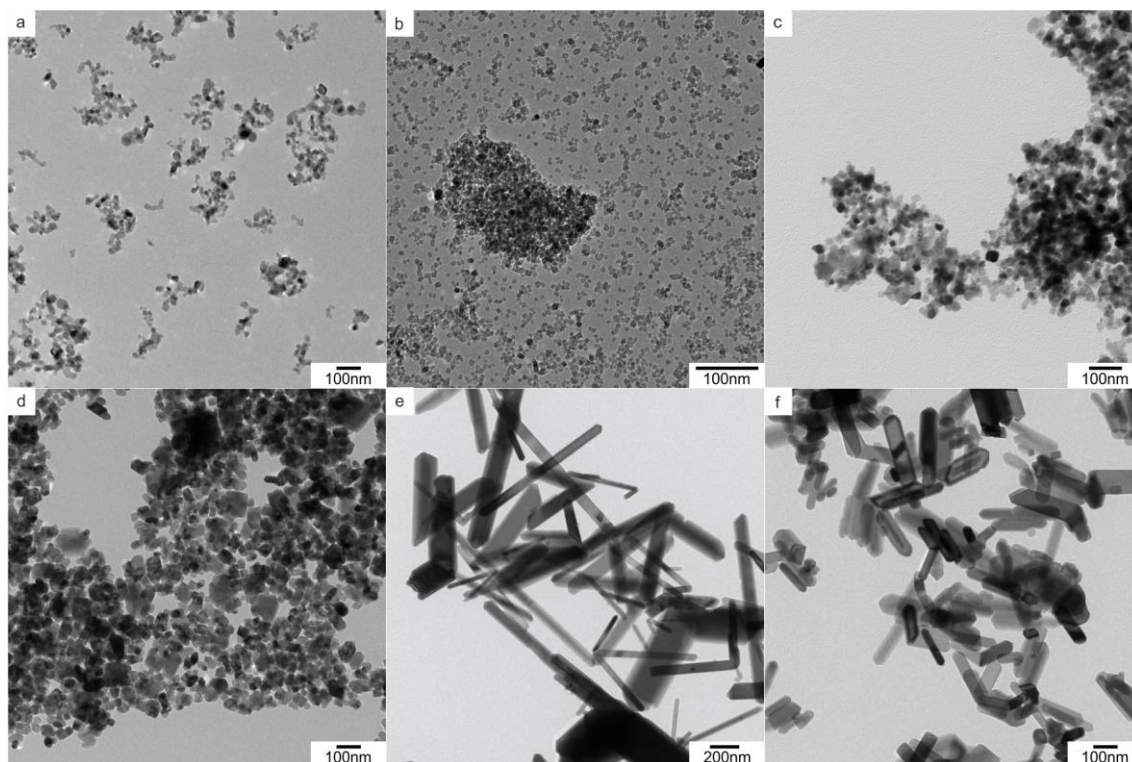
Figure 2.9 TEM images of different solid precursors and the resulting product after hydrothermal treatment; a) displays the rutile precursor nanomaterial, d) shows the product after the hydrothermal treatment; b) shows the anatase precursor with the resulting product in e); c) displays the commonly used TiO_2-P25 powder with the obtained sub-micron rods in f).

Varying the mineral acid also led to a growth of rods of a comparable length as to when HCl was used. Briefly, TiO_2-P25 was again employed as titania precursor, and the acid was first changed to

HBr, and then to HI. Here, a growth of rods was also observed, as shown in Figure 2.10. In both cases the concentration of the acid in solution had to be increased, but still only for HBr could a quantitative reaction be achieved. Using even concentrated HI did not lead to a complete reaction. The stabilization of the hydro iodic acid, here hypophosphorous acid, could have disrupted the reaction. The assumption made for the reaction using HCl was that the acid facilitated the titania precursor to dissolve and form a $[TiCl_6]^{2-}$ ion or similar hydrated/hydroxylated Ti^{4+} species. In the next step, this complex decomposed again and formed TiO_2, while the released and excess Cl^- ions acted as mineralizer to accomplish the growth of rutile rods. Using HBr and HI should not have changed a lot concerning the general mechanism, but the sizes, and thereby the polarization, as well as the ability to stabilize a Pearson-hard Ti^{4+} ion should also be considered. Cl^- as anion is Pearson-hard, while I^- is a rather large ion and, thus, exhibits a good polarizability and is Pearson soft. The soft iodide ion did not seem to be able to promote either the formation of the intermediate species or the surface complexation during the rod formation.
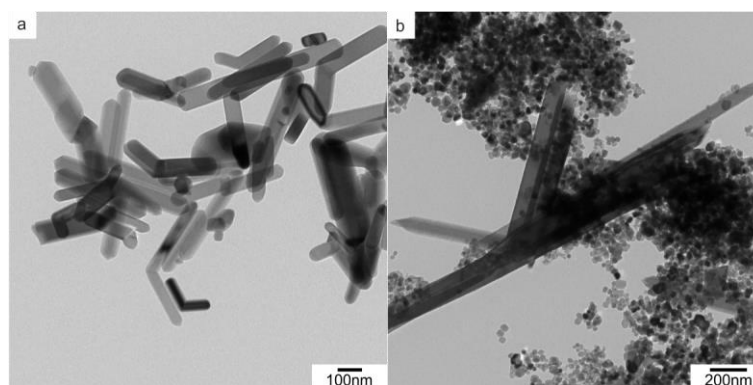
Figure 2.10 TEM images of the product when HBr (a) and HI (b) were employed as precursor acid. In both cases the acid concentration had to be increased due to a decreased reaction velocity. For HBr it was evident that a quantitative reaction took place, while the reaction using HI did not proceed quantitatively.

It was attempted to simulate the reaction conditions by adjusting the H^+ and Cl^- concentrations of 6 M HCl while using H_2SO_4 or HNO_3 in combination with NaCl. The result after the hydrothermal treatment is displayed in Figure 2.11. H_2SO_4, in general, should have been able to dissolve at least traces of the TiO_2-P25 precursor, since it is the main ingredient for the standard method for chemical digestion of TiO_2, but nonetheless, no rods could be observed. The reason therefore is probably that SO_4^{2-} is a strong complexing agent for the positively charged surface of titania and also a promoter for the formation of anatase particles. The usage of HNO_3 did not lead to any change in the precursor, which might indicate that HNO_3 did not facilitate the precursor to dissolve. The effect of the addition of NO_3^- has been controversial, as it was reported to promote either anatase- or rutile-type or to not have any effect, and thereby, a mixture of anatase and rutile was obtained. [35]
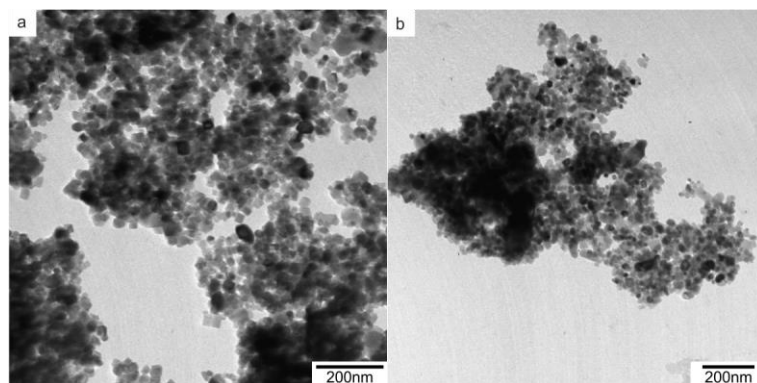
Figure 2.11 TEM images of product particles when HCl was replaced by H_2SO_4 (a) or HNO_3 (b) with adjusted Cl⁻ concentration by addition of NaCl.

Summing up the different aspects of the growth mechanism starting from the observations caused by an elongated reaction time. The TEM images in Figure 2.8 show particles after a completed reaction and after an elongated reaction time. It appeared that rods, after the precursor was consumed, coalign and merge with time in the reaction medium. However, the pathway by which oriented attachment occurs is difficult to establish. Here, Figure 2.8c) suggests that a whole particle-particle fusion is most likely. Although the preservation of primary particle morphology and the formation of twins and stacking faults at particle-particle boundaries strongly suggest a sequence of whole-particle alignment followed by interface elimination,[28,59] atom-by-atom reorientation via dislocation and grain-boundary migration after attachment might be another potential mechanism.[60]

In order to elucidate the driving forces of the growth process, we varied the reaction parameters. (i) When HCl was replaced by sulfuric acid or nitric acid with adjusted Cl⁻ concentrations, no rutile TiO_2 sub-micron rods were formed. The reason for this could be that the other acids do not facilitate the dissolution of the TiO_2-P25 precursor. Additionally, it was shown by Wu *et al.*[35] that anatase grows preferentially in H_2SO_4 due to the strong surface stabilization of the positively charged TiO_2 surface by SO_4^{2-}, while HNO_3 does not show a preference in crystal structural growth.[35] Thereby, HCl stabilizes the formation of rutile. Performing a hydrothermal treatment in pH neutral media with adjusted Cl⁻ concentration did not lead to any change of the precursor in phase or morphology, while using NaOH can lead to anatase or various sodium titanates depending on the experimental conditions.[37,44,61] (ii) In contrast, when the reactions were carried out in HBr and HI (Figure 2.10), rutile sub-micron rods were formed in an analogous manner. This indicates that $[TiX_6]^{2-}$ halogentitanate anions (X= Cl⁻, Br⁻, I⁻) or a hydrated or hydroxylated species similar to this could be involved as intermediate species in a dissolution and growth transport mechanism.[62] Surprisingly, we did not observe rutile sub-micron rod growth in HF or NH_4F solution. We assume that in the various reactions either the fluoride concentration was too low for TiF_6^{2-} to form or that the solubility of the hexafluoro-anion in the acidic solution was too high to allow a "chemical transport reaction" to proceed. HCl, HBr, or HI act as mineralizers that aid the solubilization of the nutrient solid and, thereby, facilitate the transport of the insoluble TiO_2 "nutrient" to a seed crystal via a reversible transport reaction. Over time, the seed nanocrystals

accumulate the material that was before in the nutrient and, therefore, keep growing. Many hydrothermal reactions involve the crystallization of solids, as the properties of solvents under subcritical conditions may undergo dramatic changes.[58] Attempts to demonstrate the presence of intermediate species by Raman and infrared as well as UV-Vis spectroscopy were not successful. Further, the intermediate species could not be crystallized and, thus, trapped by addition of a sterically demanding cation. *In situ* measurements might be useful with respect to determining the intermediate species, but are not possible at such extreme conditions as 30 bar and pH 0. It was tried to transfer the reaction to boiling HCl under standard pressure conditions, but no growth of rutile sub-micron rods could be observed, and, therefore, no intermediate species was present at these reaction conditions that might have enabled *in situ* investigations.

Applying soluble precursors like $TiCl_4$ and $Ti(OBu)_4$ enables a reaction to anisotropic rutile particles at temperatures as low as 40 °C.[46,57,63] Such reactions were performed under standard conditions and enable the possibility of *in situ* measurements. Starting from soluble Ti^{4+} precursors, Yin *et al.* proposed a growth via a $[Ti(OH)_nCl_{6-n}]^{2-}$-anion, however, the higher the HCl concentration, the lower was also the resulting n.[29] Showing that $TiCl_4$ decomposes at 40 - 70 °C in HCl via $[Ti(OH)_nCl_{6-n}]^{2-}$ might explain why it was not possible to find intermediate species for the reaction described here.[29,46,57,63] This finding corroborated the assumption that the intermediate that is active in the growth of TiO_2 sub-micron rods is a similar Ti^{4+} species as published by Yin *et al.*, who started from soluble Ti^{4+} precursors. The disadvantage of soluble Ti^{4+} precursors is their sensitivity to air, humidity, and their price. Therefore, other solid precursors (pure anatase and rutile) were tested to identify the driving force behind the formation of the sub-micron rods. Bulk precursors (micron-sized particles) did not show any reactivity, presumably because their lattice energy was too high. Rutile nanoparticles (size ≈ 30 nm), obtained from TiO_2-P25 by ball milling, did not show a significant reactivity either, whereas anatase nanoparticles (size ≈ 15 nm) easily transformed to rutile rods. Calculations by Curtiss and Banard revealed a crossover of the thermodynamic stability for TiO_2 caused by different surface and crystallization energies for rutile and anatase.[64] Below a critical size, anatase becomes more stable than rutile due to its lower surface energy. The surface energy is highly dependent on the surrounding medium, as demonstrated by the formation of rutile nanorods in the presence of 3-hydroxytyramine ligands.[65] For hydrogen-rich surfaces, Banard and Curtiss calculated the crossover at a particle size of 18.4 nm at ambient temperature.[64] The critical size, however, decreases dramatically with increasing temperature. This finding might explain the lack in reactivity of well-crystallized rutile nanoparticles under strongly acidic conditions, as they are the most stable phase. In contrast, the stability of anatase decreases with increasing temperature. As result, the transformation to rutile sub-micron rods is more favorable. For TiO_2-P25, the poorly crystalline particles are expected to be highly defective, and, hence, show some reactivity under the given conditions. The results from Banard and Curtiss explain well the different behavior of the nano particular precursors in the shown growth, which is mainly the explanation

why the precursor is instable and dissolves. The reason why rutile sub-micron rods assemble is that a high H^+ concentration facilitates the growth of rutile on the one hand, and on the other hand also ensures a positively charged TiO_2-surface, which enables the Cl^- to act as mineralizer.[46,57] The presence of Cl^- herein acts as mineralizer to promote the growth of rutile sub-micron rods as well. The synergy of instability of the precursors and surface stabilization of the product by the reaction medium enabled this reaction. The reaction parameters were adjusted for the use of HBr and HI, which also facilitated the growth of rutile sub-micron rods. However, the reaction with HI was not quantitative. The change in the reaction conditions when using these acids was presumably caused by the distinct Pearson hardness and, therefore, was due to changed stabilities of the formed intermediate and surface stabilization. The performed snapshots revealed that the reaction occurred already, while ramping up to the reaction temperature, and that the chosen temperature is rate-determining.

2.4 Application as a photo-catalyst

Titanium dioxide is known to be a photo-catalytic active material, and, hence, is applied in various functions, *e.g.* as coating material for self-cleaning surfaces,[15] pollutant decomposition,[66] or water splitting.[8] This effect is due to the generation of free surface charges when TiO_2 is irradiated with light of an energy higher than the band-gap. Titanium dioxide itself exhibits a fast recombination of photo-generated electrons and holes, and, therefore, is as bare material good to generate charges, but not necessarily suitable to perform photo-catalytic reactions at a suitable yield. To enhance the activity of the TiO_2, the separation of charges has to be conserved, which can be ensured by surface functionalization with Pt, Au, Pd, Rh, Ni, Co, or Ag nanoparticles. Herein, electrons from the conduction band of TiO_2 are injected into the metal domains ensuring that recombination of electrons and holes in TiO_2 is not possible anymore. A simple test to demonstrate the photo-catalytic activity is the decomposition of Rhodamin B. Briefly, a solution of Rhodamin B was added to Pt functionalized or unfunctionalized TiO_2 sub-micron rods. This mixture was irradiated with UV-light. After different times, the reaction mixture was centrifuged, and the absorption was measured. The measured aliquot was returned, subsequently the sub-micron rods were re-dispersed and irradiated again. A commonly described reaction is the de-ethylation of Rhodamin B, where the maximum of Rhodamin B at 554 nm vanishes and an absorption at 498 nm arises, which is caused by Rhodamin. The reaction is shown in Figure 2.12. An additional absorption maximum did not arise during the reaction, indicating that the de-ethylation did not occur during the reaction.
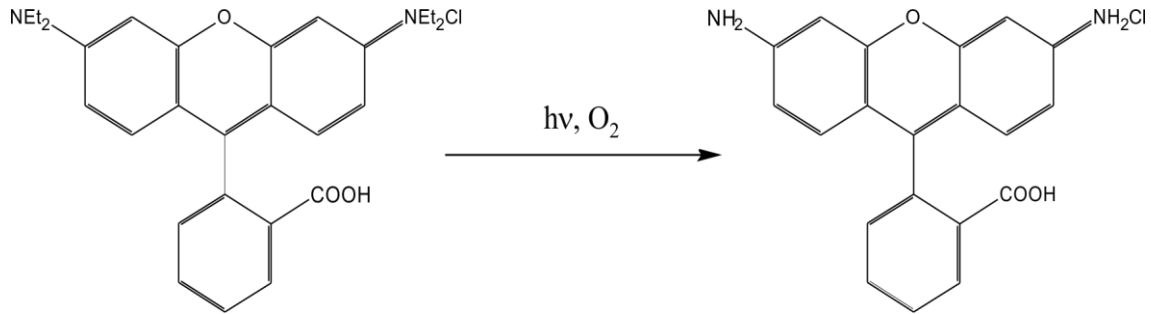
Figure 2.12 De-ethylation reaction of Rhodamin B to Rhodamin. Adapted from Wilhelm and co-workers.[66]

It is frequently observed that it is not the de-ethylation reaction of Rhodamin B that takes place, but rather a complete degradation of the organic material in the sample. Wilhelm *et al.* investigated the degradation of Rhodamin B under irradiation at TiO$_2$ surfaces.[66] They showed that about 70 % of the organic carbon in the samples could not be found after degradation of Rhodamin B. It was likely that aldehydes and carboxylic acids remained in the samples, but no aromatic rings could be found anymore. The reactions taking place while irradiation change depending on the wavelength of the light used. If the energy of the light is lower than the band-gap of TiO$_2$, Rhodamin B is excited and transfers its electron to TiO$_2$; it is used as sensitizer. In contrast, when the energy of the light is higher than the band-gap, such as with UV-light, a direct charge separation takes place in the TiO$_2$. The reaction can be seen below.

When irradiated with Vis/IR-light:

$$TiO_2 + RB^* \rightarrow RB^{+\cdot} + TiO_2(e^-)$$
$$TiO_2(e^-) + O_2 \rightarrow TiO_2 + O_2^{\cdot-}$$
$$TiO_2(e^-) + O_2^{\cdot-} + H^+ \rightarrow TiO_2 + HO_2^-$$
$$HO_2^- + H^+ \rightarrow H_2O_2$$
$$H_2O_2 + e^- \rightarrow OH^{\cdot} + OH^-$$
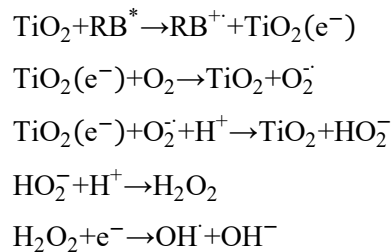
While when irradiated with UV-light:

$$2\ TiO_2 \xrightarrow{h\upsilon} TiO_2(e^-) + TiO_2(h^+)$$
$$RB + TiO_2(h^+) \rightarrow RB^{+\cdot} + TiO_2$$
$$H_2O + TiO_2(h^+) \rightarrow OH^{\cdot} + H^+ + TiO_2$$
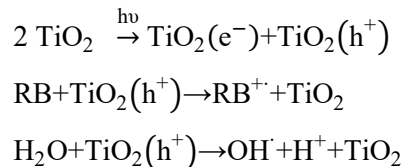
Figure 2.13 shows the UV-Vis spectrum of Rhodamin B (left), while the graph on the right displays the trend of the decomposition of Rhodamin B as control sample (red), with addition of bare TiO$_2$ sub-micron rods (green), and with addition of Pt-functionalized sub-micron TiO$_2$ rods (black). The trend of the bare rutile rods includes only a few datapoints due to measurement faults. The particles got dispersed during the measurement, and the samples scattered too much to ensure significant results. It is clearly visible that the absorption with Pt-functionalized TiO$_2$ rods decreases continuously until the

25

_____

slope flattens. This already shows the photo-catalytic activity of the Pt-functionalized rods. Using unfunctionalized rods also led to a decomposition of Rhodamin B, but with a decreased reaction speed. For TiO_2 particles, it is known that charge recombination happens very fast with respect to the surface reaction that has to take place to decompose Rhodamin B. Platinum particles attached to the surface disable a fast recombination by offering a host for electrons, while holes remain in the TiO_2 and the charges could efficiently be separated. Due to this charge separation, the surface exposed free charges available for reaction. Various noble metals such as Pt, Au, Pd, Rh, Ni, Co, and Ag are known to be beneficial for the charge separation in TiO_2 and, therefore, enhance the photocatalytic activity.[67–69] Herein, the noble metal exhibits a conduction band that is placed beneath the conduction band of TiO_2. By photon irradiation generated electrons are injected into the noble metal due to its conduction band position, while holes remain in the valence band of TiO_2. Due to this separation, the usually fast recombination is suppressed and the surface charges can more easily be used for photocatalytic processes. The tested activity shows clearly that the particles can be used for several catalytic applications, including hydrogen production and pollutant decomposition.
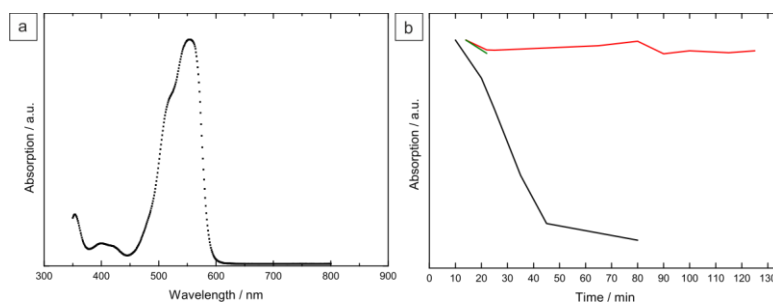
Figure 2.13 UV-Vis spectrum of Rhodamin B (a), and absorption vs irradiation time (b) of a control sample (Rhodamin B only, red), bare TiO_2 sub-micron rods (green) and Pt-functionalized sub-micron rods (black).

2.5 Conclusion

In conclusion, a hydrothermal treatment starting from fumed titania using HCl as reactant was presented. After the reaction, using a microwave assisted reaction system, single-crystals of rutile TiO_2 were obtained. Several methods were employed to characterize the samples: XRD and Raman spectroscopy revealed that the crystalline phases were > 96 wt% rutile and only a trace of anatase remained. TEM measurements showed that the powders consisted of well-faceted sub-micron rods with a length of 100 - 400 nm. The lengths of crystallites determined from XRD data modelling was 221 nm. The coinciding length of crystallites and particles, as well as the well-formed facets suggested the particles to be single-crystals, which was confirmed by HAADF TEM, electron diffraction, as well as nano-electron diffraction. In addition to the single crystals, twinned crystals were also frequently found. By changing the reaction conditions, *i.e.* the used acid concentration, it was possible to gain control over

the length of the resulting rods. Though decreasing the concentration too far led to a failure of growing rutile sub-micron rods.

The microwave-assisted heating did not only enable us to employ high heating rates, but also enabled us to quench the reaction and, thereby, take snapshots. By changing the reaction times, it was observed that the initial formation of rutile rods already occurs during the ramping time, which was varied down to even only 5 min. A full conversion of the precursor was achieved after only 90 min reaction time, while heating far beyond this time triggered a secondary particle growth, which probably could be assigned to a whole particle-particle fusion process.

All applied precursor materials were systematically changed to verify a driving force and growth mechanism for this reaction. By changing the titania precursor, it was obvious that bulk precursors did not show any reaction; while inserting phase-pure nanometer sized materials, such as anatase and rutile nanoparticles, showed that only materials, which are instable in the reaction medium, could transform to sub-micron rutile rods. Rutile nanoparticles were well crystallized, and as the thermodynamically stable phase, not able to react. TiO_2-P25 probably undergoes the reaction to rutile rods, since it is presumed to be highly defectious. The particles were only formed using HX (X= Cl$^-$, Br$^-$, I$^-$). It is assumed that a $[TiX_6]^{2-}$ acts as intermediate species and decomposes again under reaction conditions to perform a short range chemical transport reaction. It was not possible to perform a growth of rutile rods with simulated conditions using NaCl for the Cl$^-$ concentration and HNO_3 or H_2SO_4 for the pH value.

TiO_2 particles are known to have a variety of possible applications. In this Chapter, initial tests for their photo-catalytic activity were demonstated, while their applictation in DSCs will be the topic of Chapter 5. Other applications include as an electrode material for Li-ion batteries, self-cleaning surfaces or watersplitting, where initial tests were also performed. First photo-catalytic activity tests for pollutant decomposition were performed using the degradation reaction of Rhodamin B. Herein, rutile sub-micron rods were incubated with Rhodamin B, while irradiated with UV-Light. It could be traced via UV-Vis spectroscopy that the presence of the rods decomposes the dye and the colorless product remains. It could additionally be shown that a functionalization with Pt-nanoparticles onto the TiO_2 surface could enhance the activity of the particles by disabling a fast recombination of the surface charges.

2.6 Experimental Section

2.6.1 Synthesis

Materials. All materials were used as received without any further purification. TiO_2-P25 nanoparticles were purchased from Degussa. Aqueous HCl solutions of various concentrations were made by dilution of conc. HCl ($\geq$ 37 %, Fluka, analytical grade) with MilliQ-water (18.2 MΩ/cm). Ethanol (p.A.) was purchased from VWR. HBr (48 % aqueous solution), HI (57 % aqueous solution with 1.5 % Hypophosphorous acid), dihydrogen hexachloroplatinate (IV) (99.9% trace metals basis, H_2PtCl_6), and Ti(IV) bis(ethyl acetylacetato) diisopropoxide (TAD, > 95 %) were purchased by ABCR.

_____

Sodium hydroxide solutions were made from NaOH (98.5 %) pellets. They and tri-sodium citrate (99.8 %, $Na_3C_6H_5O_7$) were purchased from Acros Organics.

Rutile sub-micron r ods. A hydrothermal microwave-assisted treatment was employed using a MARS5 high-pressure digestion set-up, equipped with XP-1500 vessels and pressure control (CEM Corporation). Alternatively, the reaction was carried out in teflon-lined stainless steel autoclaves (DAB-2, 50 mL) by Berghof Corporation. 500 mg TiO_2-P25 powder was mixed with ~6 M HCl and, with a stirring bar added, transferred to the reaction system. It was ramped up to 30 bar over a time of 10 min with a maximal power output of 1600 W. This pressure was held for 90 min, and then cooled down passively to room temperature in another 30 min. Alternatively, the reaction was performed in an autoclave in 12 h at a temperature of 220 °C. In both cases, the reaction mixture was centrifuged at a speed of 9000 rpm for 5 min, the supernatant was discarded, and the solid was rinsed repeatedly with water and, subsequently, ethanol until the solution was neutral. Afterwards, the residue was dried overnight at 80 °C.

Mechanism study. Snapshots of the reactions were performed changing the (i) heating times, (ii) aimed pressures, and (iii) ramping times. Additionally, the concentrations of the used HCl was lowered to 3 M and increased to 12 M. Thereafter, the HCl was replaced by HBr and HI of various concentrations. Furthermore, anatase-TiO_2 and rutile-TiO_2 nanoparticles were separately employed as titanium precursor. Rutile nanoparticles were synthesized by ball milling TiO_2-P25. Here, 3 g TiO_2-P25 were suspended in 5 mL ethanol and ball milled for 4 h at a frequency of 30 Hz. The nanoparticles were collected by centrifugation (9000 rpm, 5 min) and dried overnight at 80 °C. To obtain anatase nanoparticles, 1 mL TAD was added to 20 mL 10 mM NaOH and heated up to a pressure of 20 bar in 8 min using a MARS5 microwave reaction system. The reaction mixture was centrifuged at 9000 rpm for 5 min, the supernatant was discarded, and the solid repeatedly rinsed with water and, subsequently, ethanol until the solution was colorless. Afterwards, the residue was dried overnight at 80 °C.

Photo-catalytic activity. For a better charge separation rutile sub-micron rods were functionalized with Pt nanoparticles following a reported procedure of Sammelis and co-workers.[69] Briefly, 45 mg sodium citrate were solved in 50 mL water, and 12 mg hexachloroplatinate were added. This mixture was heated to reflux for 1 h. The nanoparticles were collected by centrifugation at 9000 rpm for 15 min, the supernatant was discarded, and the nanoparticles were re-dispersed in 10 mL water. For functionalization, 4 mL of the Pt nanoparticle solution were added to 50 mg rutile sub-micron rods, the pH was adjusted to 2 by adding dropwise HCl. The slurry was filled up to a volume of 10 mL and stirred overnight. The functionalized sub-micron rods were collected by centrifugation (9000 rpm, 5 min) and dried overnight at 80 °C without any further purification.

_____

2.6.2 Characterization

Powder X-ray diffraction. X-ray diffraction patterns were recorded using a Siemens D5000 diffractometer equipped with a Braun M50 position sensitive detector in transmission mode using Ge (200) monochromatized CuK_α radiation. Crystalline phases were identified according to the PDF-2 database. Diffraction data were modeled by Rietveld refinements using TOPAS Academic V5 applying the fundamental parameter approach. Alternatively, phase analysis was made according to the PDF-2 database using Bruker AXS EVA 10.0.[70,71]

Powder X-ray diffraction of films. X-ray diffraction patterns were recorded using a Bruker AXS D8 Discover diffractometer equipped with a HiStar detector using graphite mononchromatized $CuK\alpha$ radiation. Samples were attached to substrates by a prior sintering process. Individual frames were typically recorded at $2\theta = 24°, 34°, 44°, 54°, 64°, 74°$, and $84°$ (detector distance 150 mm, detector range $\Delta (2\theta) = 35°$).

Transmission electron microscopy. All samples were characterized by (high angle annular dark field) transmission electron microscopy (HAADF TEM) and low-resolution transmission electron microscopy (TEM). A Philips EM 420 instrument with an acceleration voltage of 120 kV and LaB_6 cathode was used for low-resolution TEM images and electron diffraction patterns. HAADF TEM images and further electron diffraction patterns were recorded employing a HR FEI Tecnai F30 S-Twin using an accelerating voltage of 300 kV with a field emission gun. For preparation, the samples were dispersed in ethanol and dropped on a carbon-coated copper grid.

Raman spectroscopy. Raman spectra were recorded using a Horiba Jobin Yvon LabRAM HR 800 spectrometer equipped with a CCD-detector. The Raman spectrometer was coupled to an Olympus BX41 optical microscope using a 50-fold magnification with a slit width of 100 µm. For excitation, a HeNe-laser with a wavelength of 632.8 nm and a spotsize of 2 x 2 µm was used. The spectra were recorded in the range of 150 - 1400 cm^{-1}.

Dynamic light scattering. Dynamic light scattering measurements (DLS) were performed using a Uniphase He/Ne Laser (λ=632.8 nm, 22 mW), a ALV-SP125 Goniometer, a ALV/High QE Avalanche photo-diode with fibre optical detection, a ALV 5000/E/PCi-correlator and a Lauda RC-6 thermostat unit. Angular dependent measurements were carried out in the range $30° \leq \theta \leq 150°$. For data evaluation experimental intensity correlation functions were transformed into amplitude correlation functions applying the Siegert relation extended to include negative values after baseline subtraction by calculation $g_1(t)=SIGN(G2(t))\cdot SQRT(ABS((G2(t)-A)/A))$.

$g_1(t)$ was evaluated by fitting a biexponential function $g_1(t) = A_1\cdot exp(-q^2\cdot D_1\cdot t) + A_2\cdot exp(-q^2\cdot D_2\cdot t)$ to take polydispersity into account with the scattering vector $q = 4\cdot\pi\cdot sin(\theta/2)$, the amplitudes A_1 and A_2, and the diffusion coefficients D_1 and D_2. Average apparent translational diffusion coefficients D_T were

_____

determined according to $D_T = (A_1 \cdot D_1 + A_2 \cdot D_2)/(A_1 + A_2)$. $D_T(q=0)$ was extrapolated from that data. Hydrodynamic radii were then extracted from the Stokes-Einstein equation $R_h = \langle 1/R_h \rangle_Z^{-1} = k \cdot T \cdot (6 \cdot \pi \cdot \varsigma \cdot D_T)^{-1}$. Average apparent rotational diffusion coefficients were calculated from $\Gamma = q^2 \cdot D_T + 6D_R$. All samples were diluted in dust free cylindrical scattering cells (Hellma, Suprasil, 1 cm diameter) using syringe filters for the solvent DMSO (PALL GHP 200 nm).

Photo catalytic activity tests. For photo-catalytic tests, 10 mg of the particles were added to 1 mL of a 10 µg/mL solution of Rhodamin B in water and irradiated with UV-light. The slurry was centrifuged after different irradiation times at 13600 rpm for 1 min, and the UV-VIS absorption was measured using a Cary Varian 5G UV-Vis-NIR spectrometer in a range of 350 - 800 nm. The measurements were performed in quartz cuvettes of a volume of 0.1 mL. The decrease in intensity was monitored at the absorption maximum of Rhodamin B at around 548 nm.

2.7 References

1   P. Leidich, O. Linker, M. Panthöfer and W. Tremel, *CrystEngComm*, 2014, **16**, 8486.
2   S. P. Albu, A. Ghicov, J. M. Macak, R. Hahn and P. Schmuki, *Nano Lett.*, 2007, **7**, 1286–1289.
3   S.-J. Bao, C. M. Li, J.-F. Zang, X.-Q. Cui, Y. Qiao and J. Guo, *Adv. Funct. Mater.*, 2008, **18**, 591–599.
4   D. Deng, M. G. Kim, J. Y. Lee and J. Cho, *Energy Environ. Sci.*, 2009, **2**, 818.
5   M. Stefik, F. J. Heiligtag, M. Niederberger and M. Grätzel, *ACS Nano*, 2013, **7**, 8981–8989.
6   A. Hagfeldt, G. Boschloo, L. Sun, L. Kloo and H. Pettersson, *Chem. Rev.*, 2010, **110**, 6595–6663.
7   A. Fujishima and K. Honda, *Nature*, 1972, 37–38.
8   A. Kudo and Y. Miseki, *Chem. Soc. Rev.*, 2008, **38**, 253.
9   D. Deng, M. G. Kim, J. Y. Lee and J. Cho, *Energy Environ. Sci.*, 2009, **2**, 818.
10 H. J. Yun, H. Lee, J. B. Joo, W. Kim and J. Yi, *J. Phys. Chem. C*, 2009, **113**, 3050–3055.
11 Q. Zhang, D. Q. Lima, I. Lee, F. Zaera, M. Chi and Y. Yin, *Angew. Chem. Int. Ed.*, 2011, **50**, 7088–7092.
12 H. Chen, C. E. Nanayakkara and V. H. Grassian, *Chem. Rev.*, 2012, **112**, 5919–5948.
13 K. Nakata and A. Fujishima, *J. Photoch. Photobio. C*, 2012, **13**, 169–189.
14 T. Yuranova, R. Mosteo, J. Bandara, D. Laub and J. Kiwi, *J. Mol. Catal. A*, 2006, **244**, 160–167.
15 T. Kamegawa, Y. Shimizu and H. Yamashita, *Adv. Mater.*, 2012, **24**, 3697–3700.
16 N. Tétreault, É. Arsenault, L.-P. Heiniger, N. Soheilnia, J. Brillet, T. Moehl, S. Zakeeruddin, G. A. Ozin and M. Grätzel, *Nano Lett.*, 2011, **11**, 4579–4584.
17 A. A. Gribb and J. F. Banfield, *Am. Mineral.*, 1997, 717–728.
18 M. R. Ranade, A. Navrotsky, H. Z. Zhang, J. F. Banfield, S. H. Elder, A. Zaban, P. H. Borse, S. K. Kulkarni, G. S. Doran and H. J. Whitfield, *Proc. Nat. Acad. Sci.*, 2002, **99**, 6476–6481.
19 H. Zhang and J. F. Banfield, *J. Mater. Chem.*, 1998, 2073–2076.
20 H. Zhang and J. F. Banfield, *J. Phys. Chem. B*, 2000, **104**, 3481–3487.
21 A. Navrotsky, *Geochem. Trans.*, 2003, **4**, 34.
22 C. J. Barbé, F. Arendse, P. Comte, M. Jirousek, F. Lenzmann, V. Shklover and M. Grätzel, *J. Am. Cer. Soc.*, 1997, 3157–3171.
23 R. Penn and J. F. Banfield, *Geochim. Cosmochim. Acta*, 1999, **63**, 1549–1557.
24 M. P. Finnegan, H. Zhang and J. F. Banfield, *J. Phys. Chem. C*, 2007, **111**, 1962–1968.
25 H. Cheng, J. Ma, Z. Zhao and L. Qi, *Chem. Mater.*, 1995, 663–671.
26 Qi Feng, Yuichi Yamamoto, Nakamichi Yamasaki and Kazumichi Yanagisawa, *J. Mater. Res.*, 1998, 825–829.
27 K. Yanagisawa and J. Ovenstone, *J. Phys. Chem. B*, 1999, **103**, 7781–7787.
28 S. T. Aruna, S. Tirosh and A. Zaban, *J. Mater. Chem.*, 2000, **10**, 2388–2391.

29 H. Yin, Y. Wada, T. Kitamura, S. Kambe, S. Murasawa, H. Mori, T. Sakata and S. Yanagida, *J. Mater. Chem.*, 2001, **11**, 1694–1703.

30 J.-G. Li, T. Ishigaki and X. Sun, *J. Phys. Chem. C*, 2007, **111**, 4969–4976.

31 A. Pottier, C. Chanéac, E. Tronc, L. Mazerolles and J.-P. Jolivet, *J. Mater. Chem.*, 2001, **11**, 1116–1121.

32 E. Matijevic, *Langmuir*, 1986, 12–20.

33 A. Zaban, S. T. Aruna, S. Tirosh, B. A. Gregg and Y. Mastai, *J. Phys. Chem. B*, 2000, **104**, 4130–4133.

34 G. Oskam, A. Nellore, R. L. Penn and P. C. Searson, *J. Phys. Chem. B*, 2003, **107**, 1734–1738.

35 M. Wu, G. Lin, D. Chen, G. Wang, D. He, S. Feng and R. Xu, *Chem. Mater.*, 2002, **14**, 1974–1980.

36 T. Nagase, T. Ebina, T. Iwasaki, H. Hayashi, Y. Onodera and C. Maya, *Chem. Let.*, 1999, 911–912.

37 T. Kasuga, M. Hiramatsu, A. Hoson, T. Sekino and K. Niihara, *Adv. Mater.*, 1999, 1307–1311.

38 Q. Chen, G. H. Du, S. Zhang and L.-M. Peng, *Acta Crystallogr B Struct Sci*, 2002, 587–593.

39 J. Yang, Z. Jin, X. Wang, W. Li, J. Zhang, S. Zhang, X. Guo and Z. Zhang, *Dalton Trans.*, 2003, 3898.

40 R. Ma, Y. Bando and T. Sasaki, *Chem. Phys. Let.*, 2003, **380**, 577–582.

41 S. Zhang, Q. Chen and L.-M. Peng, *Phys. Rev. B*, 2005, **71**.

42 A. Gloter, C. Ewels, P. Umek, D. Arcon and C. Colliex, *Phys. Rev. B*, 2009, **80**.

43 I. Andrusenko, E. Mugnaioli, T. E. Gorelik, D. Koll, M. Panthöfer, W. Tremel and U. Kolb, *Acta Crystallogr B Struct Sci*, 2011, **67**, 218–225.

44 D. Koll, I. Andrusenko, E. Mugnaioli, A. Birkel, M. Panthöfer, U. Kolb and W. Tremel, *Z. anorg. allg. Chem.*, 2013, **639**, 2521–2526.

45 C.-C. Wang and J. Y. Ying, *Chem. Mater.*, 1999, **11**, 3113–3120.

46 W. Wang, B. Gu, L. Liang, W. A. Hamilton and D. J. Wesolowski, *J. Phys. Chem. B*, 2004, **108**, 14789–14792.

47 K. Tomita, V. Petrykin, M. Kobayashi, M. Shiro, M. Yoshimura and M. Kakihana, *Angew. Chem. Int. Ed.*, 2006, **45**, 2378–2381.

48 A. Birkel, F. Reuter, D. Koll, S. Frank, R. Branscheid, M. Panthöfer, E. Rentschler and W. Tremel, *CrystEngComm*, 2011, **13**, 2487.

49 C.-W. Peng, M. Richard-Plouet, T.-Y. Ke, C.-Y. Lee, H.-T. Chiu, C. Marhic, E. Puzenat, F. Lemoigno and L. Brohan, *Chem. Mater.*, 2008, **20**, 7228–7236.

50 D. V. Bavykin and F. C. Walsh, *Eur. J. Inorg. Chem.*, 2009, **2009**, 977–997.

51 Lim, Ying Wen Linda, Y. Tang, Y. H. Cheng and Z. Chen, *Nanoscale*, 2010, **2**, 2751.

52 M. Andersson, L. Österlund, S. Ljungström and A. Palmqvist, *J. Phys. Chem. B*, 2002, **106**, 10674–10679.

53 E. Hosono, S. Fujihara, K. Kakiuchi and H. Imai, *J. Am. Chem. Soc.*, 2004, **126**, 7790–7791.

54 B. Ohtani, O. O. Prieto-Mahaney, D. Li and R. Abe, *J. Photochem. Photobio. A*, 2010, **216**, 179–182.

55 C. A. Melendres, A. Narayanasamy, V. A. Maroni and R. W. Siegel, *J. Mater. Res.*, 1989, 1246–1250.

56 W. Schärtl, *Light scattering from polymer solutions and nanoparticle dispersions*, Springer, Berlin, 2007.

57 R. S. Yelamanchili, Y. Lu, T. Lunkenbein, N. Miyajima, L.-T. Yan, M. Ballauff and J. Breu, *Small*, 2009, **5**, 1326–1333.

58 D. Bröll, Kaul, C., A. Krämer, P. Krammer, T. Richter, M. Jung, H. Vogel and P. Zehner, *Angew. Chem. Int. Ed.*, 1999, 2998–3014.

59 R. L. Penn and J. F. Banfield, *Am. Mineral.*, 1998, 1077–1082.

60 C. W. Passchier and Trouw, R. A. J, *Microtectonics*, Springer, Berlin, New York, 2nd edn., 2005.

61 J.-N. Nian and H. Teng, *J. Phys. Chem. B*, 2006, **110**, 4193–4198.

62 M. Kakihana, M. Kobayashi, K. Tomita and V. Petrykin, *Bull. Chem. Soc. Jpn.*, 2010, **83**, 1285–1308.

63 Y. Wang, L. Zhang, K. Deng, X. Chen and Z. Zou, *J. Phys. Chem. C*, 2007, **111**, 2709–2714.

64 A. S. Barnard and L. A. Curtiss, *Nano Lett.*, 2005, **5**, 1261–1266.

_____

65 M. N. Tahir, P. Theato, P. Oberle, G. Melnyk, S. Faiss, U. Kolb, A. Janshoff, M. Stepputat and W. Tremel, *Langmuir*, 2006, **22**, 5209–5212.

66 P. Wilhelm and D. Stephan, *J. Photochem. Photobio. A*, 2007, **185**, 19–25.

67 M. Ni, M. K. Leung, D. Y. Leung and K. Sumathy, *Renew. Sust. Energ. Rev.*, 2007, **11**, 401–425.

68 S. Kim, S.-J. Hwang and W. Choi, *J Phys Chem B*, 2005, **109**, 24260–24267.

69 M. R. John, A. Furgals and A. F. Sammelis, *J. Phys. Chem*, 1983, 801–805.

70 A. Coelho, *TOPAS Academic*, Coelho Software, Brisbane, Australia, 2007.

71 P. D. File, *International Centre for Diffraction Data*, 2007.

<div align="right">

3

</div>

Growth of Tin Dioxide Nanorods

This Chapter contains an adapted reproduction of a manuscript submitted to "Zeitschrift für Anorganische und Allgemeine Chemie" by Wiley.

3.1 Introduction

In recent years, there has been a major interest in inorganic nanostructures, which are advantageous due to their outstanding high surface area. Therefore, they are suitable for all surface demanding reactions, such as heterogeneous catalysis,[1] dye-sensitized solar cells (DSCs),[2–7] or gas sensors.[8–11] Herein, semiconducting nanostructures composed of titanium(IV) oxide (TiO_2) or tin(IV) oxide (SnO_2) are of particular interest. SnO_2 is a prominent n-type wide band gap semiconductor with a direct band gap of 3.8 eV.[12] It is transparent in the visible region and exhibits electrical properties, which makes it an ideal candidate for the aforementioned applications. Other applications for this material are transparent conducting oxide substrates,[13] transistors,[14] or Li-ion batteries.[15–17] The morphologies of SnO_2 nanoparticles, including spherical nanoparticles,[2] nanorods,[18] nanotubes,[11] nanowires,[16] and nanosheets,[19] were tailored for a plethora of applications. Various methods, like sol-gel or non-aqueous synthesis, hydro- or solvothermal treatments,[20] thermal evaporation,[21] or molten salt synthesis,[17] were employed to realize this plurality of morphologies. Despite the large variety of methods and approaches, the large scale synthesis of 1D nanostructures of SnO_2 with precise size control remains challenging.

Herein, we present a synthesis of size-tunable, single crystalline SnO_2 nanorods in acidic media via a hydrothermal treatment using HCl. A facile one-pot synthesis starting from $SnCl_4 \cdot 5H_2O$ in aqueous HCl solution is described, retaining the size control of the resulting nanorods by adjusting the reaction temperature. The particles were characterized by powder X-ray diffraction (PXRD), transmission electron microscopy (TEM), and selected area electron diffraction (SAED). Furthermore, we investigated the influence of the used acid and tin precursor. This study revealed that nanorods also grew starting from SnO_2 nanoparticles. Additionally, we trapped the intermediate species that decomposes to

_____

form SnO_2 nanorods. The trapped intermediate species was found to be $[SnCl_5H_2O]^-$, identified by solid state nuclear magnetic resonance spectroscopy (ssNMR), Raman spectroscopy, and PXRD.

3.2 Growth of Single Crystalline SnO$_2$ Nanorods

In Chapter 2, a facile and fast method was described to grow sub-micron rutile-TiO_2 rods starting from solid state precursors. This has the advantage of being cheap, and it can be stored as well as handled using standard conditions. No further precautions have to be made. Due to the similar behavior of TiO_2 and SnO_2, the same reaction mechanism could be applied. Only few adjustments had to be made to achieve a quantitative reaction yielding SnO_2 nanorods. The most apparent difference, from the perspective of solid state chemistry, between TiO_2 and SnO_2 is that TiO_2 exhibits three common crystal structures, brookite, anatase, and rutile, while SnO_2 only shows one, the rutile-type cassiterite. The sub-micron TiO_2 rods in Chapter 2 are assumed to grow easily by a disintegration-recrystallization process because of a certain instability of the precursor's crystal structure under the reaction conditions. Due to its sole crystal structure, distinct behavior can be expected for SnO_2. Owing to this difference, the majority of the following investigations were made by using $SnCl_4 \cdot 5H_2O$ as precursor.

It was possible to investigate a facile one-pot synthesis to yield size-tunable single crystals of SnO_2, which exhibited an aspect ratio of about 2, with lengths between 14 nm and 67 nm. Briefly, $SnCl_4 \cdot 5H_2O$ was solved in 0.6 M HCl and hydrothermally treated at temperatures between 200 °C and 240 °C for 12h. The resulting product could be collected by centrifugation. The grey-white precipitate was identified by PXRD to be SnO_2, and cassiterite was the only crystalline phase present. The PXRD patterns of the products synthesized at different temperatures can be seen in Figure 3.1. From top to bottom, the reaction temperature was lowered from 240 °C to 200 °C in steps of 20 °C. It is evident that upon decreasing the reaction temperature a significant broadening of the reflections took place. This broadening was due to the decrease in the resulting crystallite size. The crystallite sizes were determined to be 67(1) x 33(1), 32(1) x 14(1), and 14(1) x 6(1) nm, from full pattern profile modelling for reaction temperatures of respectively 240 °C (a), 220 °C (b), and 200 °C (c). Here, the elongation took place along the c-axis. By further increasing the reaction temperature, an additional increase in crystallite sizes was possible, but was not closely investigated due to technical restrictions.
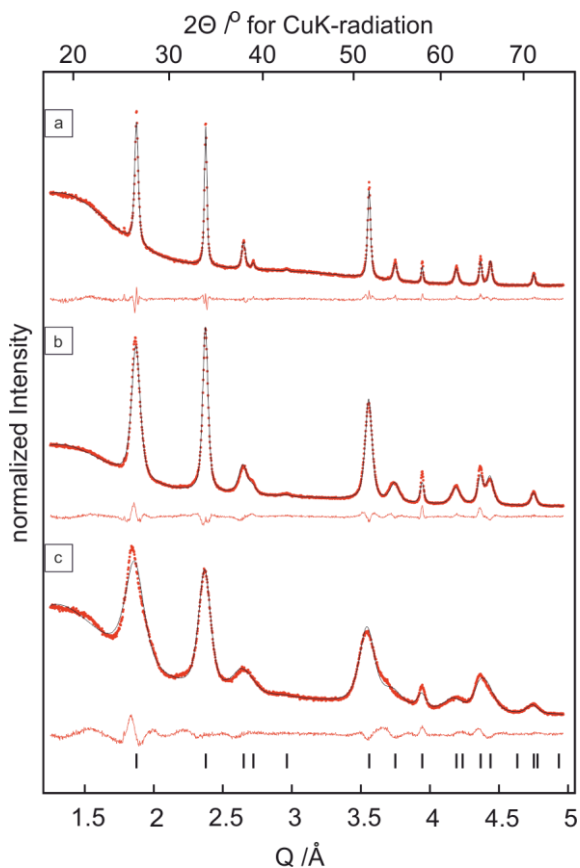
Figure 3.1 Rietveld refinement (black lines) of the powder X-ray diffraction data (red rots) and residues (red lines) of SnO_2 nanorods synthesized at a) 240 °C, b) 220 °C, and c) 200 °C, respectively. The shown tick marks indicate the reflex positions of the reference cassiterite crystal structure. The data treatment was performed by █████████████.

Figure 3.2 shows two typical TEM images, while a) displays an overview image and b) a close-up image with an SAED pattern as inset. The particles were synthesized at 220 °C and the polydisperse rods exhibit a mean length of 32 nm. However, the overview image shows that the samples exclusively yielded nanorods. Herein, it is harder to state, whether all Sn^{4+} precursor was depleted as compared to the TiO_2 rods described in Chapter 2, since the precursor is well soluble in H_2O. The close-up image in b) shows three nanorods, which were aligned next to each other. As the selected area electron diffraction pattern in the inset displays only one set of reflections, only one crystal orientation was present, revealing the nanorods to be single crystals. The alignment of particles next to each other with respect to their c-axis was an often observed feature, which will be discussed in detail later on (see Figure 3.6).

_____
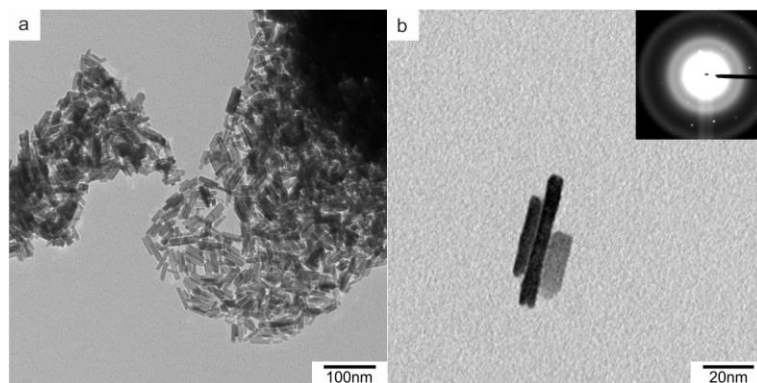
Figure 3.2 TEM images of SnO$_2$ nanorods synthesized at 220 °C: a) overview image and b) close-up image of three rods aligned next to each other. The inset shows the corresponding SAED image revealing the single crystalline character.

The length of the synthesized rods was easily tunable, while retaining an aspect ratio of about 2. Increasing the reaction temperature yielded longer rods. Figure 3.3 displays representative TEM images of SnO$_2$ nanorods, proving the possibility to tune the length by changing the temperature: in a) a reaction temperature of 240 °C was chosen, in b) 220 °C, and in c) 200 °C. The particle lengths determined from TEM images were 65 ± 20 nm, 35 ± 10 nm, and 13 ± 2 nm, respectively. The sizes for particles and crystallites, determined by TEM and PXRD as comprehensive techniques, correlated well with each other and, therefore, also confirm the rods to be single crystalline, as was shown by SAED. The particles synthesized at 240 °C show well-formed facets and, therefore, already show the single crystalline nature. In contrast, particles synthesized at only 200 °C do not exhibit clear facets. Thus the reaction temperature is the parameter to change in order to control the length of the nanorods. This can be explained by a faster formation and decomposition of the present intermediate species to form SnO$_2$ nanorods, resulting in the assembly of longer rods.
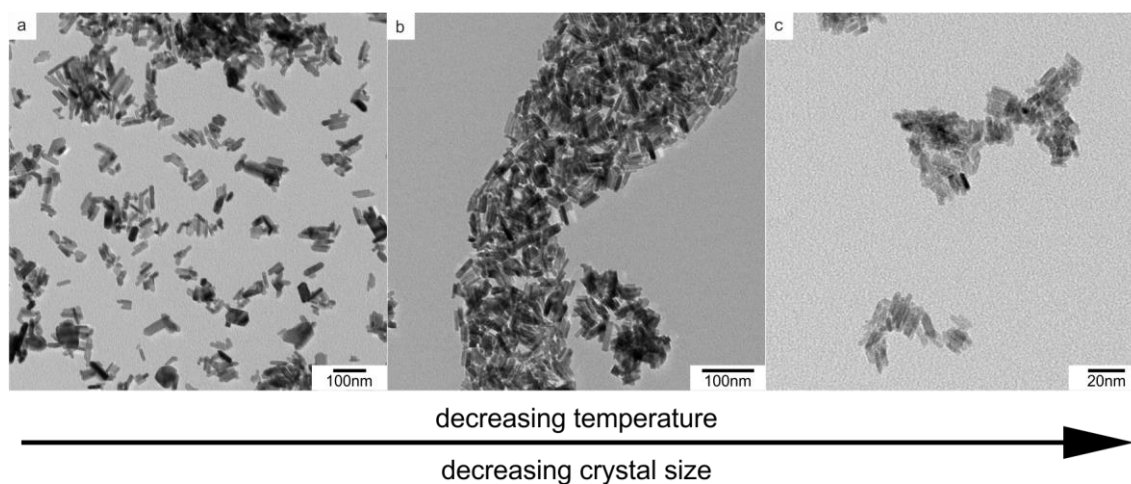
Figure 3.3 TEM images of SnO$_2$ nanorods synthesized at different temperatures leading to rods of different length: the lower the chosen temperature, the shorter the rods. Synthesis temperatures were 240 °C (a), 220 °C (b), and 200 °C (c), respectively.

The longest nanorods with a mean length of 65 nm were dispersed in DMSO and analyzed using dynamic light scattering (DLS) as a complementary characterization technique to TEM. The possibility to measure DLS already showed that the particles were, at least for 30 min, stable in dispersion. Figure 3.4 shows the results of the measurements. In a) the apparent diffusion coefficient D_{app} is plotted as a function of the scattering vector q^2, where a linear fit with positive slope can be seen. This shows that the measured diffusion coefficients were dependent on the scattering angle. This indicates the sample to be polydisperse, which is a fact that was already observed before. The hydrodynamic radius was determined to be $R_h(SnO_2) = 177.2$ nm $\pm$ 12.8 nm using the Stokes-Einstein equation assuming pseudo-spherical geometry. Considering the sizes determined by PXRD and TEM, the hydrodynamic radius is 2.7-fold larger. This increase can be attributed to aggregation of particles in solution on the one hand and, on the other hand to the z-weighted average, which is given by DLS analysis. In this case, higher molecular weight species contribute more strongly to the determined diffusion coefficient. In Figure 3.4b) the autocorrelation functions for the angles of 30°, 90°, and 120° with the according fits and residues are displayed. It can be seen that the particles show higher correlation times for 30° as compared to the other two angles. Such a shifted and strong correlation at small angles confirms that particles were strongly aggregated, because larger particles are weighed more intensely at small angles as compared to higher angles due to the angular dependence of the particle form factor.[22]
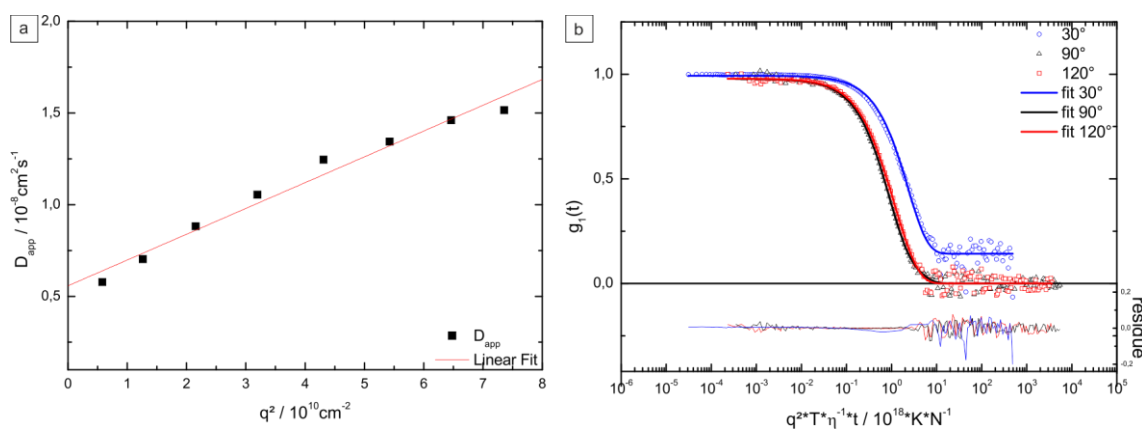
Figure 3.4 Dynamic light scattering results of SnO_2 nanorods synthesized at 240 °C dispersed in DMSO. a) Apparent diffusion coefficients as a function of the scattering vector q^2 in the range of 30° ≤ θ ≤ 135°, b) universally-scaled and normalized field autocorrelation functions measured at 30°, 90°, and 120°, together with bi-exponential fitting functions and appending residues. The measurements and data treatment was performed by ███████████.

The reaction durations were varied, keeping the reaction temperature fixed at the same time. The tested reaction times were 12 h, 24 h, and 72 h at a reaction temperature of 200 °C, which can be seen in Figure 3.5. This variation aimed to analyze the dependency of the length of the rods as a function of the reaction time. In Figure 3.3 the reaction time was set to 12 h, and since the precursor is soluble in the reaction medium, it could not be stated whether all precursor was already depleted. Further, it was questionable whether the nanorods only grew faster at higher temperatures, and therefore, were just interrupted at lower temperatures and, finally, ended up shorter. It could be shown that no further growth

_____

in c-direction of the rods resulted, even for increased reaction times of up to three days at 200 °C. However, the nanorods obtained after 12 h did not elongate upon increasing the reaction time (b, c). In b) rods could partly still be identified, while in c) the former nanorods could not be assigned as rods anymore. The particles lost their facets and appeared nearly spherical. These findings demonstrated that no further elongation along the c-axis took place upon increased reaction duration, but the change in the particle morphology by merging together with increasing time gave rise to further investigate the influence of the reaction time on the formation of SnO_2 nanorods. It was evident that the reaction time controlled the yield of the product, it took around 12 h for a reaction performed at 200 °C to deplete all precursor. However, a comprehensive investigation of the achieved yield was not performed and should only be mentioned as a side effect, since the unreacted precursor in this reaction did not contaminate the product.
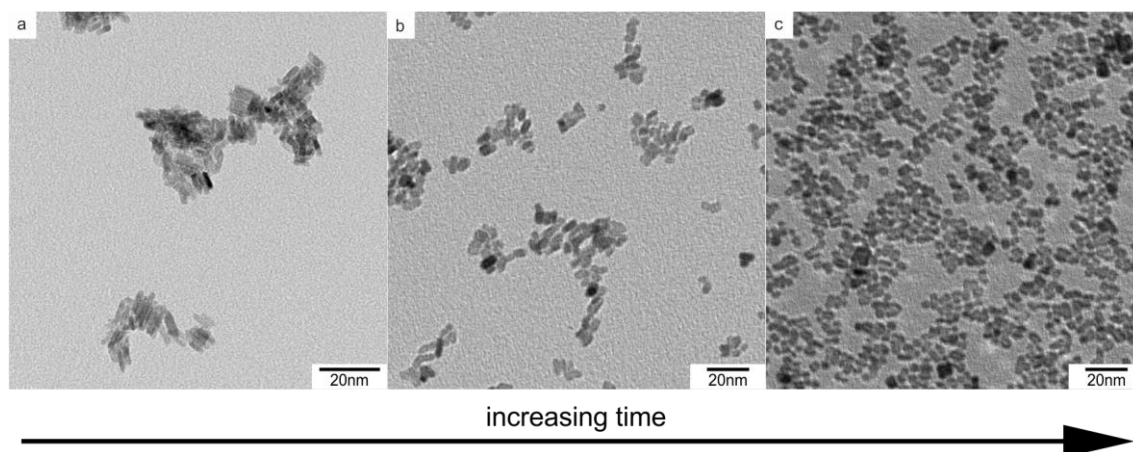
Figure 3.5 TEM images of SnO_2 nanorods synthesized at 200 °C. The applied reaction times were a) 12 h (standard reaction time), b) 24 h, and c) 72 h. The images display a) growth of well-formed nanorods, and b), c) nanorods merging together along their long axis, leading to spherical-like particles, without further growth along the c-axis.

Aside from controlling the product yield, the reaction time was found to also feature other properties, as shown in Figure 3.6. Herein, a) displays a TEM image of nanorods synthesized at 200 °C with a duration of 12 h. This image shows an alignment of SnO_2 nanorods with respect to their c-axis, and this particular example displays a large amount of rods aligned to each other. The image in a) was chosen due to the particularly high amount of aligned particles, while, the samples in b) and c) were synthesized at a higher temperature (220 °C), and, therefore, a comparison with a) is unreasonable. However, the images in b) and c) were synthesized at 220 °C with reaction times of b) 12 hours and c) 24 h. After a 12 h-reaction, all particles were rod-shaped, though it seemed that in c) particles also merged together in a secondary growth step, as described in Chapter 2 for sub-micron TiO_2 rods. The mechanism of this secondary growth step is suggested to be the same as described for TiO_2. During the first reaction step, all precursor depletes and nanorods are formed. These nanorods are too stable to re-dissolve and act as novel precursor for a further growth. As they still lack stabilization in the reaction medium, they merge together. A prerequisite to enable the merging process is the prior alignment of

particles next to each other. This merging process can only be prevented by stopping the reaction as soon as all precursor is depleted. Here it was also tried to trace former particle-particle boundaries, which was not possible. The former interface was completely eliminated after the merging process.
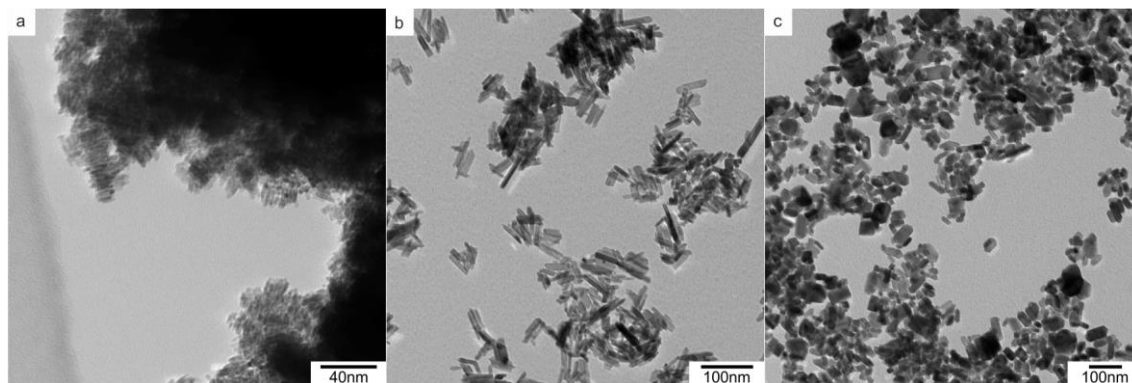
Figure 3.6 TEM images of SnO_2 nanorods synthesized at 200 °C a) and 220 °C b), c). After 12 h at 200 °C the formed rods tend to align with each other with respect to their c-axis. In the images b) and c) the reaction time was changed, showing that after a regular reaction time of 12 h b) single rods are present, while after a reaction time of 24 h c) merged particles were present.

The maximum acid concentration of HCl was determined to be 0.6 M, while higher concentrations of acid led to the formation of a more stable, soluble Sn^{4+} species, and thus no solid precipitated anymore. The same result was found when the acid concentration and volume were kept fixed, as the concentration of $SnCl_4 \cdot 5H_2O$ was increased in an attempt to increase the yield per batch. No SnO_2 precipitated, and therefore this way of upscaling failed. Applying lower concentrations of HCl down to only water led to a decreased reactivity and finally resulted in precipitating spherical SnO_2 nanoparticles (Figure B1a)), which is a result of the thermal decomposition of $SnCl_4 \cdot 5H_2O$.

After investigating the two most obvious parameters, temperature and time, the acid HCl was also exchanged to its related species, HBr and HI. Herein, Cl^- was still present due to the application of $SnCl_4 \cdot 5H_2O$, however, a comparison of samples using only Cl^- and I^- in the samples can be seen in the Appendix in Figure B1b) and c). Figure 3.7 displays TEM images with HCl (a), HBr (b), and HI (c) employed as mineralizing agent. To achieve a growth yielding nanorods using HBr and HI, the parameters time and acid concentration had to be adjusted. When employing HI, for instance, it was needed to increase the acid concentration up to 1.8 M for a quantitative reaction. Nevertheless, the duration of the reaction had to be prolonged up to 36 h as well. The reason therefore was that the complexation abilities of I^- ions for SnO_2 nanorods was by far weaker than those of Cl^-. When the reaction using HI was terminated after 12 h, large amounts of spherical SnO_2 nanoparticles were found, while nanorods could only rarely be found. This observation suggested that, at least when HI was used, first isotropic nanoparticles formed, and then re-dissolved to form nanorods in a second step. In contrast, these observations could not be confirmed when HCl was used as acid, but both can be explained by the Pearson concept of hard and soft Lewis acids and bases. Sn^{4+} and Cl^- are both considered as rather hard, while I^- is a large anion with only a low charge and is, therefore, soft. Chloro-stannate complexes, which

are assumed to form as intermediate species and be, hard-hard complexes, can be considered as stable. This explains further the findings that no solid precipitates when Cl⁻ concentrations were increased, as well as no spherical SnO_2 nanoparticles were intermediately found. When HI was used, the complex would be an iodo-stannate complex, which would be less stable due to the combination of a soft base and a hard Lewis acid. That is why an increase in acid concentration up to 1.8 M HI is possible, and the formed intermediate was still able to precipitate SnO_2. In fact, even during the reaction, spherical SnO_2 nanoparticles precipitated because a sufficient stabilization was not possible. For the growth of SnO_2 nanorods, the usage of Cl⁻ is additionally beneficial, since it is small enough to ensure a sufficient surface stabilization when the first SnO_2 already precipitated. This surface stabilization by Cl⁻ is possible due to the fact that SnO_2 exhibits positive surface charges when it is handled in acidic media with a pH lower than about 4.[23]
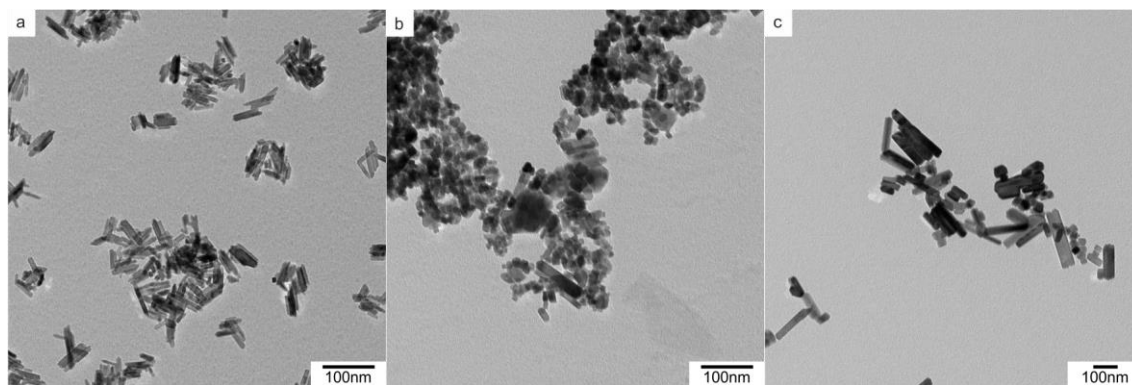
Figure 3.7 TEM images of SnO_2 nanorods obtained after a reaction of $SnCl_4 \cdot 5H_2O$ with HCl (a), HBr (b), and HI (c), respectively. The concentrations of the used acids were adjusted to ensure quantitative reactions: HCl 0.6M, HBr 0.45 M, and HI 1.8 M.

The commonly used method to dissolve the insoluble metal oxide SnO_2 is the so-called Freiberger digestion. Here, SnO_2 is transferred into the easily soluble SnS_2 by reaction with sodium carbonate and sulfur. Against this background, the observed two-step procedure of first precipitating SnO_2, then re-dissolution, and assembly to nanorods is unexpected. Herein, it was possible to facilitate a hydrogen halogen acid to dissolve of SnO_2. To verify these findings, micron-sized SnO_2 was added to a 1.8 M solution of HI and reacted at 230 °C for 12 h. The result of this reaction indicated that the precursor did not change. The TEM images of the product can be seen in the Appendix in Figure B2. The same behavior could analogously be found for TiO_2 in Chapter 2. Further, spherical SnO_2 nanoparticles with a size of 3 - 5 nm were applied as precursor, as displayed in Figure 3.8a), while b) and c) show the samples after the hydrothermal treatment using HCl and HI as employed acid. For both it could be shown that compared to using $SnCl_4 \cdot 5H_2O$ the reaction velocity was decreased. In both images (Figure 3.8b) and c)) it was possible to identify nanorods, which confirmed that preformed spherical SnO_2 particles had to dissolve to form these nanorods. Nevertheless, a certain amount of the SnO_2 precursor was still present. In Figure 3.8c), HI was used as acid, which led to an additionally decreased reaction velocity as compared to HCl. In this image, it seemed that an amorphous film was

formed on the spherical SnO_2 precursor. As a consequence of the reduced reaction velocity, this amorphous film might be an intermediate of the disintegration process. It has to be emphasized that this part of the study should only act as a proof of principle to demonstrate that the reaction to form SnO_2 nanorods in HCl solutions could also be described as a disintegration-recrystallization process or a chemical transport reaction in solution. Due to this reason, no further research was performed to achieve a full conversion of SnO_2 precursors to SnO_2 nanorods. The decreased reaction velocity was already observed for the growth of TiO_2: with $TiCl_4$ employed as precursor, the reaction velocity was also significantly higher as compared to TiO_2-P25 nanoparticles.
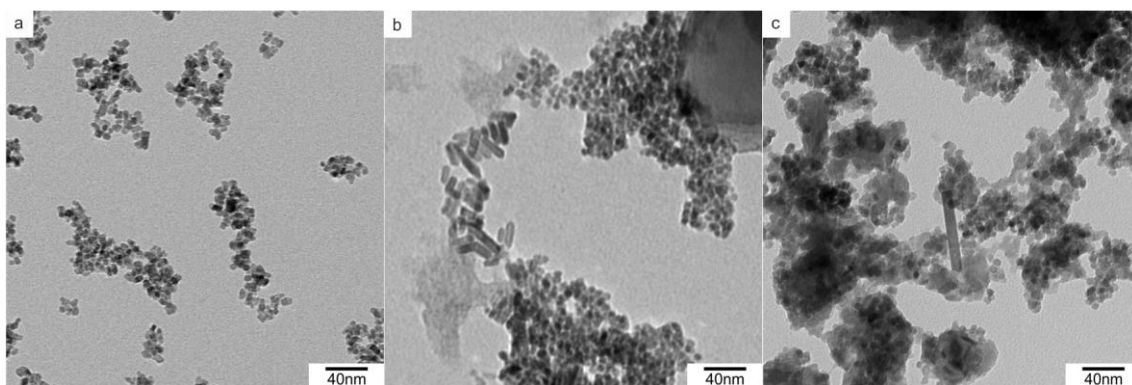
Figure 3.8 TEM images of spherical and anisotropic SnO_2 nanoparticles: a) the nanoparticles synthesized following Birkel *et al.* that were used as precursor, b) and c) show the product after hydrothermal treatment at 220 °C using HCl and HI as acid.

Previous findings indicated $SnCl_4$ not to be the species present during the reaction when suggesting that stable and instable complexes can form depending on the Cl^- concentration and, thereby, facilitate a precipitation or disable the formation of nanorods. Furthermore, other groups also investigated the present Sn^{4+} species upon changing the concentration of the present HCl solution.[24] Based on these results, a halogen stannate such as $[SnX_6]^{2-}$ (X= Cl, Br, I) or a related hydrated/hydroxylated species was suggested to occur as intermediate species. The following part of the study aimed to identify the active species decomposing to SnO_2 nanorods. In order to trap the intermediate species of the initial reaction of $SnCl_4 \cdot 5H_2O$, HCl, and H_2O, a sterically demanding cation, namely Ph_4P^+, was added in the form of its chloride. The colorless precipitate was characterized using PXRD, Raman spectroscopy, and ^{119}Sn ssNMR (Figure 3.9). In the ^{119}Sn solid state NMR spectrum of the product recorded at 10 kHz MAS (Figure 3.9), several resonances were observed. As two of the signals exhibited significant chemical shift anisotropy (CSA), it was not possible to determine directly their isotropic chemical shifts. For this reason a second experiment at another magic angle spinning (MAS) was performed (see Appendix Figure B3), as only the centerband retains its shift value independent of the spinning frequency. The signal at -460.8 ppm arises from a ^{119}Sn species in a crystalline environment with a CSA of ca. 340 ppm and asymmetry $\eta = 0.2$, as determined by the simulation. It was assigned as $Ph_4P[SnCl_5.H_2O]$.[25] To confirm this structure, a reference compound was synthesized according to published data and studied by PXRD, Raman and solid state NMR

spectroscopy, respectively.[26] The ^{119}Sn ssNMR spectrum of the reference shows the same isotropic chemical shift value as well as manifold spinning sidebands. A small amount of another Sn-containing compound with an electronic environment of the [119]Sn nucleus similar to $Ph_4P[SnCl_5 \cdot H_2O]$ and a similar [119]Sn chemical shift was found in the precipitate. The resonance signal with an isotropic shift of -455 ppm, CSA of ca. -230 ppm, and asymmetry $\eta = 0.8$ arose most probably from $Ph_4P[SnCl_5]$. However, a reliable statement at the current stage of the investigation is hardly possible.
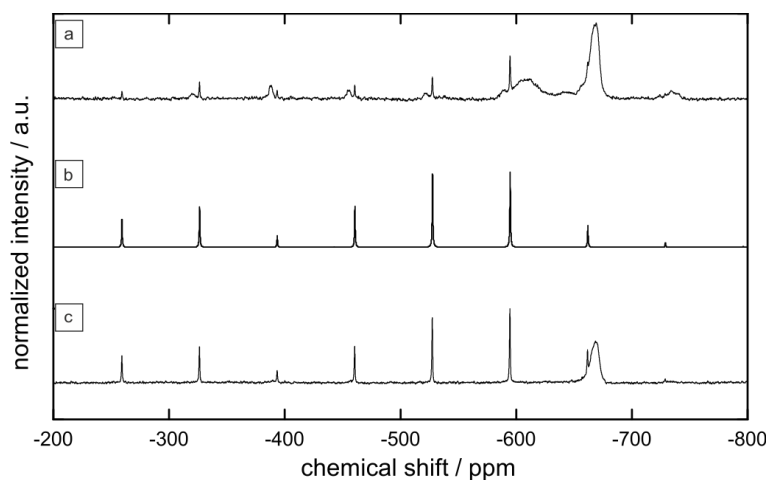
Figure 3.9 ^{119}Sn ssNMR spectra of a) the precipitated intermediate found during hydrothermal treatment, b) a simulation of the signal positions of $[SnCl_5H_2O]^-$, and c) synthetic $Ph_4P[SnCl_5H_2O]$ following a reported protocol by Müller and co-workers.[26] All spectra were normalized to the most intense spinning sideband of $[SnCl_5H_2O]$ at -595 ppm. The measurement and data treatment was performed in collaboration with ████████████.

Further broad signals with maxima at -607 ppm, -640 ppm, and -668.7 ppm were additionally detected in the ^{119}Sn ssNMR spectrum of the product, the latter one being most probably due to the presence of amorphous $[SnCl_5H_2O]^-$ (Figure 3.10). By comparison with other tin compounds likely to appear in this experiment, it could be shown that the signal at -640 ppm originates from the precursor $SnCl_4 \cdot 5H_2O$. The signal centered at -607 ppm might be due to SnO_2 present in the sample, while the signal is broadened and shifted to high fields.
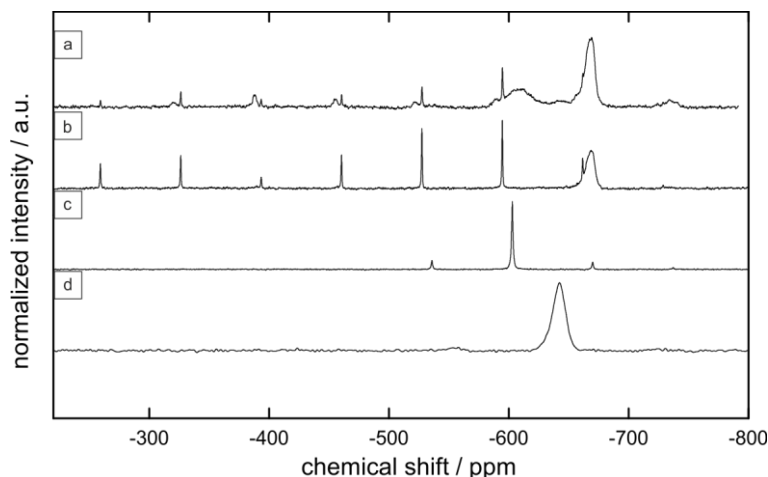
Figure 3.10 ^{119}Sn ssNMR spectra of different compounds for comparison: a) precipitated intermediate of the as-performed hydrothermal treatment, b) $Ph_4P[SnCl_5H_2O]$, c) SnO_2, and d) $SnCl_4 \cdot 5H_2O$, respectively. The measurement and data treatment was performed in collaboration with ███████████████.

Further confirmation of the structure was amongst other techniques provided by Raman spectroscopy. The spectrum of the precipitate was compared to the reference sample synthesized following the published protocol by Müller and co-workers. In Figure 3.11, it can be seen that the measured spectra correlate very well with each other, while in the spectrum of the precipitate, bands of $SnCl_4 \cdot 5H_2O$ could also be found. The Raman bands of the identified $[SnCl_5H_2O]^-$ also correlated with the data determined by Shihada and co-workers.[27]
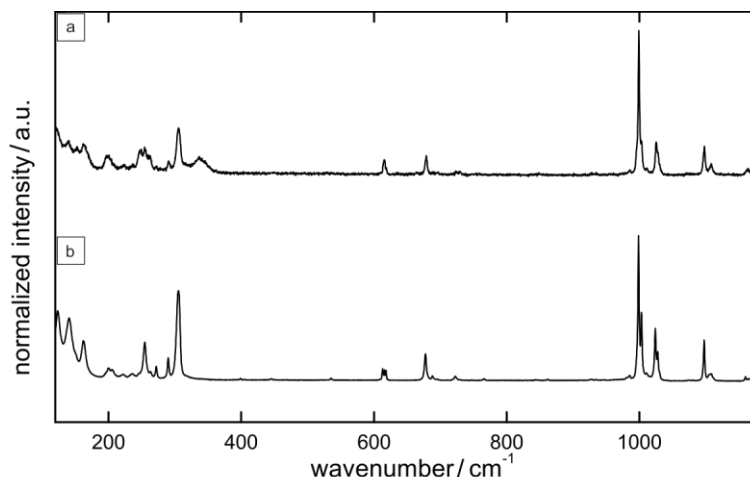
Figure 3.11 Raman spectra of the intermediate species found during hydrothermal treatment a) in comparison to the synthesized compound $Ph_4P[SnCl_5H_2O]$ b). The measurement was performed by ████████.

Additionally, the intermediate was characterized using PXRD as seen in Figure 3.12. A Pawley fit was performed to match the determined structure data by Müller and co-workers. Yet, the high intensity reflections of $Ph_4P[SnCl_5H_2O]$ are significantly observed. On the one hand, Müller *et al.* described the crystal structure of $Ph_4P[SnCl_5H_2O]$ to be tetragonal with lattice parameters of a = 13.173(1) Å and c = 7.590(1) Å. Though on the other hand, he also described the crystal structure of $Ph_4P[SnCl_5]$, which was determined to be monoclinic with the lattice parameters of a = 13.113(3) Å,

_____

b = 13.315(3) Å, and c = 7.405(2) Å. The difference between these two structures is so small that a clear identification, whether only $Ph_4P[SnCl_5H_2O]$ or both species were present, and in which ratio to each other, was not possible. Our findings using ssNMR spectroscopy indicated two chemically similar ^{119}Sn species to be present, which could be explained by the presence of both these species.
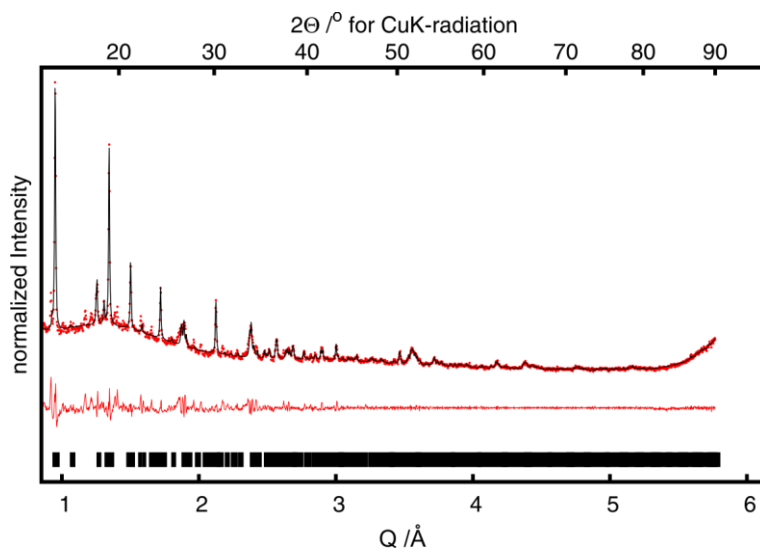
Figure 3.12 X-ray diffraction pattern (red dots) of the intermediate species $Ph_4P[SnCl_5(H_2O)]$ found when growing SnO_2 rods with Pawley fit (black line), and residuum (red line). The tick marks indicate the reflex position of $Ph_4P[SnCl_5(H_2O)]$ according to published structure data.[26] The data treatment was performed by ▬▬▬▬▬▬.

Concluding, it was possible to trap and identify the intermediate species decomposing during this hydrothermal treatment by addition of a sterically demanding cation and employing various methods, such as ssNMR spectroscopy, Raman spectroscopy, and PXRD.

3.3 Excursus - Other Rutile-type Compound: GeO₂

Germanium dioxide is used for several applications, such as being an optical material for wide angle and optical microscope lenses.[28] Additionally, it is used as a catalyst for PET-production,[29] as feedstock to produce several semiconducting materials,[30] and is applicable for optical fibers when in a mixed composition with SiO_2.[31] GeO_2 behaves to some extent similar to SnO_2. Both crystallize in a rutile-type structure and, therefore, show also a certain similarity to TiO_2. Due to the smaller size of Ge^{4+} as compared to Sn^{4+}, GeO_2 can be regarded as an interstage of SnO_2 and SiO_2. Further, germanium dioxide also crystallizes analogous to silicon dioxide in the α-quartz structure. As another similarity, it can easily be transformed into the amorphous GeO_2 by melting and slowly cooling down, which corresponds to "quartz glass".

Inspired by initial results and success to grow sub-micron and nano-sized rods of the rutile structures of TiO_2 and SnO_2, GeO_2 was suspected to be another promising candidate to form anisotropic

nanostructures. The results from this excursus will demonstrate that the behavior of TiO_2 and SnO_2 can be transferred to synthesize phase-pure GeO_2 sub-micron rods exhibiting rutile-type structure, though the reproduction of this compound was challenging.

Starting from GeO_2 as precursor and using various concentrations of HCl and temperatures between 130 and 220 °C led to two different results, depending on the acid concentration: (i) no processing of the precursor occurred, or (ii) the precursor dissolved completely and did not precipitate anymore. To ensure a similar disintegration-recrystallization process as found for TiO_2 and SnO_2, it was necessary to, on the one hand, facilitate the dissolution of the precursor, but on the other hand, also ensure that the formed intermediate was sufficiently instable to precipitate again. The reaction mixture was changed to promote the dissolution of the precursor to a solution containing hydrogen peroxide and 2.4 M HCl solution. During the reaction at temperatures between 130 and 220 °C traces of Cl_2 evolved, which facilitated GeO_2 to dissolve and react. In Figure 3.13a) and b), TEM images of a sample employing the parameters described before at a temperature of 130 °C for 12 h are shown. In c) the corresponding XRD pattern is displayed: the red ticks indicate the hexagonal phase, the blue ticks the rutile-type structure. The TEM images show clearly that nano-sized structures were formed, but also that precursor remained. The XRD pattern revealed that the rutile-type structure argutite formed only in traces.
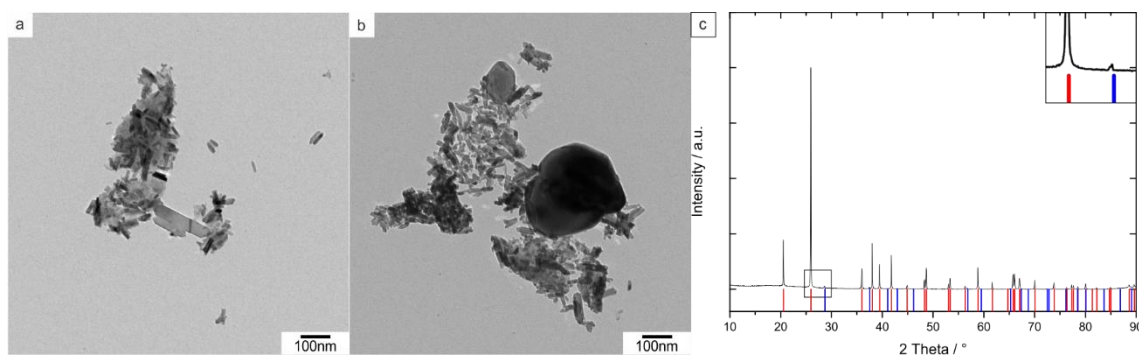
Figure 3.13 TEM images of GeO_2 nanorods synthesized from bulk GeO_2 at 130 °C for 12 h a) and b), c) PXRD pattern with red reference ticks for the hexagonal phase (96-230-0366) and blue for argutite (JCPDS entry 96-900-9081). The inset displays a magnification of the pattern between 25° and 30° 2 Theta to show the trace of argutite.

To evaluate the influence of reaction temperature, the experiments were carried out at 220 °C. Figure 3.14 displays three TEM images of a reaction using GeO_2 as precursor and 2.4 M HCl and H_2O_2 as reactants at 220 °C for 12h. This example showed that higher reaction temperatures facilitated the rods to become longer, as compared to Figure 3.13. The inset in Figure 3.14a) shows the electron diffraction pattern, which proved the rods to be highly crystalline. In b), the rods seem to exhibit an amorphous shell, which was a frequent observation. An explanation of why an amorphous shell should form has not yet been found. Figure 3.14c) shows an image of unreacted precursor. Regularly, the applied precursor remained the main product. Raising the reaction temperature as well as increasing the reaction time increased the amount of formed product, although lots of precursor still remained unreacted.

_____
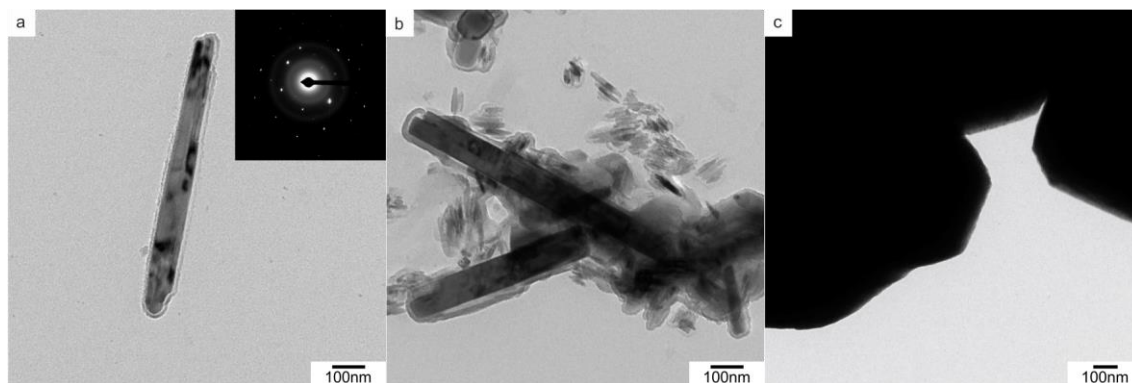
Figure 3.14 TEM images of GeO$_2$ synthesized from GeO$_2$ at a temperature of 220 °C for 12 h: a) well crystallized rod with corresponding electron diffraction pattern in the inset, b) particles having a variation in size as well as an amorphous shell, c) unreacted material.

The further used precursor was chosen to be GeCl$_4$. Prior to heating, it was solved in ethanol and then carefully added to the reactants to prevent a sudden decomposition of GeCl$_4$ in the aqueous solution. Since no precursor had to be dissolved anymore, the no addition of hydrogen peroxide was done. The results of changing precursor as well as increasing reaction time and temperature are displayed in Figure 3.15. The TEM images show in a) well-defined rods with a length of about 100 nm, while b) shows particles without a defined shape, as the side product.
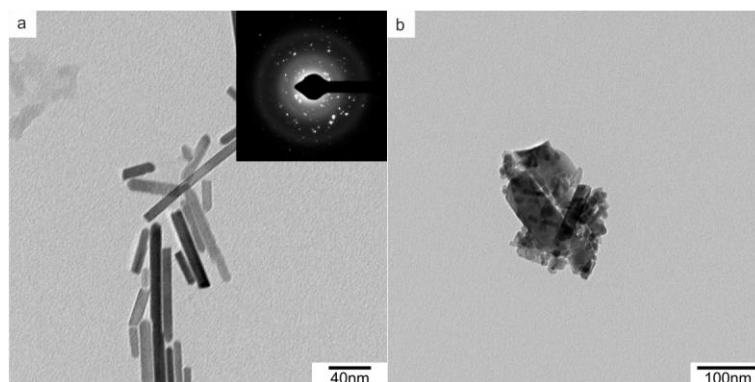
Figure 3.15 TEM images of GeO$_2$ synthesized from GeCl$_4$ as precursor at 230 °C for 36.5 h: here GeCl$_4$ was dissolved in ethanol to slow down the decomposition prior to addition to the reaction mixture: a) well-formed and crystallized rods were generated, b) samples were very heterogeneous.

By fast addition of GeCl$_4$ to the reaction mixture of 2.4 M HCl, freshly-formed germanium oxides and hydroxides were generated. This preformed starting material exhibited a high reactivity toward rod formation. The TEM images and a PXRD pattern of the result are displayed in Figure 3.16. Here, the reaction parameters were chosen to enable the growth of sub-micron sized rutile-type GeO$_2$ rods. Partly, cubic particles were observed, but only in very rare cases.
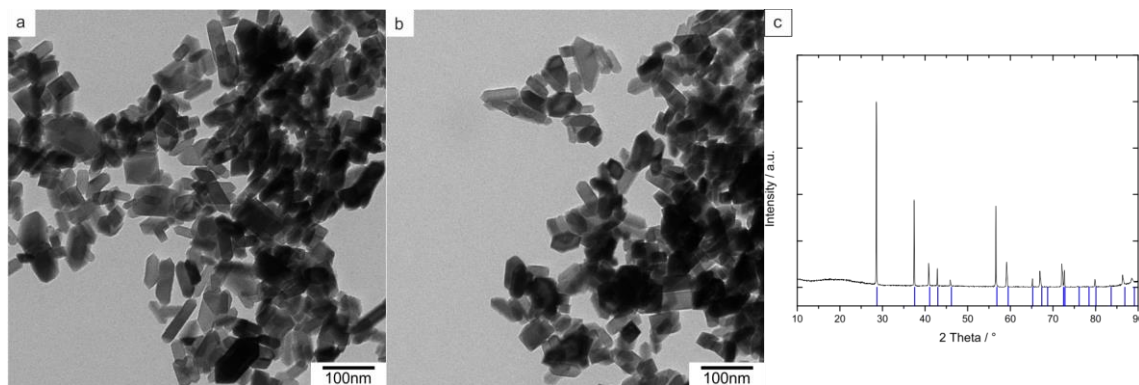
Figure 3.16 TEM images of GeO₂ sub-micron rods a) and b). The corresponding XRD-pattern is displayed in c). GeO₂ was synthesized starting from GeCl₄ as precursor at 200 °C for 36.5 h. Blue ticks in the XRD pattern represent the reflex positions of the reference data of argutite (JCPDS entry 96-900-9081).

Summing up the results of this excursus, it could be shown that not only the rutile-type structures of TiO₂ and SnO₂, but also of GeO₂, could be obtained while performing this chemical transport reaction or a similar mechanism. Synthetically a few variations had to be made, but the similarity of the reaction behavior was astonishing. The one-pot synthesis of GeO₂ sub-micron rods was hard to establish, due to its strong hexagonal side phase, and sometimes an amorphous solid was also obtained. Additionally, the choice of the employed precursor was challenging to adjust the intermediate's reactivity between stable and highly reactive. The discussed parameter variations were additionally performed with HI as reactant and showed, similar to the result of TiO₂ and SnO₂, also the ability to promote the formation of argutite rods. As discussed earlier, HI decreased the reaction velocity and, therefore, changed the outcome of the reaction.

3.4 Conclusion

The two parts of this Chapter showed that the hydrothermal growth of other rutile-type structured compounds such as SnO₂ and GeO₂ can be performed analogously to the procedures described in Chapter 2 for TiO₂. Nevertheless, several changes had to be made and were discussed.

SnO₂ nanorods could be grown in a facile one-pot synthesis. The obtained nanoparticles were single-crystalline, which was indicated by the coincidence of crystallite and particle sizes, and was also confirmed by selected area electron diffraction. The length of the particles could be tuned in the range of 14 to 67 nm by adjusting the reaction temperatures between 200 °C and 240 °C. By varying the reaction durations, nanorods could be produced in a first reaction step, while, when reaction durations were elongated, a secondary growth took place. Herein, particles aligned with respect to their c-axis and merged together. By changing the applied precursor, it was possible to show that this growth could also be described as a disintegration-recrystallization process, which is an uncommon observation for SnO₂, since it is hardly soluble and can usually not be dissolved by HCl or HI. However, by employing the other hydrogen halogen acids, HBr and HI, the assumption arose that the species decomposing to form the SnO₂ nanocrystals are $[SnX_6]^{2-}$ complexes or related hydrated or hydroxylated species. In fact, it was

possible to trap the intermediate species by addition of a sterically demanding cation, namely Ph$_4$P$^+$. The trapped insoluble compound was analyzed by means of ssNMR spectroscopy, Raman spectroscopy, and PXRD and could be determined to be Ph$_4$P[SnCl$_5$H$_2$O], while the signals in the ^{119}Sn ssNMR spectrum of this compound were accompanied by a second set of signals being chemically similar to the identified species. The combination of PXRD and ssNMR spectroscopy suggested that the second ^{119}Sn species is [SnCl$_5$]$^-$, which was also identified with Ph$_4$P$^+$ as counterion.

Aside from the application in DSCs, which will be discussed in Chapter 6, initial tests for the synthesized SnO$_2$ nanorods as Li-ion battery electrode material as well as antibacterial and catalytic-active coatings are currently being performed.

Due to the distinct similarity, it was decided to employ the analogue hydrothermal reaction, which was demonstrated to occur for TiO$_2$ and SnO$_2$, for GeO$_2$. By changing a few reaction parameters, it was achieved to state a proof of principle: a similar growth of sub-micron rods was possible. Up to now, the reaction involving GeCl$_4$ or GeO$_2$ as precursors still lack reproducibility. Nevertheless, it was also achieved for GeO$_2$ to yield phase-pure samples in the rutile-type crystal structure of the mineral argutite leading to sub-micron rods only.

3.5 Experimental section

3.5.1 Synthesis

Materials. All materials were used as received without any further purification. Tin(IV) chloride pentahydrate (98+ %, SnCl$_4$·5H$_2$O) and hydrogenperoxide solution (35 % in H$_2$O, p. A., H$_2$O$_2$) were purchased from Sigma-Aldrich. Aqueous HCl solutions of various concentrations were obtained by dilution of conc. HCl ($\geq$ 37 %, Fluka, analytical grade) with MilliQ-water (18.2 MΩ/cm). Ethanol (p.A.) was purchased from VWR. Tin(IV) iodide (98+ %, SnI$_4$), HBr (48 % aqueous solution), HI (57 % aqueous solution, stabilized with 1.5 % hypophosphorous acid), and germanium tetrachloride (99.9%, GeCl$_4$) were purchased from ABCR. Tetraphenylphosphonium chloride (98 %, Ph$_4$PCl) was purchased from Acros Organics.

Tin(IV) oxide

Synthesis. In a typical synthesis, 500 mg SnCl$_4$·5H$_2$O was dissolved in 20 mL of a ca. 0.6 M HCl$_{(aq)}$ solution (1:19 HCl:H$_2$O mixture by volume). This solution was transferred to a 50 mL teflon-lined stainless steel autoclave (DAB-2 autoclave, Berghof Corporation). The autoclave was sealed, heated up to 200 - 240 °C, and was passively cooled down after 12 h of heating time. The grey-white precipitate was collected by centrifugation (9000 rpm, 5 min). The supernatant was discarded, and the solid was repeatedly rinsed with water and ethanol. Then, the mixture was dried at 75 °C overnight.

Further, the tin precursor, the acid, and the reaction temperature were varied. In order to gain deeper insight into the reaction mechanism, the reactive intermediate was trapped by addition of sterically demanding cations. Therefore, 300 mg Ph_4PCl were added to the reaction mixture and heated up to 220 °C and kept at this temperature for 12 h. The following sample processing was as described above. For further mechanistic investigations, SnO_2 nanoparticles were synthesized as described by Birkel *et al.* using a microwave-assisted growth with $NH_{3(aq)}$ utilized as base.[32] For confirmation of our data and further measurements $Ph_4P[SnCl_5H_2O]$ was synthesized according to the protocol published by Müller and co-workers.[26]

Excursus

Synthesis. Two different precursors were used, GeO_2 and $GeCl_4$. Using GeO_2, 0.5 - 1 g GeO_2 were mixed in a teflon vessel with 20 mL 6 M HCl, in some reactions, 7 mL H_2O_2 were added. The teflon vessel was sealed in a stainless steel autoclave and subsequently heated for 12 to 36 h to temperatures between 130 °C and 220 °C. After passively cooling down, the mixture was transferred into a centrifuge tube and the solid was collected by centrifugation (9000 rpm, 5 min). The precipitate was repeatedly rinsed with water and ethanol and dried overnight at 75 °C. When $GeCl_4$ was used as Ge^{4+} source, it was mixed with 20 mL 3 M or 2.4 M HCl, while in some reactions 2 mL ethanol were added to avoid immediate decomposition of $GeCl_4$. This mixture was sealed in a stainless steel autoclave, and heated to temperatures between 200 °C and 230 °C for 36 h. The formed precipitate was collected by centrifugation (9000 rpm, 5 min) and repeatedly rinsed with water and ethanol. The solid was dried overnight at 75 °C.

3.5.2 Characterization

For characterization of the herein presented particles and their growth mechanism, various methods, *i.e.* TEM and electron diffraction, XRD, DLS, and Raman spectroscopy, were used, as was already described in Chapter 2. For the data treatment of the X-ray diffraction data, a different method was employed, as described below. Additionally, ssNMR spectroscopy was used to identify the intermediate species found in the growth mechanism study on SnO_2 nanorods.

X-ray diffraction. Powder X-ray diffraction patterns were recorded with a Siemens D5000 diffractometer equipped with a Braun M50 position sensitive detector in transmission geometry using Ge(200) monochromatized CuK_α-radiation. Crystalline phases were identified according to the PDF-2 database. Diffraction data were modeled by Rietveld refinements using TOPAS Academic. Reflection profiles were generated according to the fundamental parameter approach applying a correction for anisotropic crystallite morphologies.[33] Within this model, individual crystallite (CS_h) sizes are computed for each reflection (*hkl*) according to the quadratic form $CS_h = 1/\text{norm} \{\underline{h}T \times \underline{C}_{ij} \times \underline{h}\}$, in which *h* is the

_____

reciprocal lattice vector corresponding to (*hkl*). $\underline{C}_{ij} = (a_i)^{1/2} \times (a_j)^{1/2}$ is the symmetric second rank tensor of the square roots of the crystallite dimensions in direction *i* and *j* in the basis of the crystal lattice.[33,34]

Solid state NMR spectroscopy. The solid state NMR experiments were performed on a Bruker Advance DSX spectrometer with a ^{1}H frequency of 399.87 MHz and ^{119}Sn frequency of 149.11 MHz. A Bruker double resonance probe and supporting rotors of 4.0 mm outer diameter at a spinning frequency of 10 kHz was used in all cases. At this moderate spinning frequency, no additional heating effects due to bearing gas friction were present, such that the sample's temperature was not further corrected. For all solid state ^{119}Sn cross-polarization (CP) magic angle spinning (MAS) NMR experiments, an initial 90° pulse with a length of 4.0 µs and 3 s recycle delay was used. The duration of the variable amplitude contact pulse (64 - 100 %) was 3 ms and a two-pulse phase-modulation (TPPM) ^{1}H decoupling scheme was applied while acquiring the ^{119}Sn signal. Between 18 and 80 k transients were averaged for the different experiments. In cases when cross-polarization was not possible, as no protons were present in the sample, a 30° single pulse excitation scheme under the same MAS conditions were used. In these cases, the recycle delay was 30 s, and 16 transients were averaged. A broadening of 50 Hz was applied when processing all the spectra. The signal of tetracyclohexyltin at -97 ppm was used as a secondary reference.

3.6 References

1 G. Waghoo, R. V. Jayaram and M. V. Joshi, *Synthetic Commun.*, 1999, **29**, 513–520.
2 E. Lee, C. Ribeiro, T. R. Giraldi, E. Longo, E. R. Leite and J. A. Varela, *Appl. Phys. Lett.*, 2004, **84**, 1745.
3 S. Luo, J. Fan, W. Liu, M. Zhang, Z. Song, C. Lin, X. Wu and P. K. Chu, *Nanotechnology*, 2006, **17**, 1695–1699.
4 A. Birkel, Johannes Gutenberg-Universität Mainz, 2012.
5 H. J. Snaith and C. Ducati, *Nano Lett.*, 2010, **10**, 1259–1265.
6 Green, Alex N. M., E. Palomares, S. A. Haque, J. M. Kroon and J. R. Durrant, *J. Phys. Chem. B*, 2005, **109**, 12525–12533.
7 M. A. Hossain, J. R. Jennings, Z. Y. Koh and Q. Wang, *ACS Nano*, 2011, **5**, 3172–3181.
8 A. Kolmakov, D. O. Klenov, Y. Lilach, S. Stemmer and M. Moskovits, *Nano Lett.*, 2005, **5**, 667–673.
9 Y.-J. Choi, I.-S. Hwang, J.-G. Park, K. J. Choi, J.-H. Park and J.-H. Lee, *Nanotechnology*, 2008, **19**, 095508.
10 T. Oyabu, *J. Appl. Phys.*, 1982, **53**, 2785.
11 L. Shi and H. Lin, *Langmuir*, 2011, **27**, 3977–3981.
12 S. Gubbala, V. Chakrapani, V. Kumar and M. K. Sunkara, *Adv. Funct. Mater.*, 2008, **18**, 2411–2418.
13 W.-H. Baek, M. Choi, T.-S. Yoon, H. H. Lee and Y.-S. Kim, *Appl. Phys. Lett.*, 2010, **96**, 133506.
14 E. N. Dattoli, Q. Wan, W. Guo, Y. Chen, X. Pan and W. Lu, *Nano Lett.*, 2007, **7**, 2463–2469.
15 C. Kim, M. Noh, M. Choi, J. Cho and B. Park, *Chem. Mater.*, 2005, 3297–3301.
16 M.-S. Park, G.-X. Wang, Y.-M. Kang, D. Wexler, S.-X. Dou and H.-K. Liu, *Angew. Chem.*, 2007, **119**, 764–767.
17 Z. P. Guo, G. D. Du, Y. Nuli, M. F. Hassan and H. K. Liu, *J. Mater. Chem.*, 2009, **19**, 3253.

18 B. Cheng, J. M. Russell, W. Shi, L. Zhang and E. T. Samulski, *J. Am. Chem. Soc.*, 2004, **126**, 5972–5973.

19 Y.-L. Wang, M. Guo, M. Zhang and X.-D. Wang, *CrystEngComm*, 2010, **12**, 4024.

20 H.-C. Chiu and C.-S. Yeh, *J. Phys. Chem. C*, 2007, **111**, 7256–7259.

21 Z. Ying, Q. Wan, Z. T. Song and S. L. Feng, *Nanotechnology*, 2004, **15**, 1682–1684.

22 W. Schärtl, *Light scattering from polymer solutions and nanoparticle dispersions*, Springer, Berlin, 2007.

23 G. A. Parks and De Bruyn, P. L., *J. Phys. Chem.*, 1962, 967–973.

24 M. Xi-an, Y. Xiao-zeng and D. An-bang, *Inorg. Chim. Acta*, 1989, **156**, 177–178.

25 M. Bak, J. T. Rasmussen and N. C. Nielsen, *J. Magn. Reson.*, 2000, **147**, 296–330.

26 U. Müller, J. Siekmann and G. Frenzen, *Acta Crystallogr. C*, 1996, 330–332.

27 A.-F. Shihada, A. S. Abushamleh and F. Weller, *Z. anorg. allg. Chem.*, 2004, **630**, 841–847.

28 H. Nishiyama, J. Nishii, M. Mizoshiri and Y. Hirata, *Appl. Surf. Sci.*, 2009, **255**, 9750–9753.

29 G. P. Karayannidis, C. P. Roupakias, D. N. Bikiaris and D. S. Achilias, *Polymer*, 2003, **44**, 931–942.

30 J. Gu, S. M. Collins, A. I. Carim, X. Hao, B. M. Bartlett and S. Maldonado, *Nano Lett.*, 2012, **12**, 4617–4623.

31 H. Takahashi, J. Chang, K. Nakamura, I. Sugimoto, T. Takabayashi and A. Oyobe, *Opt. Lett.*, 1986, 383–385.

32 A. Birkel, N. Loges, E. Mugnaioli, R. Branscheid, D. Koll, S. Frank, M. Panthöfer and W. Tremel, *Langmuir*, 2010, **26**, 3590–3595.

33 A. Coelho, *TOPAS Academic*, Coelho Software, Brisbane, Australia, 2007.

34 P. D. File, *International Centre for Diffraction Data*, 2007.

4

Formation of 1D Hybrid-Structured Materials

Hybrid materials are very interesting in various fields of application. They represent a large field of research due to the tunable combination of properties originating from their single components. Composites usually refer to a loose mixture of components that are not connected to each other and, therefore, show the properties of the single components that mix upon measuring the properties of the whole sample. On a micro-scale, however, the properties differ in the sample. On the contrary, hybrid particles are connected on a micro- or nano-scale. They form one unit, even though the properties are usually not the properties of each of the single components, due to the fact that the single components of the hybrid particle interact with each other. The properties that originate from the sample do not differ in the sample due to the homogeneous distribution of the sample. Different two-component structures are possible, while the four most common of them are depicted in Figure 4.1. The scheme shows a) core/shell particles,[1–5] b) hybrid particles,[6,7] where the surrounding particles are spherical, c) branched hybrid particles,[5,8–10] and d) Janus-type hetero-particles.[11,12] For the application in DSCs hybrid and branched particles seem to be most promising. As core/shell structures a) exhibit most likely a small surface area, they might be inferior to the structures in b) and c). All three of them most likely exhibit an advantageous combination of properties of the components, while b) and c) will exhibit a higher dye adsorption compared to a) and, therefore, the aim is to synthesize these hetero-structures. However, to simplify the discussion it will also be referred to as "core" and "shell", when regarding to the inner and the outer component. The structure in d) plays a minor role for DSCs since the Janus-type particles do not have any superior applicable properties concerning the improvement of DSCs.
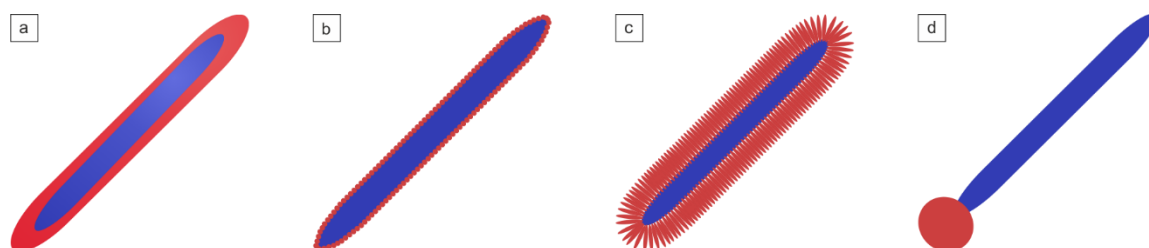
Figure 4.1 Scheme of various two-component hetero-structures: a) core/shell, b) hybrid, c) branched, and d) Janus heterostructures.

_____

4.1 SnO$_2$@TiO$_2$ Hybrid Materials

SnO$_2$@TiO$_2$ hybrid particles are very interesting for dye-sensitized solar cells (DSCs), as they combine the surface and properties of TiO$_2$ with the internal SnO$_2$ core's electronic conduction properties. TiO$_2$ as "shell" material features advantageous properties in DSCs, as it has a high conduction band (-0.1 V against the standard hydrogen electrode SHE[8]) and exhibits a high dye adsorption for common sensitizers such as N3 or N719. Additionally, due to the commonness of using TiO$_2$ as a material for the photo-active layer in DSCs most dyes were customized to provide best performance in combination with TiO$_2$. The advantages of SnO$_2$ are clearly attributed to its fast electron conduction properties, which are by magnitudes higher when compared to TiO$_2$.[13] When SnO$_2$ is used as a single component in DSCs, it suffers from several major disadvantages: the dye adsorption remains on a poor level, and the charge carrier recombination at the dye-SnO$_2$/electrolyte-SnO$_2$ interface is very fast, which, therefore, is a dominating process. Additionally, the conduction band's energy was determined to be +0.4 V against SHE,[8] which narrows the maximum V_{oc} obtained in a DSC.

It was already shown by several research groups that 1D semiconductors enhance the electron lifetime as well as the electron diffusion length.[14–17] This enables working with thicker electrodes without having to take recombination as major problem into account. Although 1D nanostructured semiconductors could improve the electric conduction properties, a drawback is their smaller surface area as compared to spherical nanoparticles. A high surface area is desirable due to the dye adsorption, which only takes place on the surface, and the amount of adsorbed dye, being the main factor contributing to the produced current: the more dye that is adsorbed, the higher the generated currents. It was aimed for hybrid particles having a 1D SnO$_2$ "core", while spherical TiO$_2$ nanoparticles were supposed to grow onto the 1D structures to join the advantages of a high surface area, 1D nanostructures, and the combination of the two materials SnO$_2$ and TiO$_2$. Many research groups aim for core/shell structures to achieve a complete encapsulation, neglecting the impact of the surface area.[18,19] In this Chapter, the synthetic progress toward SnO$_2$@TiO$_2$ hybrid structures will be discussed. A two-step procedure was always chosen for the synthesis: first the 1D SnO$_2$ nanoparticles were synthesized, and, in a second step, the encapsulation with spherical TiO$_2$ nanoparticles was performed via various methods. To investigate only the properties of the hybrid particles themselves, emphasis was drawn to synthesize hybrid particles without separate, excess TiO$_2$. In addition, it was attempted to minimize the amount of uncovered SnO$_2$ and the surrounding TiO$_2$ "shell" was made as thin as possible to still enable the charge extraction from the SnO$_2$ "core" to the FTO substrate in the later DSC.

In the first step, 1D SnO$_2$ structures were synthesized following either the established protocol discussed in Chapter 3 or a modified synthesis according to Chen *et al.* as well as Birkel and co-workers.[20,21] Figure 4.2 displays TEM images of SnO$_2$ nanoparticles obtained by following a modified hydrothermal method in basic medium. The size distribution in the samples was very heterogeneous,

_____

while the length of the rods could be tuned by varying the duration and temperature of the reaction. The length of the particles was in a range of 50 - 900 nm, while the width ranged between 10 and 100 nm.
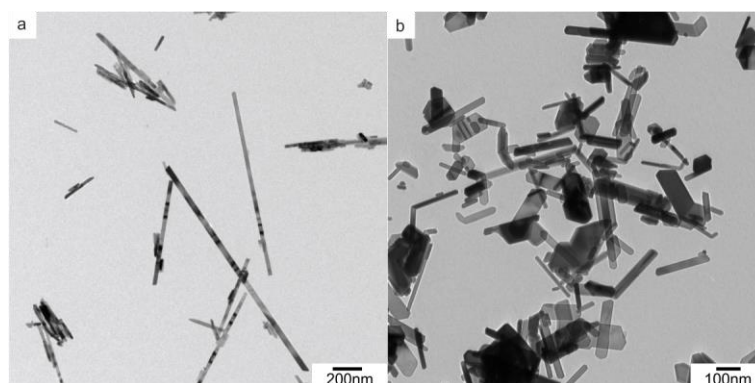
Figure 4.2 TEM images of SnO$_2$ rods synthesized following modified published protocols.

Chen *et al*. established a method to achieve epitaxial growth of TiO$_2$ branches onto SnO$_2$ wires: TiO$_2$ was grown onto the wires subsequent to the deposition of the wires onto a substrate.[22] In the published procedure, the wires were placed with the substrate in an autoclave, toluene served as solvent, and tetrabutyl titanate was employed as Ti^{4+} source. The treatment duration was the directing factor controlling the length of the branches as well as the complete coverage. In concerns of excess TiO$_2$ not fixed to the SnO$_2$ wires, the substrate assisted growth was advantageous, because excess TiO$_2$ could be washed away from the substrate. A similar approach was tried in this study, while two changes were made: (i)Ti(IV) bis(ethyl acetylacetato) diisopropoxide (TAD) was inserted as Ti^{4+} source, which should not make a major difference, due to similar behavior in solubility, reactivity, and decomposition, and (ii) it was not aimed for a substrate assisted reaction, the inserted 1D structures were free-standing. Figure 4.3 displays the results leaned on to the synthesis of Chen *et al*., while in a) toluene was used as solvent and in b) cyclohexane. Partly TiO$_2$ grew onto SnO$_2$ rods, but the majority of the rods' surface remained untouched, and a lot of excessive TiO$_2$ was formed. The metal organic precursor TAD, but also the by Chen *et al*. used Ti^{4+} source, are well soluble in organic non-polar solvents. As soon as the decomposition temperature was reached, they decomposed to TiO$_2$ and did not necessarily grow onto the SnO$_2$ rods, because they were equally distributed in the reaction medium. Also, other organic solvents, *i.e.* acetonitrile, butyl alcohol, and ethanol, were unavailingly tested.

_____
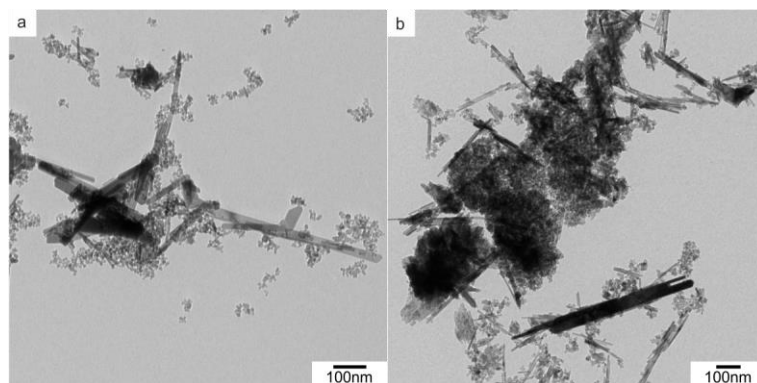
Figure 4.3 TEM images of $SnO_2@TiO_2$ hybrid structures synthesized using a solvothermal method in a stainless steel autoclave facilitating TAD as Ti-precursor and a) toluene as well as b) cyclohexane as solvent.

Taking into account that TAD is soluble in most organic solvents, TAD was incubated with the preformed SnO_2, rods and, subsequently, 10 mM NaOH was added. The careful addition of NaOH ensured that the oily TAD remained on the surface of the SnO_2 and formed an intermediate layer on the liquid-solid interface between SnO_2 and NaOH. Next, this mixture was heated up in a microwave reaction system to 20 bar or 30 bar, respectively, the resulting TEM images can be seen in Figure 4.4a), b), as well as c). In Figure 4.4a) and b), a goal pressure of 20 bar was used. It is visible that a certain amount of TiO_2 attached onto the SnO_2 rods, and even some rods were completely covered. Only small amounts of excessive TiO_2 were formed, but still parts of the SnO_2 surface remained uncovered. By introducing a solvent, in which the titanium precursor is insoluble, it was obviously possible to induce a decomposition at the solid-liquid interface between the solvent and the rods. The resulting hybrid particles were well-crystallized, as can be seen in the Appendix (Figure C1). The preformed SnO_2 was made of the crystal structure cassiterite, while the formed TiO_2 was determined to be anatase. Anatase is commonly obtained when the resulting particles are in the nano regime, and when the synthesis is being started with a liquid precursor. It was attempted to enhance the crystallinity of the TiO_2 even more, upon increasing the reaction temperature (TEM image in Figure 4.4c)). Herein, it was clearly visible that the formed anatase particles were larger and better crystallized, but it appeared doubtful, if the formed TiO_2 was attached to the SnO_2 or just assembled next to each other while drying on the TEM grid.
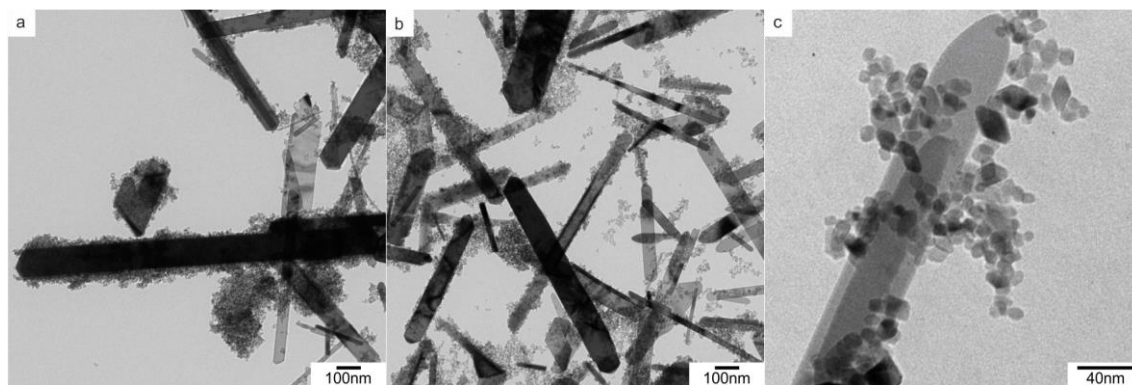
Figure 4.4 TEM images of SnO_2@TiO_2 hybrid structures synthesized using a microwave-assisted hydrothermal treatment procedure. In a) and b) a pressure of 20 bar was used. The SnO_2 rods were not completely covered with TiO_2 particles, also, segregated TiO_2 is observed. Using a pressure of 30 bar c) led to more separated particles.

To overcome the incomplete coverage of the SnO_2 rods, and at the same time avoid the formation of excessive TiO_2, a multistep procedure was applied, while maintaining the same amount of added TAD. Herein, the amount of TAD was divided in four equal portions, while the first portion was mixed with SnO_2 rods and NaOH and heated up to 20 bar for 1 h. After cooling down, the second portion was added, and heated to 20 bar for 1 h, the same procedure was applied for the third portion. Subsequent to the addition of the fourth portion, it was heated to 20 bar for 2 h. The results can be seen in Figure 4.5a) and b). The approach to deposit a small amount of TiO_2 onto the SnO_2 in a first step, and use this sites as seeds for further growth did not lead to the desired result, because only poor coverage and a high amount of excessive TiO_2 was achieved. Another disadvantage of the previously discussed one-step procedure was the small yield that was gained from the reaction. Herein, a maximum amount of 100 mg SnO_2 was inserted into the reaction, which is impracticable for later applications in DSCs. Figure 4.5c) and d) display the attempt to upscale the aforementioned one-step procedure by a factor of four by increasing the used concentrations. The result shows that there was no possibility to upscale the reaction, while maintaining the same amount of solvent, which was unchangeable due to the reaction set-up using a microwave-assisted hydrothermal treatment with pressure control. Again high amounts of excessive TiO_2 and uncovered SnO_2 were formed.

_____
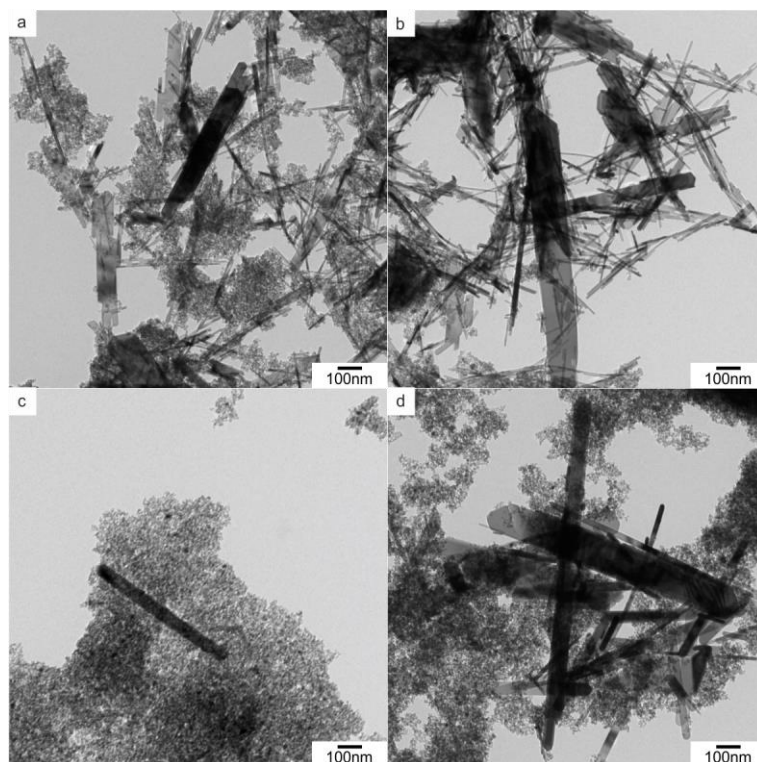
Figure 4.5 TEM images of SnO$_2$@TiO$_2$ hybrid structures. In a) and b) a multistep procedure was employed, while a heat-treatment was performed four times, subsequent to addition of TAD to prevent a fast decomposition to TiO$_2$; c) and d) show the attempt to upscale the synthesis up to an inserted mass of 400 mg SnO$_2$.

These results were a retrograde step as compared to the synthesis performed with a low yield at a reaction pressure of 20 bar. The reaction solution was modified by adding PEG to slow down the mobility of the precursor in solution. The PEGs added were PEG600 (Figure 4.6a) and c)) and PEG20k (Figure 4.6b)). When using PEG600 (Figure 4.6a)) as an additive to the NaOH solution, the resulting anatase particles that attached to the SnO$_2$ rods were not spherical but anisotropic. Still, certain amounts of excessive TiO$_2$ were present, but the majority of the SnO$_2$ rods were covered. Nevertheless, this procedure was discarded due to an unreliable product formation, as can be seen in Figure 4.6c), where the same reaction parameters were used, but nearly no coverage of the SnO$_2$ rods was achieved. When PEG20k was used to modify the viscosity of the reaction mixture, again spherical anatase particles attached to the SnO$_2$ rods. Due to the small amounts of excessive TiO$_2$, a post synthesis sample purification by selective centrifugation was attempted. However, it was not possible to achieve a complete separation by the selective centrifugation method. Additionally, this reaction procedure was unreliable and was condemned.
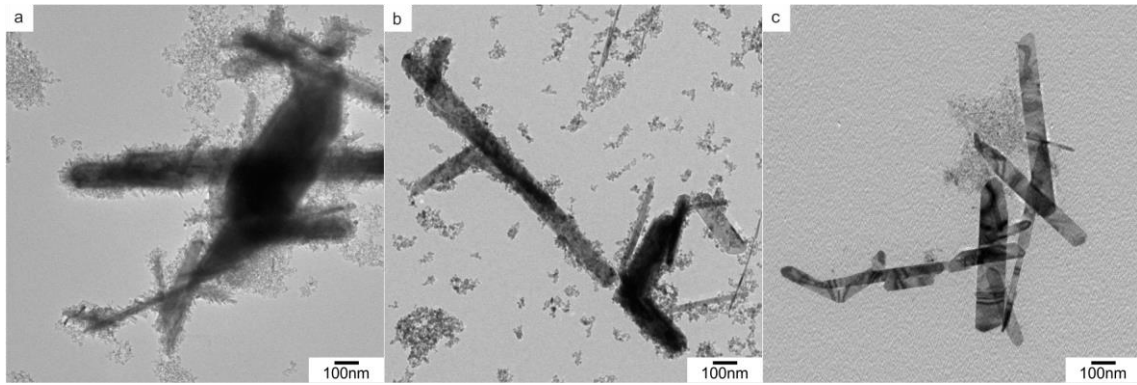
Figure 4.6 TEM images of SnO$_2$@TiO$_2$ hybrid structures after hydrothermal treatment with the addition of PEG: a) inserted rods were well encapsulated by TiO$_2$, while in b) still some amounts of separated TiO$_2$ were available, and c) shows that the encapsulation was actually incomplete.

To gain more control over the decomposition process but maintain the high crystallinity, which results from a high reaction temperature, a hydrolysis step prior to the hydrothermal treatment was applied. The NaOH solution was herein replaced by ethanol, meaning the reaction mixture contained the preformed SnO$_2$ rods, ethanol, and TAD. In the first approach, this reaction mixture was incubated overnight in a desiccator with water. The elevated humidity induced the decomposition of the humidity-sensitive TAD. Subsequently, the reaction mixture was treated in a solvothermal process. The TEM image of this reaction is displayed in Figure 4.7a). Before the hydrothermal treatment, a sample was taken, centrifuged, and prepared for TEM imaging. During the sample preparation, the decomposed TAD was washed away, and no trace of the preformed hybrid particles was identified. Nevertheless, after the hydrothermal treatment, it was possible to clearly identify that TiO$_2$ deposited on the SnO$_2$, while no excessive TiO$_2$ was generated. In the second approach, a gas stream was led through a gas-wash flask filled with water and, afterwards, through the reaction mixture, the same decomposition occurred as in the first approach. The result after the hydrothermal treatment is shown in Figure 4.7b). Here, the major product was also composed of completely covered hybrid particles exhibiting a SnO$_2$ "core" and surrounding TiO$_2$ particles, but still some uncovered SnO$_2$ and separated TiO$_2$ were present. Again, due to the low yields and the unreliable synthetic procedure, further changes had to be made. To gain more control, the hydrothermal method was rejected, and classical wet chemical approaches had to be evaluated to achieve a high coverage of the SnO$_2$ rods with a low amount of excessive TiO$_2$, coupled with a high reproducibility.

_____
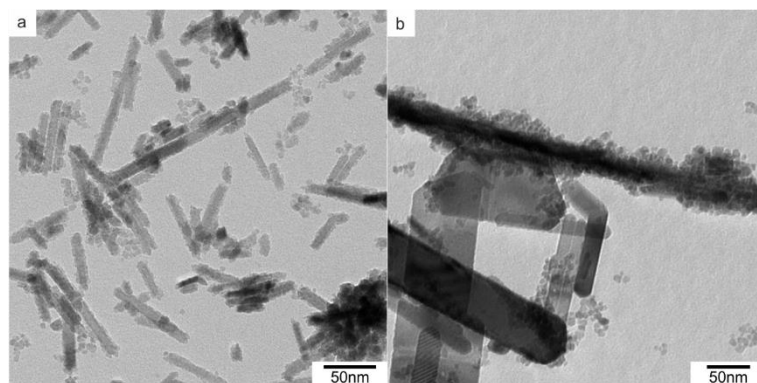
Figure 4.7 TEM images of $SnO_2@TiO_2$ hybrid structures synthesized in ethanol via solvothermal treatment. Herein, the pre-synthesized SnO_2 rods, ethanol and TAD were mixed, and then humidity was introduced prior to the hydrothermal treatment. The sample in a) was incubated in humid atmosphere overnight, and the sample in b) was treated with a humid N_2-stream through the reaction mixture.

Although surfactant-mediated wet chemical approaches usually just offer low yields, they can feature a high degree of process control to modify the resulting product as demonstrated by various groups.[23–25] Herein, a water-in-oil microemulsion was chosen, while CTAB was used as surfactant. Briefly, hexane, CTAB, and NaOH were mixed with preformed SnO_2 rods and vigorously stirred until a clear solution formed. TAD was added and slowly decomposed overnight. The result is shown in Figure 4.8. These three images indicate very clearly that the goal of complete coverage, without any unattached TiO_2 was not achieved. Most of the rods were covered at least to a high extent with titania. But still few rods remained completely untouched by precipitated TiO_2. Reason for this was that the SnO_2 rods were hardly colloidally stable. Nonetheless, when particles could disperse in either hexane or water, a preference to water was clearly observable, which in the beginning enabled this synthetic approach. Still, since the rods did not quantitatively migrate into the aqueous phase, but partly remained in the oil phase, it was clear that those particles would not undergo any hybrid formation. At that point, the change of the polar solvent should have been performed. In the last stage of the synthetic work for this thesis, it was observed that the SnO_2 rods formed a stable dispersion in combination with DMSO, so this would be a very promising exchange solvent. Additionally, it is immiscible with hexane and, therefore, could easily facilitate the discussed approach. The complete encapsulation, herein, is dependent on the ratio of TAD to surface of the rods, while the formation of excess TiO_2 depends on the ratio of CTAB to surface of the rods.
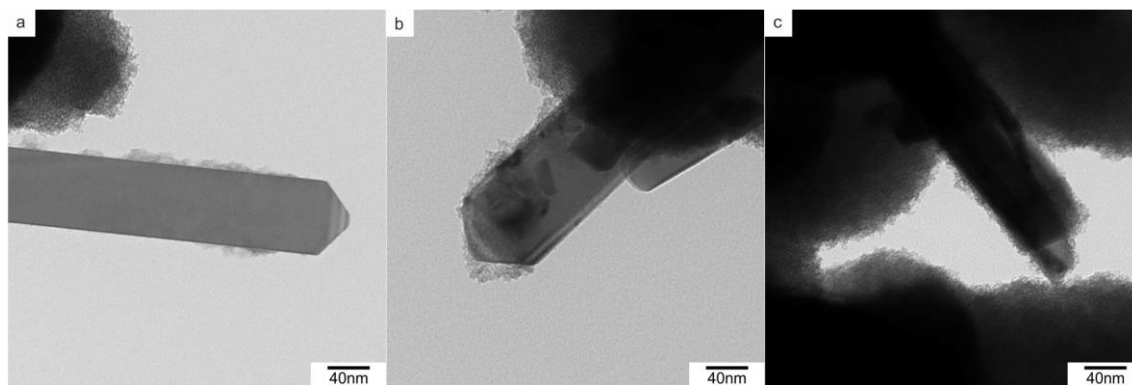
Figure 4.8 TEM images of hybrid structures synthesized using a surfactant-mediated decomposition at room temperature. The samples show that TiO_2 deposited on the SnO_2 rods, but a complete encapsulation was not achieved, while excess TiO_2 formed apart from SnO_2 rods.

Next, the ratio of rods to TAD was changed and the resulting TEM images can be seen in Figure 4.9. The TEM images indicate that upon decreasing the aforementioned ratio, very heterogeneous samples resulted. A part of the rods were completely encapsulated a), where the attached TiO_2 was mainly of anisotropic nature, it grew in form of branches. This fact would have been advantageous for a later dye adsorption in a solar cell, due to the large TiO_2 surface per SnO_2 rod. Unfortunately, a high extent of excess TiO_2 (as seen in b)) was simultaneously formed. The precipitated TiO_2 was partly rod-shaped, although no SnO_2 rod was present as the core, which was caused by the CTAB-micelles as the reaction template. Additionally, fully untouched rods appeared as well, due to the already discussed solubility that rods did not exclusively migrate to the aqueous phase.
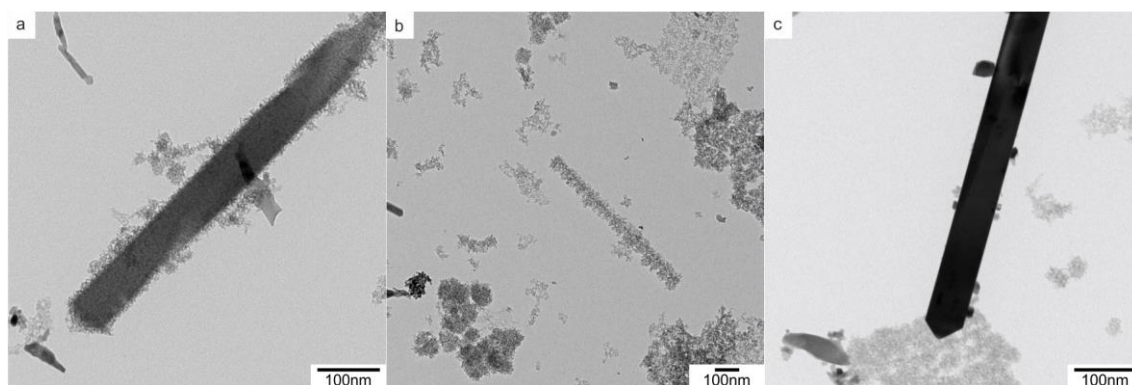
Figure 4.9 TEM images of samples during the adjustment of the TAD needed for complete encapsulation. All three images originate from the same sample, showing that a) a complete encapsulation, b) excess TiO_2, and c) untouched SnO_2 appeared in the same sample. The growth control still remained difficult.

Upon trying to control the precipitation of TiO_2, the Ti^{4+} source was added stepwise to the reaction (Figure 4.10) to enable the growth onto preformed TiO_2 on the SnO_2 rods. On the one hand this technique was advantageous, since the amount of completely encapsulated rods increased and at the same time the amount of excessive TiO_2 was reduced, as confirmed by TEM images, but on the other hand, the achieved yields were very low. However, it has to be taken in account that TEM does not depict the whole sample and is highly dependent on the sample's ability to disperse in the used solvent,

_____

as it is questionable if all components will respond similarly to the solvent. Due to this uncertainty and the remaining problems of an incomplete and spotty encapsulation of rods, this method was also discarded. Nevertheless, it should be mentioned that in Figure 4.10 not only hybrid particles, where the particles attach onto the rods a), but also core/shell structures b) were observable. Generally, all already discussed approaches, except for the surfactant-mediated technique, led to crystalline precipitated TiO_2, namely anatase. When the surfactant-mediated precipitation was applied, the resulting titania remained amorphous and further thermal treatment at 450 °C was necessary, which simultaneously removed remained CTAB. The resulting crystals were anatase phase, which is the preferred crystal structure for DSCs. (Appendix Figure C2)
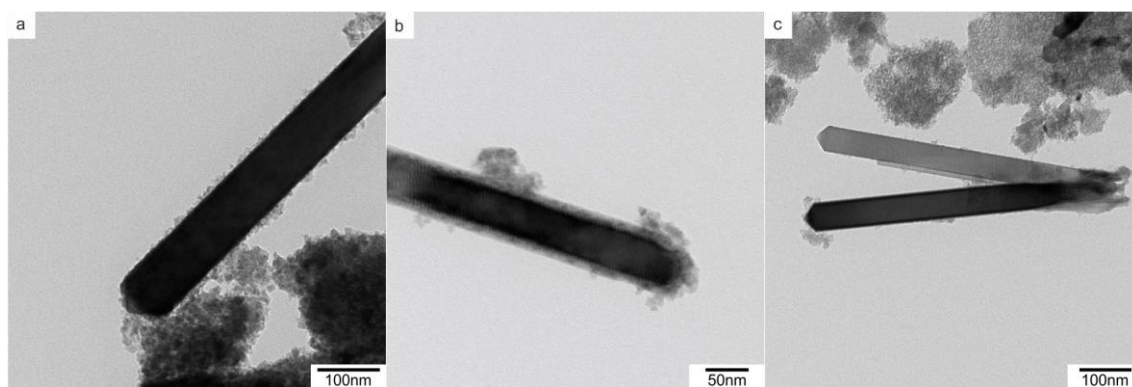
Figure 4.10 TEM images of hybrid structures grown using a micelle mediated growth. TAD was added stepwise to avoid a growth of separated, excess TiO_2: a) shows a well-grown $SnO_2@TiO_2$ hybrid rod, while in b) the rod appeared more to have a core/shell structure; c) displays two only partly covered rods and separated excess TiO_2.

In order to instantly achieve a high crystallinity, it was tried to thermally decompose TAD in a high boiling solvent. Briefly, tri-*n*-octylamine was added to the preformed rods and heated under stirring, until the solvent was boiling. The TAD was injected stepwise into the hot mixture, while a sudden decomposition took place. After the addition of the whole amount of TAD, the mixture was kept boiling for another hour. The resulting product exhibited the crystal structure of anatase for TiO_2 and cassiterite for SnO_2 immediately after the reactions, as can be seen in the Appendix (Figure C3). The TEM images of samples produced following this procedure are displayed in Figure 4.11. The images in a) and b) present a complete coverage of the SnO_2 rods with spherical TiO_2 particles, which corresponded to the desired aim. Additionally, the two images show no excessively formed, unattached TiO_2. Figure 4.11c) displays a small amount of excessive TiO_2 formed during the reaction, and also that the hybrid formation did not necessarily lead to only spherical TiO_2 particles in the SnO_2 rods, but also branched hybrid particles. Figure 4.11d) shows that the particles with uncovered SnO_2 surface were also formed. Indeed, this approach led to fulfilling of many of the set requirements: (i) the degree of encapsulated particles was very high, (ii) the amount of excessively formed TiO_2 was low, and (iii) the yield was comparably high. One reaction yielded 0.6 g hybrid particles. Hence, these type of particles suffered a major problem: the resulting products changed immensely and, therefore, the reaction was

neglected. It was mandatory to establish a reproducible synthesis to ensure the unity of the later produced DSCs.
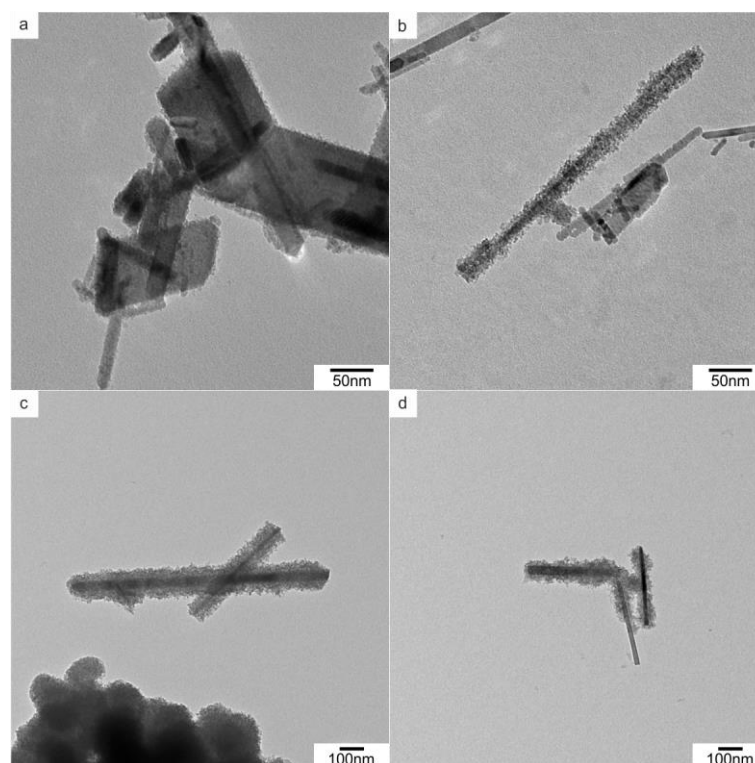
Figure 4.11 TEM images of SnO_2@TiO_2 hybrid structures synthesized using a high boiling solvent, namely tri-*n*-octylamine: a) and b) mainly show well-grown hybrid particles with a SnO_2 core and accumulate TiO_2 particles with neither uncovered SnO_2 nor separated TiO_2, while upon reproducing these results it was evident, that also excess TiO_2 (c) and uncovered SnO_2 appeared (d).

All the employed approaches did not lead to a sufficient product formation when taking into account all preset goals. Therefore, a completely different approach was tested and it led to the desired product formation. Briefly, preformed rods were added to 20 mL water in a Teflon vessel. To this mixture a so-called TiCl-treatment solution, which contained $TiCl_4$ dissolved in aqueous HCl, was added and hydrothermally treated using very mild conditions (0.5 bar). After 2 h reaction time, SnO_2 rods that were completely covered with TiO_2 resulted. A formation of excessive TiO_2 was not observed and the reaction easily yielded 500 mg product per synthesis. The formed TiO_2 was not well-crystallized, and also a subsequent thermal treatment at 450 °C did not lead to crystallization of the "shell" (Figure C4). The usage of a water-soluble, highly charged Ti^{4+} precursor in combination with also highly charged rods was probably the key factor to enable the exclusive attachment of TiO_2 on SnO_2, while the mild and slow decomposition of the Ti^{4+} precursor might have also contributed to this result.
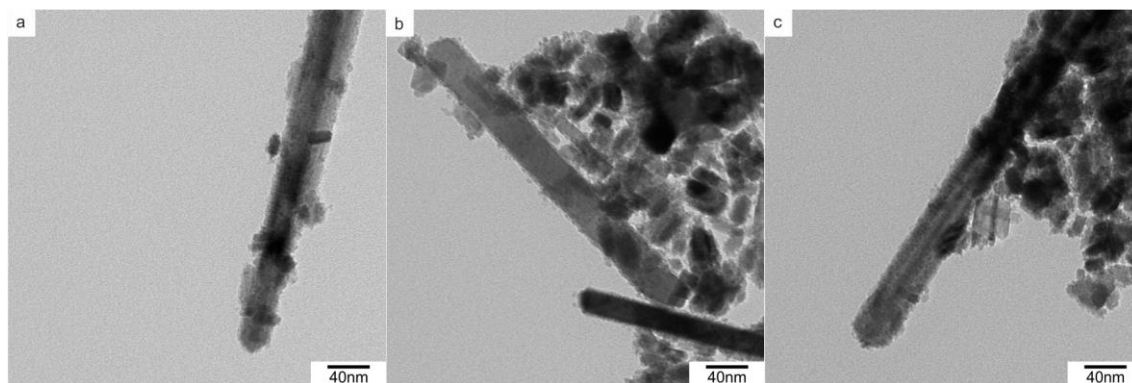
Figure 4.12 TEM images of SnO$_2$ rods completely encapsulated by amorphous TiO$_2$. Here, a mild hydrothermal treatment with 0.5 bar pressure was employed, and TiCl$_4$ was inserted as Ti^{4+} source.

4.2 TiO$_2$@TiO$_2$ Hybrid Materials

As already discussed for SnO$_2$@TiO$_2$, hybrid structures are desirable due to the possible combination of different "core" and "shell" material properties. For SnO$_2$ and TiO$_2$, it was the combination of SnO$_2$'s fast conductivity with a high dye adsorption of anatase phase TiO$_2$ and the high positioned conduction band. In contrast, when TiO$_2$ is used as a core material, the advantages seem to be less obvious, but are still there due to the different properties of the various crystal structures of TiO$_2$.[26] A key focus was set to the combination of rutile as core and anatase as shell, since anatase exhibits a slightly higher conduction band compared to rutile, and, therefore would force charge carriers, *i.e.* electrons, in one direction, namely from the anatase shell into the rutile phase TiO$_2$. Additionally, such hybrid structures would present anatase as surface for anchor groups of metal organic dyes. This is beneficial for the amount of adsorbed dye, while the surface area is simultaneously increased by synthesizing TiO$_2$@TiO$_2$ hybrid structures as it was possible for SnO$_2$@TiO$_2$ particles. Due to the similar behavior of TiO$_2$ and SnO$_2$, the following part of this Chapter will discuss analogue approaches, as they were presented in the aforementioned part for SnO$_2$@TiO$_2$ hybrid structures. The preformed rods used in this part of the Chapter were all synthesized according to the presented procedure in Chapter 2. Due to the fact that both, the "core" and the "shell" are made of TiO$_2$ it is necessary to simplify the discussion. The "core" material always consisted of rutile TiO$_2$, and will be regarded as rutile, while the formed "shell" mostly consisted of anatase, and will be assigned as such, although partly the "shell" might have been amorphous or no PXRD pattern might be provided.

The work of Chen *et al.* also served as a starting point for TiO$_2$@TiO$_2$ hybrid structures. Briefly, preformed rutile rods were mixed with TAD and toluene or cyclohexane was added. This mixture was sealed in a stainless steel autoclave and heated to temperatures between 150 and 220 °C for durations between 12 and 60 h. The results of the reactions can be seen in Figure 4.13 while toluene (a, b) and cyclohexane c) were employed as solvents. Using other solvents for instance, glycols, ethanol, butyl alcohol, or acetonitrile did not lead to beneficial results and are, therefore, not shown. Figure 4.13a)

shows a sub-micron rutile rod that exhibits large amounts of anatase grown on its surface, while a lot excess anatase particles were still formed aside from the desired hybrid particles. The TEM image in Figure 4.13b) originates from the same sample as in a), although less anatase was attached to the rutile sub-micron rods. Changing the solvent to cyclohexane (Figure 4.13c)) had no visible positive influence on the formation of rutile@anatase hybrid structures. All present rutile rods were kept without anatase grown onto the surface. Here, the majority of formed anatase was also excessive anatase, and not attached to rutile. The reason is probably, as mentioned for the SnO_2@TiO_2 hybrids before, that TAD is soluble in toluene and cyclohexane, and the thermal decomposition takes place all over the reaction medium and a directing effect is missing.
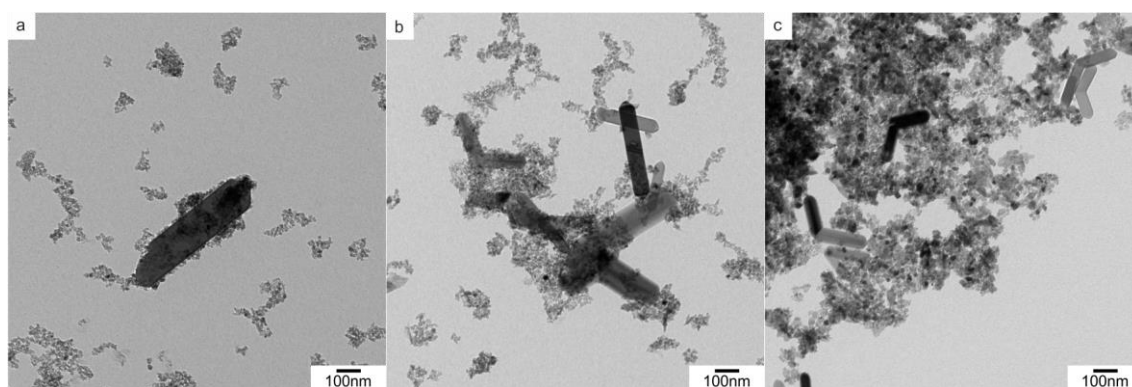
Figure 4.13 TEM images show TiO_2@TiO_2 hybrid structures solvothermally grown using toluene (a, b) and cyclohexane c) as solvents. In both cases excess TiO_2 and uncovered rods were present as well.

In analogy to SnO_2, the reaction for TiO_2 rods was also transferred from a non-polar organic solvent to an aqueous system, *i.e.* 10 mM NaOH solution. Briefly, rutile rods, TAD, and NaOH were mixed in a teflon vessel and heated to 20 or 30 bar for several hours. The resulting product was collected by centrifugation, washed, and dried. Figure 4.14 shows TEM images of this reaction. It can be seen that compared to the pictures in Figure 4.13 the change of the solvent had a beneficial effect on the formation of hybrid particles. Large amounts of the formed anatase were attached to the rutile rods, while the excessively formed anatase could be reduced. This was already observed for the system of SnO_2@TiO_2 hybrids, although the positive effect for TiO_2@TiO_2 hybrids was lower. The increased hybrid formation was assigned to the insolubility of the used TAD in NaOH solution. An effect of differing pressures used could not be observed for TiO_2@TiO_2 hybrids: the quantity of attached anatase and excessive TiO_2 remained constant. The only result that changed was that the formed anatase exhibited a larger particle size. This is a common observation upon increasing reaction temperatures, when Ti^{4+} precursors are thermally decomposed. Figure 4.14c) gives rise to the doubt that the formed anatase particles, which accompanied the rutile rods, where completely attached to the rutile rods. Low resolution TEM images could not doubtlessly prove that a thorough attachment was achieved, but it appeared partly that there was no merged interface. HR TEM images could probably prove the common interface by showing lattice fringes migrating from one particle to the next. Using low resolution TEM

images often provides only an indication, which could have been strengthened by measuring tomography. The co-assembly of rutile rods and anatase could be also an effect during the sample preparation on the TEM grid. Briefly, also the influence of the pH value was evaluated. The TEM images of the reaction performed at pH 9 and pH 5 can be seen in the Appendix. For adjusting the pH 5, HCl was used. Figure C5 in the Appendix shows that no obvious influence of the used solvent was present.
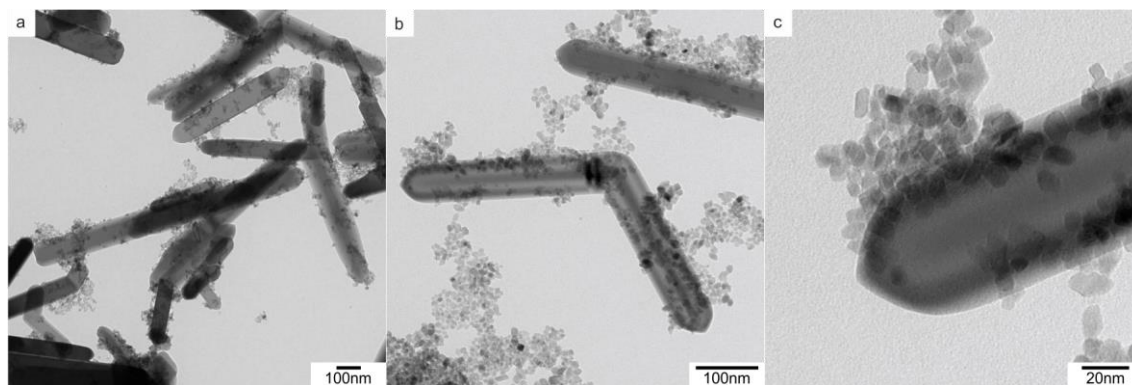
Figure 4.14 TEM images show $TiO_2@TiO_2$ hybrid structures grown via a hydrothermal treatment at a pressure of 30 bar. Comparably to $SnO_2@TiO_2$ hybrid structures, excess TiO_2 and incomplete encapsulated rods were present.

Upon increasing the viscosity of the reaction solution, an advantageous effect was also observable for $TiO_2@TiO_2$. Figure 4.15a) and b) shows the TEM images with an increased viscosity, which was adjusted using PEG600, while the additive in c) was PEG20k. It is obvious that compared to Figure 4.14 more anatase grew onto the rutile rods. The adjustment of the viscosity was performed using PEG600 or PEG20k, while no difference of the product was observed: In both cases, lots of rutile@anatase hybrid structures formed. Upon decreasing the amount of added TAD to lower the amount of excessive anatase, more and more uncovered rutile surface remained and excessive anatase remained in the samples. For this, as well as for several other approaches when synthesizing $SnO_2@TiO_2$ hybrids, it was tried to optimize the parameters of a fractionated centrifugation procedure to ensure the highest degree of coverage of the rods, but at the same time have a minor amount of excessive TiO_2. Only little success could be acknowledged using these attempts, and especially similar densities had to be assumed for $TiO_2@TiO_2$ hybrids. It was possible to enrich the fraction of hybrid particles, but the remaining fraction of excessive anatase was considered to be too high and, therefore, this procedure was neglected not only for $SnO_2@TiO_2$, but also for $TiO_2@TiO_2$ hybrid particles.
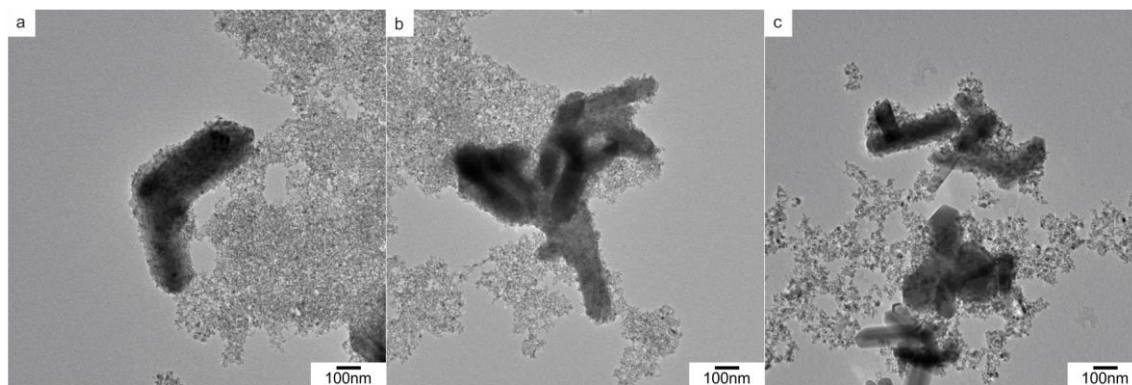
Figure 4.15 TEM images show TiO$_2$@TiO$_2$ hybrid structures grown via a hydrothermal treatment at a pressure of 30 bar. Upon increasing the viscosity the amount of TiO$_2$ particles attached to the TiO$_2$ rods increased as well. The adjustment of the viscosity was made by addition of PEG20k.

Inspired by the high control achieved for other synthetic questions such as the synthesis of inorganic Janus particles it was attempted to apply a similar synthetic approach by addressing a similar wet chemical route. Herein, a high boiling solvents, such as tri-*n*-octylamine, octadecen, and benzylether were tested. A hot injection method, when preformed rods were already present, was used. Briefly, preformed rutile rods were added to tri-*n*-octylamine and heated to its boiling point under vigorous stirring. The Ti^{4+} precursor TAD was injected stepwise into the hot solution. The mixture was kept boiling for another hour after completed addition of TAD. After cooling down, the product was collected by centrifugation and washed. This approach exhibited various advantages concerning the path of the reaction. Since the reaction was performed at standard pressure, an addition of several substances was possible during the reaction. On the other hand, it also enabled us to take samples during the reaction and, therefore, trace several steps of the reaction. A disadvantage of the aforementioned technique of the surfactant-mediated encapsulation of SnO$_2$ by TiO$_2$ was that the resulting TiO$_2$ was amorphous. While using a high boiling solvent, a crystalline product should be expected, since the reactions were performed at ca. 300 °C. Figure 4.16 shows TEM images of hybrid particles synthesized in tri-*n*-ocytlamine, a) and b) represent samples taken 10 min after injection of TAD, c) and d) show the same sample after a prolonged heating period of 50 min. It has to be noted that the rutile rods, used as a precursor, were contaminated with unreacted TiO$_2$-P25 precursor, which is visible in Figure 4.16d). Nevertheless, this fact did not change any results of this reaction. In Figure 4.16a) and b), it can be observed that large amounts of anatase were formed. Partly rutile rods can be seen in the blurry anatase film, which was probably at this step still amorphous. It is evident that lots of rods were covered by anatase, although some rods remained uncovered, as well as in some parts of the anatase it is visible that no TiO$_2$ rods were embedded. After the additional heating time of 50 min (Figure 4.16c) and d)), the anatase particles had sharp boundaries, and clearly exhibited the crystal structure of anatase, as all the blurry boundaries had vanished. The prior observations made for SnO$_2$@TiO$_2$ hybrids could be confirmed. Large amounts of excessive anatase were formed, while a complete coverage of the rutile

_____

rods could not be achieved. The good SnO_2@TiO_2 hybrids using this method could not easily be transferred to TiO_2@TiO_2 hybrids. Further, the lack of reproducibility was a reason to reject this method.
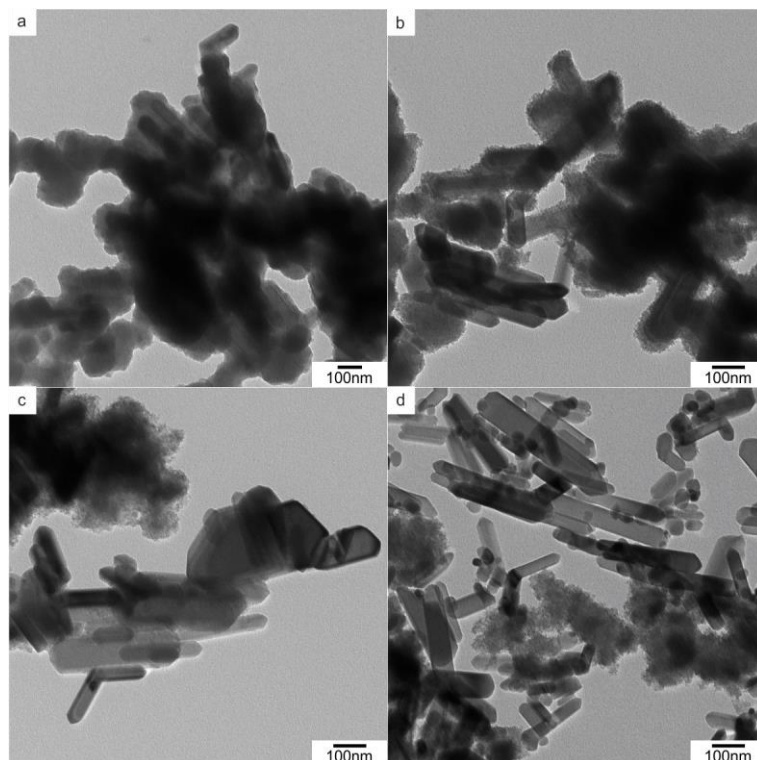
Figure 4.16 TEM images of TiO_2@TiO_2 hybrid structures synthesized using the hot injection method in combination with a high boiling solvent, tri-*n*-octylamine: a) shows the sample immediately after the injection of TAD into the reaction mixture, while b) depicts the sample after additional thermal treatment for further 50 min; c) and d) reveal that also here high amounts of excess TiO_2 and uncovered rods were present.

A coating method used for DSCs gave rise to a mild reaction path using an aqueous solution of $TiCl_4$ as Ti^{4+} source. Herein, the preformed photo-anodes composed of TiO_2 nanoparticles attached to a FTO substrate are soaked in water, where a few milliliters of a TiCl-treatment solution are added. This mixture is kept at 70 °C for 1 h. Afterwards, the substrates are rinsed and sintered to ensure a crystalline product. Here, the desired product, unfortunately, should be free of a substrate such as FTO, and, therefore, the method had to be slightly tailored for the requested demands. Briefly, preformed rutile rods and water were mixed in a teflon vessel. A TiCl-treatment solution was added, as also described in the mild hydrothermal treatment for SnO_2@TiO_2 hybrid particles, and, subsequently, the teflon vessel was sealed and heated to 0.5 bar in a microwave-assisted reaction system. This low pressure can be correlated to a temperature of about 80 to 90 °C, which strictly speaking is not assigned as hydrothermal. Nevertheless, to simplify the discussion it will be described as a mild hydrothermal treatment. The reaction duration was chosen to be 2 h. Figure 4.17 shows TEM images of the product of the reaction. It can be seen that small amounts of excessive anatase were present. The majority of the surface of the rutile rods was covered with anatase. In Figure 4.17a), the rods are not only covered with spherical particles, as can be observed in b) and c), but also quite long branches of anatase formed on the rutile rods. The TiCl-treatment solution is highly acidic, which reinforces the assumption that a $[TiCl_6]^{2-}$ or

[TiCl$_5$H$_2$O]$^-$ is the present Ti^{4+} species. The surface of the rutile rods, which were synthesized in 6 M HCl, is most likely positive due to the isoelectric point of TiO$_2$ at pH 6.7.[27] The charges of the soluble Ti^{4+} complex and the rods suggest that this growth might be charge controlled and, therefore, yield very good results concerning the complete coverage as well as the formation of excessive anatase. *De facto*, the formed TiO$_2$ is not crystalline directly after the synthesis and cannot be transferred into anatase-phase TiO$_2$ by a subsequent thermal treatment at 450 °C. (Figure C6)
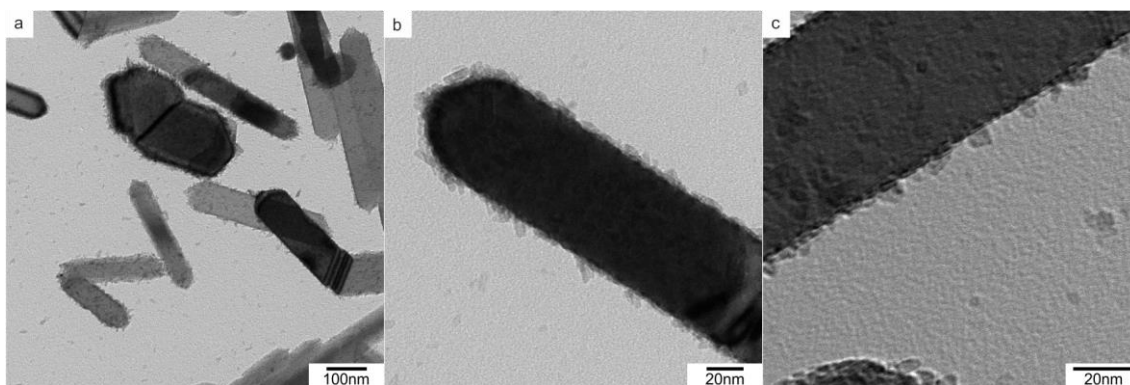
Figure 4.17 TEM images of TiO$_2$@TiO$_2$ hybrid structures showing entirely encapsulated TiO$_2$ rods. The thorough coverage was achieved by using a mild hydrothermal treatment in combination with TiCl$_4$ as Ti^{4+} source for the cumulative TiO$_2$ particles.

4.3 Conclusion

This Chapter aimed to describe the synthesis of two different types of hybrid structures, namely SnO$_2$@TiO$_2$ and TiO$_2$@TiO$_2$. For both, the outer TiO$_2$ was composed of the crystal structure anatase, while the inner part was rutile-type SnO$_2$ and TiO$_2$, respectively. Those hybrid structures are interesting for several reasons, as they combine the properties of both materials, while they additionally exhibit an increased surface area as compared to the employed rods. To profit from the combination of the properties, four aims were set:

(i)   The samples should show no (or a minor amount) of excessively formed TiO$_2$ to study only the behavior of the hybrid structures.

(ii)   The particles should be fully covered with surrounding TiO$_2$.

(iii)   The formed shell was demanded to avoid a predominance of the TiO$_2$ component.

(iv)   To ensure that the synthesized particles can find an application in DSCs, they had to match two further requirements for technical reasons: the synthesis had to be reliable and a high yield, due to the high amount of substance needed for the assembly and optimization of DSCs.

For SnO$_2$@TiO$_2$ a large variety of methods were employed, *i.e.* solvo- and hydrothermal, surfactant-mediated, multistep techniques, synthesis in high boiling solvents, as well as mild

_____

hydrothermal treatments. At first glance, several methods appeared promising. A yield of hybrid particles was attempted, exhibiting all stated demands. Using a solvothermal as well as a facile hydrothermal treatment did not lead to the desired morphologies. By adjusting the viscosity of the solvent, an enhancement of the product could be achieved, but did not work out upon further optimization. An additional promising method was the surfactant-mediated encapsulation, where the TiO_2 precursor decomposed in the micelles. The observations made later-on upon the solubility of the preformed rods in dimethylsulfoxide (DMSO) could have improved the synthesis by far. Promising initial results were achieved with this technique, but upon optimizing the product to adjust it for application this method was rejected as well. When aiming for a thick shell on SnO_2 rods, the synthesis in high boiling solvents can be a suitable choice. This facile synthesis mostly led to quantitatively encapsulated rods, while the formed shell was too thick for the planned application. By employing a mild hydrothermal treatment with an acidic Ti^{4+} precursor, it was possible to meet all demands set for the product: (i) the excessively formed anatase was kept at a minimum, (ii) the particles were fully encapsulated, (iii) the synthesized hybrid particles exhibited a thin "shell" of spherical anatase nanoparticles, and (iv) the procedure was reliable and yielded nearly 500 mg per batch. Further, the method allowed an upscaling at the same time of up to 2 g.

Analogous developments were made for a synthesis toward $TiO_2@TiO_2$ hybrid structures. The goal to reliably produce hybrid structures of rutile and anatase could be met by employing a mild hydrothermal treatment. Herein, an aqueous solution of $TiCl_4$ was mixed with preformed rods and reacted for 2 h at about 80 to 90 °C. The product exhibited a "core" of rutile and a "shell" of spherical anatase nanoparticles, while these particles also partly evolved as branches. Additionally, the yield was found to be as high as by 500 mg per batch, and the method also allowed an upscaling by a factor of 4. Also the other employed techniques seemed to be less promising, as compared to the synthesis of $SnO_2@TiO_2$ hybrid structures. However, the surfactant-mediated encapsulation of rutile rods, which were not described, showed similar results to the synthesis of $SnO_2@TiO_2$ hybrid particles. Thereafter, it was found that the rutile rods also formed a stable dispersion in DMSO, which could, therefore, improve this reaction path and lead to fully encapsulated $TiO_2@TiO_2$ hybrid structures.

All-in-all several methods were tested concerning their suitability to lead to free standing hybrid structures of $SnO_2@TiO_2$ and $TiO_2@TiO_2$, with thin shells, low amounts of excessive TiO_2, full encapsulations, and high yields and reliability. A mild hydrothermal treatment was the most promising method for both hybrid structures. The hybrid particles were able to be tested as electrode materials in DSCs, which will be discussed in Chapter 5 and 6. The $TiO_2@TiO_2$ hybrid particles are characterized in DSCs in Chapter 5. The $SnO_2@TiO_2$ hybrid particles formed in high boiling solvents and using the mild hydrothermal treatment are, aside from other electrode types, the topic of Chapter 6.

_____

4.4 Experimental Section

4.4.1 Synthesis

Materials. All materials were used as received without further purification. Cyclohexane (99.5 %), toluene (absolut), tri-*n*-octylamine (98 %, TOA), and titanium tetrachloride ($\geq$ 98 %, TiCl$_4$) were purchased from Sigma Aldrich. Hexane (95 %) was purchased from Fluka. Cetyltrimethylammoniumbromide (99 %, CTAB) was provided by Acros Organics. All other materials were used as stated in the previous Chapters.

All approaches were equivalently performed for SnO$_2$ rods as well as TiO$_2$ rods. Rutile TiO$_2$ was synthesized as described in Chapter 2, while for SnO$_2$ two different approaches were applied. The first approach is described in Chapter 3, as well as a synthesis following a published protocol by Zhang *et al.* that was also used, as described in the following.

SnO$_2$ rods following Chen and co-workers.[20] In a teflon vessel, 3.5 mL of a 0.5 M aqueous solution of SnCl$_4$ 5H$_2$O were mixed with 3.5 mL of 5 M NaOH solution and 12.5 mL of a mixture of ethanol and water (1:1 by volume). The mixture was stirred for 15 min until a clear solution was formed. The vessel was inserted into a stainless steel autoclave, sealed, heated up to 250 °C, and kept at this temperature for 48 - 90 h. The reaction mixture was transferred into a centrifuge tube and centrifuged at 9000 rpm for 5 min. The supernatant was discarded and the precipitated solid was repeatedly washed with water and ethanol until the supernatant was neutral. The solid was dried overnight at 75 °C.

Solvothermal method using organic solvents. 100 mg preformed rods were mixed with 10 mL toluene, cyclohexane, butyl alcohol, or acetonitrile in a teflon vessel, and 1.5 mL TAD were added. The reaction mixture was sealed, heated up to temperatures of 150 - 200 °C, and held for 15 to 60 h. The reaction mixture was transferred into a centrifuge tube and centrifuged at 9000 rpm for 5 min. The supernatant was discarded and the precipitated solid was repeatedly washed with water and ethanol until the supernatant was neutral. The solid was dried overnight at 75 °C.

Hydrothermal method employing NaOH as solvent. 100 mg preformed rods were mixed with 0.5 - 1.5 mL TAD in a microwave Teflon vessel. 20 mL of a 10 mM NaOH solution were added under stirring. The vessel was sealed and transferred to the microwave chamber. The solution was heated to a pressure of 20 bar to 30 bar in a duration of 10 min with a maximum power output of 1600 W. The mixture was kept at this pressure for 2 h under continuous stirring. Next, the precipitate was collected by centrifugation (9000 rpm, 5 min), the supernatant was discarded, and the solid repeatedly rinsed with water and ethanol. The product was dried at 75 °C overnight. The description of the alternative reaction pathways only mention the changed parameters, and all other procedures remained unchanged. For the multistep version, the mixture was kept at 20 bar subsequent to an addition of 0.4 mL for 1 h. This was repeated three times, and the last heating period was chosen to be 2 hours. Using the third variation, all

_____

inserted precursors were multiplied by 4, whilst the amount of solvent remained constant. In the last variation, either 2.5 g PEG20k was added to the NaOH solution or the NaOH solution was replaced by a mixture of PEG600 and 10 mM NaOH (1:1 by volume).

Decomposition prior to hydrothermal treatment. 100 mg preformed rods were added to 1 mL TAD in a Teflon vessel and, subsequently, 10 mL ethanol was added. The TAD was decomposed overnight either by incubation in a humid atmosphere in a desiccator or by a flow-through of humid air. Before heating up to 20 bar for 90 min, the amount of ethanol was adjusted to 20 mL. The product was collected by centrifugation (9000 rpm, 5 min), the supernatant discarded, and the solid was repeatedly rinsed with water and ethanol. The product was dried overnight at 75 °C.

Surfactant-mediated technique. 2 g CTAB was dissolved in 35 mL hexane. 20 mg preformed rods were added together with 0.5 mL 10 mM NaOH. This mixture was vigorously stirred for 20 min in a gentle N_2-stream. Subsequently, 0.3 mL TAD were added and the mixture was stirred overnight. The product was collected by centrifugation (9000 rpm, 5 min), the supernatant was discarded and the solid thoroughly rinsed with ethanol several times to completely remove all CTAB residues. The product was dried at 75 °C overnight.

Fast decomposition in high boiling solvents. 300 mg preformed rods were added to 20 mL tri-*n*-octylamine and heated until boiling, using a heating mantle equipped with a power regulator. As soon as the solvent was boiling, 3 mL TAD was added stepwise in portions of 0.5 mL into the hot mixture. After the complete addition of TAD, the mixture was kept under reflux for another hour. The product was collected by centrifugation (9000 rpm, 5 min), the supernatant was discarded, and the solid was thoroughly rinsed with cyclohexane, ethanol, and water. The product was dried overnight at 75 °C.

Mild hydrothermal treatment. 450 mg preformed rods were immersed in 25 mL water in a teflon vessel and 0.6 mL of a mixture containing $TiCl_4$ (TiCl-treatment solution) were added. This mixture was heated up to 0.5 bar for 2 h using the microwave-assisted reaction system. The solid was collected by centrifugation (9000 rpm, 5 min), the supernatant was discarded, and the solid was repeatedly rinsed with water and ethanol. The solid was dried at 75 °C overnight.

TiCl-treatment solution. The TiCl-treatment solution was prepared following a reported protocol.[28] Briefly, 200 g $TiCl_4$ was cooled down to -18 °C. Meanwhile, 1 mL HCl was added to 350 mL water, and frozen as well. When the HCl solution was completely solid, it was allowed to slowly defrost. The $TiCl_4$ was poured slowly into the HCl solution, while allowing large amounts of HCl gas set free. As the reaction is exothermal, after a short time, ice cooling was applied. After all the $TiCl_4$ was added, the mixture was stirred until a clear solution was formed. The solution was stored at - 18 °C.

4.4.2 Characterization

All used characterization methods were described in Chapter 2.

4.5 References

1   N.-G. Park, M. G. Kang, K. M. Kim, K. S. Ryu, S. H. Chang, D.-K. Kim, van de Lagemaat, J., K. D. Benkstein and A. J. Frank, *Langmuir*, 2004, **20**, 4246–4253.
2   S.-W. Choi, J. Y. Park and S. S. Kim, *Nanotechnology*, 2009, **20**, 465603.
3   M. Law, L. E. Greene, A. Radenovic, T. Kuykendall, J. Liphardt and P. Yang, *J Phys Chem B*, 2006, **110**, 22652–22663.
4   J. Pan, S.-M. Hühne, H. Shen, L. Xiao, P. Born, W. Mader and S. Mathur, *J. Phys. Chem. C*, 2011, **115**, 17265–17269.
5   S. Mathur and S. Barth, *Small*, 2007, **3**, 2070–2075.
6   X. W. Lou, J. S. Chen, P. Chen and L. A. Archer, *Chem. Mater.*, 2009, **21**, 2868–2874.
7   L. Zhao, M. Choi, H.-S. Kim and S.-H. Hong, *Nanotechnology*, 2007, **18**, 445501.
8   S. Gubbala, V. Chakrapani, V. Kumar and M. K. Sunkara, *Adv. Funct. Mater.*, 2008, **18**, 2411–2418.
9   S. Park, S.-D. Seo, S. Lee, S. W. Seo, K.-S. Park, C. W. Lee, D.-W. Kim and K. S. Hong, *J. Phys. Chem. C*, 2012, **116**, 21717–21726.
10 S. Park, S. Lee, S. W. Seo, S.-D. Seo, C. W. Lee, D. Kim, D.-W. Kim and K. S. Hong, *CrystEngComm*, 2013, **15**, 2939.
11 C. Ribeiro, E. Longo and E. R. Leite, *Appl. Phys. Lett.*, 2007, **91**, 103105.
12 S. Pradhan, D. Ghosh and S. Chen, *ACS Appl Mater Interfaces*, 2009, **1**, 2060–2065.
13 C. G. Fonstad, *J. Appl. Phys.*, 1971, **42**, 2911.
14 K. Pan, Y. Dong, C. Tian, W. Zhou, G. Tian, B. Zhao and H. Fu, *Electrochim. Acta*, 2009, **54**, 7350–7356.
15 X. Feng, K. Shankar, O. K. Varghese, M. Paulose, T. J. Latempa and C. A. Grimes, *Nano Lett.*, 2008, **8**, 3781–3786.
16 C. Wang, Y. Zhou, M. Ge, X. Xu, Z. Zhang and J. Z. Jiang, *J. Am. Chem. Soc.*, 2010, **132**, 46–47.
17 D. Koll, Johannes Gutenberg-Universität Mainz, 2011.
18 S. Chappel, S.-G. Chen and A. Zaban, *Langmuir*, 2002, **18**, 3336–3342.
19 J. Huo, Y. Hu, H. Jiang, W. Huang and C. Li, *J. Mater. Chem. A*, 2014, **2**, 8266.
20 Y. J. Chen, X. Y. Xue, Y. G. Wang and T. H. Wang, *Appl. Phys. Lett.*, 2005, **87**, 233503.
21 A. Birkel, N. Loges, E. Mugnaioli, R. Branscheid, D. Koll, S. Frank, M. Panthöfer and W. Tremel, *Langmuir*, 2010, **26**, 3590–3595.
22 C. Cheng, Y. Y. Tay, H. H. Hng and H. J. Fan, *J. Mater. Res.*, 2011, **26**, 2254–2260.
23 T. Tago, T. Hatsuta, K. Miyajima, M. Kishida, S. Tashiro and K. Wakayabayashi, *J. Am. Cer. Soc.*, 2002, 2188–2194.
24 B. D. Busbee, S. O. Obare and C. J. Murphy, *Adv. Mater.*, 2003, 414–416.
25 Z. L. Wang, M. B. Mohamed, S. Link and M. A. El-Sayed, *Surf. Sci.*, 1999, **440**, L809.
26 B. Liu, A. Khare and E. S. Aydil, *ACS Appl. Mater. Interfaces*, 2011, **3**, 4444–4450.
27 G. A. Parks and De Bruyn, P. L., *J. Phys. Chem.*, 1962, 967–973.
28 L. Vesce, R. Riccitelli, G. Soscia, T. M. Brown, A. Di Carlo and A. Reale, *J. Non-Cryst. Solids*, 2010, **356**, 1958–1961.

_____

5

TiO₂-Based Dye-Sensitized Solar Cells

The results in this Chapter partly originate from a cooperation with ▮▮▮▮▮▮▮ and ▮▮ ▮▮▮▮▮▮ in the group of ▮▮▮▮▮▮▮ at the Seoul National University, Seoul, South Korea, as well as a cooperation with ▮▮▮▮▮▮ in the group of ▮▮▮▮▮▮ at the Max-Planck-Institute of Polymerchemistry, Mainz. Nanoparticle synthesis, photo-anode formation, and respective characterization was performed at the Johannes Gutenberg University, Mainz.

5.1 Introduction

Initiated by a publication by Michael Grätzel and Brian O'Regan in 1991, dye-sensitized solar cells (DSCs) became an extensively growing field of research.[1] Since then, the number of publications increased from one in 1991 to 599 in 2009, and then 1959 in 2013.* The increasing interest is due to two reasons: first, the importance of the field to find low-cost renewable energy sources,[1–4] and, second, the facile fabrication to prepare a basic DSC.[5–7] A dye-sensitized solar cell is composed of three main components:[3,8] (i) the photo-anode, (ii) the counter electrode, and (iii) the electrolyte. While the counter electrode and the electrolyte remained unchanged for a very long time, the research of the composition of the photo-anode always represented an intensive field of investigation. The electrolyte is usually composed of a mixture of I⁻ and I₃⁻ dissolved in acetonitrile, with a few additives to optimize the interactions in the DSC. In the last few years, the improvement in concerns of the electrolyte consisted of the replacement of a liquid electrolyte to solid state hole-conductors. The giant improvement in assembling solid state devices is that the sealing process is not necessary anymore and leakage danger does not exist, which is an important step toward possible industrial applications. Few materials were reported to act as suitable hole-conducting electrolytes, such as CuI,[9] or CuSCN,[10] while the superior material turned out to be spiro-OMeTAD.[11] This organic hole-conductor is easily solution process-able and commercially available. The counter-electrodes consist of platinized or carbon-coated FTO substrates in combination with liquid electrolytes. However, when solid state electrolytes are used, a counter electrode of Ag or Au is evaporated onto the electrolyte. Above all other components, however, the optimization of the photo-anode attracted most interest and was, therefore, focus of extensive

*based on a search using the key words "dye-sensitized" and "solar" using the data source ISI Web of Knowledge

research. It is composed of a porous semi-conductor network deposited onto a transparent conductive oxide (TCO) substrate, such as fluorine-doped tin oxide (FTO) or indium-doped tin oxide (ITO). Photo-anodes for liquid electrolyte dye-sensitized solar cells consist of a photo-active layer, which consists of a dye and a porous semiconductor. The composition of the layer containing the semiconductor usually has a thickness of 10 - 12 µm and offers great potential for improving the DSC efficiency. In addition to the porous semiconductor, other components can also be incorporated into this layer. The possible constructions here offer a large variety for improvements.[12,13] A dye, most commonly a Ru-complex, is adsorbed on the surface of the porous electrode.[14] When the dye is excited by light it is able to inject an electron into the porous electrode. Much focus was drawn to the development of stable charge-transferring dyes: at its best, it should absorb large ranges of the visible light spectrum, while also showing high transfer rates. Over time, various new materials for the porous electrode were also developed, which are usually prepared starting from nano-sized precursors as they offer a large surface area. The most common material is anatase-TiO$_2$, while also Nb$_2$O$_5$, ZnO, and SnO$_2$ were used.[15] TiO$_2$ nanoparticles are easy to synthesize and to handle, furthermore, it is a very cheap material that showed good results in the first studies in 1991. Furthermore, Nb$_2$O$_5$ offers a higher conduction band edge as compared to TiO$_2$ and an extraordinary high dye adsorption.[16] ZnO also shows a higher conduction band edge as compared to TiO$_2$ and offers a low degree of recombination. Although SnO$_2$ exhibits a significantly lower conduction band edge, it offers potential to improve DSCs by its outstanding electron conduction properties. However, the exchange of the material itself is only one way to optimize the properties of the electrode. Controlling and manufacturing certain morphologies of the employed nanoparticles is another suitable method to enhance the electrode features. A proper electrode allows a high dye adsorption and exhibits good electron conduction properties. However, these are two counter-intuitive characteristics: a high surface area is realized by employing very small particles, while an electrode of a finite thickness composed of small particles has a large number of particle-particle boundaries that can always act as electron trap sites. Basic approaches disperse anatase nanoparticles in an organic solvent, apply them onto a fluorine-doped tin oxide glass (FTO) substrate, and sinter this dispersion such that an interconnected porous electrode forms. Other more elaborated constructions involve anodized titanium oxide (ATO) structures as semi-conducting electrodes or anisotropic nanostructures directly deposited onto the FTO substrate.[17] So far they all suffer some difficulties that should be overcome to further improve the efficiency of the solar cells. Comparing photo-anodes of the same thickness reveals the difficulties: the spherical anatase nanoparticles exhibit a high surface area, therefore, a high dye adsorption and, consequently, a high light absorption. Here, the electron diffusion through the semiconductor limits the thickness of the layer, which leads again to lower light harvesting. The incorporation of 1D structures will certainly decrease the number of trap sites on a possible pathway through the electrode, as well as simultaneously decreasing the surface area and, therefore, the achievable dye adsorption. Additionally, the incorporation of 1D structures decreases the packing

density and the interconnection of the particles in the electrode. To benefit from 1D particles, a compromise has to be found to enable proper conduction and, at the same time, a sufficient dye adsorption. On the other hand, anisotropic structures grown onto the FTO can improve the electron diffusion, and, therefore, allow thicker layers of semiconductor.[18–20] Simultaneously, the surface area drops drastically and low amounts of dye are only adsorbed, and, therefore, the light harvesting can also be reduced. In this Chapter, a different approach was followed. Composite electrodes of anatase nanoparticles and rutile sub-micron rods were used in different ratios to investigate which amount of 1D structures could enhance the efficiency of the solar cells at most.[21,22] Additionally, TiO_2@TiO_2 hybrid particles were incorporated into photo-anodes to investigate if the increased surface area has a beneficial effect on the DSC.

5.2 Composite Electrodes of Rutile Rods and Spherical Particles

5.2.1 Characterization of the Nanoparticles

As reference material for TiO_2 (Figure 5.1a)), TiO_2-P25 was used, as it exhibits several advantages compared to commercially available pastes for DSCs, or self-made nanoparticles. It is available on large scale and the particles in one batch are homogenously distributed, which enables us to use them as reference system due to comparable nanoparticle composition. In addition, the prepared pastes have the same ingredients, and, therefore, are better to compare. The synthetic procedures to obtain the used particles are described briefly in the following: anatase nanoparticles (Figure 5.1b)) were synthesized by a basic decomposition of TAD in a hydrothermal treatment at 20 bar for 2 h, as described in Chapter 2, where they were used as precursor material to grow rutile sub-micron rods. These sub-micron rods (Figure 5.1c)), obtained after a hydrothermal treatment with 6 M HCl at 30 bar for 90 min, were also used. TiO_2@TiO_2 hybrid particles were synthesized by a mild hydrothermal treatment as described in Chapter 4. Herein, rutile sub-micron rods were taken and, in a second step, TiO_2 particles were grown onto the surface of the rods at 0.5 bar for 2 h (Figure 5.1d)).
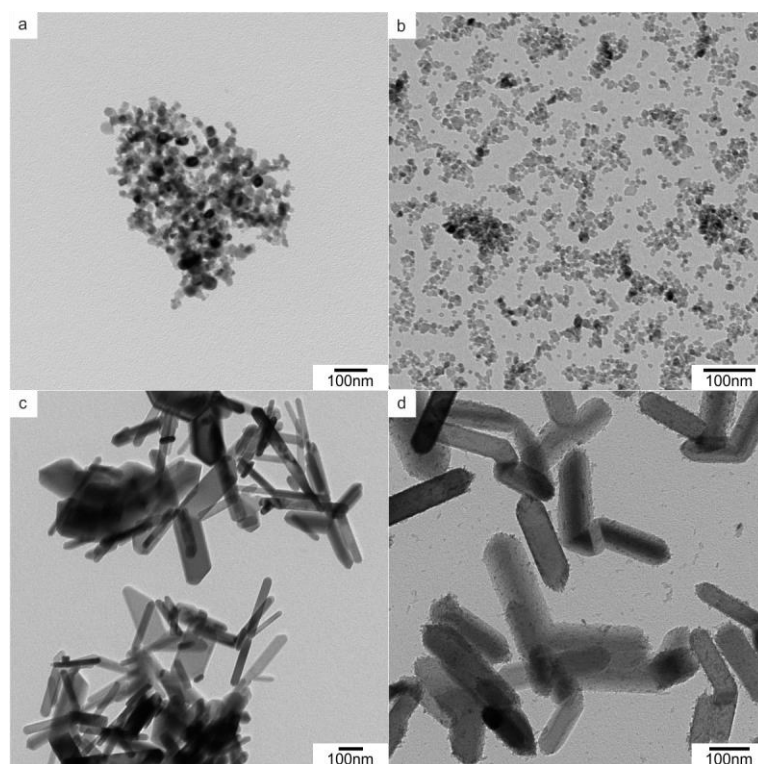
Figure 5.1 TEM images of particles used in this Chapter to synthesize photo-anodes for DSCs: a) TiO$_2$-P25, b) anatase nanoparticles, c) rutile sub-micron rods, and d) TiO$_2$@TiO$_2$ hybrid particles, respectively.

The determining factor for dye adsorption onto TiO$_2$ and, thereby, the possible electrons generated, is the surface area available on the nanoparticles. Due to the large number of variations made to investigate the DSCs, the bare precursor particles were used for determination of the surface area. Albeit, the surface area is slightly overestimated with this method, because particles merge together during sintering, which decreases the available surface area. The sizes of the TiO$_2$-P25 nanoparticles range between 20 to 40 nm, while the size of the anatase nanoparticles was measured to be between 10 to 15 nm. According to these obtained from TEM, it was supposed that the surface area of anatase nanoparticles was higher than for TiO$_2$-P25, which was confirmed by BET measurements as seen in Table 5.1. Rutile sub-micron rods with a length of about 221 nm exhibited a significantly decreased surface area, while adding an outer layer of TiO$_2$ onto the sub-micron rods to form TiO$_2$@TiO$_2$ hybrid particles resulted in an increase in the surface area by about 33 %.

Table 5.1 Surface area of the precursor TiO$_2$ particles determined by BET isotherms. Measurements were conducted by Martin Klünker.

Sample	BET surface area / m²/g	Size / nm
TiO$_2$-P25	50.8	20 - 40
Rutile sub-micron rods	15.2	150 - 400
Anatase nanoparticles	128.5	10 - 15
TiO$_2$@TiO$_2$ hybrid particles	20.3	150 - 400

Further, the band-gap of the used particles is of particular interest, as it represents the maximum possible extractable voltage from a DSC, while the optimization of the electrolyte and dye has to be presumed. However, having a given electrolyte, the actual position of the conduction band compared to the potential of the electrolyte is the demanding factor, which can be measured against the standard hydrogen electrode (SHE). Nonetheless, it was only possible to determine the band-gaps. Therefore, diffuse reflection spectra in a range between 200 and 800 nm were recorded, while the range between 300 and 500 nm includes the change of reflectivity and is plotted in Figure 5.2a). The change of reflection of the TiO_2-P25 precursor (green) occurs at an extraordinary low wavelength, while the change for rutile sub-micron rods (blue) occurs at a significantly higher wavelength. Interestingly, the synthetic alteration from sub-micron rods to $TiO_2@TiO_2$ hybrid particles did not lead to a change of the wavelength, where the reflection drops. The absorption of the anatase nanoparticles lies in between the rutile sub-micron rods and the TiO_2-P25. The obtained spectra enabled to calculate the Kubelka-Munk plots for the particles following a method described by Valencia and co-workers (Figure 5.2b)).[23] Herein, F^2 represents the Kubelka-Munk function for direct band transitions, which was calculated from the reflectivity. An extrapolation of the linear range of this plot leads to a function, where the point of intersection with the x-axis represents the band-gap energy. The calculated band-gaps can be seen in the Appendix in Table D1. Qualitatively, the band-gap of TiO_2-P25 is the largest, while the one of rutile sub-micron rods is the smallest, and the band-gap of the anatase nanoparticles lies in between. As already described for the reflection, the modification of rutile sub-micron rods to $TiO_2@TiO_2$ hybrid particles did not lead to a significant change in width of the band-gap.
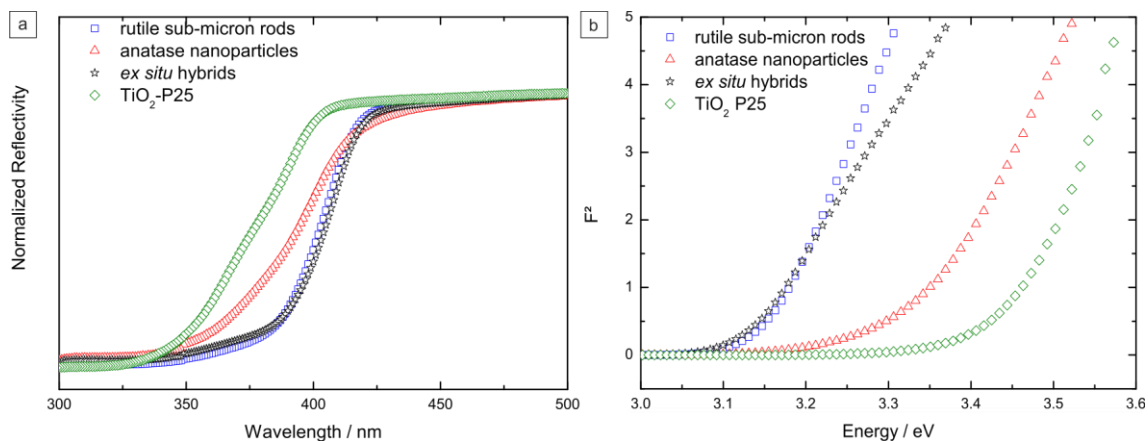
Figure 5.2 UV-Vis spectra of all used precursor particles measured in diffuse reflection mode (a) and Kubelka-Munk plot to extrapolate the band-gaps (b).

5.2.2 Composite Electrode Films

The as-described particles were incorporated in pastes to form the photo-anodes. Briefly, particles were mixed with ethanol, PEG400, and an aqueous solution containing PEG20k. This mixture was ultrasonicated and stirred in a sealed container to yield a homogenous paste. Afterwards, the mixture was ground to allow some of the ethanol to evaporate and, thereby, to adjust the viscosity of the paste.

In general, there are two suitable techniques to apply thin and homogenous layers to a substrate on laboratory scale: spin-coating and doctor-blading. However, spin-coating leads to a thickness of 1 µm or below, while up to 12 µm were desired. Thus, the method of choice was doctor-blading. Using this technique, the adjustment of viscosity and particle concentration in the paste plays a crucial role. Decreasing the viscosity can yield thinner layers, but at the same time the applied layers become more inhomogeneous. Increasing the viscosity can increase the thickness of the layer, but also decreases the interconnection of particles, which is usually achieved while sintering. This would lead to dead ends in the pathway for the electron conduction in the DSC afterwards. A thickness of the TiO$_2$ layer of 10 - 12 µm was desired, because it was previously shown that this thickness is beneficial for high efficiency DSCs. In general, there is a plethora of techniques to further enhance the efficiency of DSCs, *i.e.* addition of a scattering layer on top of the photoactive layer or scattering agents like gold nanoparticles in the layer itself.[24,25] Another technique is to use more than one dye or co-functionalization to eliminate bare TiO$_2$ surface having contact with the electrolyte added later on. All these methods were neglected in this study, because the focus was drawn to investigate the influence of the addition of anisotropic semiconductors to the electrodes.

The final DSC assembly, *i.e.* addition of the counter electrode, sealing, and addition of the electrolyte, as well as efficiency measurement was done at the SNU, South Korea. Due to this fact, the durations between dye adsorption and measurements varied, as well as alterations during the shipping process could occur, such as passivation of the surface of the electrode. To prevent any false data interpretation the shown *J-V*-data can only be evaluated with regards to the reference photo-anodes. The reference photo-anodes consisting of TiO$_2$-P25 are well known and usually yield an efficiency of 3.5 - 4.5 %. Due to these circumstances, in some of the tables more than one reference will be shown.

The thickness and optical homogeneity was measured by confocal laser scanning microscopy (CLSM). This method allowed to evaluate the quality of the photo-anode on a large scale, in both measuring modes optical microscopy and confocal laser scanning microscopy. Optical measurements revealed if the samples were free of cracks and free of agglomerates, while the confocal laser scanning technique enabled to measure the height of the sample. In other words, on the one hand it could be determined how thick the photo-anode was, but, on the other hand, also if the height was equally distributed. Figure 5.3 shows CLSM images of photo-anodes containing TiO$_2$-P25 (Reference 1, a)), 5 wt% rutile sub-micron rods (b), 50 wt% rutile rods (c), and 100 wt% rutile rods (d), respectively. It shows that all electrodes had an equal height all-over the whole sample, though a few hills were still present. The quality of this photo-anodes could be considered to be good, in regards to the CLSM measurements. It was commonly observed that a few agglomerates were present, when synthesized particles in tailor-made pastes were used for the assembly of photo-anodes. This fact was due to the electrostatic interaction of bare TiO$_2$ particles. When commercial pastes were used, these particles are

in a stable dispersion, which is ensured by using particles smaller than 8 nm and a sufficient surface functionalization (for images of a commercial paste see Figure D1in the Appendix).
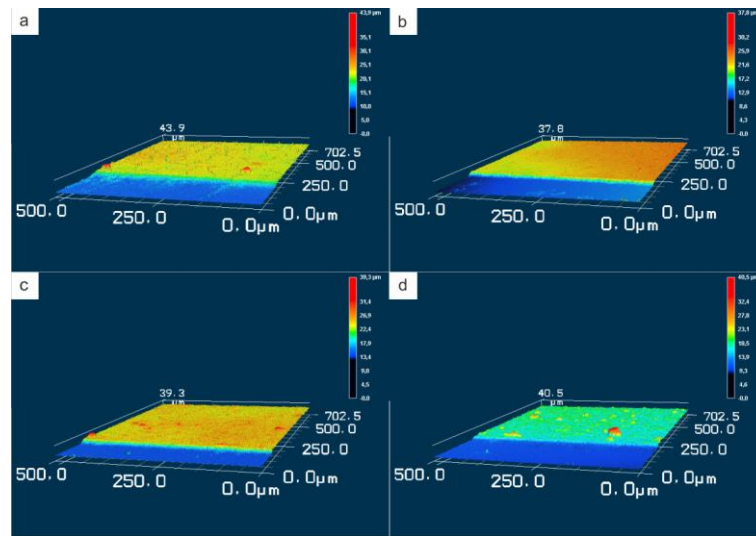
Figure 5.3 CLSM profile images of photo-anodes having different weight percentages of rutile, while the remaining amount consisted of anatase nanoparticles. The measurement was made at the edge of the photo-active area to determine the height of the TiO$_2$-film: a) Reference 1, b) 5 wt% rutile rods, c) 50 wt% rutile rods, and d) 100 wt% rutile rods, respectively.

In Figure 5.4, SEM overview images of photo-anodes containing a) TiO$_2$-P25, b) 5 wt%, c) 10 wt%, d) 50 wt%, and e) 100 wt% rutile sub-micron rods are displayed, f) shows the 100 wt% sample in higher magnification. Samples containing 10 wt% or less rutile rods exhibited cracks in the photo-anode. Cracks are unfavorable, because they cause volume where no current can be generated, but, even worse, the interconnection of the TiO$_2$ electrode is interrupted. This interruption is disadvantageous for the electron transfer from the place, where the carriers are generated, to the FTO substrate, where they are extracted from the device. A crack-free layer could probably be achieved by optimization of the ingredients of the paste as well as the sintering profile. Figure 5.4d) and e) show no cracks of the electrodes. The origin of crack-free electrodes is twofold: on the one hand, the pastes were slightly less viscos and a tiny bit of flow was allowed, which allowed the cracks to be filled, and on the other hand, the anisotropic particles enabled to construct a network. For the film containing 50 wt% sub-micron rutile words the voids of the network were filled with spherical anatase nanoparticles. Using 100 wt% rutile rods showed that very clearly by leaving large voids in between interconnection of rods (see Figure D2 in the Appendix). Thus, it is crucial to investigate the amount of rods, which is necessary to allow the formation of a sufficient network to enable better electron transport. In addition, it has to have enough surface left for dye adsorption, such that sufficient charge carriers are generated. The higher the amount of rods, the higher the number of dead ends where electrons are trapped and not transferred to the FTO. The photo-anodes displayed in Figure 5.3 and Figure 5.4 served for the initial investigation on the optimum ratio of rutile rods to anatase particles.
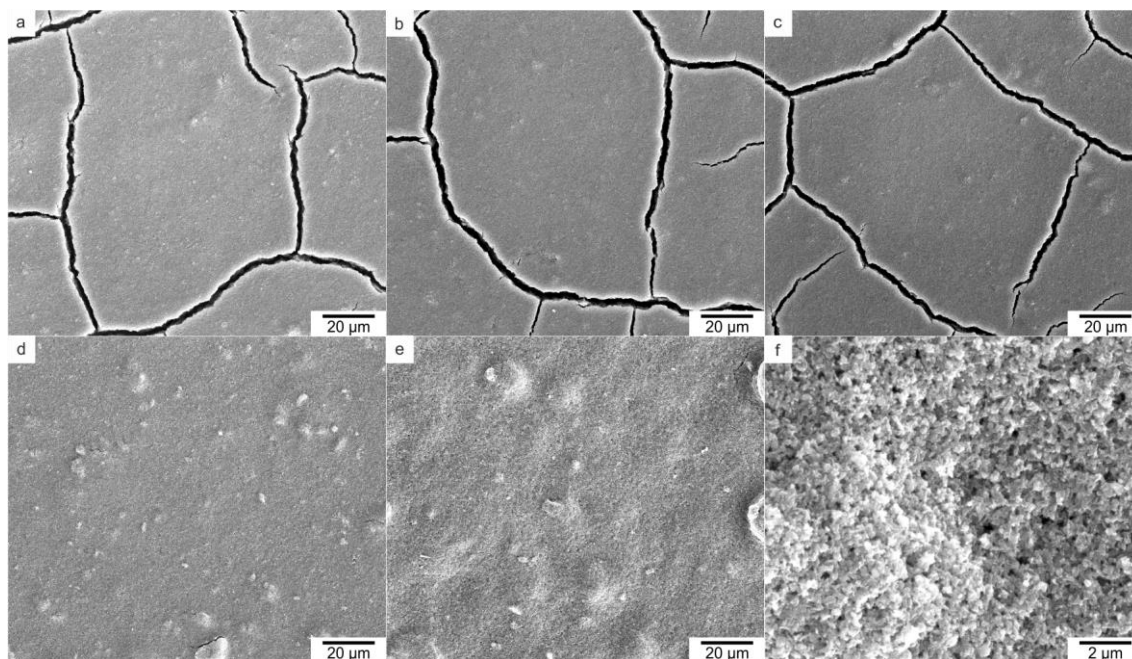
Figure 5.4 SEM overview images of photo-anodes of different weight percentages of sub-micron rutile rods, while the remaining amount TiO₂ consisted of anatase nanoparticles: a) Reference 1, b) 5 wt% rutile, c) 10 wt% rutile, d) 50 wt% rutile, and e) 100 wt% rutile, respectively. f) shows the photo-anode with 100 wt% sub-micron rutile rods in a higher magnification.

The photo-anodes in Figure 5.5 and Figure 5.6 served for a closer investigation focusing around the range of 10 - 20 wt% rutile sub-micron rods. Figure 5.5a) shows the CLSM profile images of the Reference 2 electrode, while b) and c) shows the photo-anodes with 10 and 20 wt% rutile sub-micron rods. The profile images illustrate that the second batch, used for the closer investigation, was slightly rougher than the ones described before. Nevertheless, the deviation of the roughness of the electrodes was considered to be rather small, and was, therefore, neglected.
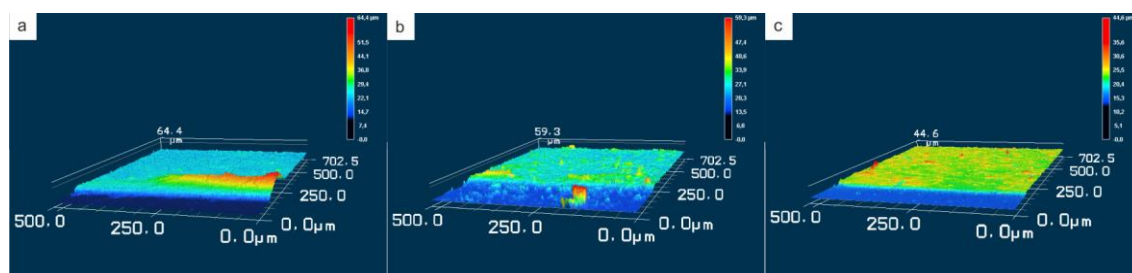
Figure 5.5 CLSM profile images of photo-anodes having different weight percentages of sub-micron rutile rods, while the remaining amount of TiO₂ was anatase nanoparticles. The measurement was made at the edge of the photo-active area to determine the height of the TiO₂-film: a) Reference 2, b) 10 wt% rutile rods, and c) 20 wt% rutile rods, respectively.

The SEM images displayed in Figure 5.6 show photo-anodes of a) Reference 2 as well as overview images of electrodes containing b) 10 wt% rutile rods and c) 20 wt% rutile rods. Figure 5.6d) shows a close-up image zoomed into a crack of the sample containing 20 wt% rutile. The reference electrode exhibits again deep cracks, but is, except for that, very homogenous. Figure 5.6b) and c) reveal that the electrodes containing rutile rods had a few cracks, while these cracks appear to not be deep and to not cross the whole TiO₂ layer, which was discovered by close-up images into the cracks.

Additionally, it is obvious that agglomerates were present in the samples, confirming the previous observation made in the CLSM measurements. Figure 5.6d) nicely shows a part of the network that is made by the rutile rods, where a few of the rutile rods visibly protrude into the crack.
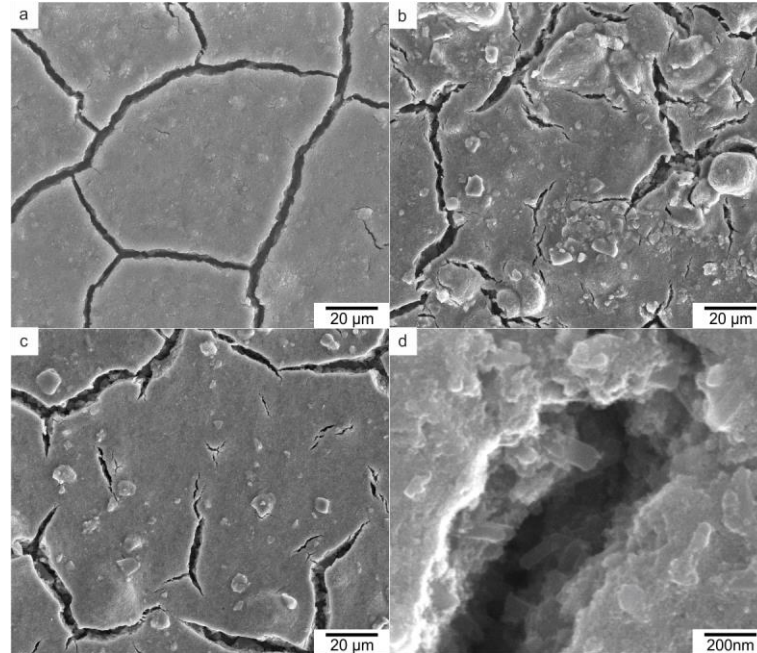
Figure 5.6 SEM overview images of photo-anodes of different weight percentages of sub-micron rutile rods, while the remaining amount of TiO_2 consisted of anatase nanoparticles: a) Reference 2, b) 10 wt% rutile, c) 20 wt% rutile. d) shows the photo-anode with 20 wt% rutile in a higher magnification.

5.2.3 Dye-Sensitized Solar Cells: Characterization of Composite Electrodes

The characteristics of the DSCs can be found in Table 5.2. They represent mean values of DSCs of the same type, while every DSC was measured at least three times. Comparing the open circuit voltages (V_{oc}) of the first batch, it became evident that there was no significant influence of the different compositions, as the values vary between 0.74 V and 0.79 V. In addition, the highest value of the pure rutile sample cannot be explained by the band-gap. It is likely that parallel resistances differ in the cells, and, therefore, a higher V_{oc} is obtained, but still the difference is negligible. The short circuit current density (J_{sc}) follows the expected trend: the higher the amount of rutile rods, the lower the J_{sc}. This trend was expected to invert at a certain point, where the lower surface area and, therefore, the lower dye loading is overcompensated by the better electron conduction, which is enabled by the incorporation of anisotropic semiconductors. This inversion was observed to occur between 5 wt% and 50 wt% rutile rods, in the first batch represented by 10 wt% rutile rods. The fill factors (FF) were all around 65 % and higher, which represents that the assembled DSCs did not suffer extraordinarily high amounts of losses caused by recombination or series resistances. The peak efficiency of pure rutile rods was determined to be 2.43 %, while the reference exhibited an efficiency of 4.38 %. Upon increasing the amount of anatase nanoparticles and, therefore, increasing the surface area, an optimization to up to 4.75 % was achieved in the first batch. This represents an improvement of 8.5 % regarding the reference electrode.

_____

During the further investigation in a second batch, it was focused on the range between 10 wt% and 20 wt% rutile sub-micron rods in the electrode. The DSC characteristics can be seen in the bottom part of Table 5.2. The V_{oc} of the reference (TiO₂-P25) is higher than of the composite material, while the changes of the two composite electrodes are not significant. These data represent the expected difference concerning the V_{oc}, which was made with regards to the band-gap measurements of TiO₂-P25 and the tailor-made particles. It has to be taken into account that only a trend was observable, as the difference was still very small. However, the incorporation of 20 wt% rutile rods had a beneficial effect on the Jsc as compared to 10 wt% rutile. The fill factor for all photo-anodes of the second batch were higher than 70 %, which again represents the high quality of the material and the assembled photo-anodes. For these solar cells, the improvement concerning the reference was 22 % for the photo-anode with 10 wt% rutile rods and 25 % for the one with 20 wt% rutile rods.

Table 5.2 Solar cell characteristics determined from *J-V*-curves for DSCs with different compositions of the photo-anodes. Samples designated with [1] were referred to Reference 1, the ones with [2] to Reference 2. The measurements were performed by ▮▮▮▮▮▮▮▮▮▮.

Sample	V_{oc} / V	J_{sc} / mA/cm²	FF / %	Mean η / %	Peak η / %
Reference 1	0.74	8.64	66.94	4.28	4.38
100 wt% rutile[1]	0.79	4.46	68.89	2.42	2.43
50 wt% rutile[1]	0.75	6.59	64.73	3.20	3.20
10 wt% rutile[1]	0.74	8.74	67.01	4.34	4.75
5 wt% rutile[1]	0.75	7.95	68.82	4.11	4.33
Reference 2	0.75	5.61	72.91	3.04	3.25
20 wt% rutile[2]	0.70	7.87	70.90	3.89	4.06
10 wt% rutile[2]	0.69	7.53	72.41	3.77	3.97

The amount of adsorbed dye is the crucial factor for the photo-induced charge separation: The higher the amount of adsorbed dye, the higher the possible generated current. Therefore, the dye loading was measured by UV-Vis spectroscopy and can be found in Table 5.3. The obtained trend between J_{sc} and adsorbed dye correlates very well, except for the sample containing 100 wt% rutile rods.[26] Here, an unexpectedly high amount of dye was adsorbed as compared to other electrodes, taking into account that the surface area of the anatase nanoparticles was higher by more than a factor of 8, but still the obtained current was suspiciously low. It has to be assumed that when only sub-micron rods were present in the electrode, the interconnection between rods as well as the connection to the FTO was reduced and, therefore, the generated current remained trapped in the TiO₂ layer. Further, it is obvious that although a higher dye loading was obtained for the photo-anode with 50 wt% rutile, the current of the sample with 5 wt% rutile was higher. It is most likely that the high amount of anisotropic structures leads to a decreased interconnection in the semiconducting layer and, therefore, causes losses. This can be explained by the same phenomenon as described for 100 wt% rutile rods. All in all, the results

obtained from *J-V*-characteristics measurements reflect the trends determined by the band-gap and the dye-adsorption measurements.

Table 5.3 Amount of adsorbed dye per volume unit determined by UV-Vis spectroscopy.

Sample	Dye-Loading / mmol/cm³
Reference 1	0.1770
100 wt% rutile	0.0997
50 wt% rutile	0.0834
10 wt% rutile	0.1370
5 wt% rutile	0.0769
Reference 2	0.0807
20 wt% rutile	0.1960
10 wt% rutile	0.1630
ex situ TiO$_2$@TiO$_2$ hybrids	0.1100
in situ TiO$_2$@TiO$_2$ hybrids	0.1530

The measured *J-V*-curves of the two batches of the different DSCs are displayed in Figure 5.7. The first batch, with the samples containing 100 wt%, 50 wt%, 10 wt%, and 5 wt% rutile rods as well as the Reference 1, is displayed in Figure 5.7a), while b) shows the characteristics of DSCs containing 10 wt%, 20 wt% rutile rods, as well as the corresponding Reference 2. In Figure 5.7a), the significant changes in the *J-V*-characteristics did not occur due to the V_{oc}, but by changing the J_{sc}. The J_{sc} was lowered for all cells, except for the sample containing 10 wt% rutile as compared to the reference DSC. Further optimization of the J_{sc} was possible by adjusting the amount of incorporated rutile rods to 20 wt% as displayed in Figure 5.7b). The form of the *J-V*-curves reveals that neither series nor parallel resistances were dominant in the samples. The form of the curves also verifies the high fill factors of up to 72.9 %, but not lower than 64.7 %.
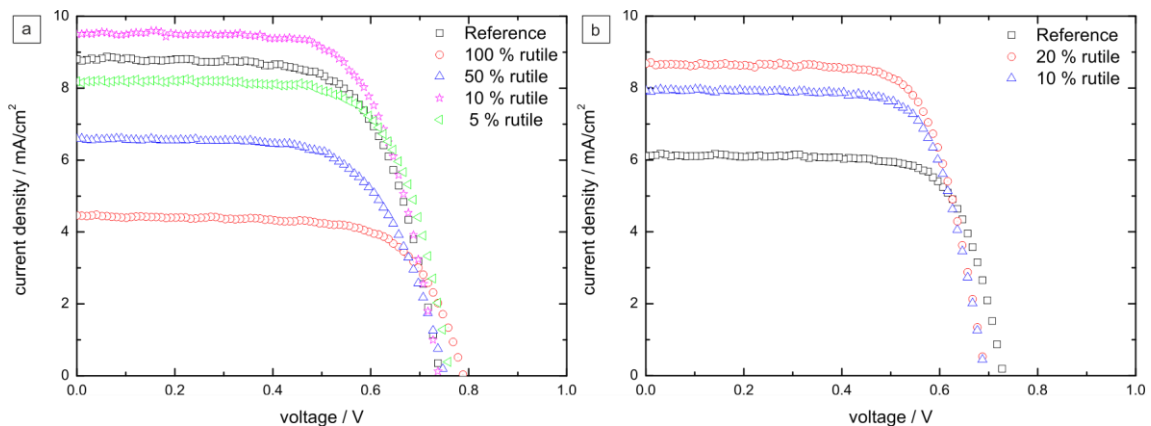
Figure 5.7 *J-V*-curves of two batches of TiO$_2$ composite photo-anodes. In a) DSCs with 5 wt%, 10 wt%, 50 wt%, and 100 wt% rutile rods, as well as a reference cell were measured. b) displays the *J-V*-curves of the photo-anodes of the second batch containing 10 wt% and 20 wt% rutile rods as well as a reference. The measurements were performed by ████████

_____

5.2.4 Hybrid Electrode Films

After the successful optimization of the obtained J_{sc} by employing composite materials in the photo-anode for DSCs, the next goal was to optimize the V_{oc}. In theory, it should be possible to tune the position of the conduction band by using anatase instead of rutile: not only is the band-gap larger, but the position of the conduction band also exhibits a larger potential difference with regards to the used I^-/I_3^- redox couple. The combination of the high conduction band of anatase and the enhanced conductivity due to the rutile sub-micron rods was supposed to offer a great potential, when such hybrid particles are used. In addition, recombination should be lowered by the encapsulation of the rutile rods by the anatase "shell" and, furthermore, the resulting hybrid particles exhibited a higher surface area as can be seen in Table 5.1.

Photo-anodes containing hybrid particles were prepared using two different approaches. In the first approach, TiO₂@TiO₂ hybrid particles, referred to as "*ex situ* hybrids", were synthesized prior to the assembly of the photo-anode. In the second approach, referred to as "*in situ* hybrids", an aqueous solution of TiCl₄ was added as soluble Ti^{4+} precursor to the pastes and decomposed during the sintering process. The CLSM profile images are displayed in Figure 5.8a) and b), while the used reference was the same as displayed in Figure 5.5a). When the aqueous solution of TiCl₄ was added to the paste, the viscosity had to be adjusted by further addition of PEG20k. But except for this deviation, the procedure remained the same as described before for composite photo-anodes. The images in Figure 5.8 show differences in the homogeneity of the prepared electrodes. While the *ex situ* hybrids in Figure 5.8a) form a very smooth and homogeneous surface, the *in situ* hybrids in Figure 5.8b) have a rather rough surface, and, therefore, is an inhomogeneous electrode. This is due to the fact that the composition of the paste had to be changed, and also large amounts of liquid ingredients contributed, which usually decreased the homogeneity. Additionally, the decomposition of TiCl₄ is exothermic, which might have caused sudden evaporation of the liquid compounds during the sintering process, causing the observed inhomogeneity.
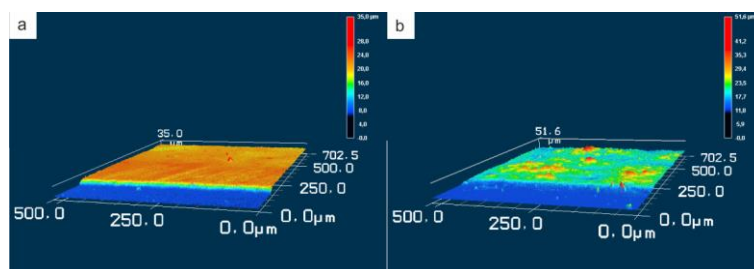
Figure 5.8 CLSM images of the edge of the photo-active area of photo-anodes consisting of TiO₂@TiO₂ hybrid particles: a) *ex situ* hybrids and b) *in situ* hybrids.

To confirm the observations made in CLSM measurements, SEM measurements were also conducted, which can be seen in Figure 5.9a) and b) for *ex situ* as well as in c) and d) for the *in situ* hybrids, respectively. The SEM image for the corresponding reference can be seen in Figure 5.6. The

overview image of the *ex situ* hybrids shows a very smooth surface, which confirms the observations made by CLSM. The close-up image depicts the rods having bright spots. These spots are the additional spherical TiO_2 particles, which were nucleated on the preformed rods in the second reaction step of the hybrid formation. The rods did not show any preferred orientation, as was expected for this synthetic method. The photo-anode prepared from *in situ* hybrids was comparatively rough, which was caused for sure by the not optimized paste formulation as well as the uncontrolled decomposition of the liquid precursor during the sintering process. Not only were elevations observable in the electrode, but also cracks, which are both undesirable. Elevations could lead to short cuts, if they were too high, while cracks can interrupt any conduction of the generated electrons. In the close-up image for the *in situ* hybrids, it is evident that more additional TiO_2 was formed during the sintering process as compared to the *ex situ* hybrid formation. In the photo-anode made of *in situ* hybrids, the rods were hard to identify due to the growth of additional TiO_2. Another noteworthy fact is that the voids observed with the *ex situ* hybrids were not present with the *in situ* hybrids, which ensured a higher surface area due to a higher packing density at the same electrode thickness.
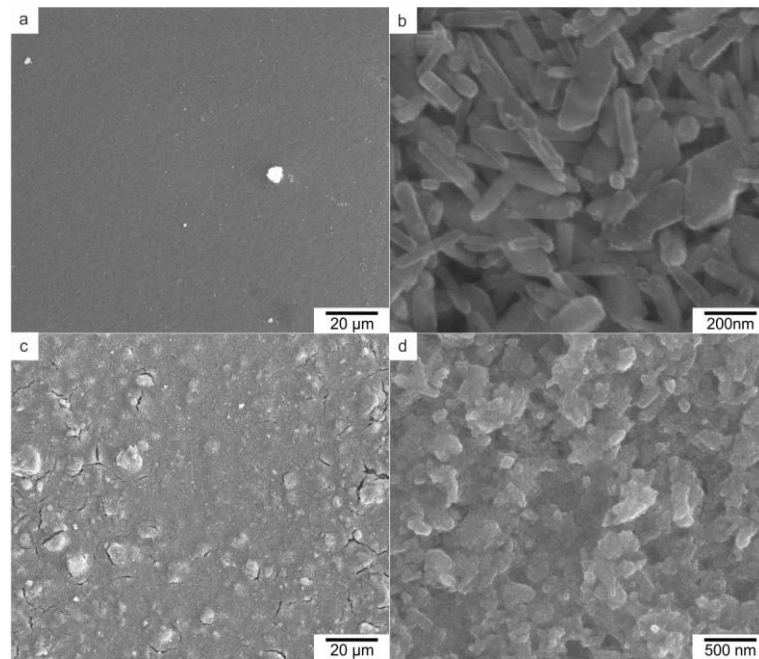
Figure 5.9 SEM overview and higher magnification images of photo-anodes made of *ex situ* (a, b) and *in situ* hybrids (c, d).

5.2.5 Dye-Sensitized Solar Cells: Characterization of Hybrid Electrodes

The measured *J-V*-characteristics can be seen in Table 5.4, while the dye loading was already shown in Table 5.3, and the *J-V*-curves are displayed in Figure 5.10. V_{oc} of the different photo-anodes followed the expected trend: it had the highest value for the reference, which also exhibited the highest band-gap. The *ex situ* hybrids were mainly composed of rutile, and, therefore, had the lowest band-gap. The additionally formed TiO_2 with the *in situ* hybrids was anatase (Figure D3in the Appendix), such that V_{oc} lies in-between the *ex situ* hybrids and the reference. The J_{sc} follows the trend expected from the

dye loading amounts in Table 5.3. Nevertheless, it has to be mentioned that the measured J_{sc} for both hybrid materials was very low as compared to the reference, when the dye loading amount is taken into account. This was even more pronounced for the *ex situ* hybrids than for the *in situ* hybrids. For all anodes the fill factor was above 66 %, which is a comparatively good value, as commercial solar cells exhibit fill factors around 70 %. The efficiency obtained for the *ex situ* hybrids was negligible, the cause for the poor efficiency can clearly be assigned to the low J_{sc}. This again was caused by a low dye adsorption and probably also by a lack of interconnected conduction pathways and resulting "dead ends". The efficiency obtained for the *in situ* hybrids was slightly below the efficiency of the reference, which was remarkable considering that no optimization of the composition of the electrode had been performed, yet.

For the bare particles, it was observed that the use of only rutile rods was disadvantageous, especially for the J_{sc}, while upon optimization of the composition a raise of J_{sc} by 95 % was observed. Inferential, it has to be assumed that a further optimization of the composition of the paste would lead to even better results. The composite electrodes with the highest efficiency were composed of 20 wt% rutile and 80 wt% anatase. Using the technique of preparing *in situ* hybrids in combination with composite mixtures in the paste could improve J_{sc} by far, and, therefore, consequently the efficiency. However, the expected ratio of rutile:anatase would slightly shift to an increased amount of rutile due to the *in situ* formation of anatase nanoparticles during the sintering process. The improvement regarding the change from 100 wt% rutile rods to *in situ* hybrids can be explained by a few reasons. The additional anatase phase TiO$_2$ did not improve the V_{oc}, although this was expected from the increased band-gap of the anatase phase TiO$_2$. The J_{sc} improved by 1.5 mA/cm² corresponding to an increase of 33 %. This gain correlates very well with the improved dye adsorption, which was also raised by 33 %. Additionally, it is likely that the interfaces between particles were better interconnected by the *in situ* decomposition of TiCl$_4$. These well connected interfaces in the electrode ensure that electrons can be transferred from one particle to the next without being trapped at the particles' boundaries. Electrons that are trapped cannot contribute to the J_{sc} and are likely to recombine.

Table 5.4 Solar cell characteristics determined from *J-V*-curves for DSCs made from hybrid particles. The measurements were performed by ▬▬▬▬▬▬▬.

Sample	V_{oc} / V	J_{sc} / mA/cm²	FF / %	Mean η / %	Peak η / %
Reference 2	0.75	5.61	72.91	3.04	3.25
ex situ **hybrids**	0.71	2.10	66.37	0.99	1.04
in situ **hybrids**	0.73	5.91	72.91	3.16	3.16

Only slight changes in V_{oc} were evident from the measured *J-V*-curves, when comparing the intersection with the x-axis. The J_{sc} of the *ex situ* hybrids is very low regarding the intersection with the y-axis, unexpectedly low actually, as it was even lower than for the sample containing 100 wt% pure rutile rods (compare Figure 5.7, Table 5.2). The J_{sc} of the other hybrid sample and the reference were

slightly below 6 mA/cm², a common value. Further, the deviation between the two samples was also rather small. The shape of the *J-V*-curves indicated a dominant resistivity not to be present in the DSC. Both series and parallel resistances contribute to losses and can both be in a small amount identified by the shape of the *J-V*-curves.
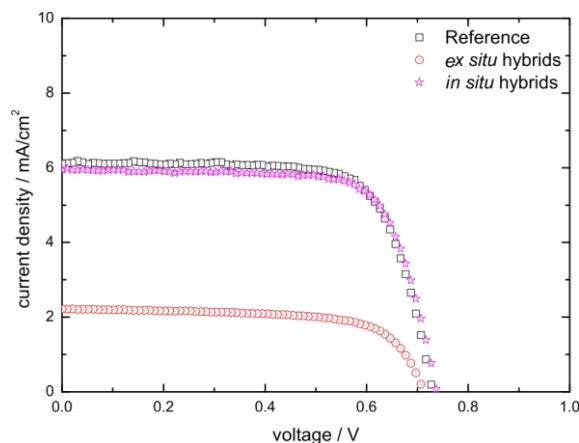
Figure 5.10 *J-V*-curve of DSCs made of photo-anodes containing $TiO_2@TiO_2$ hybrid particles made *in situ* and *ex situ* as well as a reference containing TiO_2-P25 nanoparticles. The measurements were performed by ▮▮▮▮▮▮▮▮.

5.2.6 Electrochemical Characterization

Figure 5.11 shows the electrochemical characterization of the reference DSC, the cells containing 10 and 20 wt% rutile from the second batch, as well as of a DSC consisting of *in situ* hybrids. The plot in a) shows the quantum efficiency QE, in b) the charge extraction is plotted against the applied voltage, while in c) the electron lifetime can be seen, as well as the electron diffusion in d). The quantum efficiency was measured by incident-photon-to-current-conversion efficiency (IPCE) using a monochromatic light source. The IPCE of the reference is all-over the spectrum lower than all the other measured samples. This could have several reasons: (i) the dye loading amount was significantly lower, reducing the light harvesting efficiency (LHE), (ii) the injection into the rutile rods was preferred due to the lower band-gap, (iii) the charge collection was improved by the rutile rods, while (iv) the dye regeneration efficiency seemed to have less of an impact on the quantum efficiency when comparing different electrode materials. Some emphasis should be put on a few features concerning the IPCE measurements: the peak efficiency did not exceed 40 %, a rather low value. The improvement of the quantum efficiency by employing the *in situ* hybrids regarding the reference was remarkable, so much more as this represented a method, which was not yet optimized. Additionally, it is noteworthy that the QE of the sample containing 10 wt% rutile was higher than the one containing 20 wt%, although the dye loading amount was higher for the one having 20 wt%. Thus, the LHE should have been higher. Hence, either the charge collection efficiency or the electron injection efficiency was higher for the sample containing 10 wt% rutile rods. The measured charge extraction in Figure 5.11b) confirmed this assumption: the charge extraction was highest for the sample containing 10 wt% rutile rods, while it was the only sample having a significantly increased charge extraction at a given voltage.[27] The electron

lifetime, which was measured by intensity-modulated-photo-voltage-spectroscopy (IMVS) did not allow any clear statements. At low light intensities, the reference showed the highest electron lifetime, while the electron lifetime at higher intensities was higher for the samples containing 10 and 20 wt% rutile, respectively. Upon evaluation of these results it should also be considered that the maximum intensity used in this experiment was 270 W/m^2, while the standard intensity of 1 sun and an AM1.5 is equivalent to 1000 W/m^2. The electron diffusion was characterized using intensity-modulated-photocurrent-spectroscopy (IMPS) and can be seen in Figure 5.11d). The electron diffusion coefficients for the *in situ* hybrids were low as compared to the reference. This was unexpected, but could be explained by the formation of very small anatase particles that were generated during the *in situ* decomposition. The smaller the particles, the more particle-particle boundaries present, which decrease the length of the path an electron can walk through the electrode without recombination. Additionally, this could also cause the low obtained charge extraction. The other samples containing rods, but especially the one containing 10 wt% rods, increased the electron diffusion coefficient with regards to the reference DSC. The increased electron diffusion of these samples clearly shows that the incorporation of anisotropic semiconductors into the DSCs can be beneficial, although they initially decrease the surface area.
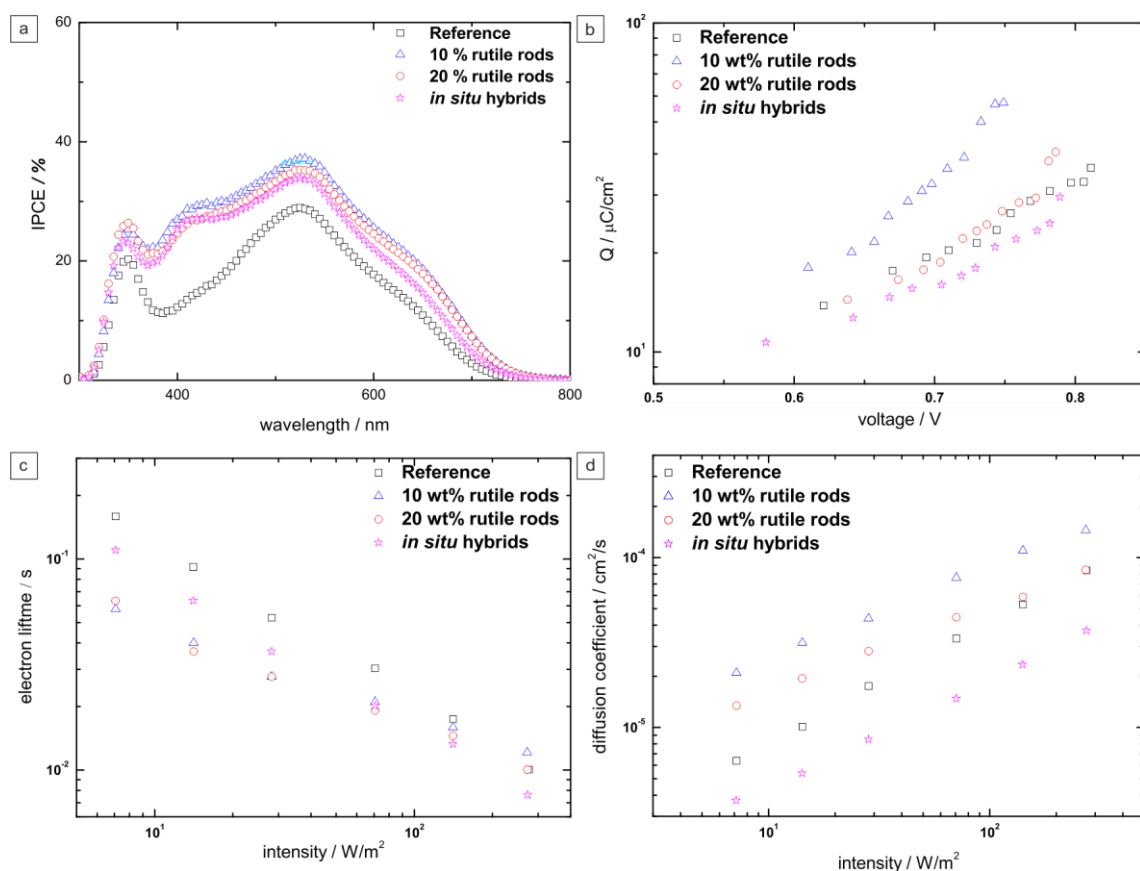
Figure 5.11 Electrochemical analysis of the DSCs Reference 2, 10 wt% rutile rods, 20 wt% rutile rods, and *in situ* hybrids: a) quantum efficiency, b) charge extraction at a given voltage, c) electron lifetime determined by IMVS, and d) electron diffusion coefficient determined by IMPS. The measurements were performed by ████████████.

5.3 Excursus: Perovskite-Sensitized Solar Cells

Aside from their low efficiency, which was improved step-by-step, the previously discussed DSCs had since their invention in 1991 two major problems: (i) the electrolyte consisted of a solution of LiI and I_2 in acetonitrile, which is not practicable in a commercial application due to the problems regarding the sealing process and the evaporation of acetonitrile and (ii) the photo-degradation of the used dyes.[28,29] Since a few years, several organic and inorganic hole-conductors were tested as electrolyte systems, such as CuI, CuSCN, and Spiro-OMeTAD, an organic hole-conductor. Initially, all of them showed promising results, while the application methods were rather different. CuI and CuSCN were applied by layer-by-layer deposition from solution, while the experimental setup was very sensitive concerning the technical setup. Spiro-OMeTAD is also solution processable by spin-coating and, therefore, is a facile technique on laboratory scale. It got established as standard solid state electrolyte for DSCs. These became completely a solid state device and will be referred to as solid state dye-sensitized solar cell ssDSC in the following. Until 2013, ssDSCs and DSCs using metal-organic dyes were the state-of-the-art. Here, the dyes were replaced by superior organic-inorganic hybrid lead halides.[30–32] The perovskite methylammonium lead iodide $CH_3NH_3PbI_3$ is still most commonly used. These solar cells represent a completely new generation, because the occurring reactions also differ significantly, but are also not yet well understood. The abbreviation for perovskite solar cells is PSC. In literature it is often used in combination with an electrode material containing nanoparticles of Al_2O_3 and TiO_2, which is then referred to as meso-superstructured solar cell (MSSC).[30] Using this perovskite structure already resulted in reports obtaining short circuit currents of 21.5 mA/cm² and open circuit voltages of 1.07 V, which combine to all-over efficiencies of up to 15.4 %.[33] These MSSCs, although being fully solid state devices, require a sealing, because the perovskite is sensitive to air, and decomposes over time. If an effective sealing is applied, long-term tests were already successfully conducted. However, the strongest disadvantage remains: the use of toxic lead materials. They were shown by Kanatzidis *et al.* to be overcome by replacing Pb^{2+} ion by Sn^{2+}.[34,35] Thus, the disadvantage of the perovskite $CH_3NH_3SnI_3$ is the instability against oxidation since tin has a high tendency to form the four-fold positive ion, and is ineffective as such species. Additionally, traces of the Sn^{4+} species in the perovskite already act as trap sites and decrease the efficiency drastically. As soon as the stability problems of the $CH_3NH_3SnI_3$ will be overcome, this type of solar cells will be a very promising candidate for large scale applications.

In this study, we would like to present initial promising results that give rise to further investigations on this type of solar cells. Briefly, we tried to transfer the results of the DSCs using a liquid electrolyte to a solid state electrolyte to also enable us to investigate the perovskite $CH_3NH_3PbI_3$. The requirements for the TiO_2 electrode differed significantly for liquid electrolytes and solid state electrolytes. When a liquid electrolyte is used, the demands on the electrode are rather low as compared

_____

to ssDSCs. The charge transport in the I^-/I_3^- electrolyte occurs via diffusion, the ions can travel rather long ways and, therefore, electrode thicknesses of 15 µm is easily realizable. The limiting factor is the electron transport in the photo-anode. When the Spiro-OMeTAD electrolyte is used, the charge transport is ensured by hole-transport through the organic electrolyte, while usually thicknesses of only 1 - 3 µm of the electrode can be realized. Here, the counter-electrode is directly applied onto the hole-conductor and, thus, the TiO_2 layer has to be very smooth to avoid a direct contact of the TiO_2 through the hole transporting medium (HTM) with the counter-electrode. To ensure a high quality electrode, and, at the same time, a thin film, it was decided to change the preparation method of the electrodes from doctor-blading to spin-coating. The particles that were analyzed were the described rutile sub-micron rods. A paste by Dyesol© served as reference system due to the higher quality of the resulting electrodes. Briefly, rutile sub-micron rods were dispersed in ethanol and PEG400, while continuous stirring over at least one hour ensured the homogeneity of the paste. For the reference, the commercially available paste was diluted with ethanol and stirred overnight in a sealed container. Both pastes were applied to FTOs by spin-coating at 8000 rpm, the film was first dried at 100 °C and then sintered at 450 °C. The resulting films can be seen in Figure 5.12, while a) to c) shows films consisting of rutile sub-micron rods and d) to f) the films made using the commercial Dyesol© paste. Both pastes led to high quality electrodes that were very homogeneous over a wide range. The close-up image in b) shows the large rutile particles that are easy to identify. The particles in the Dyesol© paste had a size of 8 nm according to the manufacturer, which was too small to be resolved by SEM imaging e). It is evident that the packing of the small particles was tighter as compared to the large rutile rods. Although the rutile rods exhibited a length of up to 400 nm, the surface could be considered as very smooth over a wide range, as demonstrated by the cross section image in c). The Dyesol© paste also formed a constant film thickness over a large scale (Figure 5.12f)).
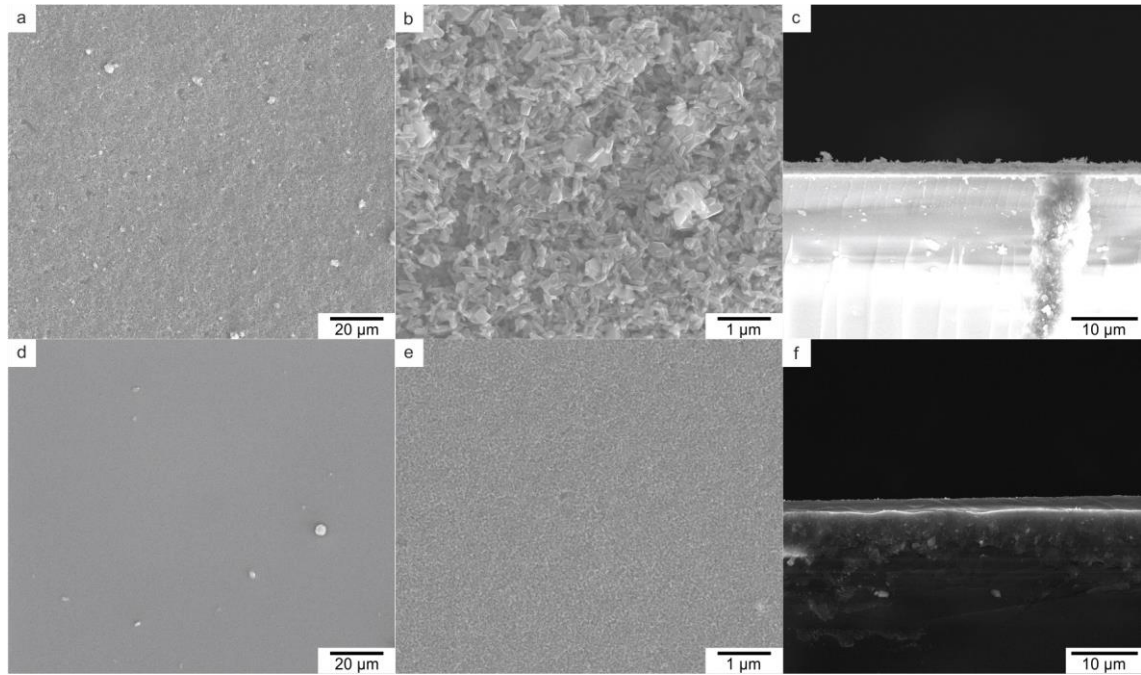
Figure 5.12 SEM images of different electrode materials suitable for ssDSCs and ssPSCs: rutile sub-micron rods in photo-anodes of a thickness of 1 µm (a, b, c) and spherical anatase nanoparticles prepared from a commercial paste by Dyesol (d, e, f).

CH$_3$NH$_3$PbI$_3$, a solution-processable perovskite, forms upon evaporation of the solvent. Briefly, CH$_3$NH$_3$I and PbI$_2$ were dissolved equimolar in a mixture of γ-butyrolacton and acetonitrile, applied onto the electrode, and spin-coated at 1000 rpm. Afterwards the solvent was evaporated at 70 °C on a hotplate. Next, the HTM was also applied by spin-coating, the counter-electrode was sputtered onto the HTM. During the preparation of the Au or Ag counter-electrode, the photo-anode was partly masked to control the shape and size of the counter electrode. The measured solar cell characteristics and *J-V*-curves can be seen in Table 5.5 and Figure 5.13, respectively. The Dyesol© paste contains anatase nanoparticles, which should exhibit a band-gap larger than the one of rutile. However, this was not represented in the results of the V_{oc}, which was 0.8 V for the rutile electrode and 0.6 V for the Dyesol© electrode. This observation was unexpected and cannot be explained up to date. The obtained short circuit currents were 1.64 and 3.34 mA/cm² , respectively. The fill factors of 34.9 and 43.0 % were rather poor as compared to the ones of the DSCs described at the beginning of this Chapter. The peak efficiencies of 0.9 and 2.1 % can be used as a promising starting point for further investigation.

Table 5.5 *J-V*-characteristics obtained from ssPSCs using rutile sub-micron rods and a Dyesol© paste as electrode material with Methyl-ammonium lead iodide as sensitizer. The measurement was performed by ███████████████ .

Sample	V_{oc} / V	J_{sc} / mA/cm²	FF / %	Mean η / %	Peak η / %
Rutile rods	0.80	1.64	34.89	0.66	0.90
Dyesol paste	0.60	3.34	42.95	1.40	2.12

_____

The *J-V*-curves visualize the higher V_{oc} for the rutile electrode, but the lower J_{sc}. The shape indicates that the losses were probably to a high extent caused by parallel resistances, but series resistivities are also present. So far, it is hard to evaluate the results and also explain them on behalf of the physical processes. The synthesis of the perovskite layer, especially, seems to be a very crucial reaction, while only slight changes of the synthesis might alter the solar cell characteristics significantly. The field of the perovskite solar cells is still in its infancy. Up to now, they are poorly understood concerning the particular reaction in the solar cell as well as the focused optimization of the solar cell. Initially, it could be shown that solar cells with rutile sub-micron rods and anatase nanoparticles in combination with $CH_3NH_3PbI_3$ can convert light into electricity, where the synthesis is very facile on first glance, but so far it is unknown, which parameters control the production of an efficient high quality PSC.
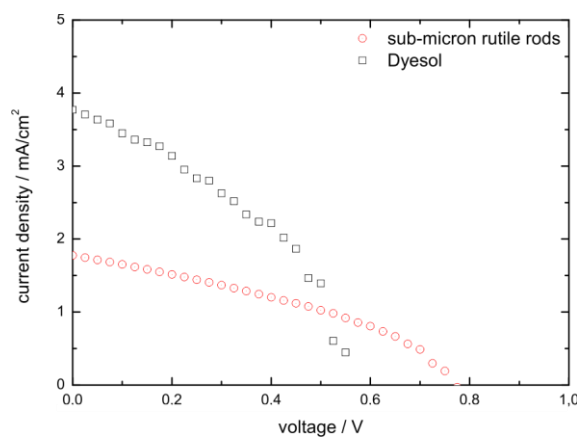
Figure 5.13 *J-V*-curve obtained from photo-anodes consisting of rutile sub-micron rods and a Dyesol© paste, respectively. Methyl-ammonium lead iodide was used as sensitizer. The measurement was performed by ████████████████.

As an additional electrode material, anodized titanium oxide (ATO), a highly ordered and plane structure, is interesting for ssDSCs and PSCs.[26] ATO offers promising features, because it exhibits a high porosity and anisotropic conductive structures. There are various reports of ATOs being used in DSCs facilitating metal organic dyes for electron generation. The major drawback of organized nanostructures such as ATO is the small surface area and, therefore, the low dye loading. Herein, we demonstrate the synthesis of ATO, while the pore sizes could be controlled in a range of 40 - 100 nm. Their stability could be enhanced by applying a square-functioned voltage resulting in bamboo-type ATO.[36] Subsequent filling with TiO_2-P25 was possible. Initially developed for liquid electrolyte dye-sensitized solar cells, ATOs have an even more promising potential in the application of solid state devices, because charge transport via diffusion is decelerated due to the confinement in the pores, while hole-conduction should not be hindered. The pictures in Figure 5.14 display conventionally synthesized ATO, bamboo-type ATO, and filled ATO in both top view and cross section images. The images prove that all samples are homogeneous and flat, which enables the use of this kind of structure as an electrode material in solid state solar cells. The application in these devices is topic of ongoing research.
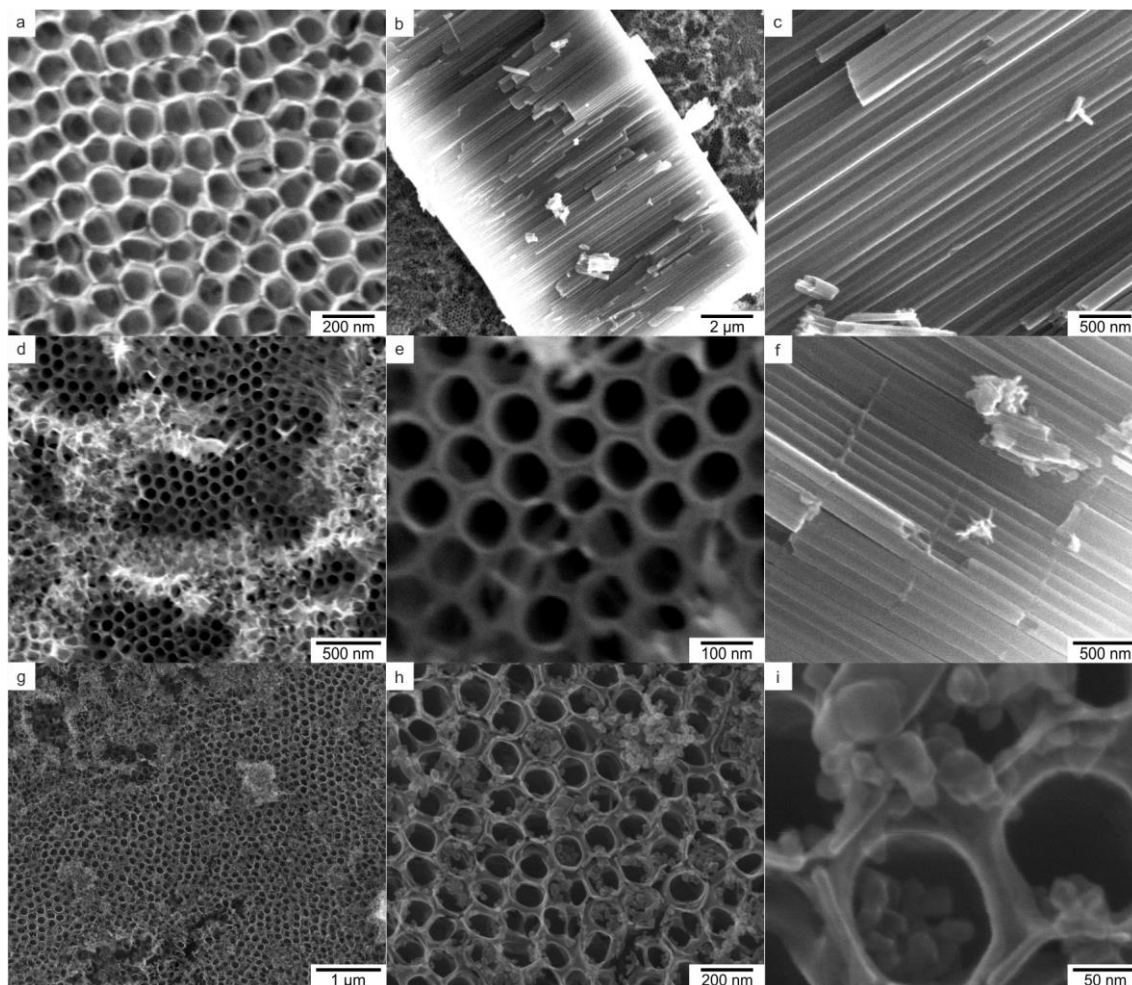
Figure 5.14 SEM images of anodized titanium oxide arrays, an alternative promising electrode material for ssDSCs as well as ssPSCs. Different constructions were realized: conical pores (a, b, c), or bamboo-type pores (d, e, f). Additionally, it was possible to increase the surface area by incorporation of spherical particles into the pores (g, h, i).

5.4 Conclusion

In this Chapter, the applicability of rutile sub-micron rods in dye-sensitized solar cells was tested by incorporating these particles into photo-anodes. Furthermore, various modifications were evaluated, such as (i) changed contents of the electrode by applying composite electrodes of a mixture of anatase and rutile particles and (ii) by employing hybrid particles that exhibited a rutile "core" and an amorphous, high surface "shell". Aim for both approaches was to decrease the losses caused by recombination by incorporating 1D structures into the electrode that enable a directed conduction of electrons through this pathway. Additionally, an excursus demonstrated that rutile sub-micron rods are also promising electrode materials for perovskite-sensitized solar cells.

In the first part of this study, the individual surface area and band-gaps of the later used materials, *i.e.* sub-micron rutile rods, spherical anatase particles, TiO_2-P25 and $TiO_2@TiO_2$ hybrid particles, were determined by BET measurements and UV-Vis spectroscopy, respectively. The BET

_____

measurements revealed that the surface area of the employed precursor particles varied between 15.2 m^2/g and 128.5 m^2/g, while an increase in the surface area of rutile rods by 33 % was possible due to the formation of hybrid particles. The band-gap measurements clearly showed the difference between sub-micron rutile rods and spherical anatase nanoparticles, while anatase has the larger band-gap. However, the hybrid formation did not change the size of the band-gap and, surprisingly, the TiO_2-P25 had the largest band gap of 3.45 eV. The precursor materials were mixed in various ratios, and photo-anodes were formed. For all composites, high quality electrodes were assembled, although a few of them showed minor defects such as cracks and elevations.

In a first evaluation, the most beneficial amount of rutile rods was determined to be in-between 10 and 50 wt%, while the remaining material was composed of spherical anatase nanoparticles. In a more detailed investigation, the optimum amount of rutile rods in composite electrodes was evaluated to be 20 wt%. High fill factors of up to 72.9 % were reached with an efficiency of 4.06 %. In comparison to the efficiency of the reference electrode of 3.25 %, this constitutes an improvement of 25 % due to the adjustment of the composition. However, the efficiency of 4.06 % itself is not state-of-the-art, but it has to be considered that these DSCs represent the most basic approach to photo-anodes. Thus the improvement of the solar cell efficiency by 25 % by only modifying the electrode material composition is a highly appreciable result. The solar cell characteristics could be confirmed by quantum efficiency, charge extraction, as well as electron lifetime, and electron diffusion coefficient measurements. The IPCE at its maximum could be improved by about 10 % for the samples containing 10 and 20 wt% rutile rods, while also a significant enhancement of the electron diffusion coefficients was measured for these samples. The charge extraction and the electron lifetime were also slightly improved.

In the second part of this Chapter, hybrid materials were incorporated and *in situ* formed in photo-anodes. The *ex situ* prepared hybrid particles did not have a positive influence on the DSC efficiency. The *in situ* formed hybrid particle electrodes had comparable characteristics as the reference DSCs, while quantum efficiency was improved regarding the reference. All other measured features either remained unchanged or degraded.

In a short excursus, the synthesis of perovskite solar cells was discussed. Herein, an organic-inorganic hybrid material in perovskite structure, namely $CH_3NH_3PbI_3$, was synthesized in solution and applied to the TiO_2 electrode. The perovskite material suffered from minor impurities due to unreacted precursor and oxidation. The assembled PSCs were equipped with a solid state hole-conducting electrolyte and Ag or Au counter-electrodes. The efficiency of the PSCs was tested for two different electrode materials: (i) synthesized from a commercial paste, purchased by Dyesol©, and (ii) rutile sub-micron rods. The efficiencies were 2.1 % and 0.9 %, respectively. The fill factors were low between 42 and 34 %, while it was remarkable that a very high V_{oc} of 0.8 V was achieved using the rutile rods as electrode material. It is not yet understood why the V_{oc} was so high as compared to the one of the commercial product, and remains topic of ongoing research.

In the second part of the excurses, the synthesis of alternative electrode materials, which exhibit 1D features to enable an improved electron conduction and, therefore, thicker electrodes and higher dye loadings. Such a material could be anodized titanium oxide that can be modified in many ways. It is possible to tune the diameter of the pores as well as their length, while the stability could be enhanced by growing bamboo-type ATOs. The surface area of the bare ATO, however, remains poorly small, which could be overcome by filling the pores with nanoparticles, using a hydrothermal treatment.

5.5 Experimental Section

5.5.1 Synthesis

Materials. All materials were used as received without further purification. PEG400, PEG20k (Bioultra), γ-butyrolactone ($\geq$ 99 %), acetonitrile (99.9 %), chlorobenzene (98 %), tert-butyl-pyridin (96 %, TBP), and bis(trifluoromethane)solfonimide lithium salt (99.95 %, Li-TFSI) were purchased by Sigma Aldrich. Methylamine (40 wt% in H_2O) and lead iodide (99.999 % trace metals basis, PbI_2) were delivered by ABCR. N719 (batch QN719p49) and titania paste (DSL18NR-T, batch 258, Dyesol-paste) were bought from Dyesol. 2,2',7,7'-Tetrakis-(N,N-di-4-methoxyphenylamino)-9,9'-spirobifluorene (Spiro-OMeTAD, Livilux SHT-263) was provided by Merck. All other materials were used as stated in the previous Chapters.

Paste Preparation for Composite Electrodes. 300 mg particles (TiO_2-P25, TiO_2@TiO_2 hybrids, anatase particles or rutile sub-micron rods, or mixtures of these) were mixed with 1 mL ethanol and 30 drops PEG400. This mixture was stirred for 15 min and, afterwards, treated by ultrasonication for 60 min. Subsequently, 1 drop of a solution of 5.5 g PEG20k in 5 mL water was added and stirred for another 15 min. Afterwards, the mixture was manually ground for 3 - 5 min to adjust the viscosity of the paste.

Paste Preparation for Hybrid Particle Electrodes. 300 mg rutile sub-micron rods were mixed with 1 mL ethanol, 30 drops PEG400, and 4 - 12 drops TiCl-treatment solution. The preparation of the TiCl-treatment solution was described in Chapter 4. This mixture was stirred for 15 min and treated by ultrasonication for 60 min afterwards. Subsequently, 2 - 5 drops of a solution of 5.5 g PEG20k in 5 mL water was added and stirred for another 15 min. Afterwards, the mixture was manually ground for 3 - 5 min to adjust the viscosity of the paste.

Device Preparation. First, a TiO_2 blocking layer of a few hundred nanometers in thickness was coated on the FTO substrates (sheet resistance 8 /sq, Pilkington). A 0.1 M solution of TAD in 1-butanol was administered on the substrate by spin coating, followed by calcination at 450 °C for 30 minutes. All photo-anodes were prepared by the doctor-blading method. An appropriate portion of the prepared paste was applied onto the FTO substrate. The anodes were then sintered at 450 °C for 30 min, for hybrid particles the sintering duration was elongated up to 4 h at 450 °C. For dye adsorption, the electrode films

were soaked in a solution containing 27.5 mg N719 in a mixture of acetonitrile and tert-butanol (1:1 by volume) at 30 °C overnight in a sealed container.

Excursus: Perovskite-Sensitized Solar Cells

Paste Preparation. 350 mg rutile sub-micron rods were mixed with 1 mL ethanol, 30 drops PEG400, and 2 - 3 drops Triton-X-100. This slurry was stirred for at least 15 min, subsequently, is was treated by ultrasonication for 60 min. The Dyesol© paste was prepared by mixing 800 mg Dyesol© paste with 2.2 mL ethanol, which was stirred overnight in a sealed container, and was treated by ultrasonication for 60 min.

Perovskite Preparation. Methyl ammonium hydroiodide was synthesized by mixing equimolar amounts of an aqueous solution of methylamine and hydroiodic acid. The product was isolated using a rotary evaporator at a temperature of 55 °C and 20 mbar. The methyl ammonium hydroiodide was added in an equimolar ratio to PbI_2 in a mixture of γ-butyrolacton and acetonitrile (1:1 by weight) to yield a solution of 40 wt% methyl ammonium lead iodide.

Electrolyte Solution. A solution of 160 mg/ml Spiro-OMeTAD in chlorbenzene was prepared. For every 73 mg Spiro-OMeTAD 15 µl of Li-TFSI stock solution (170 mg Li-TFSI per 1 mL acetonitrile) and 7 µl TBP were added.

Device Preparation. FTO substrates were masked with Scotch® isolation tape and the remaining area was treated with Zn and 3 M HCl to dissolve the FTO layer. Subsequently, the substrates were cleaned using surfactant, water, and acetone. A layer of about 100 nm consisting of TiO_2 were applied onto the substrates by spray-pyrolysis using a 0.1 M solution of TAD in ethanol at 450 °C. Afterwards, a few drops of the paste were applied to the substrates and spin-coated at a speed of 2000 - 8000 rpm for 10 -30 s. The pastes were dried at 100 °C for 1 h and then sintered at 450 °C for 30 min. Subsequently, the perovskite solution was applied to the TiO_2 film and spin-coated at 2000 rpm for 10 s, the perovskite was crystallized at max. 80 °C on a hotplate. To form the electrolyte layer, 65 µL of electrolyte solution was applied, infiltrated for at least 30 s, and spin-coated for 10 s at 1500 rpm. The Au counter-electrode was sputtered onto the masked photo-anode film at a pressure of $2.5*10^{-2}$ mbar with a thickness of about 150 nm.

Excursus: Anodized Titanium Dioxide as Electrode Material

Anodization. The electropolishing of Ti foil was performed following an adapted procedure of Kerschbaumer and co-workers.[37] The electropolished samples were treated using a two-step anodization procedure. In a first step, the polished foil was anodized at 75 V for 3.5 h using a solution of 0.47 wt% NH_4F and 2.1 wt% H_2O in ethylene-glycol. The obtained membrane was rinsed with water and acetone such that it peeled off the foil by itself. Imprints on the foil were left behind. For the second step, a

_____

square-function was applied onto the voltage: it was switched from 75 V to 20 V and back every 2 min over a total duration of 60 min. The resulting sample was rinsed with water and acetone. When a square function was applied, bamboo-type ATOs resulted, while when the voltage was kept constant the pores grew straight. The samples were thermally treated at 400 °C for 12 h under vacuum, which enabled a sufficient stability for a subsequent hydrothermal treatment. For filling the pores, the membrane was placed in a Teflon inlay of a stainless steel autoclave and a solution of TiO_2-P25 in water (0.12 g/100 mL) was added. The dispersion was, prior to the addition, stirred and ultrasonicated to ensure that all particles were well-dispersed. The treatment was performed for 12 h at 90 °C. Afterwards the samples were rinsed with water to remove excessive TiO_2-P25.

5.5.2 Characterization

Brunauer-Emmett-Teller Measurements. The surface area was determined via N_2 adsorption-desorption measurements using a QuantaChrome Autosorb 6B instrument applying a multipoint BET measurement.

UV-Vis Spectroscopy. For UV-Vis measurements, a Cary Varian 5G UV-Vis-NIR spectrometer was used in a range of 200 - 800 nm. The instrument is equipped with two different setups: (i) a holder for cuvettes or (ii) an integrating sphere. For dye-loading experiments, 0.1 mL quartz cuvettes were used for measurements in a range of 350 - 800 nm, for details see below. For solids, the integrating sphere was used. The samples were attached to Magic Scotch® tape, which was subtracted from the background. A white standard film of $BaSO_4$ was used. The measurements were performed in diffuse reflectance mode.

Confocal Laser Microscopy. The thickness and optical appearance of the synthesized electrode films was analyzed using a Keyence (VK8710) confocal laser-scanning microscope. The instrument also allowed optical microscopy and is equipped with an automated sample holder.

Scanning Electron Microscopy. The SEM images were taken using an FEI Nova NanoSEM630 equipped with an Everhart-Thornley detector (ETD) and a low Voltage high Contrast detector (vCD) in high vacuum mode. The acceleration voltage was chosen to be between 15 - 30 kV. The samples were attached on an aluminum stub using adhesive conductive carbon tape. For energy dispersive X-Ray-spectroscopy (EDX), a built-in EDAX-Genesis detector was used.

Dye-Loading Amount. In order to determine the amount of dye adsorbed within a composite electrode or an electrode consisting of NPs only, the respective films loaded with N719 dye were immersed into 10 mM NaOH at 30 °C for 12 h. Afterwards, the absorption spectra of the respective solutions were measured and the intensity of the peak in the region between 505 - 515 nm was compared to a calibration curve.

_____

J-V-characteristics. Solar cell characteristics were obtained using a Keithley 2400 source meter and solar simulator with 300 W Xenon arc-lamp (Newport) under 1 sun illumination (AM 1.5, 100 mW/cm^2). The intensity was calibrated according to a silicon solar cell (PV measurements, Inc.).

CE, IMVS, IMPS and IPCE. The charge extraction, electron diffusion coefficient, electron lifetime and quantum efficiency were obtained by IMPS (intensity-modulated-photo-current-spectroscopy) under short-circuit conditions and IMVS (intensity-modulated-photo-voltage-spectroscopy) under open circuit conditions as a function of light intensity using a CIMPS (controlled-intensity-modulated-photo-spectroscopy) system (Zahner). A more detailed explanation for measurements is described elsewhere.[26,27] The quantum efficiency of the cells was analyzed by an IPCE measurement device by PV measurements, Inc.

5.6 References

1   B. C. O'Regan and M. Grätzel, *Nature*, 1991, 737–740.
2   M. Law, L. E. Greene, J. C. Johnson, R. Saykally and P. Yang, *Nat Mater*, 2005, **4**, 455–459.
3   A. Hagfeldt, G. Boschloo, L. Sun, L. Kloo and H. Pettersson, *Chem. Rev.*, 2010, **110**, 6595–6663.
4   U. Bach, D. Lupo, P. Comte, J. E. Moser, F. Weissörtel, J. Salbeck, H. Spreitzer and M. Grätzel, *Nature*, 1998, 583–585.
5   S. Ito, *Sol. Energy Mater. Sol. Cells*, 2003, **76**, 3–13.
6   G. K. Mor, K. Shankar, M. Paulose, O. K. Varghese and C. A. Grimes, *Nano Lett.*, 2006, **6**, 215–218.
7   W. Yang, J. Li, Y. Wang, F. Zhu, W. Shi, F. Wan and D. Xu, *Chem. Commun. (Camb.)*, 2011, **47**, 1809–1811.
8   A. Kay and M. Grätzel, *Sol. Energy Mater. Sol.Cells*, 1996, **44**, 99–117.
9   J. A. Christians, Fung, Raymond C M and P. V. Kamat, *J. Am. Chem. Soc.*, 2014, **136**, 758–764.
10 B. C. O'Regan and F. Lenzmann, *J. Phys. Chem. B*, 2004, **108**, 4342–4350.
11 F. Fabregat-Santiago, J. Bisquert, Le Cevey, P. Chen, M. Wang, S. M. Zakeeruddin and M. Grätzel, *J. Am. Chem. Soc.*, 2009, **131**, 558–562.
12 I. G. Yu, Y. J. Kim, H. J. Kim, C. Lee and W. I. Lee, *J. Mater. Chem.*, 2010, **21**, 532.
13 S. Ito, T. N. Murakami, P. Comte, P. Liska, C. Grätzel, M. K. Nazeeruddin and M. Grätzel, *Thin Solid Films*, 2008, **516**, 4613–4619.
14 A. Hagfeldt, G. Boschloo, L. Sun, L. Kloo and H. Pettersson, *Chem. Rev.*, 2010, **110**, 6595–6663.
15 M. Grätzel, *Nature*, 2001, 338–344.
16 E. Barea, X. Xu, V. González-Pedro, T. Ripollés-Sanchis, F. Fabregat-Santiago and J. Bisquert, *Energy Environ. Sci.*, 2011, **4**, 3414.
17 K. Zhu, N. R. Neale, A. Miedaner and A. J. Frank, *Nano Lett.*, 2007, **7**, 69–74.
18 Y. Ohsaki, N. Masaki, T. Kitamura, Y. Wada, T. Okamoto, T. Sekino, K. Niihara and S. Yanagida, *Chem Phys*, 2005, **7**, 4157–4163.
19 B. Tan and Y. Wu, *J Phys Chem B*, 2006, **110**, 15932–15938.
20 D. Koll, Johannes Gutenberg-Universität Mainz, 2011.
21 J. Sheng, L. Hu, S. Xu, W. Liu, L. Mo, H. Tian and S. Dai, *J. Mater. Chem.*, 2011, **21**, 5457.
22 W. Peng, M. Yanagida, L. Han and S. Ahmed, *Nanotechnology*, 2011, **22**, 275709.
23 S. Valencia, J. Miguel and G. Restrepo, *The Open Materials Science Journal*, 2010, 9–14.
24 V. Dhas, S. Muduli, W. Lee, S.-H. Han and S. Ogale, *Appl. Phys. Lett.*, 2008, **93**, 243108.
25 S. Hore, C. Vetter, R. Kern, H. Smit and A. Hinsch, *Sol. Energy Mater. Sol. Cells*, 2006, **90**, 1176–1188.
26 Y. Alivov and Z. Y. Fan, *Appl. Phys. Lett.*, 2009, **95**, 063504.

27 G. Schlichthörl, N. G. Park and A. J. Frank, *J. Phys. Chem. B*, 1999, **103**, 782–791.

28 K. Fredin, K. F. Anderson, N. W. Duffy, G. J. Wilson, C. J. Fell, D. P. Hagberg, L. Sun, U. Bach and S.-E. Lindquist, *J. Phys. Chem. C*, 2009, **113**, 18902–18906.

29 F. Nour-Mohhamadi, S. D. Nguyen, G. Boschloo, A. Hagfeldt and T. Lund, *J Phys Chem B*, 2005, **109**, 22413–22419.

30 M. M. Lee, J. Teuscher, T. Miyasaka, T. N. Murakami and H. J. Snaith, *Science*, 2012, **338**, 643–647.

31 S. D. Stranks, G. E. Eperon, G. Grancini, C. Menelaou, Alcocer, Marcelo J P, T. Leijtens, L. M. Herz, A. Petrozza and H. J. Snaith, *Science*, 2013, **342**, 341–344.

32 H. J. Snaith, *J. Phys. Chem. Lett.*, 2013, **4**, 3623–3630.

33 M. Liu, M. B. Johnston and H. J. Snaith, *Nature*, 2013, **501**, 395–398.

34 F. Hao, C. C. Stoumpos, D. H. Cao, Chang, Robert P. H. and M. G. Kanatzidis, *Nature Photon*, 2014, **8**, 489–494.

35 N. K. Noel, S. D. Stranks, A. Abate, C. Wehrenfennig, S. Guarnera, A.-A. Haghighirad, A. Sadhanala, G. E. Eperon, S. K. Pathak, M. B. Johnston, A. Petrozza, L. M. Herz and H. J. Snaith, *Energy Environ. Sci.*, 2014, **7**, 3061.

36 D. Kim, A. Ghicov, S. P. Albu and P. Schmuki, *J. Am. Chem. Soc.*, 2008, **130**, 16454–16455.

37 H. Kerschbaumer, Johannes Gutenberg-Universität Mainz, 2014.

_____

6

SnO₂-Based Dye-Sensitized Solar Cells

The results in this Chapter partly originate from a cooperation with ███████████ and █████████████ in the group of ███████████████ at the Seoul National University, Seoul, South Korea. Nanoparticle synthesis, photo-anode formation, and comprehensive characterization was performed at Johannes Gutenberg University, Mainz.

6.1 Introduction

The principles and a deeper introduction to DSCs were already presented in the introduction in Chapter 1 as well as in Chapter 5, where TiO₂-based DSCs were discussed. Up to now the most commonly used electrode material in the photo-anode for DSCs is anatase-phase TiO₂, because it exhibits a conduction band position that is suitable to extract reasonably high voltages in combination with the I^-/I_3^- redox couple.[1,2] Additionally, in form of nanoparticles it has a high surface area as well as a high tendency to bind with dyes like N719. However, other materials such as ZnO and SnO₂ might also be promising candidates due to their individual properties.[3–5] ZnO, for instance, shows a higher conduction band edge than TiO₂, a low recombination rate, and a plethora of possible nanostructures.[5,6] SnO₂, herein, shows the largest band-gap of all three, while also exhibiting electron conduction velocities that are magnitudes higher than in TiO₂.[2] Additionally, SnO₂ also forms various nanostructures that are shown to differ in DSC applicability, considering their different morphologies as described by Birkel and co-workers.[7] As another feature, SnO₂-based DSCs were found to exhibit an improved long term stability by causing less photo-degradation of the employed Ru-dye.[8] SnO₂ is disadvantageous as electrode material for DSCs due to its low conduction band edge as compared to the redox couple, which limits the generation of high photo-voltages, as well as low dye adsorption and high recombination rates.[9–11] Therefore, SnO₂-based DSCs were synthesized and exhibited lower the over-all efficiency as compared to TiO₂-based DSCs. Still, SnO₂-based DSCs exhibit interesting features that are worth investigating, such as the effect of different variations of composition of the electrodes on the characteristics. Thus, all disadvantages of the low conduction band edge, the high recombination rate, as well as the low dye adsorption can be changed by modifying the shape and composition of the SnO₂ particles, *i.e.* a change from bare particles to core/shell, hybrid, or branched multicomponent particles,

which can introduce a variety of new properties and possibilities. The incorporation of anisotropic semiconductors into DSCs was already demonstrated in Chapter 5, but also in various other reports, as they increase the electron diffusion coefficients and electron lifetimes in the electrode and, therefore, lead to a higher J_{sc}.[12] The observations were mainly made for TiO$_2$, as it is the most prominent and important electrode material used in DSCs. The major drawback when using only anisotropic structures, *i.e.* nanorods, nanotubes, ATOs, or nanowires, is that they exhibit a small surface area, which is disadvantageous for dye adsorption.[4,13] Due to the decreased dye loading, smaller short circuit currents are usually observed, which results in a low efficiency. For TiO$_2$, it was, also in Chapter 5, demonstrated that a composite of spherical and anisotropic nanoparticles enhances the efficiency of DSCs by combining a high surface area with directed electron conduction.[13,14] In this study, we evaluated the influence of an increased surface area by synthesizing composite electrodes of spherical and anisotropic nanoparticles, functionalizing these with N719, and analyzing the characteristics of the DSCs.

6.2 Composite Electrodes of Spherical and Rod-Shaped SnO$_2$ Nanoparticles

Briefly, spherical SnO$_2$ nanoparticles of a size of 3 - 5 nm were prepared by a surfactant mediated solvothermal treatment reported by Chen and co-workers.[15] Herein, hexane, CTAB, urea, pentanol, and an aqueous solution of SnCl$_4$·5H$_2$O were mixed and heated to 130 °C for 12 h. The product was repeatedly rinsed with ethanol and water. The SnO$_2$ nanorods were prepared using a modified protocol by Birkel and co-workers.[7] Here, aqueous solutions of NaOH and SnCl$_4$·5H$_2$O were dissolved in a mixture of water and ethanol (1:1 by volume) and treated at 250 °C for various durations. After product collection, the sample was rinsed with diluted sulfuric acid to replace surface attached sodium ions by protons. TEM images of the products can be seen in Figure 6.1. The spherical particles had a quite narrow size distribution, but showed a tendency to agglomerate. The SnO$_2$ rods also formed large agglomerates of sizes up to 10 µm. Their tendency to agglomerate could be reduced to a large extent by washing with acid, but not completely avoided due to the ion exchange from sodium to protons. The length of the rods could be varied by changing the duration of the hydrothermal treatment as already shown by Birkel and co-workers. The PXRD patterns of the precursors showed cassiterite as the only crystalline phase present (Figure E1).
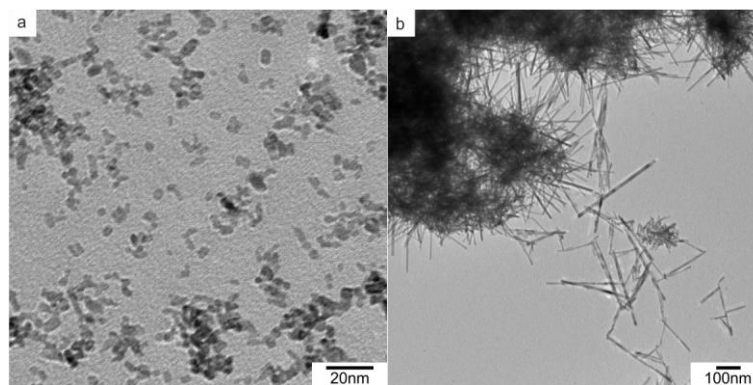
Figure 6.1 TEM images of particles used for the evaluation of the optimal content of anisotropic structures in DSCs: a) spherical SnO_2 nanoparticles of a size of 3 - 5 nm synthesized at 130 °C and b) SnO_2 nanorods synthesized via a basic hydrothermal treatment at 250 °C.

The beneficial amount of incorporated 1D structures depends on the conduction properties of the material and the length of the structures, which was shown for TiO_2 during the course of this work as well as in the literature. For instance, multi-crystalline wires of a length of up to 12 µm were demonstrated to have their most beneficial effect, when used by 5 wt% in a mixture with spherical particles.[14,16,17] In Chapter 5, it could be shown for rutile sub-micron rods that an enhanced efficiency was obtained at 10 - 20 wt% rutile in the electrode. Due to this variation, an initial test was made with a content of 0 wt%, 10 wt%, 20 wt%, 40 wt%, 60 wt%, and 80 wt% SnO_2 rods. The remaining amount was spherical SnO_2 particles of a size of 3 - 5 nm. The corresponding CLSM profile images of the photo-anodes can be seen in Figure 6.2. As no adequate SnO_2 nanoparticle system is commercially available like TiO_2-P25 for TiO_2 it was disclaimed to use SnO_2 as reference and to also use TiO_2-P25 as a reference electrode material to evaluate the assembly process and the measurements. The CLSM profile image of the reference can be seen in the Appendix in Figure E2a). In this initial test of composite electrodes, the SnO_2 nanoparticles were not rinsed with acid, so as to try and avoid the formation of large agglomerates by ball-milling the paste before doctor-blading the paste onto the FTO. It is evident from the CLSM measurements that the film quality of the SnO_2 composite films was rather low as compared to the films made of TiO_2 composites. The CLSM profile images of all prepared films show that the surface was rough, and partly exhibited a height of over 25 µm, while a thickness of 10 µm was aimed for. The CLSM images in Figure 6.2b) and f), especially, show the FTO that is not completely covered with the porous SnO_2 layer.

_____

Figure 6.2 CLSM profile images of electrode films of the first batch containing a) 0 wt%, b) 10 wt%, c) 20 wt%, d) 40 wt%, e) 60 wt%, and f) 80 wt% SnO$_2$ rods, respectively.

SEM images were made of the photo-anodes to characterize the electrode films and also to use a complementary technique in order to gain insight in a regime that is below the optical resolution. Nevertheless, the SEM overview images in Figure 6.3 confirm the observations made in the CLSM profile images. The films exhibit many, larger agglomerates of SnO$_2$ nanoparticles. Furthermore, the SEM image in Figure 6.3a) displays areas of bare FTO. All films exhibit cracks that can interrupt the electron conduction in the DSC. The reference photo-anode can be seen in Figure E3a). It appears as though the spherical SnO$_2$ nanoparticles agglomerated to an even higher extent than the nanorods, which resulted in a slightly improved film quality with an increasing nanorod content. The agglomerates in e) and f) were less in number and smaller in size as compared to the agglomerates observed in a).
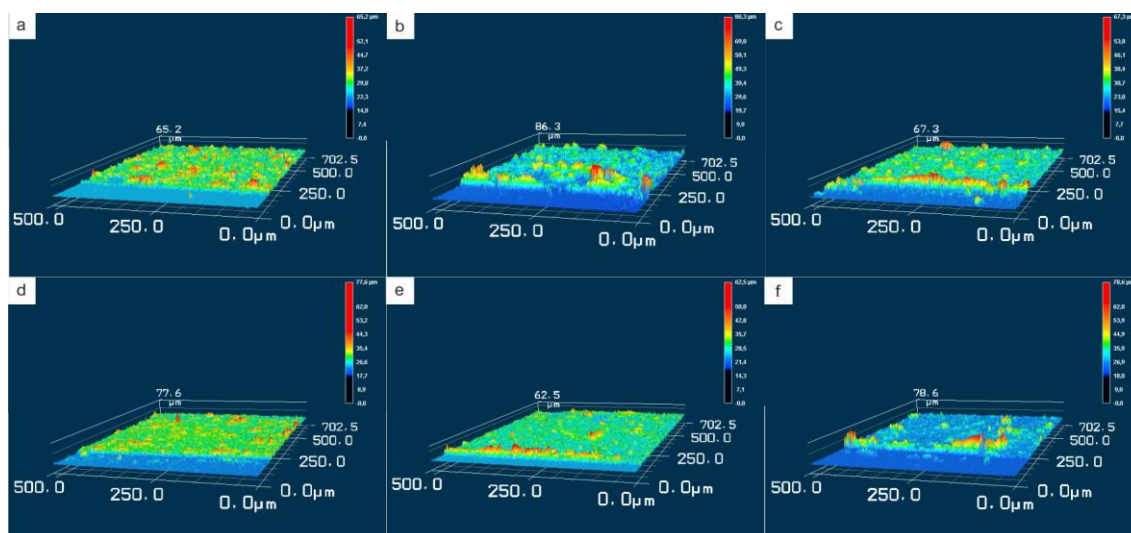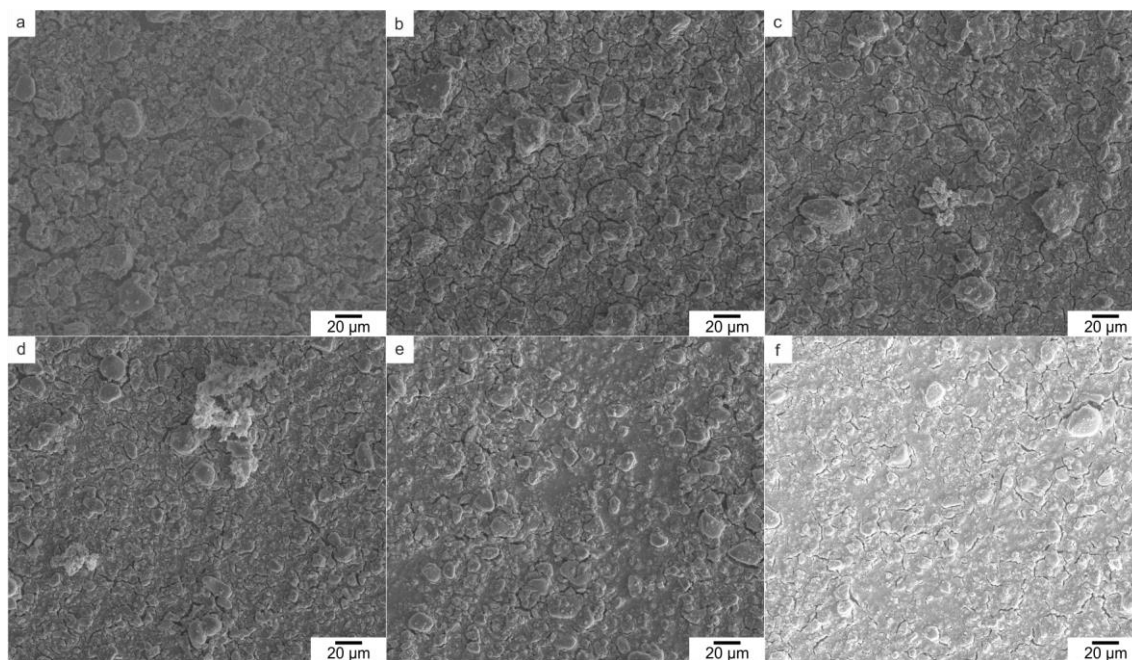
Figure 6.3 SEM overview images of electrode films of the first batch containing a) 0 wt%, b) 10 wt%, c) 20 wt%, d) 40 wt%, e) 60 wt%, and f) 80 wt% SnO_2 rods, respectively.

Subsequent to the characterization of the solar cells of the first presented batch, a second, more precise, and confined batch was synthesized to investigate the most beneficial nanorod content. The second batch contained photo-anodes made of 70 wt%, 80 wt%, 90 wt%, and 100 wt% SnO_2 nanorods. The nanorods, used in this set of electrodes were rinsed with sulfuric acid to ensure a replacement of sodium ions by protons. Figure 6.4 shows the CLSM profile images of the electrodes, while the one of the reference is displayed in the Appendix in Figure E2b). The rinsing step with acid had a beneficial effect on the homogeneity of the electrode films. The films were, especially when compared to Figure 6.2, rather smooth and only a few elevations on the surface were present. The elongated bump in c) is an artefact due to the sample preparation prior to the CLSM measurement. Additionally, no cracks through-out the whole film on the FTO were identified in the images. The film quality could be improved allover as compared to the first batch, with which the initial test was performed. Although the quality was enhanced by a large extent, it was still hardly comparable to the ones consisting of rutile sub-micron rods. The stronger tendency for SnO_2 to aggregate is probably caused by the lower isoelectric point IEP, which lies in a pH range between 4.5 and 5, the IEP for TiO_2 lies in the range around pH 6.[18]
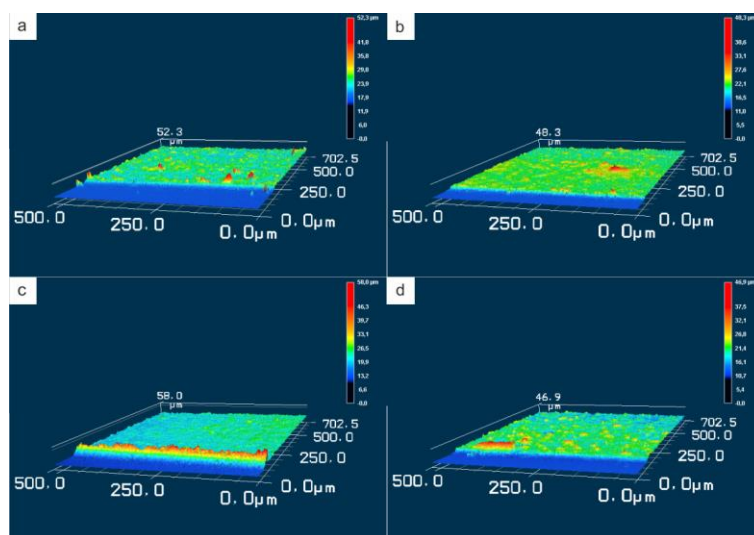
Figure 6.4 CLSM profile images of SnO₂ electrode films of the second batch containing a) 70 wt%, b) 80 wt%, c) 90 wt%, and d) 100 wt% SnO₂ rods, respectively.

For further confirmation of the high quality of the electrode films, SEM images were recorded. Figure 6.5 displays overview images of the reference a) and SnO₂ composite electrodes containing 70 wt% b), 80 wt% c), 90 wt% d), and 100 wt% e) nanorods. The image in f) represents a close-up of the sample containing 100 wt% SnO₂ nanorods. The reference had a homogeneous height without any agglomerates, while a few cracks were present, which was a common observation for the reference electrodes. In the sample containing 70 wt% nanorods a few cracks were also present, while in the samples containing a higher amount of nanorods, fewer to no cracks could be identified. This trend of inhibition of cracks when increasing the proportion of anisotropic structures was also made for TiO₂ rods as discussed in Chapter 5. Additionally, these samples confirmed the reduction of agglomerates with increasing nanorod content. The close-up image in f) makes the nanorods appear as if they were not stiff, but flexible and fiber-like. This is a common observation for all samples of this batch. The cause why some samples appeared flexible and fiber-like, while others were stiff and stick-like was beyond the scope of this work. Furthermore, the close-up image verifies the very smooth surface on the measured area. Other comparable samples also confirm the high quality of the electrode films as can be seen in the Appendix (Figure E4). In these samples, the SnO₂ rods appear rather stiff and stick-like. They were in-flexible and, therefore, formed larger voids in-between the particles, which would have been disadvantageous for the dye loading.
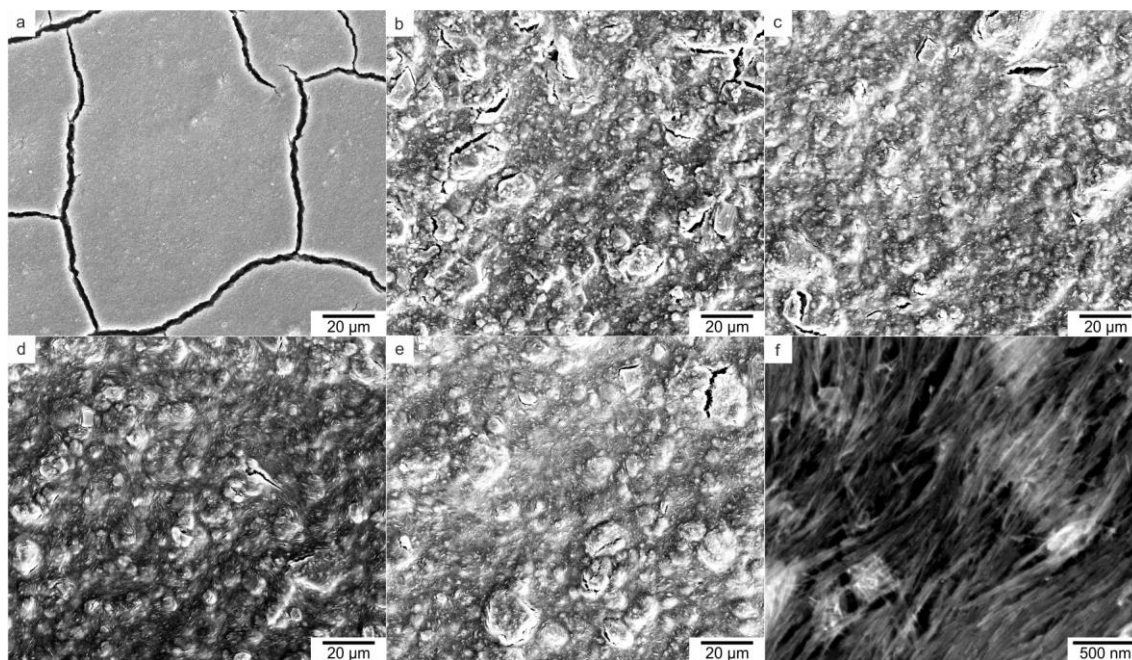
Figure 6.5 SEM overview images of electrode films of the reference (a) and SnO$_2$ composite electrode films containing b) 70 wt%, c) 80 wt%, d) 90 wt%, and e) 100 wt% SnO$_2$ rods, respectively. f) shows a close-up image of the sample containing 100 wt% rods.

The two discussed batches of electrode films were loaded with N719 and then assembled as a DSC. The solar cell characteristics and *J-V*-curves can be seen in Table 6.1 and Figure 6.6, respectively. It is clearly visible that the open circuit voltage in each batch differs only slightly, but from batch 1 to batch 2 an increase in V_{oc} of about 20 % was observed, which was probably due to the improved film quality. In the first batch, the short circuit current increases upon a rising nanorod content, while this trend reverses at 60 wt%, and the sample containing 80 wt% nanorods has again a lower J_{sc}. The fill factors were all below 40 %, which are rather low values. However, it has to be emphasized that the increasing nanorod content, which also improved the film quality, enhanced the fill factors. The efficiency of the composite films constantly roused upon increasing rods content. The obtained trend in efficiencies allowed the assumption that the optimum nanorod content lies beyond 80 wt%. The second batch of SnO$_2$ composite electrodes clearly indicated that an improved film quality leads to an enhancement of the V_{oc}. The trend in J_{sc} is rather unclear, as the sample containing 70 wt% nanorods exhibited the second highest J_{sc}. It can be stated that the peak J_{sc} was obtained with the sample containing only SnO$_2$ nanorods. The trends regarding the fill factor and efficiency coincided: the higher the nanorod content, the higher the resulting fill factor and efficiency. These findings also corroborate well with the trend of improved film quality of the initial photo-anodes. The obtained peak efficiency was 2.34 %, which is a medium value obtained for bare SnO$_2$ DSCs with using N719 as dye and I$^-$/I$_3^-$ as electrolyte redox couple.

Table 6.1 Solar cell characteristics determined from *J-V*-curves of different mixtures of composite DSCs. Samples labeled with [1] refer to Reference 1, while the ones with [2] belong to Reference 2. The solid line separates the two measured batches. The measurements were performed by ▮▮▮▮▮▮▮ and ▮▮▮▮▮▮▮.

Sample	V_{oc} / V	J_{sc} / mA/cm^2	FF / %	Mean η / %	Peak η / %
Reference 1	0.78	5.87	75.62	3.44	3.53
0 wt% rods[1]	0.34	6.35	30.56	0.65	0.65
10 wt% rods[1]	0.33	8.36	30.04	0.83	0.84
20 wt% rods[1]	0.34	8.53	31.60	0.91	0.91
40 wt% rods[1]	0.36	9.06	32.48	1.06	1.08
60 wt% rods[1]	0.36	9.90	31.97	1.13	1.14
80 wt% rods[1]	0.41	8.96	38.33	1.42	1.42
Reference 2	0.74	8.64	66.94	4.28	4.38
70 wt% rods[2]	0.41	9.74	46.00	1.83	1.84
80 wt% rods[2]	0.45	9.37	48.26	2.06	2.27
90 wt% rods[2]	0.44	9.67	48.20	2.07	2.30
100 wt% rods[2]	0.43	10.38	51.31	2.30	2.34

The *J-V*-curves of the two batches of SnO$_2$ composite photo-anodes can be seen in Figure 6.6. The reference in both cases is an electrode containing TiO$_2$-P25 and shows the obtained open circuit voltages for TiO$_2$ to always be significantly higher. It is a function of the potential difference between the redox potential of the electrolyte and the potential of the conduction band, rather than a function of the band-gap. The *J-V*-curves of the first batch in Figure 6.6a) have a round shape without a plateau, which indicates a high degree of losses. The deficiencies can be caused, for instance, by recombination, which is a very prominent pathway in DSCs made of SnO$_2$. It was already reported by various groups that recombination occurs in SnO$_2$ DSCs to a high extent.[12] Additionally, other causes for losses in these DSCs can be dead ends of the nanorods or poor connections to the FTO. *J-V*-curves of the second batch are displayed in Figure 6.6b). They exhibit a plateau and the shape comes closer to the one of a square-function as compared to the first batch. The obtained J_{sc} in both batches is significantly higher for the SnO$_2$ electrodes than for the TiO$_2$ reference, which is the major advantage of SnO$_2$ electrodes: they exhibit a faster electron conduction and, therefore, substantially higher currents can be obtained. On the other hand, the drawback of the usage of SnO$_2$ as electrode material is also indicated in this Figure, as the obtained V_{oc} is considerably lowered. A significant improvement of SnO$_2$ DSCs can actually only be realized by a modification of the electrode material such that the conduction band of the SnO$_2$ is not the demanding factor. The most promising way would be a tailor-made electrolyte and dye that ensures an adapted excited state for SnO$_2$ and an adjusted redox potential of the electrolyte, because, theoretically, SnO$_2$ can yield a higher V_{oc} than TiO$_2$ regarding their band-gaps.
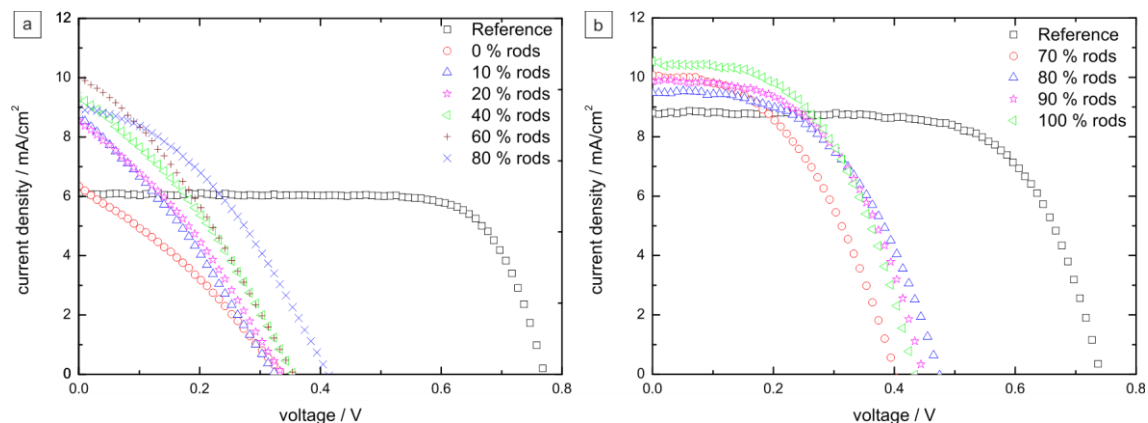
Figure 6.6 *J-V*-curves of SnO$_2$ composite electrodes containing different ratios of spherical particles and rods, while a) represents the measurements made in the first batch including Reference 1 and b) the measurements of the second with Reference 2. The measurements were performed by ███████████████ and ███████████████.

6.3 Electrodes of SnO$_2$ Nanorods and SnO$_2$@TiO$_2$ Hybrid Particles

6.3.1 Characterization of the Nanoparticles

The first part of this Chapter discussed the combination of materials that were already known in the literature, but have not been tested in combination as electrode materials in DSCs so far. The second part of this Chapter contains a more detailed investigation, as neither used particles nor their synthetic pathway were reported in literature, yet. The particles that were incorporated in electrodes for DSCs were SnO$_2$ nanorods and SnO$_2$@TiO$_2$ hybrid particles. The growth and characterization of SnO$_2$ via the acidic pathway were in particular described in Chapter 3, to mark the difference to the nanorods used in the first part of this Chapter they will be referred to acidic SnO$_2$ rods. Chapter 4 described a variety of different synthetic methods to yield hybrid particles with different morphology of the particles. The particles used for DSC characterization were hybrids synthesized following either the mild hydrothermal treatment at 0.5 bar as described in Chapter 4 or the synthesis performed in the high-boiling solvent tri-*n*-octylamine. The mentioned hybrid particles will in the following be referred to as *ex situ* hybrids and thick shell hybrids, respectively. Furthermore, the *in situ* formation of SnO$_2$@TiO$_2$ hybrid electrodes was tested for DSCs. Herein, SnO$_2$ nanoparticles were incorporated in a paste and TiCl$_4$ was added in form of a TiCl-treatment solution, which decomposes during the sintering process. They will be labeled as *in situ* hybrids.

The shape and size of the used particles is again depicted in Figure 6.7: a) shows the acidic SnO$_2$ nanorods, while b) displays the *ex situ* and c) and thick shell hybrids. The acidic SnO$_2$ nanorods had a length of about 50 - 80 nm with an aspect ratio of about 2 and were phase-pure cassiterite. The *ex situ* hybrids exhibited various lengths due to the synthetic processing, as many samples of SnO$_2$ nanorods had to be combined to serve as feed stock for the hybrid formation. By combining many batches of SnO$_2$ nanoparticles, it was ensured that the preformed nanorods for the second step were always identical.

Aside from the variation in their length, all particles were fully encapsulated with TiO$_2$ and no excessive TiO$_2$ was formed. This "shell" had a thickness of only a few nanometers and was amorphous. The amorphous shell also did not crystallize after a sintering step at 450 or 500 °C. The thick shell hybrids, synthesized by thermal decomposition of the metal-organic Ti^{4+} precursor TAD, had the same size variations of the preformed SnO$_2$ nanorods, as the same method was applied. The "shell" was formed rather in-homogeneously and exhibited a thickness of up to 100 nm. Furthermore, excessive TiO$_2$ without encapsulated SnO$_2$ nanorods was formed. The "shell" was poorly crystalline directly after the synthesis, and only traces of anatase were realizable, while after the sintering process of the DSCs it was phase-pure anatase.
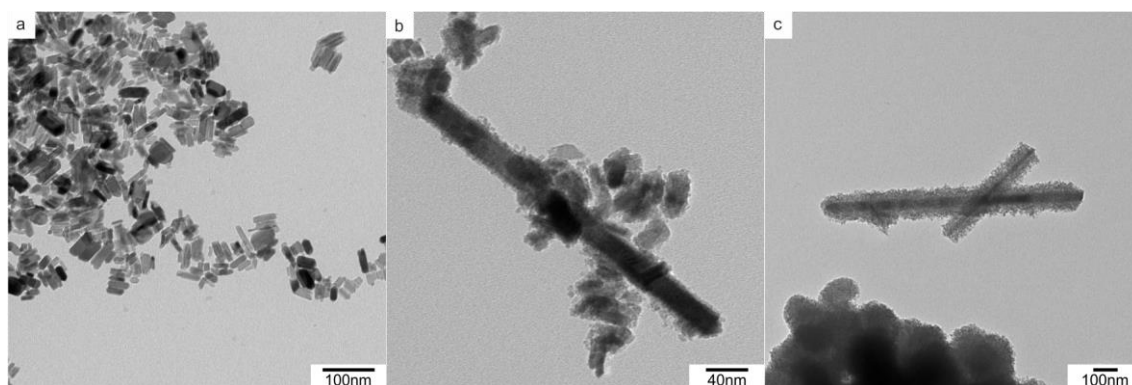
Figure 6.7 TEM images of particles used for tailor-made electrodes in the following part of the Chapter: a) acidic SnO$_2$ nanorods, b) SnO$_2$@TiO$_2$ hybrids prepared by mild hydrothermal treatment at 0.5 bar using preformed rods and TiCl$_4$, and c) SnO$_2$@TiO$_2$ made in tri-*n*-octylamine with TAD as precursor.

The available surface area of the particles is crucial for the later dye adsorption. The surface area of the particles were determined by measuring the N$_2$ adsorption to the surface at constant temperature using the Brunauer-Emmett-Teller method. The surface area of the acidic SnO$_2$ rods was determined to be 38.2 m²/g, which was an intermediate value between the rutile sub-micron rods and the TiO$_2$-P25 particles obtained in Chapter 5. By modification of the acidic SnO$_2$ rods to *ex situ* SnO$_2$@TiO$_2$ hybrids, the surface area was increased to 78.8 m²/g. The increase in surface area of more than 100 % was surprising and is expected to be beneficial for the dye loading of the DSC, which will determine the number of generated electrons and the flowing current.

Table 6.2 Surface area acidic SnO$_2$ rods and *ex situ* SnO$_2$@TiO$_2$ hybrids determined by BET isotherms. The measurements were conducted by ▮▮▮▮▮▮▮▮.

Sample	BET surface area / m²/g
acidic SnO$_2$ rods	38.2
***ex situ* SnO$_2$@TiO$_2$ hybrids**	78.8

The obtained V_{oc} in the DSC is also dependent on the size of the band-gap, which was calculated by measuring diffuse reflectance UV-Vis spectra of the powders. From the obtained spectra, the

_____

Kubelka-Munk plots were calculated.[19] The band-gap is represented by the intersection of the fit in the linear regime with the x-axis. The measured UV-Vis spectra and calculated Kubelka-Munk plots can be seen in Figure 6.8. The band-gaps were 3.58 eV for acidic SnO_2 rods and 3.22 eV for *ex situ* $SnO_2@TiO_2$ hybrids, respectively. These results show that it was possible to modify the band-gap of the particles, while the character of the TiO_2 "shell" was dominant and the band-gap was narrowed to the value measured for anatase nanoparticles in Chapter 5. To compare the values for SnO_2 and the hybrids, it should be mentioned again that the determined band-gaps of rutile and anatase were 3.15 eV and 3.22 eV. Theoretically, a higher open circuit voltage could be obtained by using SnO_2. However, for a given dye and electrolyte system, the band-gap is not the determining factor, but the absolute position of the conduction band. The absolute position of the conduction band can only be measured using a reference electrode, most commonly the standard hydrogen electrode (SHE).
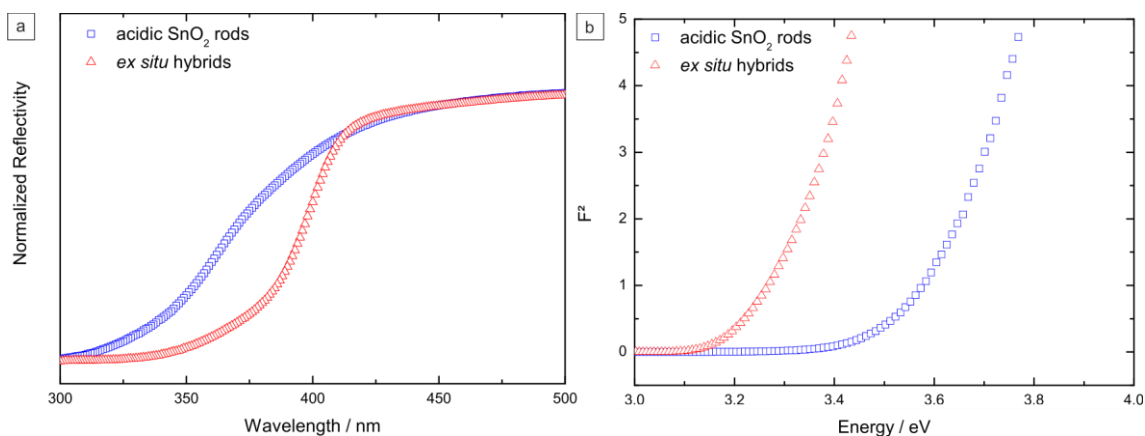
Figure 6.8 UV-Vis spectra of acidic SnO_2 rods and *ex situ* $SnO_2@TiO_2$ hybrids a) and the calculated Kubelka-Munk plot b). In the Kubelka-Munk plot is the Kubelka-Munk function for a direct band transition (F^2) plotted against the energy of the used light.

6.3.2 Electrode Films

The two discussed particle types, as well as the thick shell $SnO_2@TiO_2$ hybrids were incorporated into pastes, doctor-bladed onto FTO, and sintered to form electrode films. Additionally, acidic SnO_2 nanoparticles were mixed together with an aqueous solution of $TiCl_4$ in a paste and sintered to form a thin electrode film of *in situ* $SnO_2@TiO_2$ hybrid particles. To determine the thickness of the films and evaluate their quality on an optical scale, CLSM profile images were made and can be seen in Figure 6.9, and the reference is displayed in the Appendix (Figure E2c)). The electrode films containing the acidic SnO_2 rods (a) and the *ex situ* $SnO_2@TiO_2$ hybrids (d) formed a flat and homogeneous surface, while the one with the hybrid particles was of even better quality. On both images, a few minor elevations can be seen. On the contrary, the films formed by the thick shell $SnO_2@TiO_2$ hybrids b) and *in situ* hybrids (c) exhibited a rather low quality as compared to the two other films. The film made of the thick shell hybrids consisted of small patches and not a continuous film. The FTO substrate was still visible in-between individual patches. This is an extreme example for cracks, because the ratio between

_____

patches and cracks was low, meaning a large area was wasted in the later solar cell and electron conduction was not possible at the edge of the cracks anymore. Furthermore, the patches were small, which strengthens the last mentioned disadvantage. As a last disadvantage, the film thickness also differed between the patches. Thus the over-all film quality was low. The *in situ* hybrids c) also formed films containing defects, but had a higher quality than the ones with thick shell hybrids. The films also had large cracks due to the high amount of liquid compounds in the paste, leaving voids upon evaporation. It should also be mentioned that usually high amounts of anisotropic structures in the electrode films facilitated the electrodes to not have any cracks, because they form a network that prevents the electrode to develop cracks during the sintering step. Although the only solid ingredient was rod-shaped, cracks formed due to the drastically increased amount of liquid ingredients when TiCl$_4$ was added. This problem could be overcome upon further optimization of the paste formulation. Beneficial for this kind of hybrid particles as compared to the thick shell hybrids was that the formed patches were larger and more homogeneous, which enables better electron conduction.
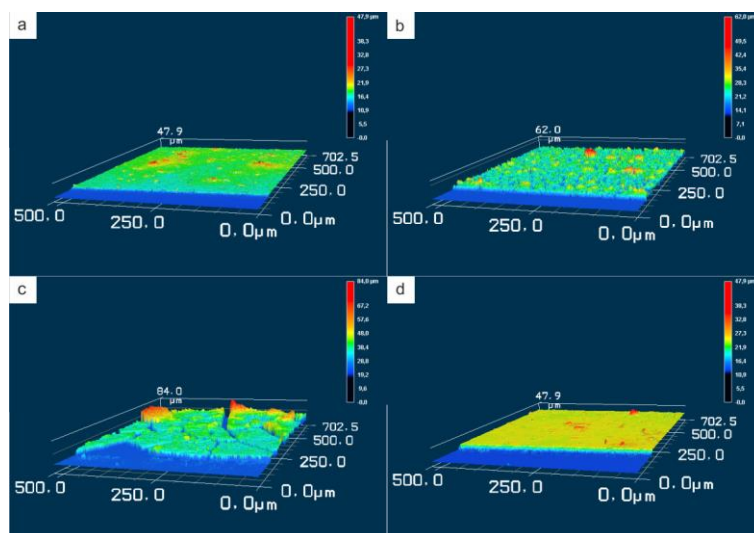
Figure 6.9 CLSM profile images of photo-anodes containing different particles: a) acidic SnO$_2$ rods, b) thick shell SnO$_2$@TiO$_2$ hybrids, c) *in situ* SnO$_2$@TiO$_2$ hybrids, and d) *ex situ* SnO$_2$@TiO$_2$ hybrids, respectively.

To confirm the results from CLSM measurements, SEM images were also taken of all the electrodes, as displayed in the overview images in Figure 6.10. The SEM measurements affirmed the CLSM profile measurements. The films of the acidic SnO$_2$ rods (a) and the *ex situ* hybrids (d) had a high quality: they showed only a few, little elevations, were completely free of cracks for the *ex situ* hybrids, and had only small cracks that do not reach the FTO for the acidic SnO$_2$ nanorods. The low film quality of the thick shell hybrids b) could also be demonstrated in the SEM image, as lots of small patches were present and the FTO is clearly visible in-between. The SEM image of the electrode containing the *in situ* hybrids also confirmed the CLSM measurements, as large patches with deep cracks that reach the FTO were formed. On the contrary, there was also an effect that was not observable in the CLSM measurements: the elevated brightness of the edges of the patches in the image in Figure 6.10c) is a

result of sample charging that occurred due to a lack of possibility to get the charges in the sample released to the instrument. This is an effect observed in samples that are poor electric conductors or lack of electric pathways to release the inserted charges that emerge as a consequence of the measurement. This phenomenon can be observed on every edge of cracks, but is best visualized in the image of the *in situ* SnO$_2$@TiO$_2$ hybrids. This observation depicts the problem that occurs later on in the DSC very well.

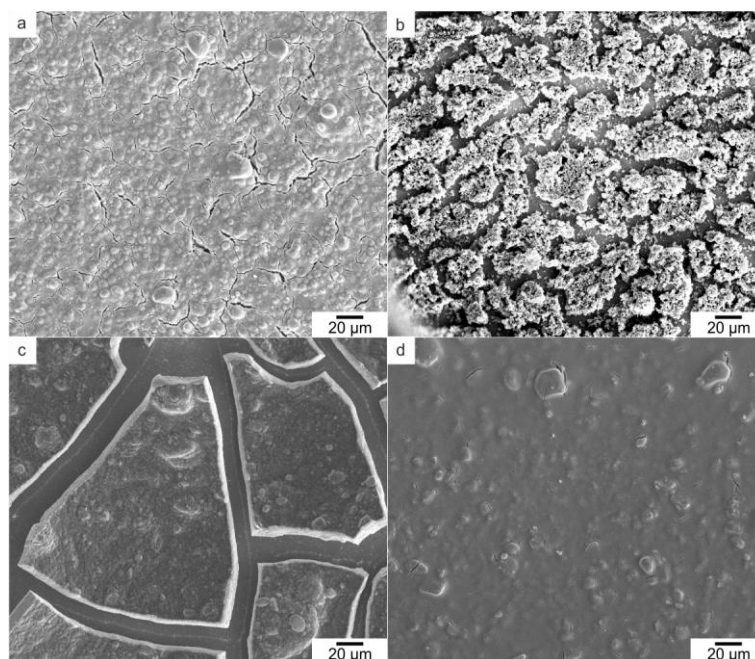Figure 6.10 SEM overview images of electrode films containing a) acidic SnO$_2$ rods, b) thick shell SnO$_2$@TiO$_2$ hybrids, c) *in situ* SnO$_2$@TiO$_2$ hybrids, and d) *ex situ* SnO$_2$@TiO$_2$ hybrids, respectively.

6.3.3 Dye-Sensitized Solar Cells: Characterization of Electrode Films

The electrode films were functionalized with N719, assembled with a counter-electrode and incubated with the electrolyte containing the redox couple I$^-$/I$_3^-$, and the *J-V*-curves measured. The solar cell characteristics can be seen in Table 6.3. The dye loading was calculated from measured absorbance spectra and can be seen in Table 6.4. The measured *J-V*-curves are displayed in Figure 6.11. The electrodes were again measured in two iterations. In the first batch, the thick shell hybrids were characterized, the reference DSCs were in both cases again made of TiO$_2$-P25. For the thick shell hybrids, it can be seen that the V_{oc} reached about the value of the reference, while the J_{sc} was significantly lower. The elevated V_{oc} as compared to bare SnO$_2$ was expected due to the higher absolute position of the conduction band. Furthermore, a higher J_{sc} was expected, as a combination of the properties of the materials was presumed. The J_{sc} value is also determined by the conduction velocity of the electrode material. SnO$_2$ as "core" material was expected to act as the electron conductor resulting in an elevated J_{sc}. Nevertheless, there are two possible reasons why the obtained J_{sc} was significantly lower: (i) the dye loading, as can be seen in Table 6.4, was very low as compared to the reference, and (ii) the electrons

were trapped in the "core" material SnO$_2$ due to its lower conduction band edge. Electrons were generated at the dye-TiO$_2$ interface and injected into the "core" of the hybrid particles, due to the lower conduction band of the SnO$_2$. The "shell" of the hybrids was too thick to enable the electrons to exit the SnO$_2$ rod and, therefore, the trapped electrons were unable to contribute to the J_{sc} anymore.

The obtained fill factors of the thick shell hybrids were determined to be 70.5 %, which is an unexpectedly high value considering the low quality of the electrode films. The high value of the fill factor demonstrates that only low amounts of losses in the electrode occurred, which could also be a result of the encapsulation. In this case, the injection of electrons into the SnO$_2$ rods would ensure that the free electrons do not have any direct contact with the electrolyte or the dye and, therefore, no possibility for recombination. On the contrary, the fill factor is not significantly higher than in every other TiO$_2$-based DSC. Since TiO$_2$ is the "shell" material, it determines the recombination behavior. In the second batch, a reference, the acidic SnO$_2$ rods, and the *in* and *ex situ* hybrids were characterized. The V_{oc} of the *in* and *ex situ* hybrids was significantly lower than the one of the thick shell hybrids, while it was elevated by 10 % as compared to the bare SnO$_2$ electrodes in the first part of this Chapter. These observations can be attributed to a too high TiO$_2$ content in the thick shell hybrids to enable conduction through the SnO$_2$ "core" of the particles. In the *in* and *ex situ* hybrids, the SnO$_2$ "core" was the dominant material and, therefore, the electron conduction can occur through the SnO$_2$ "core". Thereby, determines the maximum extractable potential. The obtained J_{sc} of the *in situ* hybrids was significantly lower than the one of the *ex situ* hybrids, although the dye loading was slightly higher. This can again only be explained by a trapping effect in the hybrid material. The fill factors were 64.3 % and 58.7 %, respectively, which shows the DSCs to be of a medium to high quality. The peak efficiencies were determined to be 1.33 % and 2.23 %. The acidic SnO$_2$ rods were tested in 100 wt% nanorod electrodes as a novel particle system. The obtained V_{oc} was unexpectedly low with 0.28 V, while the peak V_{oc} in the composite electrode tests was 0.45 V. This can only be attributed to losses by recombination or defects in the device, while a comprehensive investigation was not yet possible, and, therefore, a statement with certainty is not possible. The J_{sc} is very high with 10.10 mA/cm² as it is usually observed for SnO$_2$, due to the lower conduction band as compared to TiO$_2$ and the enhanced electron injection, as well as the increased electron diffusion and lifetime. The fill factors were rather low with 34.0 %, which is a result of losses caused by recombination at the SnO$_2$-dye and SnO$_2$-electrolyte interfaces. The peak efficiency was measured to be 0.97 %, which is caused by the low V_{oc} and fill factor. It should be noted that the SnO$_2$ particles used in the acidic SnO$_2$ rods, *in* and *ex situ* hybrids electrodes all originated from the same batch of SnO$_2$ nanoparticles. Although the novel synthesized SnO$_2$ rods did not match the high expectations in the assembled DSCs, a significant improvement of the DSC efficiency with these SnO$_2$ nanoparticles could be obtained by encapsulation of the nanorods with TiO$_2$. The improvement of efficiency was for the *in situ* hybrid formation 37 % and for the *ex situ* formation 130 %, regarding the acidic SnO$_2$ nanorods.

Table 6.3 Solar cell characteristics determined from *J-V*-curves for different electrode materials. Samples labeled with [2] belong to Reference 2, while samples marked with [3] belong to Reference 3. The measurements were performed ███████

Sample	V_{oc} / V	J_{sc} / mA/cm²	FF / %	Mean η / %	Peak η / %
Reference 2	0.74	8.64	66.94	4.28	4.38
thick shell hybrids[2]	0.72	3.17	70.54	1.62	1.64
Reference 3	0.75	5.61	72.91	3.04	3.25
acidic SnO₂ rods[3]	0.28	10.10	33.96	0.95	0.97
in situ hybrids[3]	0.48	2.93	64.27	0.92	1.33
ex situ hybrids[3]	0.49	7.70	58.71	2.22	2.23

The dye loading of the electrodes was determined by UV-Vis spectroscopy and can be seen in Table 6.4. In the first batch, the dye loading of the thick shell hybrids was considerably lower than for the reference cell. The decreased amount of dye could reasonably explain the lower obtained J_{sc}. On the contrary, such a low dye loading was not expected, since the "shell" of the thick shell hybrids appeared highly porous. However, the pores could have molten together during the sintering process, and, therefore, decreased the available surface. An investigation on this was not possible due to the low resolution in SEM measurements. In the second batch, the dye loading of both the hybrid particle classes was nearly the same, with a difference of less than 10 %, while the J_{sc} of the *ex situ* hybrids was more than twice as high as the one of the *in situ* hybrids. As already described, the lower J_{sc} was assumed to originate from trapping effects. The acidic SnO₂ rods showed by far the highest dye loading of all measured samples. This fact easily explains the high J_{sc} of the bare SnO₂ electrodes, while it is assumed that the high electron diffusion coefficients contribute as well. It should be further considered that the surface area of the *ex situ* hybrids was twice as high as the acidic SnO₂ rods. Thus, the high dye loading amount has to be due to a better anchoring of the dye to the SnO₂ surface. It is usually reported that a lower dye loading is observed using SnO₂ electrodes, and, therefore, SnO₂ is meant to be disadvantageous.[11,12] Previous reports from our group also stated that SnO₂ nanorods with an even higher surface area of 51 m²/g did not exceed a dye loading of 0.09 mmol/cm³.[8] This difference might be explained by the synthetic procedure of the SnO₂ nanorods: all previously known SnO₂ nanorods tested in DSCs were synthesized in basic medium using either NaOH, NH₄OH, or a combination of NH₄OH and NH₄Cl. Basic solutions desorb the dye again from the surface of the semiconductor, which is also used to determine the dye loading. When traces of Na⁺ remain on the surface of the nanorods or nanoparticles in general, a basic solution can form during the dye loading procedure, such that a lower amount of dye is adsorbed to the surface. This behavior does not occur when the particles react in a slightly acidic manner.

Table 6.4 Amount of adsorbed dye per volume unit determined by UV-Vis spectroscopy. Samples labeled with [2] belong to Reference 2, while samples marked with [3] belong to Reference 3.

Sample	Dye-Loading / mmol/cm³
Reference 2	0.1770
thick shell hybrids[2]	0.0583
Reference 3	0.0807
acidic SnO$_2$ rods[3]	0.2400
in situ hybrids[3]	0.1430
ex situ hybrids[3]	0.1330

The obtained *J-V*-curves can be seen in Figure 6.11. Concerning the obtained open circuit voltages, three modifications of materials to determine the V_{oc} showed different dominant behaviors for the components (i) TiO$_2$, (ii) SnO$_2$, and (iii) an intermediate of SnO$_2$ and TiO$_2$. The thick shell hybrids and the reference show a V_{oc} slightly above 0.7 V, while the acidic SnO$_2$ rods DSCs have a V_{oc} below 0.3 V, and the *in* as well as *ex situ* hybrids exhibit a V_{oc} of about 0.5 V. All DSCs, except for the acidic SnO$_2$ rods, exhibit a plateau, while the curve of the acidic SnO$_2$ rods immediately has a negative slope when applying a voltage, which demonstrates a high amount of losses due to recombination and resistances. The obtained short circuit currents scatter from about 3 to 10 mA/cm², while the low values for the thick shell and *in situ* hybrids were assumed to originate from a trapping mechanism of electrons in the DSC. The increase in J_{sc} for the *ex situ* hybrids concerning the reference was expected due to an enhanced electron conduction and a lower number of recombinations in the electrode, while also the higher dye adsorption contributed to these findings. The high J_{sc} of the acidic SnO$_2$ rods was already discussed, as it is a finding due to the high electron diffusion coefficient and the dye adsorption.
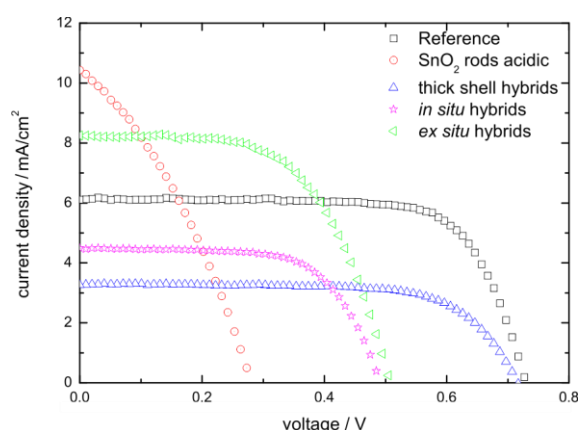

Figure 6.11 *J-V*-curves measured from DSCs made out of different photo-anodes. The shown reference sample is Reference 3, while Reference 2 is not displayed for a clearer arrangement. The measurements were performed by ▮▮▮▮▮▮▮▮▮▮▮.

6.3.4 Electrochemical Characterization

For further electrochemical characterization, we chose samples of the reference, the acidic SnO$_2$ rods, and the *ex situ* SnO$_2$@TiO$_2$ hybrids, as they showed the highest efficiencies and most promising results. Thereby, we measured the quantum efficiency, the charge extraction at a given voltage, as well

as the electron diffusion coefficients and lifetime (Figure 6.12). The measured incident-photon-to-current-conversion-efficiency (IPCE, a)), showed the expected trend for the three samples regarding the dye loading and the J_{sc} values. The peak IPCE for the reference was rather low with about 30 %, while the peak for the *ex situ* hybrids was 40 %. The acidic SnO_2 rods showed efficiencies of up to 70 %. This high IPCE is also a function of the absolute position of the conduction band. The higher the conduction band, the fewer excited states of the dye that fit the pre-condition to inject electrons into the semiconductor, and vice versa. Inferentially, it is possible to increase the number of generated electrons by decreasing the conduction band. The charge extraction at a given voltage b) is also reasonable concerning the V_{oc}. The extracted charges for SnO_2 were rather high at low voltages, which demonstrates that the conduction band has a low position in the redox system of the DSC. At the same time, the reference showed fewer extracted charges at higher voltages, because the dye adsorption and charge generation is lower and the conduction band has a higher energy. As previously discussed, the hybrids have an intermediate position as already discussed previously due to their combined properties. The electron lifetimes of the acidic SnO_2 rods and the *ex situ* hybrids were both higher than obtained for the reference cell (c). In Chapter 5, it was possible to draw a comparison between the morphologies due to the same materials used. Here, it is only possible to say that SnO_2 nanorods and $SnO_2@TiO_2$ hybrid particles are valuable in improving the electron lifetime as compared to the spherical TiO_2 nanoparticles in the reference. Thus, it cannot be stated with certainty, whether this improvement originates from the different composition or from the morphology of the particles. The analogue observation and information can be drawn from the diffusion coefficient measurements in d). The usage of SnO_2 raised the electron diffusion coefficients significantly as compared to the reference, which is most probably caused by the materials' change and the intrinsically higher electron diffusion coefficient of SnO_2. The diffusion coefficient of the *ex situ* hybrid particles was slightly lower than the reference and, therefore, did not contribute to the improvement of the J_{sc}.

At this point, a further advantage should be mentioned: long-term stability of SnO_2-based DSCs. The time between the measurement of the *J-V*-curves and the electrochemical analysis was one week. After the electrochemical characterization, *J-V*-characteristics were measured again. The *J-V*-characteristics can be seen in the Appendix in Table E1. The DSC efficiency dropped in all cases, which is caused by the instability of the dye, as only J_{sc} changes. It is remarkable that the alteration of efficiency of SnO_2-based DSCs was as low as 5 %, while the change of TiO_2-based DSCs was determined to be ca 25 %. Degradation is commonly observed for all electrode materials, probably due to a splitting of the -SCN groups in N719 and replacement by I^-. Another possible pathway could be the de-anchoring from the surface and dissolution in the electrolyte.[20–22] It is reported that N719 in combination with TiO_2 suffers from severe oxidative degradation, while the impact of degradation is rather small when SnO_2 is used as the electrode material.[8]
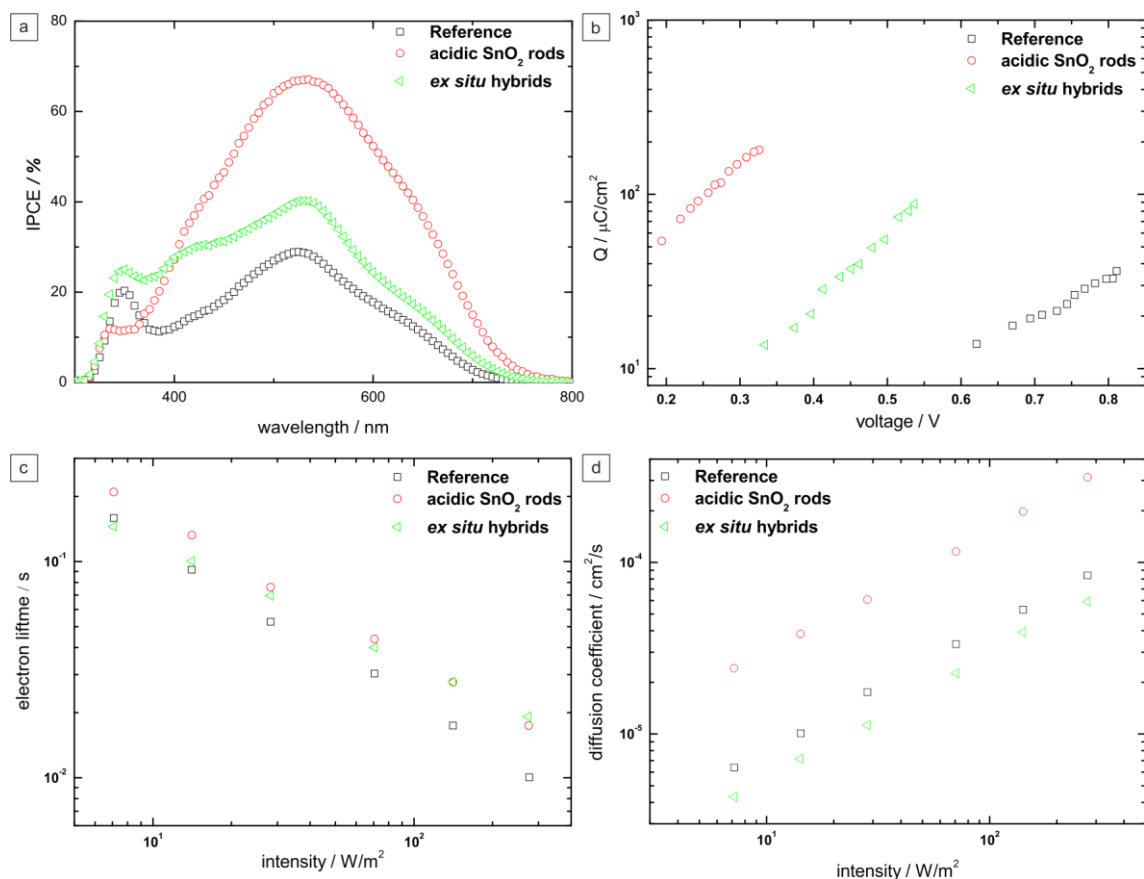
Figure 6.12 Electrochemical analysis of the DSCs Reference 3, acidic SnO$_2$ rods, and *ex situ* SnO$_2$@TiO$_2$ hybrids: a) quantum efficiency, b) charge extraction at a given voltage, c) electron lifetime determined by IMVS, and d) electron diffusion coefficient determined by IMPS. The measurements were performed by ████████████

6.4 Conclusion

This Chapter addressed the use of SnO$_2$ nanoparticles as electrode material for dye-sensitized solar cells DSCs. The general possibility to use SnO$_2$ particles for DSCs was already demonstrated by various other groups, while, herein, two new aspects were discussed. In the first part, the application of composite electrode materials containing anisotropic and isotropic particles was tested, and the most beneficial content of anisotropic structures was determined. The second part dealt with the application of SnO$_2$ particles, which were synthesized following a novel protocol, as well as various SnO$_2$@TiO$_2$ hybrid structures.

In order to determine whether the DSC efficiency could be improved by a combination of anisotropic and isotropic particles, the particles were mixed in various ratios and incorporated into photo-anodes. It could be shown that the optimal content of anisotropic nanostructures was 100 wt%, while in this study the obtained V_{oc} did not change significantly. The J_{sc} was the efficiency determining factor, since the obtained fill factors were also comparable. The treatment of the particles prior to the electrode formation was altered and showed that an acidic washing step of the nanoparticles

was beneficial for the quality of the electrode films, as the fill factor increased from about 32 % to 48 % in average.

The second part focused on the DSC characterization of novel SnO_2 nanoparticles and $SnO_2@TiO_2$ hybrid particles. It could be shown that acidic SnO_2 rods and *ex situ* $SnO_2@TiO_2$ hybrid particles formed high quality electrode films, while the quality of the thick shell and *in situ* hybrid particle electrode films were lower. A comprehensive investigation including the measurement of *J-V*-curves, dye loadings, as well as band-gaps, and electrochemical analysis led to the assumption that the encapsulation of SnO_2 nanorods was beneficial overall as compared to the bare, acidic SnO_2 nanorods. The efficiency was increased from 0.97 % to 2.23 %, which is an improvement of 130 %. Additionally, the electrochemical analysis revealed that the acidic SnO_2 nanorods have astonishingly high quantum efficiency, electron lifetime, and electron diffusion coefficients. Thus, the fill factor and the V_{oc} were the determining factors contributing to a low overall efficiency of the DSCs containing SnO_2 nanorods. The encapsulation of acidic SnO_2 nanorods with TiO_2 increased V_{oc} and fill factor, while a decreased J_{sc} was obtained. The quantum efficiency and the electron lifetime were lower than for bare, acidic SnO_2 rods but still higher as compared to the reference. The electron extraction could be shifted to higher extraction voltages due to a higher conduction band. In conclusion, it could be demonstrated that the encapsulation was advantageous for the efficiency of the solar cells, while the behavior was intermediate in-between bare TiO_2-P25 and bare SnO_2 as found in this study.

Further improvements of SnO_2-based DSCs could be obtained in a two-step procedure: first, preparation of the SnO_2 electrodes on FTO substrates, and, second, formation of hybrids by mild hydrothermal treatment. Using this method could help to overcome problems due to electron trapping. Additionally, the coating layer could be altered from TiO_2 to ZnO, which should have an even higher conduction band edge and lower recombination rates. Herein, it would be interesting to compare the two techniques: (i) to assemble electrodes from already formed hybrids and (ii) to first assemble a SnO_2 electrode and, subsequently, with ZnO.

6.5 Experimental Section

6.5.1 Synthesis

Materials. All materials were used as received without further purification. Pentanol (~98 %) was provided by Roth. Urea (p.A.) and Triton-X-100™ were purchased from Acros Organics. All other materials were used as stated in the previous Chapters.

The procedure to synthesize SnO_2 nanorods by an acidic route can be found in Chapter 3. The method to prepare SnO_2 nanorods using basic reaction conditions and $SnO_2@TiO_2$ hybrid particles was described in Chapter 4.

_____

Spherical SnO₂ particles. 6.7 g CTAB and 0.64 g urea were dissolved in 125 hexane and 15 mL pentanol under vigorous stirring in a teflon inlay of a stainless steel autoclave. To this mixture, 10 mL of a 0.5 M solution of $SnCl_4 \cdot 5H_2O$ in water was added leading to a transparent solution. The teflon inlay was transferred into a stainless steel autoclave and heated at 130 °C for 12 h. Subsequent to the passive cooling down, the reaction mixture was transferred into centrifuge tubes and the solid product was collected by centrifugation at 9000 rpm for 10 min. The remaining solid was rinsed with water and, afterwards, ethanol, and centrifuged several times until no foam formed by shaking. The product was dried overnight at 80 °C.[15]

Paste preparation. 0.5 mL ethanol, 16 drops PEG400, and 4 drops Triton-x-100 were added to 300 mg particles (SnO₂ nanorods, mixtures of nanorods and spherical particles, or hybrid particles). If *in situ* hybrids were prepared, 8 drops of a TiCl-treatment solution were added to the mixture containing SnO₂ nanorods. This mixture was either treated with a ball-mill for 45 min or ultrasonicated for 60 min subsequent to 15 min stirring. To this mixture, 2 drops of a solution containing 5.5 g in 5 mL water was added and stirred for another 15 min. When *in situ* hybrids were prepared, the number of added drops was increased to 5. The paste was afterwards ground manually for 3 - 5 min to ensure the paste to be homogeneous and to adjust the viscosity.

Device preparation. The FTO substrates were cleaned with iso-propanol, water and detergent, and acetone. Then, a 0.1 M solution of BuSnCl₃ in ethanol was either applied via spin-coating at 1500 rpm for 30 s and, subsequently sintered at 450 °C, or via spray-pyrolysis directly onto the FTOs, which were heated at 400 °C using a hotplate. The paste was applied onto the as-prepared FTO substrates via doctor-blading. The resulting films were first dried at 100 °C for 1 h and then sintered at 450 °C for 30 min. The dye-loading was performed subsequent to the sintering step by soaking the electrode films in a solution containing 28.5 mg N719 in a mixture of acetonitrile and *tert*-butanol (1:1 by volume) at 30 °C for at least 15 h.

6.5.2 Characterization

All used characterization methods are listed in Chapter 5.

6.6 References

1   H. J. Snaith and C. Ducati, *Nano Lett.*, 2010, **10**, 1259–1265.
2   P. Tiwana, P. Docampo, M. B. Johnston, H. J. Snaith and L. M. Herz, *ACS Nano*, 2011, **5**, 5158–5166.
3   A. Hagfeldt, G. Boschloo, L. Sun, L. Kloo and H. Pettersson, *Chem. Rev.*, 2010, **110**, 6595–6663.
4   C.-H. Chen, K.-C. Chen and J.-L. He, *Current Applied Physics*, 2010, **10**, S176.
5   I. Gonzalez-Valls and M. Lira-Cantu, *Energy Environ. Sci.*, 2008, **2**, 19.
6   Q. Zhang, C. S. Dandeneau, X. Zhou and G. Cao, *Adv. Mater.*, 2009, **21**, 4087–4108.
7   A. Birkel, N. Loges, E. Mugnaioli, R. Branscheid, D. Koll, S. Frank, M. Panthöfer and W. Tremel, *Langmuir*, 2010, **26**, 3590–3595.
8   A. Birkel, Johannes Gutenberg-Universität Mainz, 2012.

9   A. Green, E. Palomares, S. Haque, J. Kroon and J. Durrant, *J. Phys. Chem. B*, 2005, **109**, 12525–12533.

10   A. J. Frank, N. Kopidakis and Lagemaat, Jao van de, *Coord. Chem. Rev.*, 2004, **248**, 1165–1179.

11   A. Kay and M. Grätzel, *Chem. Mater.*, 2002, **14**, 2930–2935.

12   Green, Alex N. M., E. Palomares, S. A. Haque, J. M. Kroon and J. R. Durrant, *J. Phys. Chem. B*, 2005, **109**, 12525–12533.

13   C.-C. Chen, H.-W. Chung, C.-H. Chen, H.-P. Lu, C.-M. Lan, S.-F. Chen, L. Luo, C.-S. Hung and E. W.-G. Diau, *J. Phys. Chem. C*, 2008, **112**, 19151–19157.

14   D. Koll, Johannes Gutenberg-Universität Mainz, 2011.

15   D. Chen and L. Gao, *J Colloid Interface Sci.*, 2004, **279**, 137–142.

16   B. Tan and Y. Wu, *J Phys Chem B*, 2006, **110**, 15932–15938.

17   K. Pan, Y. Dong, C. Tian, W. Zhou, G. Tian, B. Zhao and H. Fu, *Electrochim. Acta*, 2009, **54**, 7350–7356.

18   G. A. Parks and De Bruyn, P. L., *J. Phys. Chem.*, 1962, 967–973.

19   S. Valencia, J. Miguel and G. Restrepo, *Open Mater. Sci. Journal*, 2010, 9–14.

20   A. Hinsch, J. Kroon, R. Kern, I. Uhlendorf, J. Holzbock, A. Meyer and J. Ferber, *Prog. Photovolt. Res. Appl.*, 2001, 425–438.

21   N. Kato, Y. Takeda, K. Higuchi, A. Takeichi, E. Sudo, H. Tanaka, T. Motohiro, T. Sano and T. Toyoda, *Sol. Energy Mater. Sol. Cells*, 2009, **93**, 893–897.

22   H. Tanaka, A. Takeichi, K. Higuchi, T. Motohiro, M. Takata, N. Hirota, J. Nakajima and T. Toyoda, *Sol. Energy Mater. Sol. Cells*, 2009, **93**, 1143–1148.

7

Conclusion and Outlook

The aim of the work presented in this study was the development and characterization of novel 1D semiconductor structures in the nano and sub-micron regime and their the application as electrode materials in dye-sensitized solar cells. The focus was on the investigation of the growth mechanism of TiO_2 sub-micron rods, SnO_2 nanorods, as well as hybrid particles containing a SnO_2 "core" and a TiO_2 "shell". In the second part of this study, the comprehensively characterized particles were incorporated into photo-anodes of DSCs and characterized by the means of photovoltaic efficiency.

In **Chapter 2**, the growth of TiO_2 sub-micron rods starting from fumed titania was established. The particles could be synthesized in a fast and facile microwave-assisted hydrothermal method in high yields of up to 5 g. They were characterized by PXRD, Raman spectroscopy, TEM, and DLS. The crystallographic data revealed the particles to be phase-pure rutile, while only minor impurities of 3.5 wt% anatase were present. Furthermore, the combination of PXRD, TEM, as well as SAED confirmed the particles to be single-crystalline. The particles grew starting from solid state precursors in combination with HCl as a mineralizing agent. Here, the HCl facilitated the precursor to dissolve and recrystallize again, which was suggested to be a chemical-transport reaction. The change of the acid concentration enabled a control over the length of the 1D particles: higher concentrations led to an increased dissolution velocity and, thus, longer rods, while lower acid concentrations yielded shorter rods. The acid could be exchanged with HBr and HI, which also led to a growth of sub-micron rods. In contrast, simulating 6 M HCl by the use of NaCl with H_2SO_4 or HNO_3 did not conduct rodgrowth, which was ascribed to the distinct surface-adhesion properties of SO_4^{2-} and NO_3^-. The exchange of precursors in combination with 6 M HCl revealed that the growth only occurred when starting from an instable precursor, no matter if they were in the solid or liquid state. A growth starting from micron-sized particles was never observed. The method used for the crystal growth was a microwave-assisted hydrothermal treatment, which enabled the possibility to take snapshots that revealed that the growth of rods already occurred in the very first minutes of the reaction. The precursor was continuously being depleted. In a common synthesis, yielding 500 mg product, the depletion process is continued after 90 min. Although no precursor was present after 90 min, the particles changed further. A secondary growth

_____

step occurred, in which the formed rods aligned next to each other along the c-axis and merged together. This secondary growth led to particles that were larger in width and, in some cases, had check-mark-like or trapezium-like shapes. Cube-like particles could be observed as well. In an initial test, the particles were found to be photo-catalytically active, as they decompose Rhodamin B under UV-illumination. Further photo-catalytic tests upon their halo-peroxidase and anti-bacterial activity are currently being performed and show promising first results.

Chapter 3 demonstrated that the growth of TiO_2 rods could be transferred to other rutile-structured compounds such as SnO_2 and GeO_2. For SnO_2 nanorods, a growth starting from $SnCl_4 \cdot 5H_2O$ using 0.6 M HCl was established. The particles were also characterized by means of PXRD, DLS, and TEM. X-ray diffraction showed the particles to be phase-pure cassiterite and that the variation of reaction temperature enhanced control over the crystallite size, which was demonstrated for temperatures between 200 and 240 °C. Low temperatures led to small crystallites and, thus, broad reflection profiles. The determined crystallite sizes and the measured particle sizes in TEM correlate very well and indicated single-crystalline particles, which was clearly confirmed by SAED. DLS showed that the formed nanorods were dispersible in DMSO and strongly aggregated in solution, which led to a larger obtainable hydrodynamic radius. Upon increasing the reaction time, a secondary growth step was also found as mentioned for TiO_2. In analogy to the result in Chapter 2, it was possible to facilitate HBr and HI as mineralizing agents. Furthermore, the transfer to grow SnO_2 nanorods starting from spherical SnO_2 nanoparticles was possible. This enabled us to describe this reaction as a disintegration-recrystallization process in the form of a chemical transport reaction. By addition of Ph_4PCl, it was possible to trap the intermediate species of the disintegration-recrystallization process. The precipitated species was analyzed by ^{119}Sn ssNMR spectroscopy, Raman spectroscopy, and PXRD. The intermediate ^{119}Sn species was characterized to be $[SnCl_5H_2O]^-$, although a second, chemically similar species, was present, which was most likely $[SnCl_5]^-$. The combined results of all three methods indicated that these two species were responsible for the decomposition and the growth of SnO_2 nanorods. The SnO_2 nanorods are currently under investigation for their suitability to serve as electrode material for Li-ion batteries as well as for their application in antibacterial and catalytically active coatings. In an Excursus, it was briefly described that a growth of GeO_2 sub-micron rods, using the analogous route of a chemical transport, was possible. Herein, $GeCl_4$ was facilitated to yield argutite sub-micron rods by a hydrothermal reaction. GeO_2 shows similar behavior to SnO_2 in forming rutile-type rods, but also to SiO_2 showing a strong tendency to form hexagonally formed crystals, which led to low reproducibility, due to strong side-phases that evolve upon thermal treatment.

Chapter 4 described the path of modifying 1D single-component materials to gain 1D multi-component hybrid particles consisting of SnO_2 and TiO_2, as well as rutile and anatase-phase TiO_2. These particular combinations of materials are interesting due to the different intrinsic properties of SnO_2 and

TiO_2. SnO_2 profits from high electron diffusion coefficients and good conductivity, but exhibits a low conduction band edge and a high degree of losses due to recombination. In contrast, TiO_2 exhibits a high conduction band edge, which is even higher for anatase than for rutile, but is afflicted with low electron conduction velocity. A plethora of methods was tested and evaluated upon the demands of a full coverage of the primary "core" particles, a low formation of excessive TiO_2 "shell" material, an equal distribution of "core and "shell", as well as the technical parameters of high reproducibility and yield. By doing so, $SnO_2@TiO_2$ hybrid particles as well as $TiO_2@TiO_2$ hybrid particles were established via a hydrothermal treatment of preformed 1D particles that served as the "core" and a solution of $TiCl_4$ that decomposed to form a TiO_2 "shell". The "shell" formed completely and enclosed the rods, while barely to no excessive TiO_2 was found. This method allowed for an upscaling of the synthesis and exhibited a high reproducibility.

The application of TiO_2 sub-micron rods as electrode material for DSCs was tested in comparison to TiO_2 particles of distinct size, shape, and crystalline structure in **Chapter 5**. At first, the particles that were synthesized in Chapter 2 and Chapter 4 were characterized regarding their surface areas and band-gaps using BET measurements and UV-Vis diffuse reflectance spectra. This revealed the hybrid formation to be advantageous due to an increased surface area, but in contrast to the expectations, the band-gap remained unaltered. Next, composite electrodes were prepared by doctor-blading using different particles. The obtained films were characterized using CLSM and SEM measurements, which confirmed the resulting electrodes to be of high-quality. The DSCs were characterized by determining the amount of adsorbed dye, *J-V*-curves, and electrochemical analysis. It revealed that, regarding the efficiency, a proportion of 20 wt% rutile sub-micron rods in the electrode had the most beneficial effect, with the remaining 80 wt% being anatase nanoparticles. The J_{sc} could be improved by 40 % as compared to the reference, while simultaneously enhancing the efficiency by 25 %. Furthermore, the samples containing 10 wt% rutile rods increased the obtained efficiency by 20 %, which was caused by an improved J_{sc} of 34 %. The use of $TiO_2@TiO_2$ hybrid particles did not have a significant effect on the *J-V*-characteristics. The electrochemical characterization of the reference, the composite DSCs containing 10 and 20 wt% rutile rods, and a DSC containing hybrid particles, revealed that all modifications improved the quantum efficiency regarding the reference DSC. Further improvements, such as a higher electron diffusion coefficient and an enhanced charge extraction were most prominent for the sample containing 10 wt% rutile sub-micron rods. In a short **Excursus,** the application of TiO_2 sub-micron rods in solid state perovskite-solar cells was evaluated. Herein, $CH_3NH_3PbI_3$ was used as light-harvester and Spiro-OMeTAD, an organic hole conduction material, as solid state electrolyte. It could be shown that the efficiency of the sample exhibited an efficiency of 0.9 %, with the reference cell having an efficiency of 2.1 %. Surprisingly, the obtained V_{oc} was very high, for rutile sub-micron rods as compared to the anatase nanoparticles in the Dyesol® paste. That was an unexpected outcome, since the conduction band edge of rutile is lower than the one of anatase.

_____

Chapter 6 described the incorporation of SnO_2 nanoparticles as electrode material in DSCs, while this analysis was divided into two parts: first, the evaluation of possible composite electrode materials starting from materials that are known in literature, and, second, the test of novel nanostructures such as acidic SnO_2 rods and $SnO_2@TiO_2$ hybrid particles. The employed composite electrodes had a lower quality as compared to TiO_2 electrodes, which was a common observation for all electrodes made of SnO_2. The efficiency of the solar cell was demonstrated to improve systematically upon increasing the rods content and when a composite of spherical and anisotropic nanoparticles in various ratios was used. The variations in V_{oc} and the fill factor were rather small, such that the change in efficiency was caused by the systematic improvement of J_{sc}. This effect can be correlated to a reduced amount of trap sites when more rods were incorporated in the electrodes. The highest efficiency was found for the sample containing 100 wt% rods. In the second part, the acidic SnO_2 rods and $SnO_2@TiO_2$ hybrid particles were characterized by BET measurements and UV-Vis diffuse reflectance spectroscopy. Additionally after incorporation into electrode films the *J-V*-characteristics were determined. The hybrid formation could not only be determined by large surface area twice as large as the bare SnO_2 particles, but can also clearly be traced in the determination of the band-gaps. The hybrid particles had smaller band-gaps, as TiO_2 was the dominant light-absorbing material. The formed electrodes out of SnO_2 rods and hybrid particles were of high-quality. The hybrid particles themselves were synthesized following different approaches, while the quality of the electrodes containing the respective hybrid particles varied depending on the method. The solar cell characteristics revealed the acidic SnO_2 rods to exhibit an efficiency of 0.97 %, while the hybrid formation using a mild hydrothermal treatment was most beneficial and improved the efficiency of up to 2.23 %. Regarding the solar cell characteristics of the acidic SnO_2 nanorods as compared to the reference, it was possible to improve the flowing current while the V_{oc} and fill factor decreased. All these changes can be attributed to the modification of the electrode material from TiO_2 to SnO_2. The employed hybrid materials showed characteristics in between those of SnO_2 and TiO_2. Taking the electrochemical analysis into account, all the measured parameters fit well to the observed *J-V*-characteristics. The quantum efficiency of both the SnO_2 particles and the hybrids was improved compared to the reference. The charge extraction was shifted to lower voltages, which explains the lower V_{oc}. The electron lifetime was slightly improved, and the electron diffusion coefficient was significantly increased for the SnO_2 nanoparticles.

Future work on solar cells should focus on further optimization of the developed particles toward solid state perovskite solar cells as compared to DSCs, since they exhibit the most promising potential concerning high efficiencies and long-term stability, as well as the possibility of finding industrial scale applications. Herein, an evaluation would be needed of developed materials using the commonly used perovskite $CH_3NH_3PbI_3$. For the SnO_2 electrodes, further steps are needed to perform the covering step with TiO_2 as a second subsequent step to the formation of the electrode, as SnO_2 as pure electrode material is a less promising candidate for solid state devices. The synthesis of the perovskite itself has

improved tremendously, and emphasis should be drawn to the purity of the material. Additionally, the development of perovskites that are free of heavy metals and can, therefore, be considered as non-toxic should also be a focus.

Further characterization concerning the obtained particles should focus on their suitability for other fields such as batteries or catalytic surfaces, while a few of these tests are currently already being performed.

Further characterization concerning the rutile sub-micron rods should focus on their suitability for other fields of applications. For example, do they show a certain photo-catalytic activity, which will be evaluated further by testing halo-peroxidase activity and their anti-bacterial properties. If these are confirmed, the particles could end up as a suitable material to improve ship paints. Additionally, self-cleaning surfaces can be prepared from such particles and they might also be suitable as electrode materials for Li-ion batteries.

The most common application that SnO_2 is used for in research is due to its gas-sensing properties. This is a possible application that should be evaluated further. Additionally, the tests about suitability for Li-ion batteries are already being performed. Furthermore, SnO_2 is also known to act as an anti-bacterial coating, which is also a topic of ongoing evaluation.

The synthetic approach to hybrid particles for both $SnO_2@TiO_2$ and $TiO_2@TiO_2$ using the surfactant-mediated growth should be further investigated using DMSO as a solvent for the primary particles. Further experiments on this approach could yield hybrid particles with outstanding control over the degree and thickness of encapsulation.

_____

8

Appendix A

Table A1 Diffraction and modeling parameters related to Figure 2.1 for the reactions 0 - 90 min and Figure A1 for the precursor TiO_2-P25.

	0 min reaction	15 min reaction	90 min reaction	Degussa P25
Diffractometer	Siemens D5000, Braun M50			
Sample preparation	Fine powder fixed between two stripes of Scotch™ tape			
Measuring mode	Transmission			
Wavelength / Å	1.540596			
Measuring range	$10 \leq 2\Theta /° \leq 90$; $0.71 \leq Q /Å^{-1} \leq 5.77$			
Refinement range	$17 \leq 2\Theta /° \leq 85$; $1.20 \leq Q /Å^{-1} \leq 5.51$			
Temperature / K	298			
Profile fit	Rietveld refinement according to reported crystal structure models			
Background	Chebyshev			
Profile function	Fundamental Parameters Approach, crystallite size anisotropy modeled in quadratic correction			
Program	TOPAS Academic V5			
Total No. of parameters / Background	27 / 15	27 / 15	27 / 15	26 / 15
R_{exp}	1.05	1.15	1.23	1.04
R_{wp}	1.45	1.87	1.71	1.65
GoF	1.38	1.62	1.39	1.59
DW	1.08	0.84	1.23	0.82
$TiO_2 – tP6$				
Space group	$P4_2/mnm$			
Cell parameters / Å	a = 4.592(2) c = 2.957(2)	a = 4.600(1) c = 2.962(1)	a = 4.591(1) c = 2.956(1)	a = 4.5984(4) c = 2.9611(4)
Crystallite size / nm	84(1) by 111(4)	90(1) by 135(4)	112(1) by 221(6)	70(2)
Fraction / %wt	36(1)	60(2)	96.5(5)	12.7(6)
Biso	2.6(1)	3.1(2)	1.9(2)	2.1(1)
$TiO_2 – tI12$				
Space group	$I4_1/amd$			
Cell parameters / Å	a = 3.785(2) c = 9.505(7)	a = 3.790(2) c = 9.52(1)	a = 3.783(6) c = 9.504(3)	a = 3.7891(2) c = 9.5150(5)
Crystallite size / nm	49(1)	54(1)	196(45)	41(1)
Fraction / %wt	64(1)	40(2)	3.5(5)	87.3(6)
Biso	2.6(1)	3.1(2)	1.9(2)	2.1(1)

_____
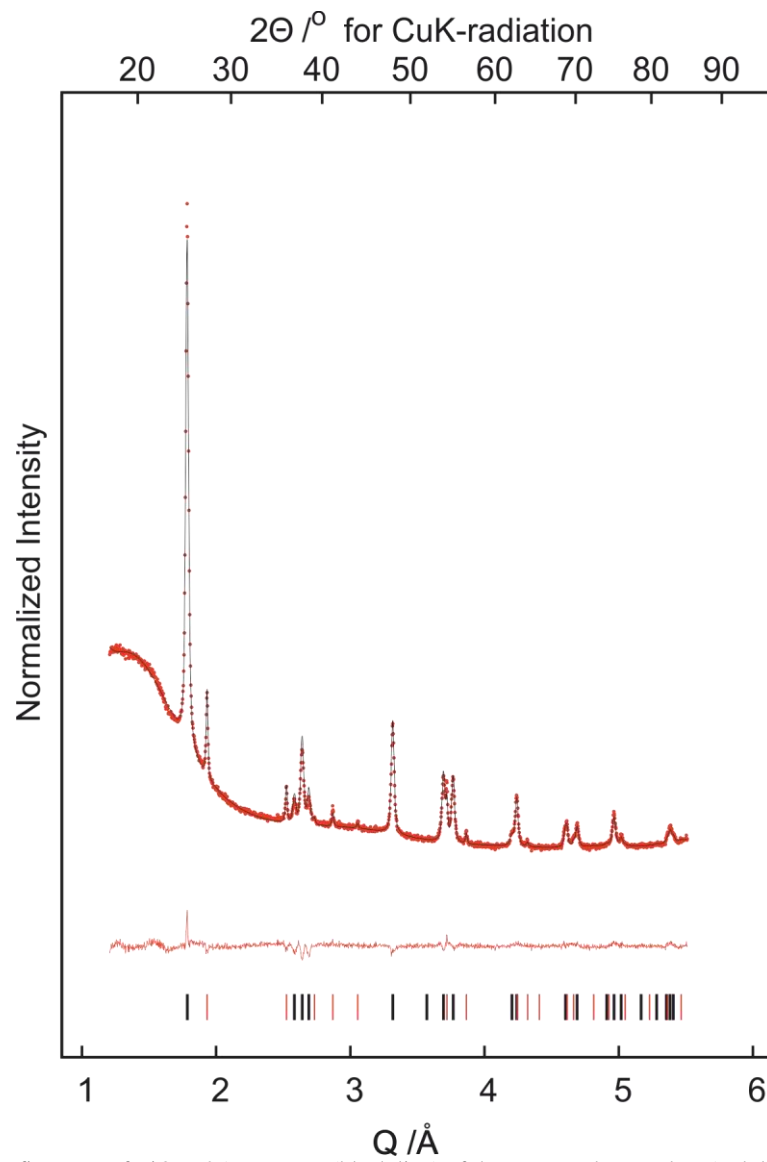
Figure A1 Rietveld refinement of TiO$_2$-P25 precursor (black line) of the measured XRD data (red dots) and residuum (red line). Black ticks indicate the reference reflex positions of anatase and the red ticks indicate those of rutile. The data treatment was performed by ▮▮▮▮▮▮▮▮▮▮▮.
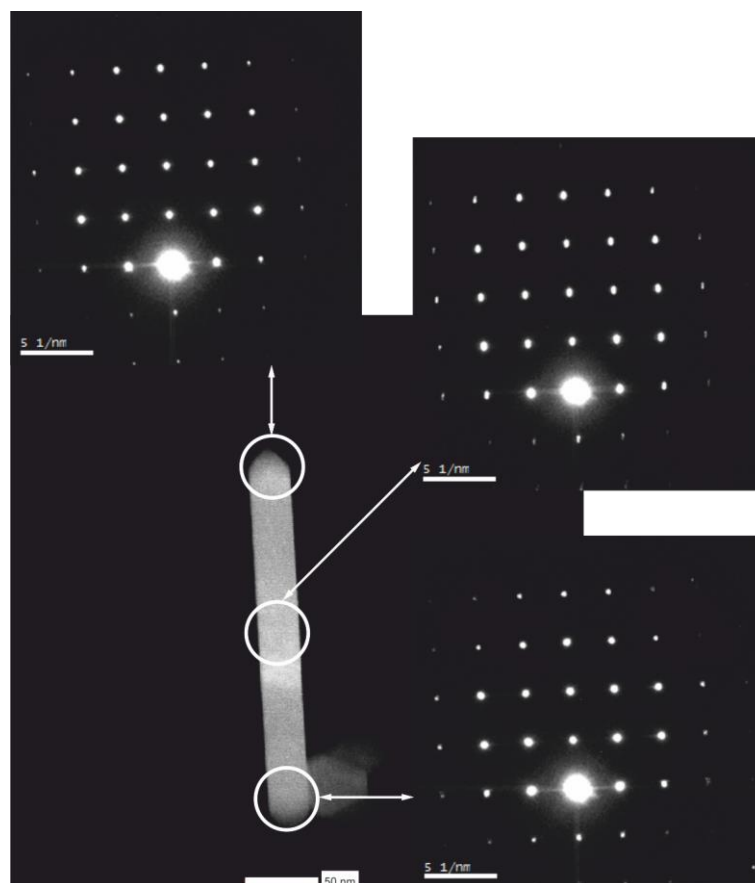
Figure A2 HAADF TEM image of a single sub-micron TiO₂ rod with nano-electron diffraction patterns of both tips and the shaft. The measurement was conducted by ███████████.
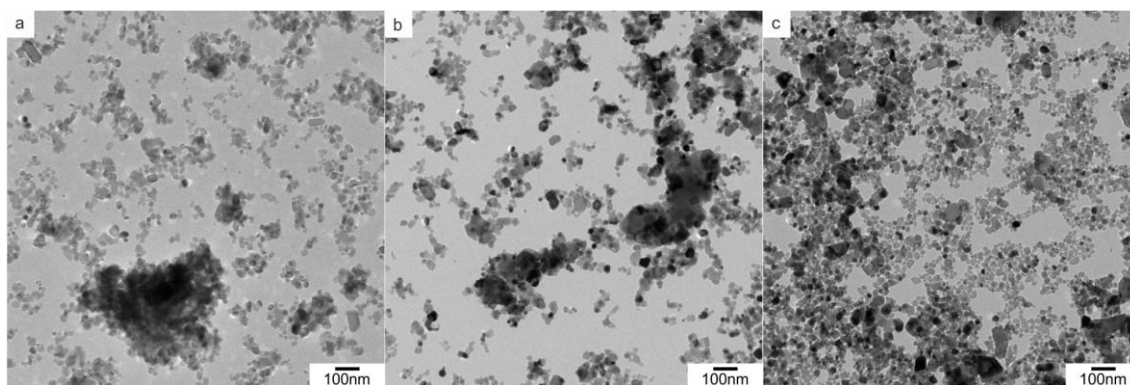

Figure A3 TEM images of varied ramping times and reaction pressures. In a) and b) the goal pressure remained at 30 bar, while the ramping times were changed to 7 min and 5 min, respectively. In c) the aim pressure to be reached after the standard ramping time of 10 min was set to 20 bar.
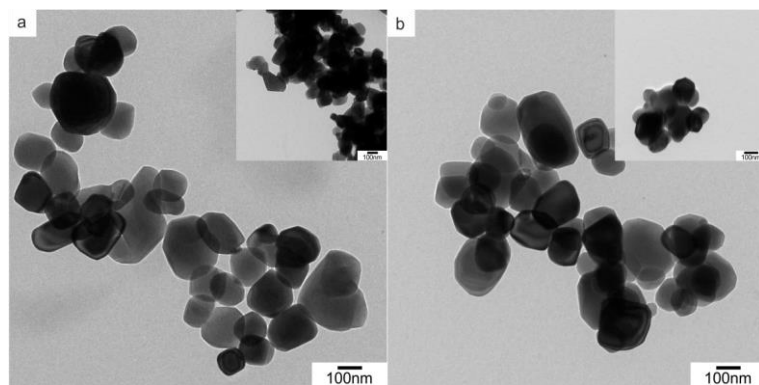
Figure A4 TEM images of the products after hydrothermal treatment when phase pure bulk precursors (inset) of rutile (a) and anatase (b) were employed
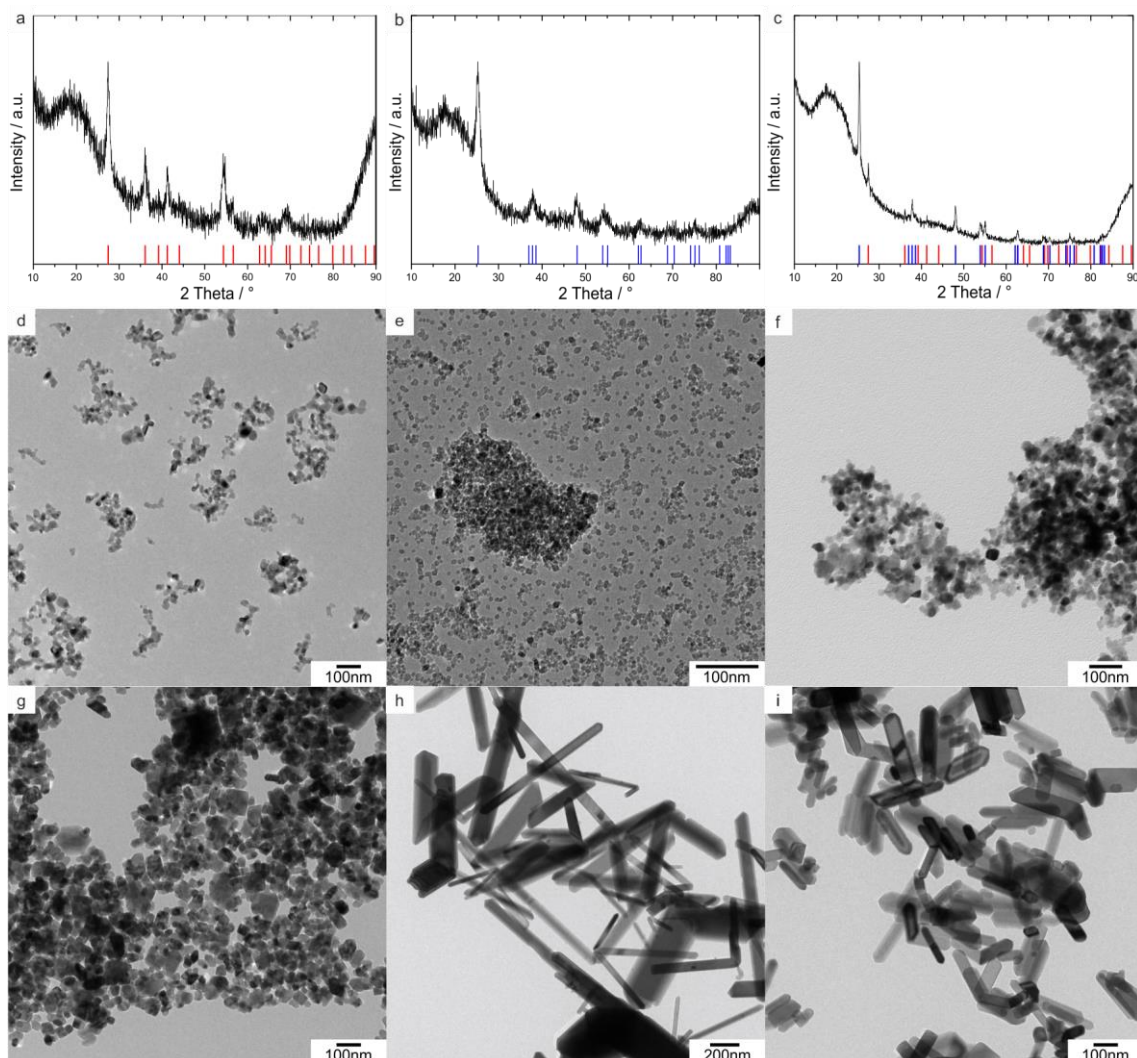
Figure A5 TEM images and XRD patterns of different solid precursors and the resulting product after hydrothermal treatment: a) XRD pattern of the rutile precursor nanomaterial depicted in the TEM image in d), g) shows the product after the hydrothermal treatment; b) and e) show the anatase precursor (XRD pattern and TEM image) with the resulting product in h); c) and f) display XRD pattern and TEM image of the commonly used TiO_2-P25 powder with the obtained sub-micron rods in i). In a) - c) the black line represents the measured PXRD data, with the red ticks showing the reference reflex positions for rutile (JCPDS 96-900-7532), and the blue ticks the reference reflex positions for anatase (JCPDS 96-900-9087).
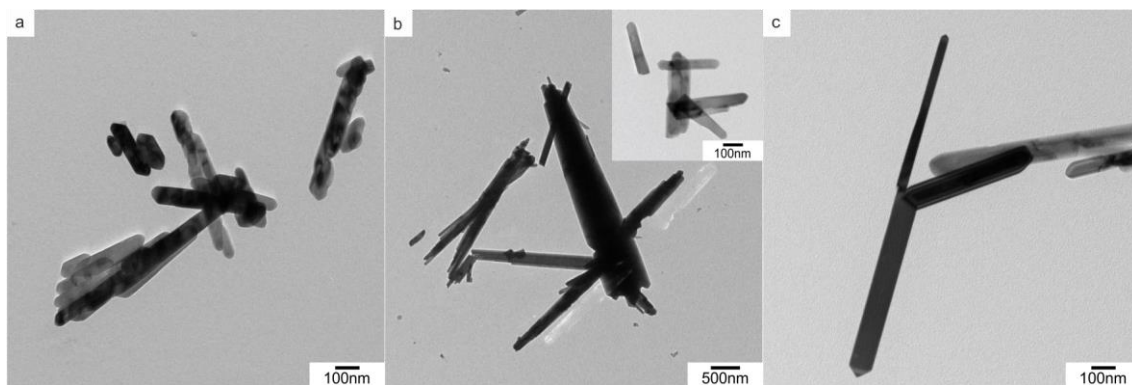
Figure A6 TEM images of TiO$_2$ rods obtained when molecular precursors were used. In a) TAD was used as precursor, b) and c) display the rods obtained when TiCl$_4$ was used as precursor. Here, the size variation was very large as can be seen from b) and the inset. In c) the HCl concentration was decreased in comparison to b).

Table B1 Measurement and refinement parameter of the X-ray data in Figure 3.3

	Figure 3.3a	**Figure 3.3b**	**Figure 3.3c**
Reaction temperature	240 °C	220 °C	200 °C
Diffractometer	Siemens D5000, Braun M50		
Sample preparation	Fine powder fixed between two stripes of Scotch™ tape		
Measuring mode	Transmission		
Wavelength / Å	1.540596		
Measuring range	$10 \leq 2\Theta /° \leq 90$; $0.71 \leq Q /Å^{-1} \leq 5.77$		
Refinement range	$15 \leq 2\Theta /° \leq 75$; $1.06 \leq Q /Å^{-1} \leq 4.95$		
Temperature / K	298		
Profile fit	Rietveld refinement according to reported crystal structure models		
Background	Chebyshev		
Profile function	Fundamental parameters approach, crystallite size anisotropy modeled in quadratic correction		
Program	TOPAS Academic V5		
Total No. of parameters / Background	23 / 15	23 / 15	23 / 15
R_{wp}	2.84	4.20	4.00
GoF	1.90	2.82	2.77
DW	0.65	0.28	0.27
$SnO_2 - tP6$			
Space group	$P4_2/mnm$		
Cell parameters / Å	a = 4.740(7) c = 3.186(5)	a = 4.744(3) c = 3.185(2)	a = 4.764(9) c = 3.186(6)
Crystallite size / nm	33(1) by 67(1)	14(1) by 32(1)	6(1) by 14(1)
Biso	0.5(1)	0.5(1)	0.5(1)
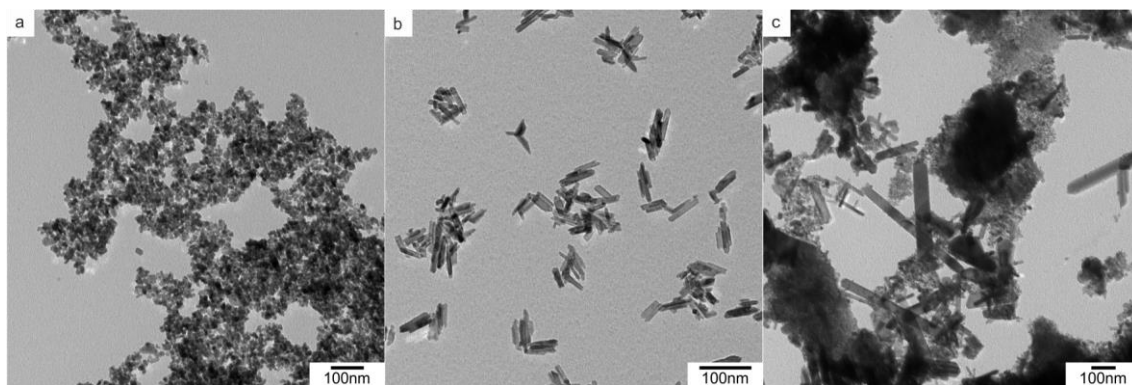
Figure B1 TEM images of SnO$_2$ nanoparticles obtained from hydrothermal treatments at 220 °C for 12 h using different reaction mixtures: a) SnCl$_4$·5H$_2$O + H$_2$O, b) SnCl$_4$·5H$_2$O + HCl, and c) SnI$_4$ + HI.
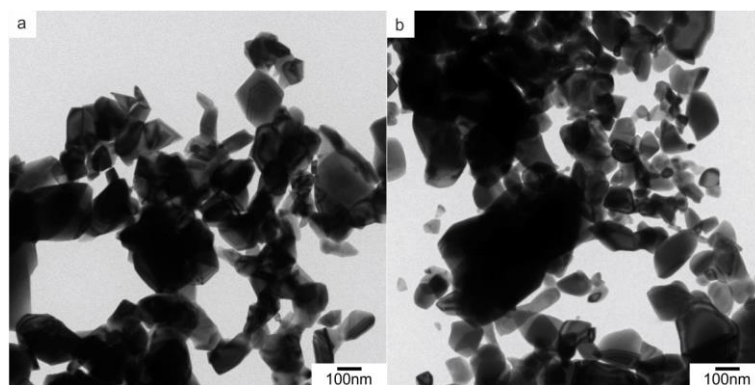
Figure B2 TEM images of SnO$_2$ precursor (a) and product after a hydrothermal treatment at 220 °C for 12 h using HCl and bulk SnO$_2$ as precursor (b).
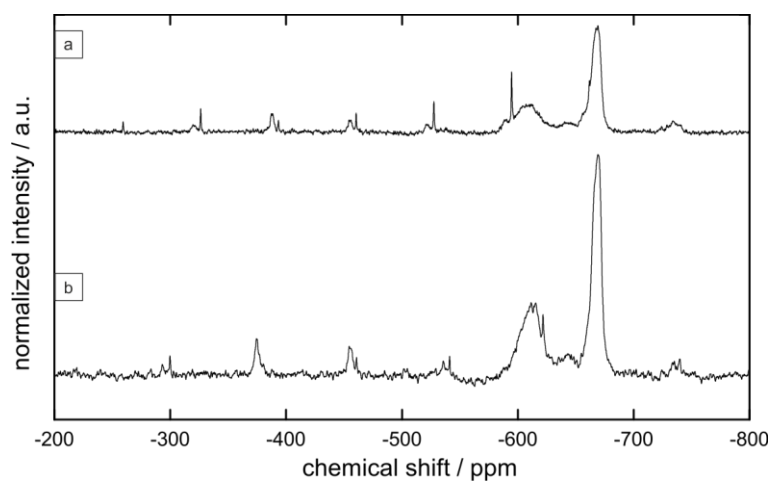
Figure B3 ^{119}Sn ssNMR spectra of the intermediate precipitated during hydrothermal treatment measured at different spinning frequencies: a) 10 kHz and b) 12 kHz. This revealed the center band of [SnCl$_5$H$_2$O]$^-$ to be positioned at -460.8 ppm.

Appendix C
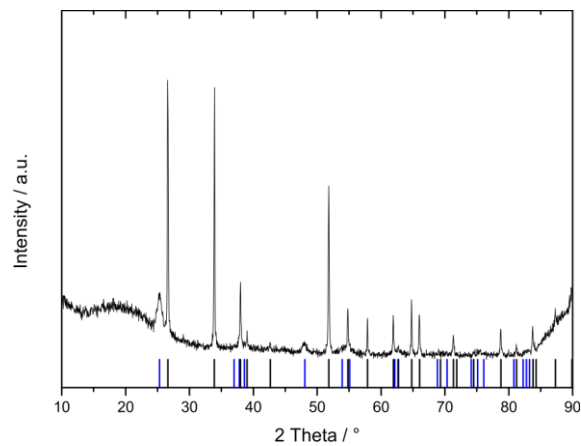
Figure C1 XRD pattern of a SnO$_2$@TiO$_2$ hybrid particles synthesized following the hydrothermal method at 30 bar in 10 mM NaOH. The reference ticks belong to cassiterite (black, JCPDS 96-900-9083) and anatase (blue, JCPDS 96-900-9087), respectively.
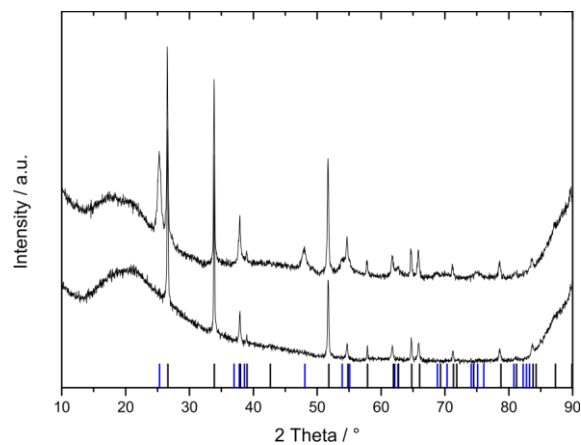
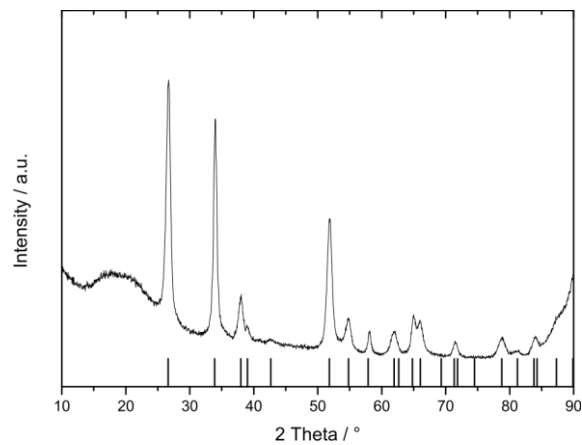Figure C2 XRD patterns of SnO$_2$@TiO$_2$ hybrid particles following the surfactant-mediated hybrid formation prior to (bottom) and after (top) a thermal treatment at 450 °C. The reference ticks belong to cassiterite (black, JCPDS 96-900-9083) and anatase (blue, JCPDS 96-900-9087), respectively.
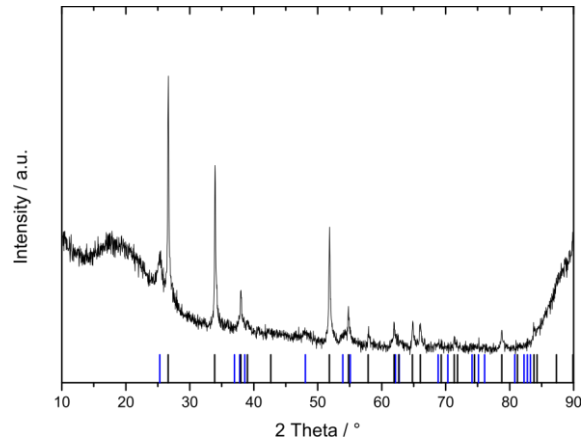
Figure C3 XRD pattern of SnO$_2$@TiO$_2$ hybrid particles synthesized in tri-*n*-octylamine. The reference ticks belong to cassiterite (black, JCPDS 96-900-9083) and anatase (blue, JCPDS 96-900-9087), respectively.
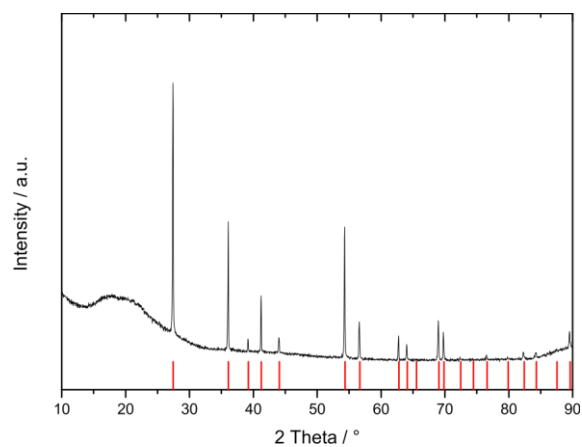

Figure C4 XRD pattern of SnO$_2$@TiO$_2$ hybrid particles synthesized using a mild hydrothermal treatment at 0.5 bar for 2 h. The reference ticks belong to cassiterite (JCPDS 96-900-9083).
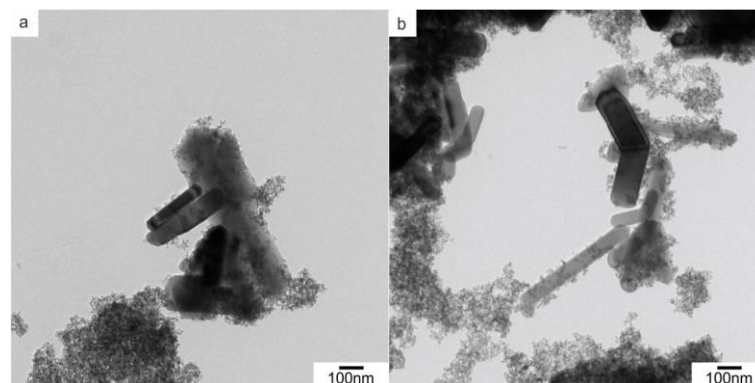
Figure C5 TEM images of TiO$_2$@TiO$_2$ hybrid particles comparing the influence of the pH during hydrothermal hybrid formation at 30 bar: a) pH 9 and b) pH 5.

_____

Figure C6 XRD pattern of TiO$_2$@TiO$_2$ hybrid particles synthesized via a mild hydrothermal treatment at 0.5 bar for 2 h. The reference ticks belong to rutile (JCPDS 96-900-7532).

Table D1 Calculated band-gaps from Kubelka-Munk plots for samples used as DSC electrode materials.

Sample	Band-Gap / eV
TiO$_2$-P25	3.45
Rutile sub-micron rods	3.15
Anatase nanoparticles	3.22
TiO$_2$@TiO$_2$ Hybrid particles	3.12
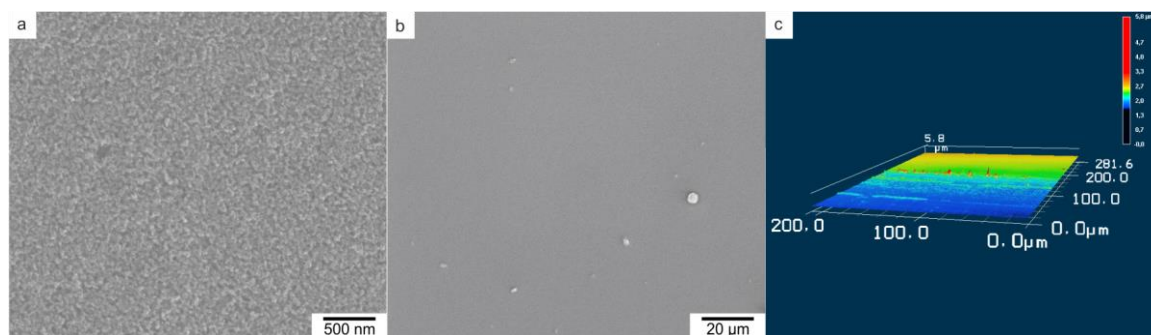
Figure D1 SEM (a, b) and CLSM profile images (c) of electrode films made of a commercial paste from Dyesol. The films, in this case, were demanded to be very thin. Herein, the images indicate the high film quality of the electrode films. The photo-anodes were fully transparent.
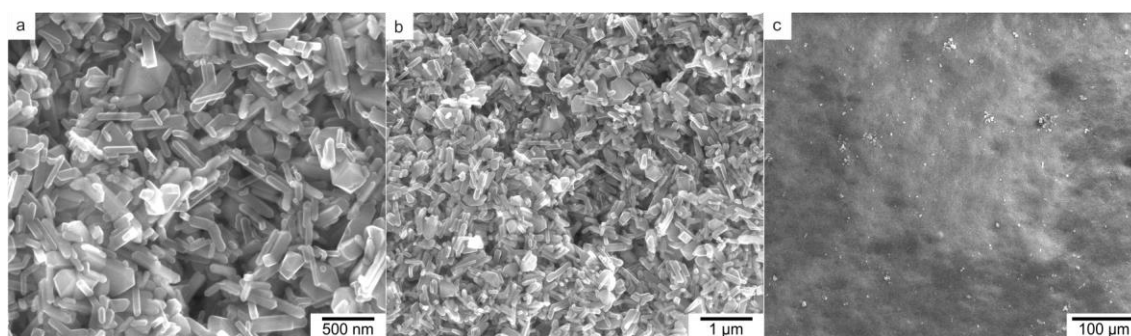
Figure D2 SEM images in different magnifications of electrode films containing 100 wt% sub-micron rutile rods. Here, also a high film quality was achieved.
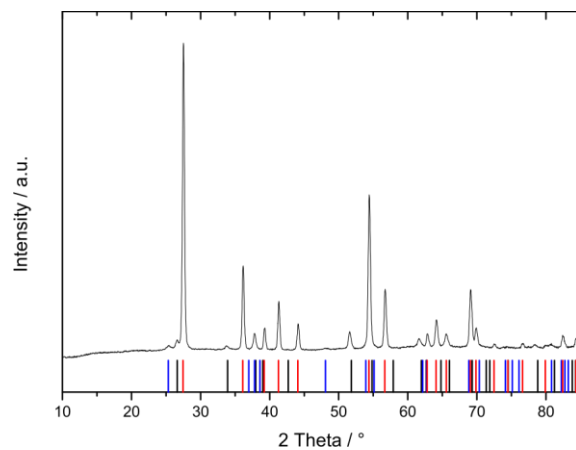
Figure D3 XRD pattern recorded of a sample made of an *in situ* hybrid electrode on an FTO glass substrate. The reference ticks belong to rutile (red, JCPDS 96-900-7532), cassiterite (black, JCPDS 96-900-9083), and anatase (blue, JCPDS 96-900-9087), respectively. The inserted particles were rutile-phase, the *in situ* formed particles anatase, while the SnO_2 originated from the FTO substrate.
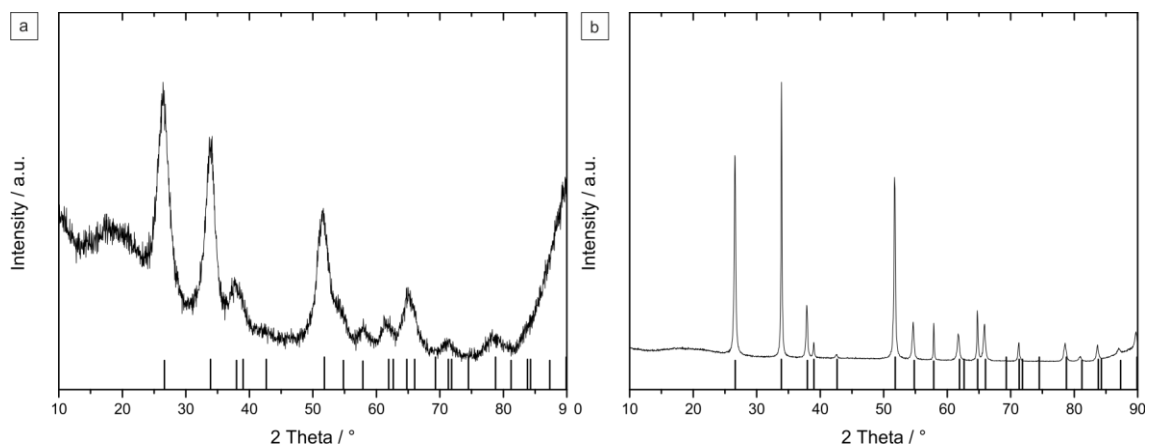
Figure E1 PXRD patterns of spherical (a) and rod-shaped (b) SnO_2 particles. The reference ticks belong to cassiterite (JCPDS 96-900-9083).
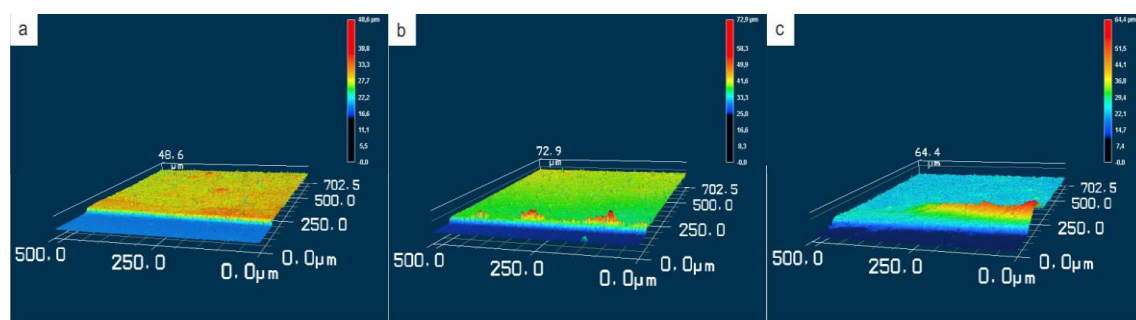

Figure E2 CLSM profile images of the references used in this chapter: Reference 1 (a), Reference 2 (b), and Reference 3 (c).
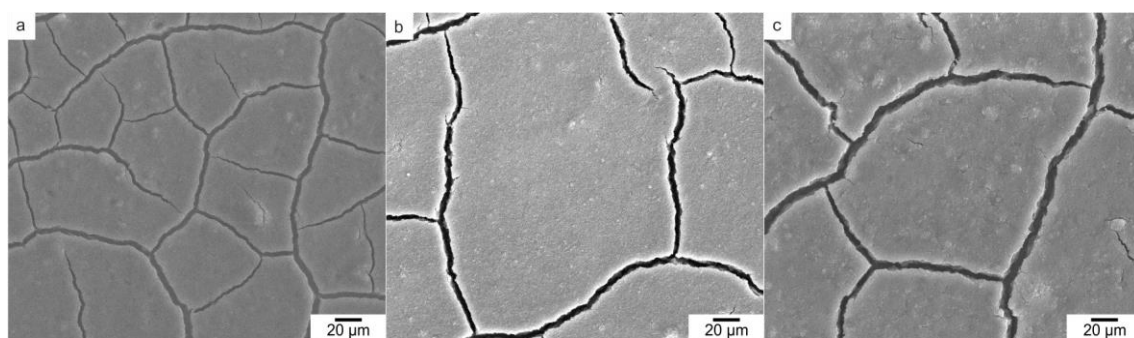

Figure E3 SEM images of the references used in this chapter: Reference 1 (a), Reference 2 (b), and Reference 3 (c).
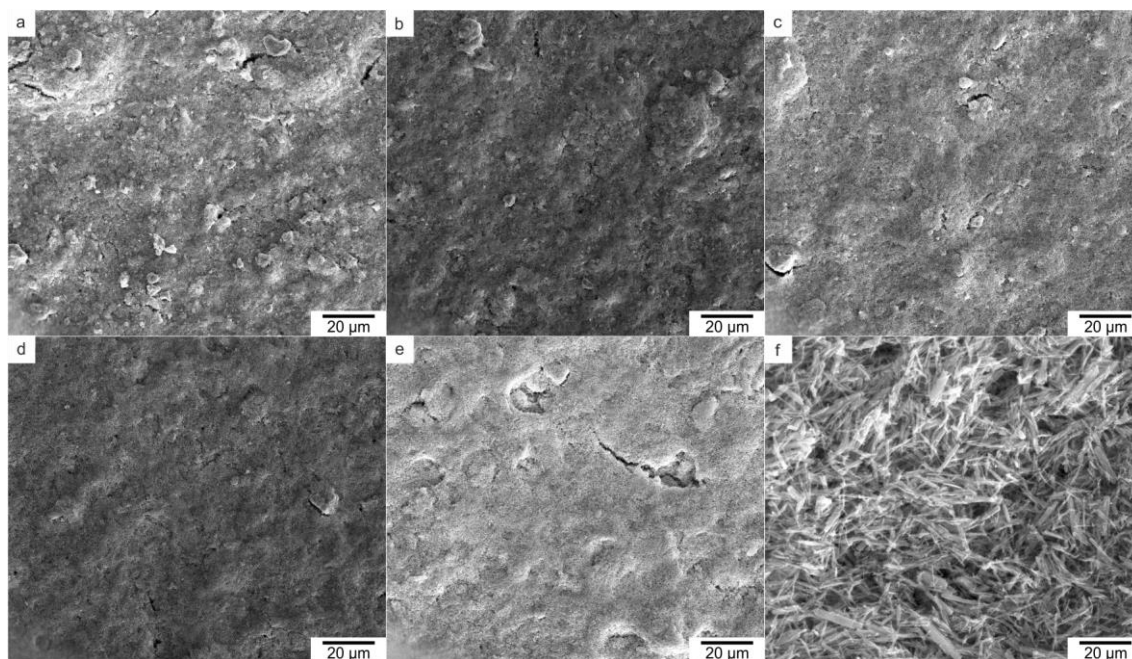
Figure E4 SEM overview images of electrode films containing 60 wt% (a), 70 wt% (b), 80 wt% (c), 90 wt% (d), and 100 wt% (e) SnO_2 rods. f) shows a close-up image of the sample containing 100 wt% rods.
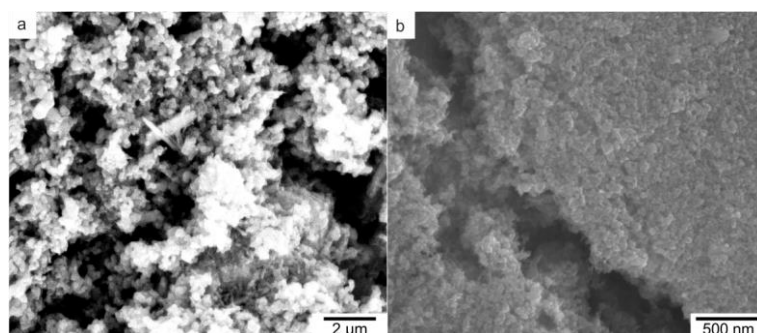

Figure E5 Close-up SEM images of electrode films made of SnO_2@TiO_2 hybrid particles: a) thick shell hybrids and b) *ex situ* hybrids.

Table E1 Solar cell characteristics of all samples that were characterized using electrochemical analysis one week after first *J-V*-measurements. The measurements were performed by ▮▮▮▮▮▮▮▮▮.

Sample	*Voc* / V	*Jsc* / mA/cm^2	FF / %	η / %
Reference	0.78	3.61	0.75	2.13
20 wt% rutile rods	0.74	5.57	0.76	3.14
10 wt% rutile rods	0.73	5.94	0.75	3.26
In situ TiO$_2$@TiO$_2$ hybrids	0.75	4.49	0.75	2.55
SnO$_2$ rods acidic	0.32	9.61	0.41	1.27
Ex situ SnO$_2$@TiO$_2$ hybrids	0.54	5.58	0.62	1.88

Patrick Leidich

Curriculum Vitae

■ **Persönliche Daten**

■ **Ausbildung**

■ **Wissenschaftlicher Lebenslauf**